Search for Single Production of Vector-like Quarks Decaying into Wb in pp Collisions at $\sqrt{s} = 13$ TeV with the ATLAS Detector

Dissertation
zur Erlangung des akademischen Grades

doctor rerum naturalium

(Dr. rer. nat.)

im Fach Physik

Spezialisierung: Experimentalphysik

eingereicht an der

Mathematisch-Naturwissenschaftlichen Fakultät
der Humboldt-Universität zu Berlin

von

M.Sc. Dustin Biedermann

Präsidentin der Humboldt-Universität zu Berlin
Prof. Dr.-Ing. Sabine Kunst

Dekan der Mathematisch-Naturwissenschaftlichen Fakultät
Prof. Dr. Elmar Kulke

Gutachter/innen:

1. Prof. Dr. Heiko Lacker
2. Prof. Dr. Thomas Lohse
3. Prof. Dr. Ulrich Husemann

Tag der mündlichen Prüfung: 19.12.2019

Abstract

This thesis presents a search for singly produced vector-like T quarks with charge $+2/3$ or Y quarks with charge $-4/3$. These exotic particles are predicted by several beyond-the-standard-model theories which try to shed light on the mechanism of electro-weak symmetry breaking, thus addressing the *Naturalness Problem*. The analysis is performed on a proton–proton collision data set with an integrated luminosity of 36.1 fb^{-1} at a centre-of-mass energy of $\sqrt{s} = 13$ TeV recorded in 2015 and 2016 by the ATLAS detector at the LHC. The focus is on leptonically decaying W bosons from $Y/T \to Wb$ decays of the heavy quarks and the event selection requires a jet leading in transverse momentum and being b-tagged, exactly one lepton, a forward jet as well as missing transverse energy beside several isolation requirements.

No significant deviation from the expected Standard Model background is observed. Therefore, upper limits on the coupling strength and mixing angle between third generation Standard Model quarks and a T from a singlet model as well as a Y from a (B, Y) doublet or a (T, B, Y) triplet model are computed using the $\mathrm{CL_s}$ method. This search represents the first analysis in which the interference effects with the Standard Model background are taken into account. The smallest upper limits are found to be $|\sin\theta_\mathrm{L}| = 0.18$ for a T singlet for a mass of 800 GeV, $|\sin\theta_\mathrm{R}| = 0.17$ in the (B, Y) doublet case at 800 GeV and $|\sin\theta_\mathrm{L}| = 0.16$ for the (T, B, Y) triplet model. The observed limits on the mixing parameter $|\sin\theta_\mathrm{R}|$ are competitive with indirect bounds from electroweak precision observables in the mass range between about 800 GeV and 1250 GeV. For the Y in the (B, Y) doublet model, also an observed mass limit of 1.64 TeV is determined for a right-handed coupling value of $c_R^{Wb} = 1/\sqrt{2}$.

Zusammenfassung

In dieser Dissertation wird die Suche nach einzeln erzeugten vektorartigen T-Quarks mit einer elektrischen Ladung $+2/3$ und Y-Quarks mit einer elektrischen Ladung von $-4/3$ vorgestellt. Diese exotischen Teilchen werden von verschiedenen Modellen jenseits des Standardmodells vorhergesagt, welche versuchen das Verständnis der elektorschwachen Symmetriebrechung zu erweitern und somit das *Naturalness Problem* zu lösen. Hierfür werden die in 2015 und 2016 bei einer Schwerpunktsenergie von $\sqrt{s} = 13$ TeV und einer integrierten Luminosität von 36.1 fb^{-1} vom ATLAS Detektor am LHC aufgezeichneten Proton–Proton–Kollisionen ausgewertet. Die Ereignisselektion ist auf leptonisch zerfallende W-Bosonen der $Y/T \to Wb$ Zerfälle ausgerichtet, weshalb ein hochenergetischer, von einem Bottom-Quark stammender Jet, ein einzelnes Lepton, ein in Vorwärtsrichtung emittierter Jet sowie fehlende transversale Energie, neben verschiedenen Isolationskriterien, verlangt wird.

Es konnte keine signifikante Abweichung zur Vorhersage des Standardmodells gemessen werden. Aus diesem Grund wurden obere Grenzen for die Kopplungsstärke und den Mischungswinkel von T-Quarks in einem Singulett-Modell sowie Y-Quarks eines (B, Y)-Dublett bzw. (T, B, Y)-Triplett-Modells mit Quarks der dritten Generation des Standard Modells bestimmt. Hierbei wurden erstmalig Interferenzeffekte mit Standardmodellprozessen berücksichtigt. Die obere Grenze für den Mischungswinkel wurden für ein T-Singulett-Modell bei einer Masse von 800 GeV zu $|\sin\theta_{\mathrm{L}}| = 0.18$, für ein Y eines (B, Y)-Dublett-Modells zu $|\sin\theta_{\mathrm{R}}| = 0.17$ sowie für ein Y eines (T, B, Y)-Triplett-Modells zu $|\sin\theta_{\mathrm{L}}| = 0.16$ bestimmt. Die ermittelten Grenzen innerhalb des (B, Y)-Dublett-Modells im Massenbereich 800 GeV bis 1250 GeV sind zu indirekten, aus elektroschwachen Präzisionsvariablen abgeleiteten Schranken kompetitiv.

Contents

List of Figures

Chapter 1.

Introduction

Experimental and theoretical efforts of particle physicists over several decades have resulted in the formulation of the Standard Model of Particle Physics (SM) [1, 2]. This quantum field gauge theory is capable in correctly predicting the outcome of every particle physics laboratory experiment within the corresponding uncertainties. However, occasionally tensions between the measurement and the theoretical prediction are observed, which usually disappear after including more data [3–5]. Beside this, several more severe problems of the SM exist and indicate the existence of physics beyond the Standard Model (BSM). Many astrophysical observations suggest the existence of some type of stable, massive particles which do not interact electromagnetically, so called *dark matter* [6–8]. Furthermore, the accelerated expansion of the universe can not be explained and the energy driving this expansion is therefore referred to as *dark energy* [8, 9].

Given these observations, it is widely believed that the Standard Model is a low energy approximation of a more general theory and thus has to be treated as an *effective field theory* [10]. If this is true, an additional inconsistency shows up: the *Naturalness Problem* [11–13]. This problem is connected to the mechanism of electroweak symmetry breaking and can be summarised in the question: Why is the Higgs boson so light? Considering the SM as lowest order of an operator product expansion, the Higgs mass would naturally correspond to the energy scale where BSM physics would occur. However, as the mass of the Higgs boson is found to be about 125 GeV, this is obviously not the case.

To address this issue, several alternative or complementary theories to the SM were developed such as little Higgs models or composite Higgs models [14–16]. In many of these theories, exotic coloured particles are predicted, so called *vector-like quarks* (VLQs). In contrast to additional chiral quarks, these particles are not excluded due to the discovery of the

Higgs boson [17, 18], especially by the measured $pp \to h \to \gamma\gamma$ cross-section [19]. The distinguishing property of VLQs is their universal right- and left-handed coupling to the vector bosons. Thus, these particles interact via a vector-current and not via a vector-minus-axial-vector-current to the W boson.
The Large Hadron Collider (LHC) [20], installed at CERN near Geneva and in operation since 2009, is designed to provide data for high precision measurements and to tackle the unsolved puzzles of particle physics. It provides proton–proton (pp) collisions in four interaction points with unprecedented centre-of-mass energies of up to 13 TeV with an instantaneous luminosity of up to 10^{34} cm^{-2}s^{-1} to its hosted experiments, whereby the largest detector is ATLAS (A Large Toroidal LHC ApparatS) [21].

This thesis uses data collected by the ATLAS detector in 2015 and 2016 with centre-of-mass energy of $\sqrt{s} = 13$ TeV to search for two kinds of VLQs, namely so-called vector-like Y and T quarks. The results have been published in [22] and in [23] for a previous version of the analysis on the 2015 data set only.
To provide a theoretical basis for the performed analysis in Chapter 2, the Standard Model of particle physics is outlined, the problems of the SM are sketched and an introduction to vector-like quarks is given. To perform an analysis on the data collected by the ATLAS detector, it is crucial to understand each relevant component of the detector itself. Therefore, Chapter 3 describes all components which are of importance for this analysis. To compare the measurement with the theoretical prediction (SM or new physics), it is necessary to model background and signal processes appropriately and Chapter 4 is dedicated to this subject. Chapter 5 explains in some detail how the raw data provided by the detector components is used to reconstruct the physical objects. In Chapter 6, theory and experiment are brought together and an analysis strategy for the search for VLQs is developed, which is focused on final states with high energetic *b-tagged jets* and *single leptons*. This eventually leads to the final event selection of this analysis. Any measurement is suffering from uncertainties. While statistical uncertainties can be treated in a general and formalised fashion, systematic uncertainties are a more challenging problem. How this issue is treated is subject of Chapter 7. The results of this thesis are of statistical nature and thus are relying on statistical methods, which are outlined in Chapter 8 followed by the final results. The last Chapter 9 gives a short summary of the performed analysis and achieved results.

Chapter 2.

Theoretical Deliberations

In order to develop an analysis for the search for new physics phenomena such as VLQs, it is important to understand the established physics model and how the new theory is related to it. This is not only important to avoid potential pitfalls but provides the basis for inventing a sensitive algorithm to enhance the fraction of potential signal over background events. For the search for VLQs the "well known physics" is the extremely successful and exhaustively tested Standard Model of particle physics.

2.1. Standard Model of Particle Physics

The Standard Model is a quantum field gauge theory and represents the condensed knowledge of elementary particles and their interactions. In this model, the known particles are described as quantum excitations of the corresponding fields and the interactions of these quanta are introduced due to the requirement of local gauge invariance with respect to the appropriate symmetry group. Its particle content is summarised in Fig. 2.1 and will be explained in the following (the discussion is based on [1, 2]).

2.1.1. Fields and Forces

The Standard Model describes six different leptonic fields with spin $\frac{1}{2}$, which are commonly arranged in three doublets of fermions, called families or generations:

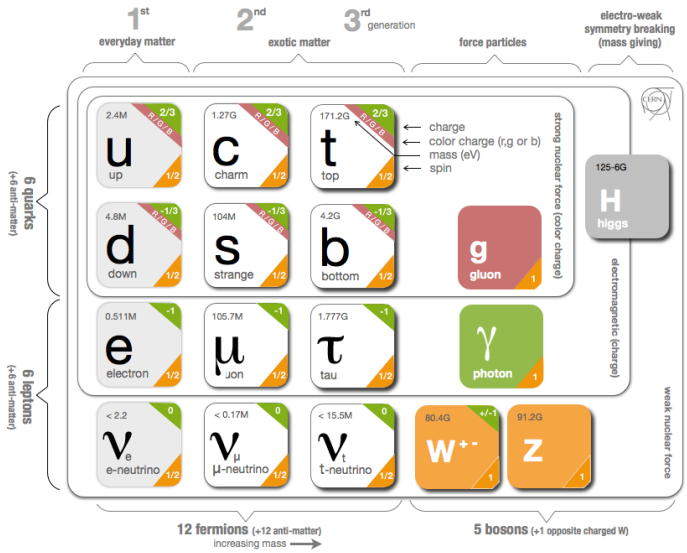

Figure 2.1.: Particle content of the Standard Model (taken from [24])

$$\begin{pmatrix} \nu_e \\ e \end{pmatrix} \text{ electron neutrino} \qquad \begin{pmatrix} \nu_\mu \\ \mu \end{pmatrix} \text{ muon neutrino} \qquad \begin{pmatrix} \nu_\tau \\ \tau \end{pmatrix} \text{ tau neutrino}$$
$$\text{electron} \qquad\qquad \text{muon} \qquad\qquad \text{tau}$$

The upper fields carry no electric charge, whereas the lower ones carry electric charge -1 (all charges are always given in units of e, the magnitude of the electron charge). Additionally, there are 3 families of quarks:

$$\begin{pmatrix} u \\ d \end{pmatrix} \text{ up quark} \qquad \begin{pmatrix} c \\ s \end{pmatrix} \text{ charm quark} \qquad \begin{pmatrix} t \\ b \end{pmatrix} \text{ top quark}$$
$$\text{down quark} \qquad\qquad \text{strange quark} \qquad\qquad \text{bottom quark}$$

The six types of quarks are referred to as *flavours*. All quark fields carry electric charge, the upper fields (up-type) $\frac{2}{3}$ and the lower fields (down-type) $-\frac{1}{3}$, respectively.

The kinetic term of the Lagrangian density of a free fermion is given by

$$\mathcal{L} = \overline{\psi}(i\partial\!\!\!/)\psi. \tag{2.1}$$

Applying the Euler-Lagrange equation

$$\partial_\mu \left(\frac{\partial \mathcal{L}}{\partial \left(\partial_\mu \psi^i \right)} \right) = \frac{\partial \mathcal{L}}{\partial \psi^i}, \tag{2.2}$$

where $\psi^i \in \{\psi,\ \overline{\psi}\}$, would lead to the Dirac equation as the equation of motion for the massless fields ψ and $\overline{\psi}$.
These free fields would propagate without any interaction and thus would not be detectable. To introduce interactions to the model, invariance of the Lagrangian under local gauge transformations of the fields

$$\psi \to e^{i\alpha^a(x)t^a}\psi \tag{2.3}$$

is required. Here, t^a are the generators of the gauge group, $\alpha^a(x)$ are numbers which depend on the space-time x and a runs over all generators. Without the derivative, Equation 2.1 would be gauge invariant. However, due to the x dependence of $\alpha^a(x)$, some difficulties occur considering derivatives. The derivative of $\psi(x)$ in direction n is defined as

$$n^\mu \partial\psi = \lim_{\epsilon \to 0} \frac{1}{\epsilon} \left[\psi(x + \epsilon n) - \psi(x) \right]. \tag{2.4}$$

Since $\psi(x + \epsilon n)$ and $\psi(x)$ transform differently under the transformation in Eq. 2.3, the derivative of ψ has no simple transformation law. In order to subtract the field at neighboring points, the derivative has to be redefined to the *covariant derivative* (for brevity, considering only transformations like $\psi \to e^{i\alpha(x)}\psi$)

$$n^\mu D_\mu \psi = \lim_{\epsilon \to 0} \frac{1}{\epsilon} \left[\psi(x + \epsilon n) - U(x + \epsilon n, x)\psi(x) \right], \tag{2.5}$$

where $U(y, x)$ follows the transformation law $U(y, x) \to e^{i\alpha(y)} U(y, x) e^{-i\alpha(x)}$ and can be chosen as $U(y, x) = e^{i\phi(y,x)}$. This *comparator* can be expanded as

$$U(x + \epsilon n, x) = 1 - ig\epsilon n^\mu A_\mu(x) + \mathcal{O}(\epsilon^2), \tag{2.6}$$

where g is an arbitrary constant and $A_\mu(x)$ is a new vector field.
Combining Eq. 2.5 and Eq. 2.6 results in (from now on the x dependence is suppressed)

$$D_\mu \psi = \partial_\mu \psi + igA_\mu \psi. \tag{2.7}$$

The so called *connection* A_μ transforms as

$$A_\mu \to A_\mu - \frac{1}{g}\partial_\mu \alpha. \tag{2.8}$$

For general transformations of the form 2.3, Equations 2.7 and 2.8 become

$$D_\mu \psi(x) = \partial_\mu \psi + igA_\mu^a t^a \psi \tag{2.9}$$

and

$$A_\mu \to A_\mu - \frac{1}{g}\partial_\mu \alpha^a + f^{abc} A_\mu^b \alpha^c, \tag{2.10}$$

where the set of numbers f^{abc} are called *structure constants* and are defined by the commutator of the generators

$$\left[t^a, t^b\right] = i f^{abc} t^c. \tag{2.11}$$

Thus, to obtain a theory exhibiting local gauge invariance, new fields A_μ^a have to be introduced. It can be shown that these connections obey Bose-Einstein-Statistics and are consequently called gauge bosons. Since these bosons show up in the definition of the covariant derivative, interactions between the "original" fermions and the gauge bosons appear. This in turn results in a potential between particles carrying the corresponding charge (defined as the eigenvalue of the generator), which eventually results in a force. Therefore, gauge bosons can be considered as mediators of the forces. Additionally, interaction terms containing exclusively gauge bosons are caused by non-zero-valued structure constants. Theories with structure constants equal to zero are called abelian and with non-zero structure constants they are referred to as non-abelian theories.
What is missing up to now is the kinetic term of the gauge bosons which has to be added to complete the construction of a locally invariant Lagrangian: a locally invariant term that depends on A_μ and its derivatives, but not on ψ ([2] page 483). These terms are constructed using the field strength tensor

$$F_{\mu\nu}^a = \partial_\mu A_\nu^a - \partial_\nu A_\mu^a + g f^{abc} A_\mu^b A_\nu^c, \tag{2.12}$$

which transforms as

$$F^a_{\mu\nu} \to F^a_{\mu\nu} - f^{abc}\alpha^b F^c_{\mu\nu}. \tag{2.13}$$

With these ingredients it is possible to construct a locally invariant Lagrangian for a given continuous symmetry group.
It is found that the observed forces and phenomena are properly described by constructing a Lagrangian density invariant under the $U(1)_Y \times SU(2)_L \times SU(3)_C$ gauge group.

The non-abelian subgroup $SU(3)_C$ accounts for the strong interactions, which couple to the colour quantum numbers of the quarks (leptons do not carry colour). Due to its eight generators, known as Gell-Mann matrices, the strong force obtains eight massless bosons, called gluons. The part of the SM describing the strong force is referred to as *Quantum Chromodynamics* (QCD).
To quantise the theory, the coupling constants and masses have to be redefined to avoid indefinite terms in observable quantities. This procedure is called renormalisation and results in a variation of the strength of the coupling constants as a function of the energy of the process (this is a general feature of quantum field theories), the coupling constant is *running*. In fact, the coupling constant of the strong force becomes larger as the energy becomes smaller or as the distance becomes larger and the QCD potential grows with distance. This means that an infinite amount of energy would be needed to separate quarks asymptotically and finite energy systems can only exist in colourless states. Thus, quarks are bound together and no free quarks are observable, which is known as *confinement* ([1] page 532). So, all physical hadrons are assumed to be singlets of $SU(3)_C$. The simplest allowed ones are mesons ($\overline{q}^i q_i$), baryons ($\epsilon^{ijk} q_i q_j q_k$) and anti-baryons ($\epsilon^{ijk}\overline{q}_i\overline{q}_j\overline{q}_k$), where ϵ^{ijk} denotes the Levi-Civita-Tensor. Due to the large coupling constant, low energy processes are not calculable using perturbation theory. On the other hand, the coupling becomes small for high-energy processes and the quarks behave like unbound particles if the energy of the process is large enough. This is called asymptotic freedom ([2] page 425-427). Therefore, an energetic threshold Λ_{QCD} exists which separates low energy processes from high energy processes which can be treated by perturbation theory and it is found that $\Lambda_{\mathrm{QCD}} \approx 200\,\mathrm{MeV}$.

The subgroup $U(1)_Y \times SU(2)_L$ accounts for the electroweak interactions, originally described by Weinberg, Salam and Glashow in 1967/1968 [25–27]. Here, one could be tempted to associate the $3+1$ connections, corresponding to the $3+1$ generators of the group, directly with the physical bosons $W^{\pm}$, Z^0 and γ, but there occurs to be a problem due to the observed non-zero masses of the $W^{\pm}$ and Z^0, since the theory does not contain mass terms for these particles up to now.

2.1.2. Higgs Mechanism

All fermions as well as the W and Z bosons are known to carry mass. Thus, a theory describing these particles has to contain corresponding mass terms but due to the requirement of local gauge invariance several problems occur in the so far developed framework.

Gauge Boson Mass Terms

A gauge boson mass term, quadratic in fields, would violate explicitly local gauge invariance due to the transformation law in Eq. 2.10. However, a theory which properly describes the observed phenomena necessarily also incorporates massive gauge bosons, the electroweak symmetry (EWS) has to be broken. It has been shown [28–30] that due to the addition of a set of scalar fields ϕ_i it is possible to generate massive gauge bosons without violating local gauge invariance. The ϕ_i transform as

$$\phi_i \to (1 + i\alpha^a t^a)_{ij}\phi_j. \tag{2.14}$$

It is convenient to treat the n complex fields ϕ_i as $2n$ real valued fields. This allows to write $t^a_{ij} = iT^a_{ij}$, where the T^a are real and antisymmetric. Now, the covariant derivative on ϕ_i reads $D_\mu\phi = (\partial_\mu + gA^a_\mu T^a)\phi$ and, thus, the kinetic energy term for the ϕ_i is

$$\frac{1}{2}(D_\mu\phi_i)^2 = \frac{1}{2}(\partial_\mu\phi_i)^2 + gA^a_\mu(\partial_\mu\phi_i T^a_{ij}\phi_j) + \frac{1}{2}g^2 A^a_\mu A^{b\mu}(T^a\phi)_i(T^b\phi)_i, \tag{2.15}$$

where the last term has the form of a gauge boson mass. If now $\langle\phi_i\rangle = (\phi_0)_i$ is a non-zero vacuum expectation value, the fields A_μ acquire mass with the mass matrix

$$m_{ab}^2 = g^2(T^a\phi_0)_i(T^b\phi_0)_i. \tag{2.16}$$

However, those fields for which the corresponding generator leaves the vacuum invariant, remains massless.

Now, in the case of the SM, the scalar field ϕ is introduced which transforms as a doublet according to $SU(2)_L$ gauge transformations. This *Higgs* field has to acquire a non-zero vacuum expectation value and in *unitarity gauge* it can be written as (see [2] p. 715)

$$\phi = \frac{1}{\sqrt{2}} \begin{pmatrix} 0 \\ v + h\,(x) \end{pmatrix} \tag{2.17}$$

with the groundstate $\langle\phi\rangle = \left(0, v/\sqrt{2}\right)$.
A possible additional Lagrangian which provides the required transformational behaviour and the requested vacuum expectation value is

$$\mathcal{L}_{higgs} = |D_\mu\phi|^2 + \mu^2\phi^\dagger\phi - \lambda\left(\phi^\dagger\phi\right)^2, \tag{2.18}$$

with $v = \left(\frac{\mu^2}{\lambda}\right)^{\frac{1}{2}}$ and

$$D_\mu\phi = \left(\partial_\mu - igA_\mu^a\tau^a - ig'B_\mu Y\right)\phi. \tag{2.19}$$

Hereby, τ^a are the generators of $SU\,(2)_L$, the charge associated to the generator Y of $U(1)_Y$ is assigned to equal $\frac{1}{2}$ (not used in the equation). The numbers g and g' are two coupling constants.
Evaluating the first term in Eq. 2.18, neglecting $h\,(x)$ and terms containing ∂_μ, leads to

$$\mathcal{L}_{higgs} = \frac{1}{2}\frac{v^2}{4}\left[g^2\left(A_\mu^1\right)^2 + g^2\left(A_\mu^2\right)^2 + \left(-gA_\mu^3 + g'B_\mu\right)^2\right] + \ldots \tag{2.20}$$

This can be written in terms of the rotated fields

$$W_\mu^\pm = \frac{1}{\sqrt{2}}\left(A_\mu^1 \mp iA_\mu^2\right) \qquad \text{with mass} \qquad m_W = g\frac{v}{2}, \tag{2.21}$$

$$Z_\mu^0 = \frac{1}{\sqrt{g^2+g'^2}}\left(gA_\mu^3 - g'B\mu\right) \qquad \text{with mass} \qquad m_Z = \sqrt{g^2+g'^2}\frac{v}{2}. \tag{2.22}$$

Now, these massive fields can be identified with the observed massive vector bosons $W^\pm$ and Z^0, as indicated by the notation.
The fourth field, orthogonal to Z_μ^0,

$$A_\mu = \frac{1}{\sqrt{g^2+g'^2}}\left(g'A_\mu^3 + gB\mu\right) \qquad \text{with mass} \qquad m_A = 0, \tag{2.23}$$

can be identified with the still massless electromagnetic field.

Certainly, it is now convenient to write the covariant derivative for a fermion belonging to a $SU(2)_L$ representation and with $U(1)_Y$ charge Y in terms of these fields, too. Before doing so, it is common to perform some substitutions.
The electron charge e is introduced by

$$e = \frac{gg'}{\sqrt{g^2+g'^2}} \tag{2.24}$$

and the electric charge operator is identified with

$$Q = \tau^3 + Y. \tag{2.25}$$

Additionally,

$$T^\pm = \tau^1 \pm i\tau^2 \tag{2.26}$$

and the *weak mixing angle* θ_w is defined by

$$\cos\theta_w = \frac{g}{\sqrt{g^2+g'^2}}, \qquad \sin\theta_w = \frac{g'}{\sqrt{g^2+g'^2}}. \tag{2.27}$$

The covariant derivative can now be written as

$$D_\mu = \partial_\mu - i\frac{g}{\sqrt{2}}\left(W_\mu^+ T^+ + W_\mu^- T^-\right) - i\frac{g}{\cos\theta_w} Z_\mu \left(T^3 - \sin^2\theta_w Q\right) - ieA_\mu Q. \tag{2.28}$$

Fermion Mass Terms

The addition of fermion mass terms reveals a similar problem as for the boson mass terms. To properly describe the observed physics, it turns out that the left- and right-handed fermion spinors have to be assigned to different representations of the appropriate symmetry group, since only left-handed spinors couple to the W bosons. However, the natural choice for a fermion mass term, a Dirac mass term, mixes these components

$$\mathcal{L}_{f_m} = -m_f \overline{f} f = -m_f \overline{f}\left(P_L^2 + P_R^2\right) f = -m_f\left(\overline{f}_L f_R + \overline{f}_R f_L\right). \tag{2.29}$$

since the projectors $P_{L/R}$ are defined as $P_{L/R} = \frac{1}{2}(1 \pm \gamma^5)$ and γ^5 anti-commutes with γ^0 in $\overline{f} = f^\dagger\gamma^0$. If f_L and f_R transform differently under gauge transformations, $\mathcal{L}_{f_m}$ is not gauge invariant.

To overcome this issue it is possible to use a similar approach as for the gauge bosons. It is possible to add the fermionic mass terms to the theory in a similar manner as the bosonic mass terms were added, namely via a coupling with the Higgs field.
This interaction, called *Yukawa coupling*, looks like (with massless neutrinos)

$$\mathcal{L}_{yukawa} = -\sum_{j=1}^{3} \lambda_f^j \overline{F}_L^j \phi f_R^j - \sum_{j,k=1}^{3}\left(\lambda_D^{jk}\overline{Q}_L^j \phi d_R^k + \lambda_U^{jk}\epsilon^{ab}\overline{Q}_{La}^j \phi_b^\dagger u_R^k\right) + h.c. \tag{2.30}$$

Here, $\overline{F}_L^j = \begin{pmatrix} \nu_{f_j} \\ f_j \end{pmatrix}_L$ is the $SU_L(2)$ spinor of the lepton family j and $Q_L^j = \begin{pmatrix} u_j \\ d_j \end{pmatrix}_L$ is the quark spinor of the j-th generation, where d_j and u_j denote the related down-type and up-type quark, respectively, the various λ_i^{jk} are the Yukawa couplings and $h.c.$ denotes the hermitian conjugate.
The $SU(2)$ indices of the left-handed spinors and ϕ contract and the $U(1)_Y$ charges Y can be chosen consistently to sum to zero. Therefore, Eq. 2.30 is manifestly gauge invariant. Plugging in the vacuum expectation value of ϕ, the mass terms become obvious

$$\mathcal{L}_{yukawa} = -\frac{1}{\sqrt{2}}\lambda_d v \overline{d}_L d_R - \frac{1}{\sqrt{2}}\lambda_u \overline{u}_L u_R + h.c. + \dots \tag{2.31}$$

2.1.3. The CKM-Matrix

Generally, in a theory which contains more than one quark generation, the appearance of generation mixing terms is possible[1]. Instead of handling such mixing terms, it is convenient to write the quark states in a basis which diagonalises the Higgs couplings. These states (unprimed) are related to the original basis (primed) by the unitary transformation U_u and U_d

$$u_L'^i = U_u^{ij} u_L^i, \qquad d_L'^i = U_d^{ij} d_L^j. \tag{2.32}$$

The unprimed states are physical because they diagonalise the mass matrix (connected with the Higgs couplings).
The terms in the Lagrangian, which couple the quarks for example to the W^+, take the form

$$\mathcal{L}_{W^+} = \frac{g}{\sqrt{2}} W_\mu^+ \overline{u}_L'^i \gamma^\mu d_L'^i = \frac{g}{\sqrt{2}} W_\mu^+ \overline{u}_L^i \gamma^\mu \left(U_u^\dagger U_d\right)_{ij} d_L^j. \tag{2.33}$$

Hereby, the substitution $\left(U_u^\dagger U_d\right)_{ij} = V_{ij}$ is convenient, where V_{ij} is the famous Cabibbo-Kobayashi-Maskawa (CKM) matrix, where the off-diagonal elements give rise for the observed quark flavour transition.
If within the transformation in Eq. 2.32 U_u^{ij} is diagonalised, only the down-type quarks are

[1] With non-zero neutrino masses this is true for leptons too, but the discussion is restricted to quarks.

rotated and it is

$$\begin{pmatrix} d' \\ s' \\ b' \end{pmatrix} = \begin{pmatrix} V_{ud} & V_{us} & V_{ub} \\ V_{cd} & V_{cs} & V_{cb} \\ V_{td} & V_{ts} & V_{tb} \end{pmatrix} \begin{pmatrix} d \\ s \\ b \end{pmatrix}. \tag{2.34}$$

Due to unitarity and a redefinition of phases of the quark fields, the matrix V_{ij} can be parameterised with three angles and one phase, where a non-zero phase gives rise to CP-violation.

2.1.4. Standard Model Lagrangian

To conclude, the full Lagrangian of the Standard Model can be written as the sum of four terms. Here, the fields will be chosen in the original form and not in the rotated, physical one.

$$\mathcal{L}_{SM} = \mathcal{L}_{fermion} + \mathcal{L}_{gauge} + \mathcal{L}_{higgs} + \mathcal{L}_{yukawa}, \tag{2.35}$$

with

$$\mathcal{L}_{fermion} = \sum_{families} \overline{F}_L \not{D}_\mu F_L + \sum_{fermions} \overline{f}_R \not{D}_\mu f_R. \tag{2.36}$$

Since fermionic fields in general belong to different representations of the different gauge groups, the covariant derivative D_μ has to be modified considering these variations.
For left-handed quark fields, it is

$$D_\mu = \left(\partial_\mu - igA^a_\mu \tau^a - ig' B_\mu Y - ig_s T_a G^a_\mu\right), \tag{2.37}$$

where T_a are the $SU(3)$ generators and G^a_μ the related connections of the strong force.
For left-handed leptonic fields, which do not carry colour, it is

$$D_\mu = \left(\partial_\mu - igA^a_\mu \tau^a - ig' B_\mu Y\right). \tag{2.38}$$

The covariant derivative for the corresponding right-handed fields contain no terms with $igA^a_\mu \tau^a$.

Additionally, a term which contains the free fields of the gauge bosons is added:

$$\mathcal{L}_{gauge} = -\frac{1}{4}A^i_{\mu\nu}A^{\mu\nu}_i - \frac{1}{4}B_{\mu\nu}B^{\mu\nu} - \frac{1}{4}G^i_{\mu\nu}G^{\mu\nu}_i, \tag{2.39}$$

with

$$\begin{aligned} A^i_{\mu\nu} &= \partial_\mu A^i_\nu - \partial_\nu A^i_\mu + g\epsilon^{ijk}A^j_\mu A^k_\nu, \\ B_{\mu\nu} &= \partial_\mu B_\nu - \partial_\nu B_\mu, \\ G^i_{\mu\nu} &= \partial_\mu G^i_\nu - \partial_\nu G_\mu + g_s\epsilon^{ijk}G^j_\mu G^k_\nu. \end{aligned} \tag{2.40}$$

The last two terms in Eq. 2.35 are given in Eq. 2.18 and Eq. 2.31, respectively.

2.2. Proton–Proton Collisions

In this thesis, the compatibility of recorded proton–proton collisions with the Standard Model prediction is tested. However, protons are not elementary but instead are composed of SM particles, i.e. quarks and gluons. The cross-section of the proton–proton collision can be computed in terms of the interactions of the constituting particles using the factorization theorem [31, 32]:

$$\sigma = \sum_{a,b}\int_0^1 dx_a dx_b \int d\Phi_n f_a^{h_1}(x_a,\mu_F) f_b^{h_2}(x_b,\mu_F) \times \frac{1}{2\hat{s}}|\mathcal{M}_{ab\to n}|^2(\Phi_n;\mu_F,\mu_R). \tag{2.41}$$

The parton distribution functions (PDFs), f_a and f_b, for the colliding partons a and b depend on the light-cone momentum fraction x with respect to the parent hadron h and describe the interactions below the factorization scale μ_F. $|\mathcal{M}_{ab\to n}|^2$ denotes the squared matrix element for the process $ab \to n$ and $1/(2\hat{s}) = 1/(2x_a x_b s)$, with s the hadronic centre-of-mass energy squared, and it depends on the phase space Φ_n, the factorization scale μ_F and the renormalisation scale μ_R. The phase space element $d\Phi_n$ is given by:

$$d\Phi_n = \prod_{i=1}^{n}\frac{d^3p_i}{(2\pi)^3 2E_i}\cdot(2\pi)^4\delta^4(p_a + p_b - \sum_{i=1}^{n}p_i), \tag{2.42}$$

with the initial state momenta p_a, p_b as well as the final state momenta and energies p_i and E_i, respectively.

2.3. Problems of the Standard Model

Albeit the fact that the Standard Model is an extremely successful theory and no direct measurement was able to disproof its validity, it is far from being satisfactory (e.g. due to its many free parameters). Furthermore, there are observations which can not be explained within the framework of the Standard Model. Some of these problems are sketched in the following subsections.

2.3.1. Non-SM Observations

Neutrino Masses

In the Standard Model, neutrinos are treated as massless particles. However, it is well known (e.g. [33]) that the flavour eigenstates are oscillating, which is only possible if the masses of the neutrinos are pairwise unequal. Thus, at least two neutrino masses need to be non-zero. It is possible to add neutrino mass terms in a similar fashion as the up-type quark masses were added:

$$L_{\nu_m} = -\lambda_{\nu^i} \epsilon^{ab} \overline{F}_{La} \phi^\dagger \nu_R^i + h.c. \tag{2.43}$$

Two general problems arise from this approach: First, in Eq. 2.43 it was necessary to couple the left-handed fermion spinor with a right-handed neutrino. Since ν_R is uncharged under the weak and electromagnetic force (and of course QCD), it interacts only gravitationally and thus is referred to as *sterile neutrino*. Therefore, even if it exists, it can not be observed. Second, from this kind of terms one would expect masses comparable with the other lepton masses ([2] p. 715) but it is known that neutrino masses are below $\mathcal{O}$(eV). If the masses of the neutrinos are generated by the same mechanism as the other leptons, why are their masses so much smaller?

Mass Hierachy

Fig. 2.2 depicts the masses of the charged fermions as circles with area proportional to the mass of the corresponding particle. The masses span a range of about seven orders of magnitude and the question arises why are they so different? It seems reasonable to assume that there is some kind of mechanism which dynamically generates this spectrum.

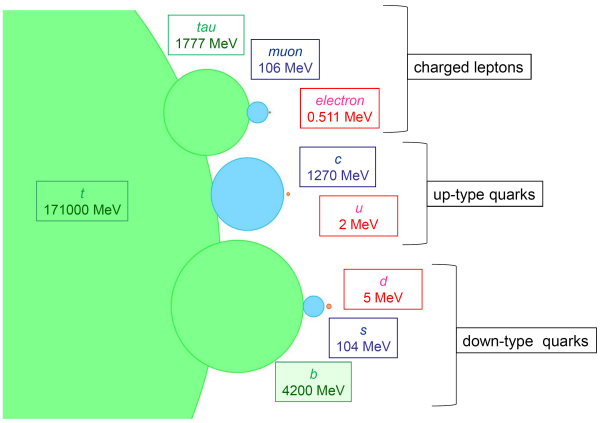

Figure 2.2.: Masses of the charged SM fermions. The area of each circle is proportional to the mass of the corresponding particle. Taken from [34].

These kind of problems might be viewed as aesthetical flaws. However, especially several astrophysical observations reveal more severe issues of the Standard Model.

Dark Matter and Dark Energy

The first indications that there is non-luminous (i.e. not interacting electro-magnetically) *Dark Matter* stem from measurements of rotation curves of galaxies and galaxy clusters [6, 7]. It was found that the velocity of stars and galaxies is not decreasing with increasing distance r after a maximum as expected by the Keplerian law but instead stays constant (see Fig. 2.3). This is most naturally explained if the mass enclosed by the sphere with radius r is also increasing if r increases. Since this is not the case for the luminous matter, there must be non-luminous matter, *Dark Matter*.
Also the strength of *gravitational lensing* on large scales in the universe, the separation of gas and stars during galaxy collisions and the measurement of the observed anisotropy spectrum of the Cosmic Microwave Background [8] points inevitable to the existence of this unknown kind of matter.

It should be stressed that these findings can not be explained by *hot*, i.e. relativistic Dark Matter such as light Standard Model neutrinos or simply non-emitting baryonic matter such as *brown dwarfs*. However, it should also be noted that there are alternative explanations [35], e.g. modifications of general relativity.

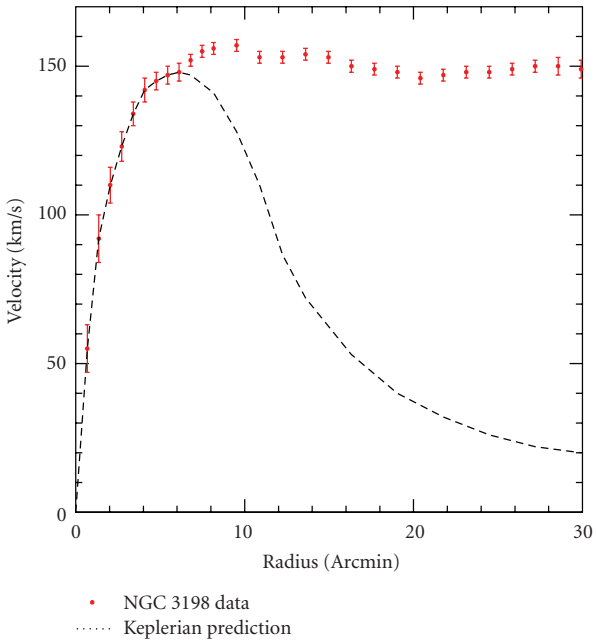

Figure 2.3.: Measured rotational velocities of HI regions in NGC 3198 compared to an idealised Keplerian behavior, taken from [36].

Furthermore, even the sum of the expected energy density of the Dark and ordinary matter is not able to account for the complete energy density of the universe but instead is only about one quarter of it [8, 9]! In principle it could be possible that vacuum expectation values might be the source of the missing energy density. However, if this is the case it would be much too large and it has to be explained if and how it could be reduced (e.g. discussion in [37] p. 405).

Gravity

Probably the most indisputable flaw of the Standard Model is its inability to explain gravity. Albeit it is possible to partially describe gravity by quantizing general relativity semiclassically, this description looses validity around the Planck mass of about $E \gtrsim$

$4\pi M_P \simeq 10^{19}$ GeV [38]. Furthermore, it is has to be explained why the gravitational force is so much smaller than all the other forces. Thus, a more complete theory of nature must exist but it may be visible only at the Planck scale.

2.3.2. Naturalness Problem

The problems described above, especially the last one, let the authors of [38] conclude that "...the SM, given that it has a finite cutoff, is for sure an effective field theory..." ([38] page 2). This means that it *is* a low-energy approximation of a more fundamental theory, where the deviations from this approximation should become visible latest at energies compatible with this cutoff scale Λ_{SM}. To see which consequences might follow from this fact, the Standard Model has to be treated in the framework of *effective field theories*.

A low-energy approximation for a given theory can be obtained by *integrating out* the fields with masses well above the energies of interest, i.e. performing the functional integral with respect to these fields. According to a theorem from Weinberg (see [10] page 6) even without knowing the correct theory, it is possible to build an effective theory by adding all operators (using the known fields) at any given order in perturbation theory with unknown coefficient (can be determined by matching if the true theory is known) which respect the symmetries of the theory. Each of these operators is suppressed by an appropriate power of $1/\Lambda_{\mathrm{SM}}$ (see [10] page 204):

$$\begin{aligned}\mathcal{L} &= \mathcal{L}_{\mathrm{SM}} + \mathcal{L}^{(5)} + \mathcal{L}^{(6)} + \dots \\ &= \mathcal{L}_{\mathrm{SM}} + \frac{1}{\Lambda_{\mathrm{SM}}} \sum_k C_k^{(5)} Q_k^{(5)} + \frac{1}{\Lambda_{\mathrm{SM}}^2} \sum_k C_k^{(6)} Q_k^{(6)} + \mathcal{O}\left(\frac{1}{\Lambda_{\mathrm{SM}}^3}\right).\end{aligned} \tag{2.44}$$

Even though this Lagrangian is not renormalisable and thus an infinite number of counter terms is needed to cancel the divergencies and to obtain finite results, it is only necessary to consider a finite subset of operators to get an approximate prediction at given accuracy, due to the $\frac{1}{\Lambda_{\mathrm{SM}}^n}$ suppression (see [10] page 57/58).
Since the predictions for low-energy phenomena of the effective theory should at most slightly deviate from the SM, Λ_{SM} should be large. For instance, the dimension five operator is the first which violates lepton number conservation and the dimension six operator violates baryon number conservation and requiring consistency with experimental data

would yield $\Lambda_{\mathrm{SM}} \simeq 10^{14} - 10^{16}$ GeV $\sim \Lambda_{GUT}$ ([38] page 4). In this case, new physics would be allowed to be very arbitrary since in any case it has only a small effect on low-energy measurements due to the large suppression of all higher order operators.
The cutoff scale Λ_{SM} does not only enter as a suppression factor for the higher order operators but instead it shows up in divergent radiative corrections to the SM parameters. While for the most parameters the correction shows only a mild $\propto log(\Lambda_{\mathrm{SM}})$ dependence, mass terms of scalar particles receive quadratically divergent corrections. The only scalar present in the SM is the Higgs boson and its mass can be written as ([38] page 8):

$$\begin{aligned} m_H^2 &= \int_0^{\infty} dE \frac{dm_H^2}{dE}(E; p_{true}) \\ &= \int_0^{\lesssim \Lambda_{\mathrm{SM}}} dE \frac{dm_H^2}{dE}(E; p_{true}) + \int_{\lesssim \Lambda_{\mathrm{SM}}}^{\infty} dE \frac{dm_H^2}{dE}(E; p_{true}) \\ &= \delta_{\mathrm{SM}} m_H^2 + \delta_{BSM} m_H^2 \end{aligned} \tag{2.45}$$

where p_{true} is the set of parameters of the "true" theory and the integral was splitted into a SM and BSM contribution. Furthermore, $\delta_{\mathrm{SM}} m_H^2 \propto \Lambda_{\mathrm{SM}}^2$ where the quadratic divergence is dominated by Feynman diagrams including top-quark loops such as in Figure 2.4.
Thus, if Λ_{SM} is large, the SM contribution is large and consequently also the BSM con-

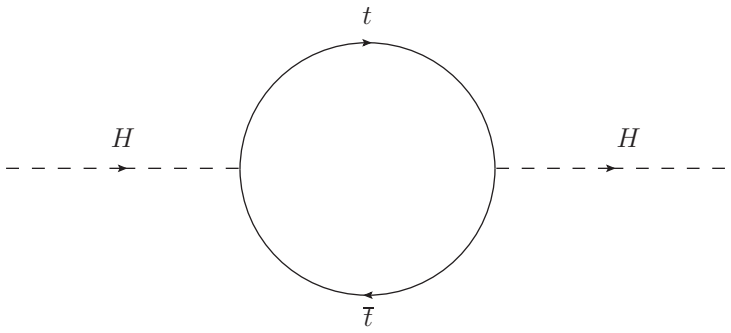

Figure 2.4.: Top-quark loop contributing to the Higgs mass corrections.

tribution must be large but with opposite sign. For instance, if $\Lambda_{\mathrm{SM}} = \Lambda_{\mathrm{GUT}}$ a 24 digit cancellation have to take place between those two terms. Since this situation would be very unnatural, this problem is referred to as the *Naturalness* or *Hierarchy Problem*.
Despite the aesthetical flaw of such unnatural cancellation, a very practical problem would follow in this situation: Even if the true theory would be known, the Higgs mass could never be computed from the true parameters, since the cancelling terms have to be known to an

accuracy of 24 digits and so do the parameters. This will be not the case in a foreseeable future.
To obtain a natural Higgs mass, Λ_{SM} needs to be small and thus new physics would be highly non-generic, i.e. baryon and lepton number should be symmetries of the new theory. Therefore, plenty indications can be taken from experimental data how a new theory should look like. Since there are very few other hints on how such a theory should be constructed, it is reasonable to consider this seriously.

It should be stressed that the Higgs mass could be of course fine tuned, which would not render any calculation incorrect. It might also be that the question was not correctly posed (anthropic principle, see [38] page 10). Thus, it is not agreed amongst theorists that the Naturalness Problem *is* a problem.

2.3.3. LEP Measurements

Despite the problems of the SM mentioned above, there is no result of any laboratory experiment which was able to disprove this theory. However, it appears that there are tensions between the theoretical prediction and a measurement. Most of them disappear quickly, where a prominent and recent example is the di-photon excess observed by ATLAS and CMS ([3–5]).
There are, on the other hand, tensions which do not vanish as quickly as the di-photon excess but instead remain until now. A well known example is the LEP measurement of the b-quark forward-backward asymmetry in $e^+\ e^-$ collisions:

$$A_{FB}^b = \frac{n_F^b - n_B^b}{n_F^b + n_B^b}, \tag{2.46}$$

where n_F^b and n_B^b is the number of b quarks produced in forward and backward direction, respectively.
The measurement deviates sizeable ($\approx 3\sigma$) from the Standard Model prediction [39]:

$$0.0992 \pm 0.0016\ (\mathrm{exp}) \quad \text{vs.} \quad 0.1037 \pm 0.0008\ (\mathrm{SM}). \tag{2.47}$$

For reference, it is noted that the measured value of the ratio $R_b = \Gamma_b/\Gamma_{had}$ is above its predicted value [39]:

$$0.21629 \pm 0.00066 \text{ (exp)} \quad \text{vs.} \quad 0.21562 \pm 0.00013 \text{ (SM)}. \tag{2.48}$$

2.4. Vector-like Quarks

2.4.1. Introduction to Vector-like Quarks

Several theories which try to shed light on the EWS breaking mechanism, thus addressing the Naturalness Problem, are proposed as an extension of the Standard Model of particle physics, e.g. little Higgs models [14], composite Higgs models [15, 16] or theories with extra dimensions based on E_6 group [40]. A common prediction of these theories are new coloured, spin $\frac{1}{2}$ particles whose right- and left-handed components transform equally under the SM gauge group. This means that these particles interact via a vector current with the W bosons, in contrast to the vector-minus-axial-vector interaction of SM quarks, and thus are referred to as vector-like quarks (VLQs) [41]. The Dirac mass term given in Equation 2.29 is not forbidden due to gauge invariance and therefore these particles do not have to acquire their mass due to the Higgs mechanism. In this case, a coupling to the Higgs boson would only be induced by the mixing of the VLQs with SM quarks. This is the reason why the effects on the Higgs-boson production and decay rates from diagrams including VLQs are much smaller than the uncertainties [41] and thus the Higgs discovery [17, 18] did not exclude the existence of VLQs, whereas a chiral[2] fourth generation of quarks is excluded [19].
Since the existence of VLQs is predicted by several theories, a model-independent search would be desirable and therefore several authors unified the VLQ description [41–44].
Effectively, the different BSM theories simply add VLQs to the SM Lagrangian, which is

[2] In the massless limit, Standard Model quarks respect *chiral symmetries* (see [1] page 620 f.), under which left- and right-handed components have opposite eigenvalues, and are therefore referred to as chiral quarks.

possible in seven different $SU(2)$ multiplets with renormalisable couplings [41]:

$$\begin{aligned} &T_{L,R}, \;\; B_{L,R} \;\; \text{(singlets)}, \\ &(X,\, T)_{L,R}, \;\; (T,\, B)_{L,R}, \;\; (B,\, Y)_{L,R} \;\; \text{(doublets)}, \\ &(X,\, T,\, B)_{L,R}, \;\; (T,\, B,\, Y)_{L,R} \;\; \text{(triplets)}, \end{aligned} \tag{2.49}$$

where the electric charges of T, B, X and Y are $2/3$, $-1/3$, $5/3$ and $-4/3$, respectively. The embedding of VLQs in complete $SU(2)$ multiplets allows the study of the effects on electroweak precision variables R_b, the ratio of the partial width for $Z \to b\bar{b}$ to the total hadronic Z-boson width and the oblique parameter S and T [45]. The Lagrangian describing the VLQ coupling to Wb given in [41] reads:

$$\mathcal{L}_W = \frac{g}{\sqrt{2}} \left(V_L^{Qb} \overline{Q}_L \gamma_\mu W^\mu b_L + V_R^{Qb} \overline{Q}_R \gamma_\mu W^\mu b_L \right) + ... \tag{2.50}$$

The mixing $V_{L,R}^{Qb}$ depends on the multiplet and is parameterised in terms of the mixing angle $\theta_{L/R}$, e.g. for a (Y, B) doublet it is $V_{R/L}^{Yb} = -\sin\theta_{R/L} e^{i\phi}$ with phase ϕ. Furthermore, within a given multiplet, the left- and right-handed couplings are related via

$$\begin{aligned} \tan\theta_R^q &= \frac{m_q}{m_Q} \tan\theta_L^q \;\; \text{(singlets, triplets)}, \\ \tan\theta_L^q &= \frac{m_q}{m_Q} \tan\theta_R^q \;\; \text{(doublets)}, \end{aligned} \tag{2.51}$$

where (q, m_q, m_Q) is either (u, m_t, m_T) (u indicates the up-sector) or (d, m_b, m_B) (d indicates the down-sector). Thus, for large m_Q only left-handed couplings are relevant in the singlet or triplet case, whereas only right-handed couplings contribute in the doublet case.

Even though VLQs do not couple directly to the Higgs boson via Yukawa couplings, a Higgs-boson coupling can be generated due to mixing with the SM quarks and thus VLQs might contribute to the loop corrections of the Higgs mass. For instance, a VLQ top partner T which is mixing with the top quark, would show up in the diagrams given in Figure 2.5. The resulting contributions would cancel those of the diagrams including top loops such as the diagram in Figure 2.4, which in turn would render the Higgs-boson mass UV stable and would solve the Naturalness Problem. Of course the cancellation is not exact but instead depends on the mass of the T quark, which means that a certain amount of fine tuning would still be necessary. To end up with a reasonably small fine-tuning, i.e. less than one

order of magnitude of accidental cancellations, the mass should not exceed ≈ 2 TeV [43]. Apart from the fact that VLQ top partners could cancel the top-loop contributions to the

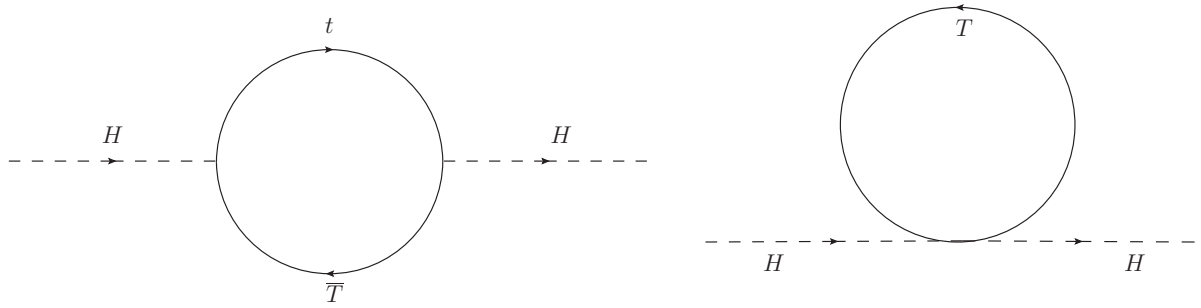

Figure 2.5.: Loops contributing to the Higgs mass corrections containing VLQ T quarks.

Higgs mass, the (B, Y) doublet would provide a simple explanation for the A_{FB}^b problem (see Section 2.3.3) as described in [41]. The $Zb\bar{b}$ vertex would be modified at tree-level due to the mixing of the bottom quark with a heavy vector-like B. This in turn modifies the prediction of A_{FB}^b and R_b and a first order approximation yields

$$\begin{aligned} R_b &= R_b^{\mathrm{SM}}(1 - 1.820\delta c_L + 0.336\delta c_R) \\ A_{FB}^b &= A_{FB}^{b,\mathrm{SM}}(1 - 0.1640\delta c_L - 0.8877\delta c_R), \end{aligned} \tag{2.52}$$

where δc_L and δc_R are the shifts of the effective left-handed and right-handed couplings of the $Zb\bar{b}$ vertex. Thus, increasing $|c_R|$ would improve the agreement with the measured values (see section 2.3.3). This can be achieved with a mixing of b_R with B_R having $T_3 > 0$, which is only the case in the (B, Y) doublet. However, it should be noted that the (B, Y) doublet would not provide a solution for the Naturalness Problem.

This analysis searches for the VLQs Y and T, where the search strategy for both can be easily combined. On one hand, the interpretation focuses on Y quarks from a (B, Y) doublet or a (T, B, Y) triplet, and on singlet T quarks. The T quarks corresponding to the (T, B, Y) triplet do not couple to Wb based on [41], where the couplings are parameterised in terms of $\sin\theta_{L/R}$, thus they can be safely neglected for the Y interpretation. On the other hand, the interpretation is done for a model which uses a phenomenological Lagrangian with non-renormalisable couplings [42, 43] which are denoted as $c_{L/R}^{Wb}$.

The ATLAS and CMS collaborations have published 95% confidence level (CL) mass and coupling limits from VLQ searches for single- and pair-production of vector-like T and Y quarks [46–64].
The results from pair-production searches for T quark vary between $m_T > 1340$ GeV [63] and $m_T > 1430$ GeV [53] depending on the considered decay channel, whereas the observed 95% confidence level lower limit on the pair-produced Y-quark mass is 1350 GeV [56].
Single-production searches report coupling limits on the QWb coupling strength for a singlet T quark or a Y quark from a (B, Y) to be as small as $|c_L^{Wb}| = 0.45$ for a T quark and $\sqrt{c_{\mathrm{L}}^{Wb\,2} + c_{\mathrm{R}}^{Wb\,2}} = 0.33$ for a Y for quark masses around 1000 GeV [23].

2.4.2. Production and Decay

States with charges 2/3 would in general mix with the SM up-type quarks, thus the mass eigenstates u, c and t would contain non-zero VLQ contribution. This in turn would lead for example to a modification of the Z-boson couplings [41], where the constrains in the up-sector are much stronger for the first two families [65]. Furthermore, given the usual Yukawa coupling hierarchy, a dominant third generation mixing is generally expected and therefore often interactions with the first two families are neglected. This is also the case in this analysis.
Of course, Y quarks (charge $-4/3$) exclusively decay to Wb. For a T singlet, the branching ratios are mass-dependent but converge towards 2:1:1 ($Wb : Zt : Ht$) in the high mass limit [41], as can be seen in Fig. 2.6. Given that the PDF of b quarks is much larger than that of t quarks, the dominant (only) production and decay for T (Y) is the Wb fusion[3]. For the T-singlet case, the TZt coupling is about a factor of $\sqrt{2}$ smaller than the TWb coupling and, as a result, $\mathcal{B}(T \to Zt)$ is about a factor of two smaller than $\mathcal{B}(T \to Wb)$. In addition, the selection efficiency in the search presented here for $tZ \to T \to Wb$ events is about a factor of two smaller than for $Wb \to T \to Wb$[4], because the accompanying top quark from the gluon splitting leads to additional jets in the final state[5].
Thus, the only relevant production and decay mode for this analysis is given in the Feynman

[3] The cross-section for Zt fusion is about one order of magnitude smaller for equal values of the TZt and TWb couplings [66].
[4] The acceptance times efficiency for $Zt \to T \to Wb$ is $\approx 0.2\%$ and for $Wb \to T \to Wb$ it is $\approx 0.5\%$ for T quarks with a mass of 900 GeV and $\mathcal{B}(T \to Wb) = 0.5$. See Table 6.6 for the acceptance times efficiency for $Wb \to Y \to Wb$ events.
[5] Jets other than the jet with the highest p_T are partially vetoed in the event selection (see Section 6.3.2 for the event selection and Section 5.4 for the definition of *jets*).

diagram in Fig. 2.7. The corresponding leading-order production cross-sections are given in Table 2.1 and were calculated in [43] using the narrow-width approximation (NWA). Since the width of the VLQ mass distribution is mass and coupling dependent, this approximation is not valid for sufficiently large couplings and masses. Thus, a cross-section correction is necessary in parts of the parameter space (see also Section 4.3).

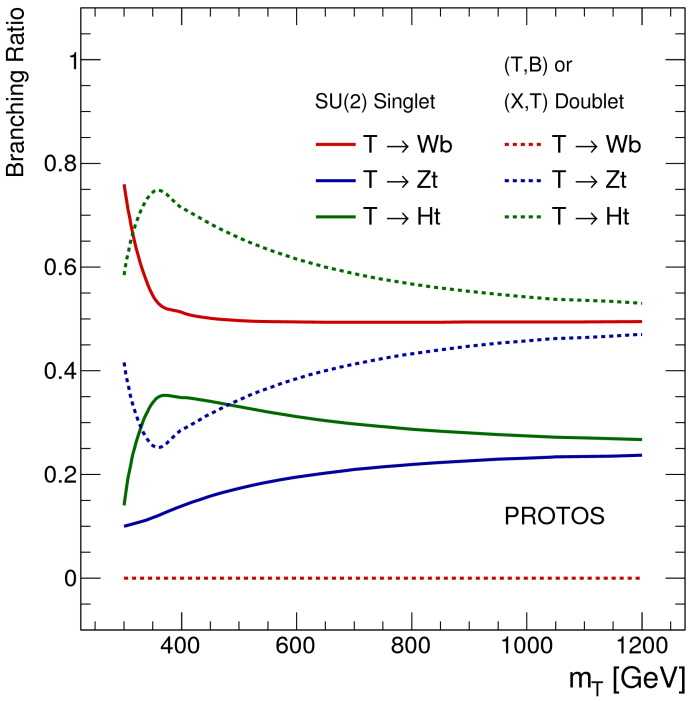

Figure 2.6.: Branching fractions of the VLQ T for different multiplets as a function of mass, taken from [67].

The Lagrangian used for the cross-section calculation reads:

$$\mathcal{L}_W = \frac{g}{2}\left(c_L^{Wb}\overline{Q}_L\gamma_\mu W^\mu b_L + c_R^{Wb}\overline{Q}_R\gamma_\mu W^\mu b_L\right) + ..., \tag{2.53}$$

where the single-production cross-sections can be parameterised in full generality as [43]:

$$\sigma_{\text{sing}}(Q\bar{b}) = \left(c_L^{Wb2} + c_R^{Wb2}\right)\sigma_{\text{Wb}}(M) \tag{2.54}$$

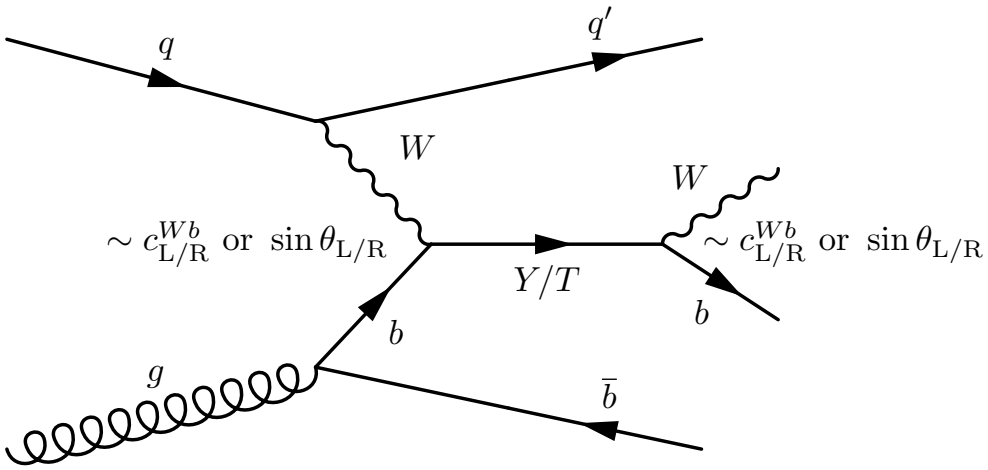

Figure 2.7.: Leading-order Feynman diagram for the process $Wb \to Y/T \to Wb$, where the amplitude scales with $\sin\theta_{\mathrm{L,R}}$ or $c^{Wb}_{\mathrm{L,R}}$, respectively.

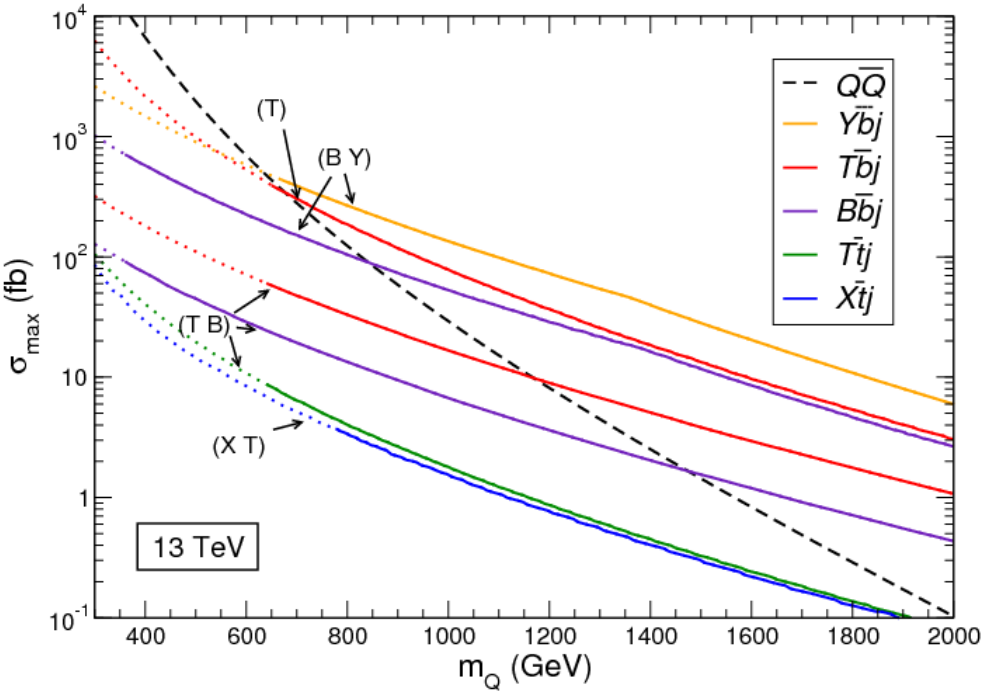

Figure 2.8.: Maximally by indirect constraints allowed single VLQ production cross-sections (coloured lines) and pair production cross-section (black dashed line) as a function of the heavy-quark mass at the LHC at $\sqrt{s} = 13$ TeV. The mass range excluded by direct searches till end of 2013 is indicated by the dotted part of the lines [41].

with $\sigma_{\mathrm{sing}}(Q\bar{b})$, the single-production cross-section for a VLQ (Y or T in this analysis) that couples to a b quark and $\sigma_{\mathrm{Wb}}(M)$, the mass-dependent cross-section corresponding to a unit coupling.

Mass [GeV]	$\sigma_{W^+\bar{b}} + \sigma_{W^-b}$ [fb]	Mass [GeV]	$\sigma_{W^+\bar{b}} + \sigma_{W^-b}$ [fb]
800	3860	1400	540
900	2720	1500	408
1000	1950	1600	305
1100	1350	1700	230
1200	982	1800	174
1300	716	1900	136

Table 2.1.: VLQ NLO single-production cross-section for Wb fusion and a unit coupling at $\sqrt{s} = 13$ TeV, taken from [43].

Thus, a measured cross-section σ_{limit} can be translated to a measurement of $\sqrt{c_L^{Wb2} + c_R^{Wb2}}$:

$$\sqrt{\frac{\sigma_{limit}}{\sigma_{theory}\left(c_L^{Wb2} + c_R^{Wb2} = 1\right)}} = \sqrt{c_L^{Wb2} + c_R^{Wb2}} \tag{2.55}$$

Comparing the different Lagrangians in Eq. 2.53 and in Eq. 2.50, it is possible to translate a coupling limit on $\sqrt{c_L^{Wb2} + c_R^{Wb2}}$ to a limit of the model specific mixing parameter $\sin\theta_{R/L}$.

It has to be noted that the signal sample production described in Section 4.2.1 is based on the model described in [44]. However, considering only VLQ decays to Wb, it is also possible to find a relation between the couplings used in [44] and those in [43]: $\kappa_T f(m) = c_{\mathrm{L,R}}^{Wb}/\sqrt{2}$, where $f(m) \approx \sqrt{1/(1 + \mathcal{O}(m_Q^{-4}))}$ with m_Q the VLQ mass in GeV, and therefore $\kappa_T \approx c_{\mathrm{L,R}}^{Wb}/\sqrt{2}$ to a very good approximation.

2.4.3. Interference between VLQ Production and SM Processes

Production and decay of T/Y result in the same final states as several SM processes, such as single-top and W+jets production, thus T/Y and these SM processes are indistinguishable in a quantum mechanical sense, which leads to interference effects.
The most relevant Feynman diagrams which lead to interference with VLQ production and corresponding Feynman diagrams containing VLQs are given in Fig. 2.9. For the single

production of VLQ T, it is t-channel top-quark production. However, since the masses of VLQ T and top quarks differ sizeable, only far off-shell top-quarks contribute significantly. The most relevant process leading to interference with single production of VLQ Y ($\overline{Y}$), is W^-bq ($W^+\bar{b}q$) production. Both of these processes are very rare.

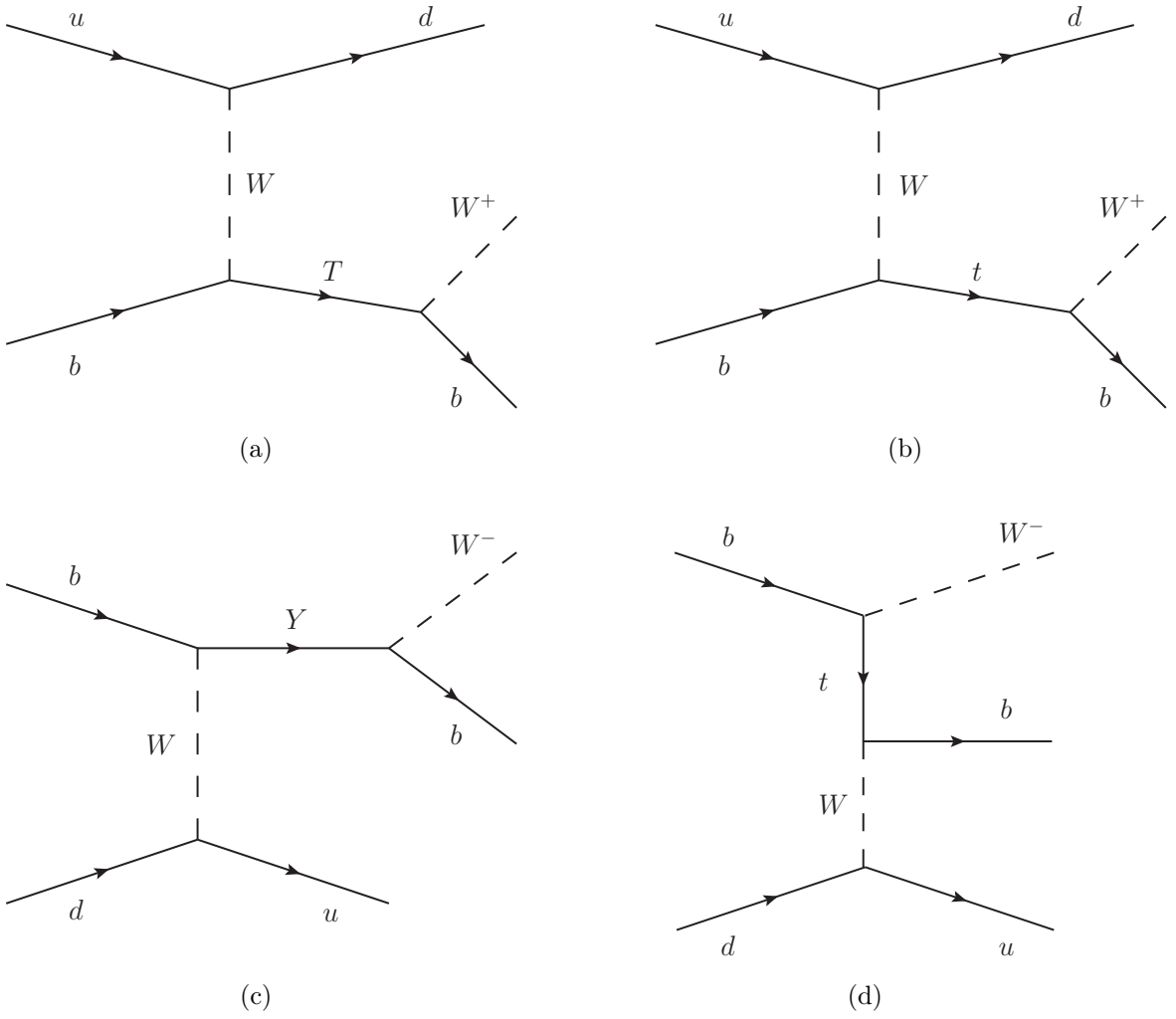

Figure 2.9.: Example Feynman diagrams of interfering VLQ processes and a corresponding SM process: single-T production 2.9(a) interferes with single-top production 2.9(b) and single-Y production 2.9(c) interferes with Wbq production 2.9(d).

If these effects are sizeable, it is not meaningful anymore to consider a VLQ cross-section but instead only the combined cross-section is physically defined

$$\sigma^{NLO} = K_{VLQ}\sigma^{LO}_{VLQ} + K_{SM}\sigma^{LO}_{SM} + \sqrt{K_{VLQ}K_{SM}}\sigma^{LO}_{int.} \,, \tag{2.56}$$

where the K-factors are explicitly considered, which are simply defined as the ratio of the leading-order (LO) and next-to-leading (NLO) order cross-section

$$k = \frac{\sigma^{NLO}}{\sigma^{LO}}. \tag{2.57}$$

However, not only the total cross-section may be influenced due to these effects but also the differential cross-section. Thus, the shape of the final discriminant may be significantly changed. Fig. 2.10 provides a comparison of the mass distribution of a VLQ Y signal with and without considering interference.

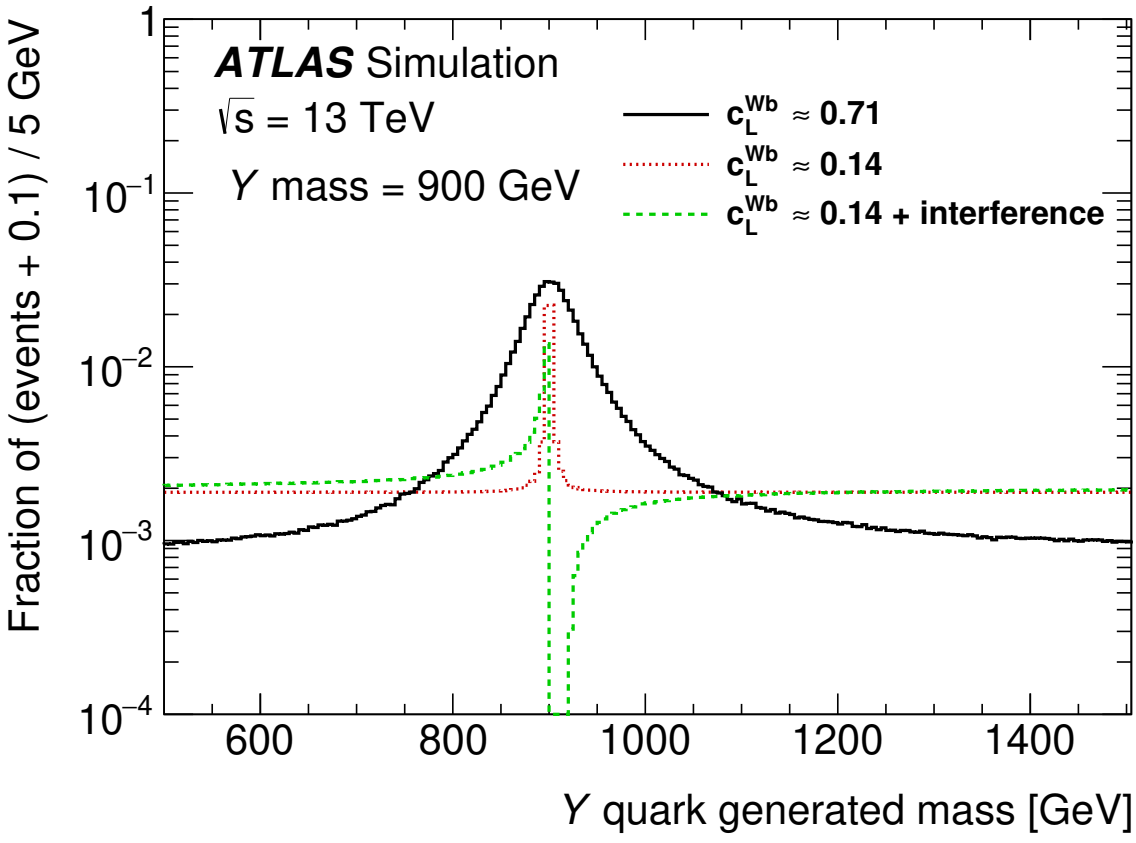

Figure 2.10.: Comparison of mass distribution at particle level for the Y quark with mass of 900 GeV for a coupling strength of $c_0 = \kappa_T \approx 0.5$ and $c_{\mathrm{L}}^{Wb} \approx 1/\sqrt{2}$ ($c_{\mathrm{R}}^{Wb} = 0$, solid line) and of $c_0 = c_{\mathrm{L}}^{Wb} = 0.14$ (dotted line) as defined in Ref. [44], both without considering interference effects. The dashed line shows the mass distribution for $c_L^{Wb} = 0.14$ when interference effects with SM processes are considered [22].

The size of the interference effects significantly depends on the handedness of the considered VLQ and it shows that the effects are small (see Sec. 8.2.2) for the right-handed VLQ Y. This may be due to the fact that the involved SM Feynman diagrams would lead to b and t quarks with preferentially positive helicity.

Chapter 3.

The ATLAS Detector and the LHC

This thesis aims for the discovery of VLQs and, thus, the disproof of the Standard Model or, if this is not possible, setting limits on the VLQ coupling strengths. This goal can only be achieved on a statistical basis and using a large dataset of high quality. The data on which this thesis relies on is collected by the ATLAS detector at the Large Hadron Collider (LHC). In the following, the LHC as well as ATLAS and its components will be presented.

3.1. The LHC

The Large Hadron Collider [20] located at CERN near Geneva is currently worlds largest particle accelerator and collider. It is installed in the existing 26.7 km long LEP tunnel and lies between 45 m and 170 m below surface. It consists of eight arcs and eight straight sections, with experiments installed in four of the straight sections where the two counter-rotating proton beams are colliding. The four main experiments hosted at the LHC are: ATLAS and CMS, which are general purpose detectors, as well as ALICE and LHCb, which were designed for specialised investigations, namely heavy-ion experiments and b-hadron physics, respectively.
The CERN accelerator complex acts as injector for the LHC and thus full use of existing infrastructure is made (see Fig. 3.1). The tunnel diameter equals only 3.7 m and therefore it was extremely difficult to install two completely separate proton rings. To overcome this issue a new magnet design, the twin-bore magnet, was invented.

The LHC was designed for a centre-of-mass energy of $\sqrt{s} = 14$ TeV of proton–proton collisions and to deliver a peak luminosity of $L = 10^{34}$ cm$^{-2}s^{-1}$ for ATLAS and CMS with a nominal bunch spacing of 25 ns. However, for Run-1 in 2010 and 2011 the collider operated only at $\sqrt{s} = 7$ TeV as well as at $\sqrt{s} = 8$ TeV in 2012. For Run-2 from 2015 to 2018, the centre-of-mass energy was increased to $\sqrt{s} = 13$ TeV and the reached peak luminosity was $L = 1.4 \cdot 10^{34}$ cm$^{-2}s^{-1}$, exceeding the design specification. The integrated luminosity is shown in Fig. 3.2.

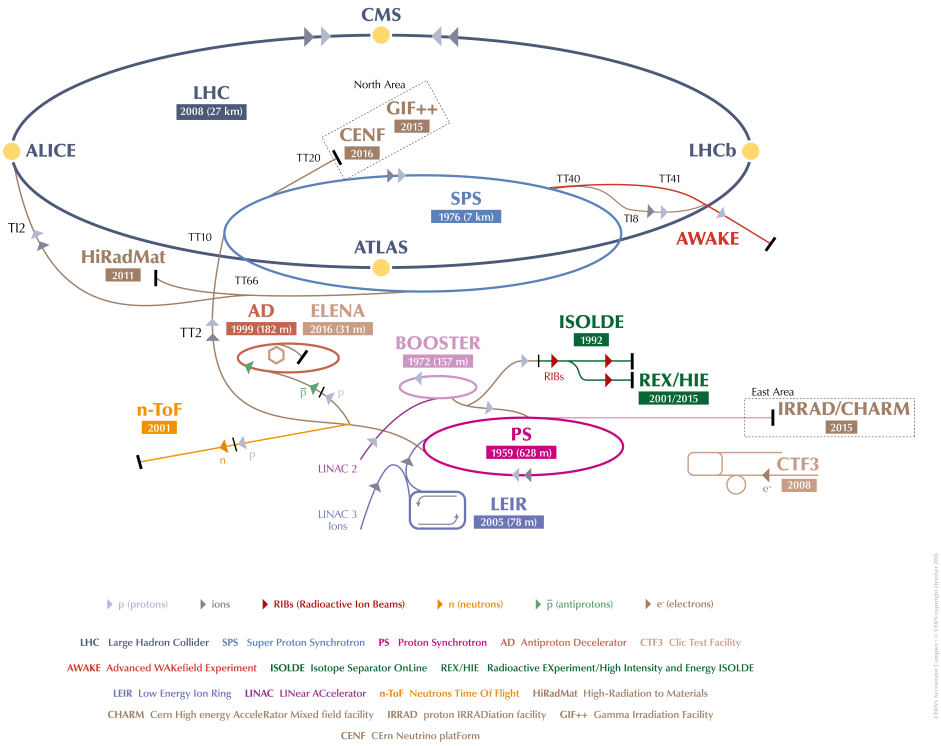

Figure 3.1.: The full LHC accelerator complex located at CERN near Geneva with its main experiments [68].

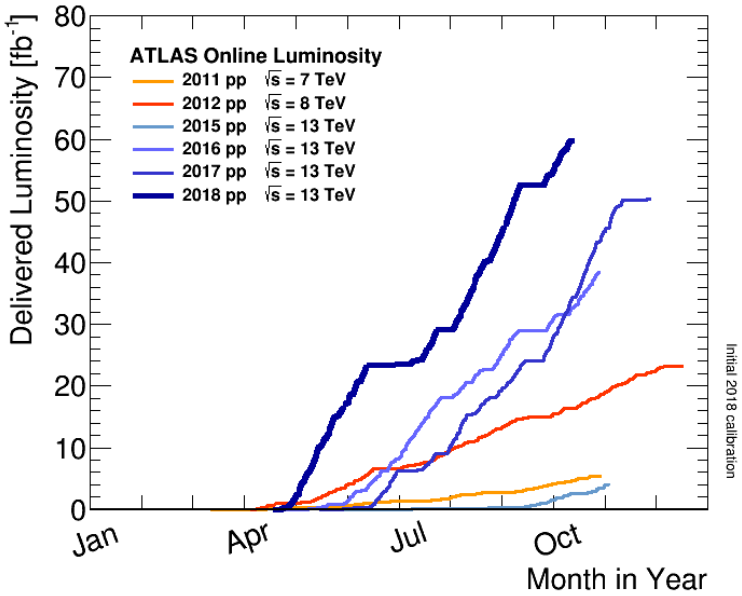

Figure 3.2.: The integrated delivered Luminosity to ATLAS as a function of time for the first six years of operation [69].

3.2. The ATLAS Detector

The ATLAS (A Toroidal LHC ApparatuS) detector [21] is designed as a general purpose detector, capable of performing precision measurements was well as discovering new particles. With a length of 44 m and height of 25 m, it is the largest detector at the LHC but with a mass of 7000 t it is only the second heaviest after CMS with 12000 t. Its main goal is to reconstruct the primary interactions in the proton–proton collisions taking place in the centre of the machine. To achieve its task, it is composed of several subdetectors which are assembled in a forward-backward symmetric onion shell structure. This overall structure is nicely visible in the cut-away view in Figure 3.3.
Mainly based on [21], each subdetector will be briefly described in the following.

3.2.1. Coordinate System

To describe the positions and directions of particles within the ATLAS detector a cylindrical coordinate system is used. The nominal interaction point where the proton–proton beams collide, is defined as the origin of the coordinate system. The beam axis defines the z-axis

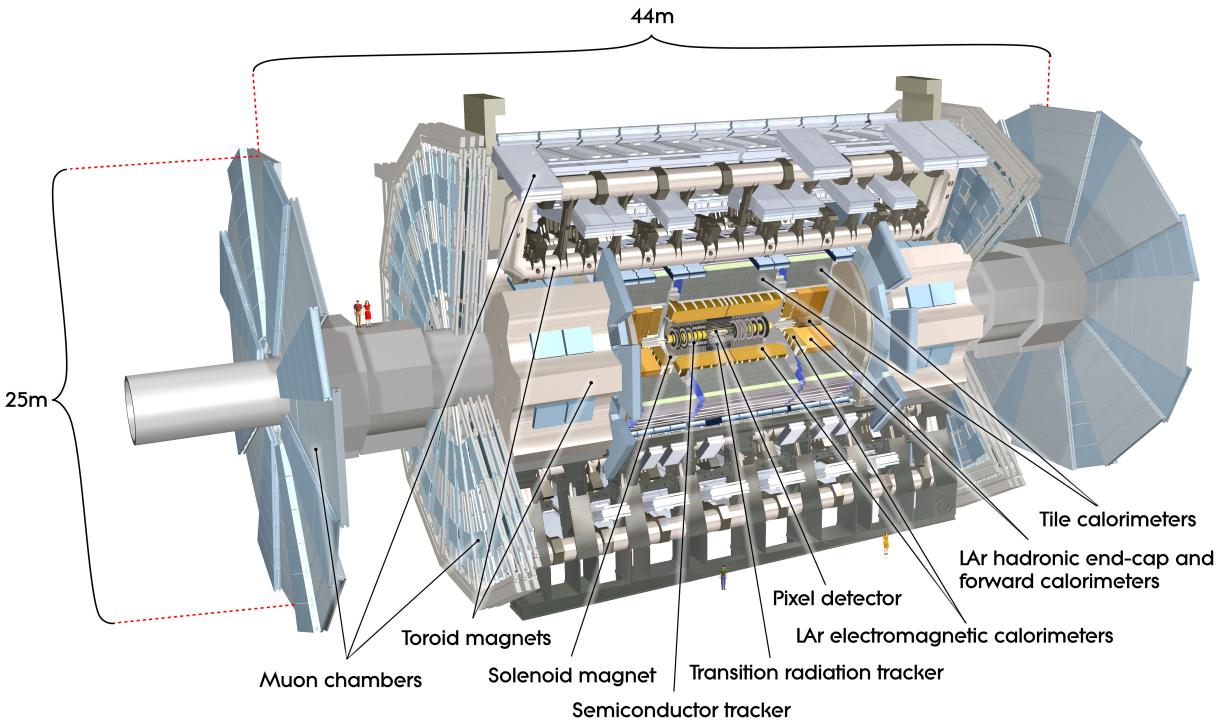

Figure 3.3.: Cut-away view of the ATLAS detector revealing it onion shell structure and subdetectors [70].

and consequently the x-y plane is perpendicular to the beams. Positive z values are defined to be in the clockwise direction around the collider ring. The azimuthal angle ϕ is measured around the beam axis and the polar angle θ is the angle from the beam axis. However, instead of θ commonly the pseudorapidity $\eta = -\ln\tan(\theta/2)$ is used which coincides with the rapidity $y = \frac{1}{2}\ln\frac{(E+p_z)}{(E-p_z)}$ in the $p \gg m$ limit for which differences are invariant under Lorentz boosts. Furthermore, it is often useful to measure the distance $\Delta R = \sqrt{(\Delta\phi)^2 + (\Delta\eta)^2}$ of particles in the $\eta - \phi$ space, which is again invariant under Lorentz boosts along the z-axis.

3.2.2. Magnet System

ATLAS' magnet system is composed of two main subsystems [21]: The first component is a 5.3 m long and 2.5 m wide solenoid immersing the inner detector into a magnetic field parallel to the beam axis. The nominal current of 7.73 kA generates a magnetic flux density of 2 T. The solenoid consists of a single-layer coil and a Al-stabilised NbTi conductor and

is surrounded by a Al support cylinder.
The second component, already acknowledged in the acronym ATLAS, is the three part toroid system, producing the magnetic field for the muon system. The magnet system is sketched in Fig. 3.4. The two 5 m long end-cap toroids provide a peak field of 4.1 T and are inserted into the barrel toroid, which has a length of 26 m and a peak field of 3.9 T. Each of the toroids is composed of eight coils assembled radially as well as symmetrically around the beam axis and are made of pure Al-stabilised Nb/Ti/Cu conductor windings. All magnets are superconducting and operate at a temperature of 4.5 K.

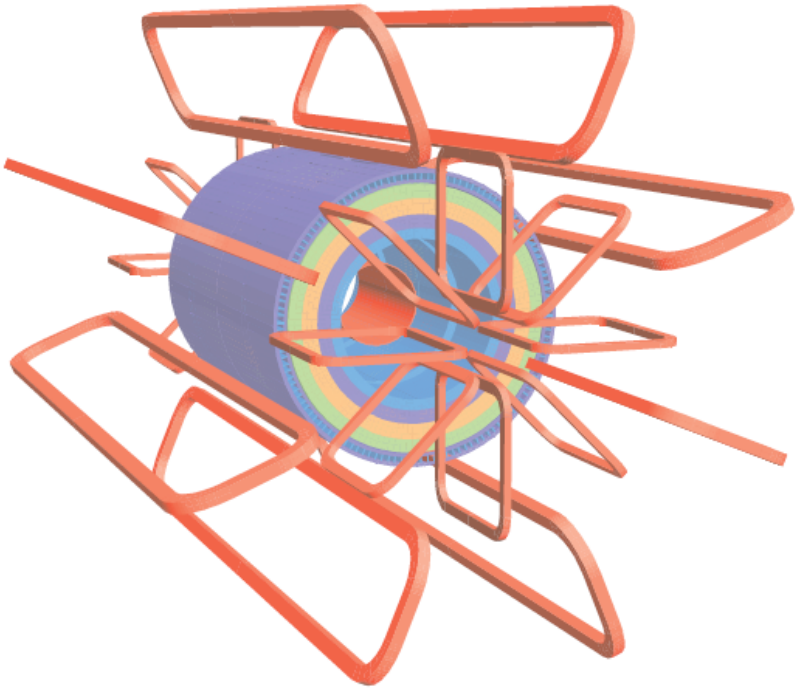

Figure 3.4.: Schematic view of the magnet system of the ATLAS detector [21].

3.2.3. Inner Detector

The Inner Detector (ID) is the innermost sub-detector of ATLAS. It is mainly responsible for the precise reconstruction of trajectories of charged particles, momentum determination as well as the identification of primary and secondary vertices. It is designed to achieve a transverse momentum resolution of $\sigma\left(p_T\right)/p_T = 0.05\% \times p_T\,[\mathrm{GeV}] \oplus 1\%$ and a transverse impact parameter resolution of 10 μm. The ID has a cylindrical shape with a total length of 6.2 m and width of 2.1 m. As can be seen in Fig. 3.5, the Inner Detector is composed of three

subsystems: the Pixel Detector, the Semi-Conductor Tracker (SCT) and the Transition Radiation Tracker (TRT).

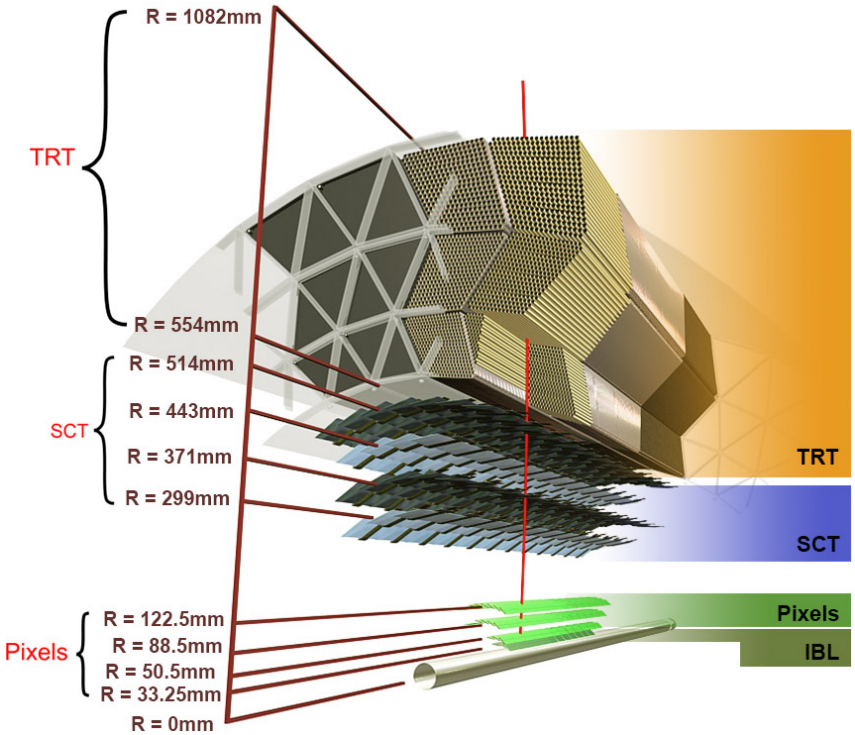

Figure 3.5.: Schematic view of the Inner Detector of ATLAS and its subcomponents, which are the Pixel detector with the Insertable-B-Layer, the Semi-Conductor Tracker and the Transition Radiation Tracker, starting from the beam pipe [71].

Pixel Detector

The component closest to the beam pipe is the Pixel Detector [21, 71, 72]. Originally, it had three cylindrical layers in the barrel region and three disks each in the forward and backward end-cap, respectively, covering the $|\eta| < 2.5$ region. The pixels contained in these three barrel layers as well as in the end-caps have a size in $R - \phi \times z$ of 50 μm $\times$ 400 μm and a sensor thickness of 250 μm with a intrinsic accuracy of 10 μm (R$-\phi$) and 115 μm (z and R-coordinate in end-caps, respectively). These sensors are made of oxygenerated n-type wafers with readout pixels on the n^+-implated side.

During the Long-Shutdown-1, a fourth layer, the Insertable-B-Layer (IBL), was added to improve the resolution of the tracking system [73]. It was inserted only about 33 mm

away from the beam axis and has a pixel size of 50 μm $\times$ 250 μm which leads to a resolution of 70 μm in the z-coordinate.

Semi-Conductor Tracker

Starting from the beam pipe, the next part of the ID behind the Pixel Detector is a silicon microstrip detector, the Semi-Conductor Tracker (SCT) [21, 74], which is located in radii between approximately 30 cm and 52 cm and within $|z| < 2.8$ m, again covering the $|\eta| < 2.5$ region. It is composed of four cylindrical barrel layers as well as nine disks for each end-cap build up from 4088 modules. The detector uses small (40 mrad) stereo silicon strips to measure both coordinates in the barrel region, consisting of 6.4 cm long daisy-chained sensors resulting in a accuracy of 17 μm (R-ϕ) and 580 μm (z). The end-caps are hosting a set of strips running radially and a set of stereo strips at an angle of 40 mrad with an equivalent accuracy as the barrel sensors.

Transition Radiation Tracker

The third and last component of the ID is the Transition Radiation Tracker (TRT) [21, 75], again consisting of a barrel and two end-cap parts. Its basic elements are thin-walled proportional drift tubes, also called straws, filled with a Xe-Co_2-O_2 mixture (70%/27%/3%) (for Run-2 an Argon-based gas mixture is used in some parts). The straws have a diameter of about 4 mm, a length of 144 cm in the barrel region and 37 cm in the end-caps. They only provide $R - \phi$ information with an intrinsic accuracy of 130 μm per straw. The barrel part is comprised of 52544 straws oriented parallel to the beam arranged in three rings. The two end-caps each contain 122880 straws radially aligned to the beam axis arranged in two sets of independent wheels. The overall envelope extends up to an radius of about 1.1 m and $|z| \lessapprox 2.7$ with a pseudorapidity coverage of $|\eta| < 2$.

3.2.4. Calorimeters

The main purpose of the calorimeter system is the detection of neutral particles such as photons and neutrons and the energy measurement. This system is divided in two main components: the Electromagnetic Calorimeter (ECal) and the Hadronic Calorimeter

(HCal), each being a liquid-Argon (LAr) based sampling calorimeter. The finer granularity of the ECal, matched to the η range of the ID, is optimal for the precision measurement of electrons and photons whereby the coarser granularity of the rest of the system is sufficient for jet reconstruction and E_T^{miss}[1] determination. The depth of the calorimeters is a crucial design decision and of special importance, since for an accurate energy measurement the electromagnetic or hadronic showers must be completely absorbed and must not leak into the Muon Spectrometer.

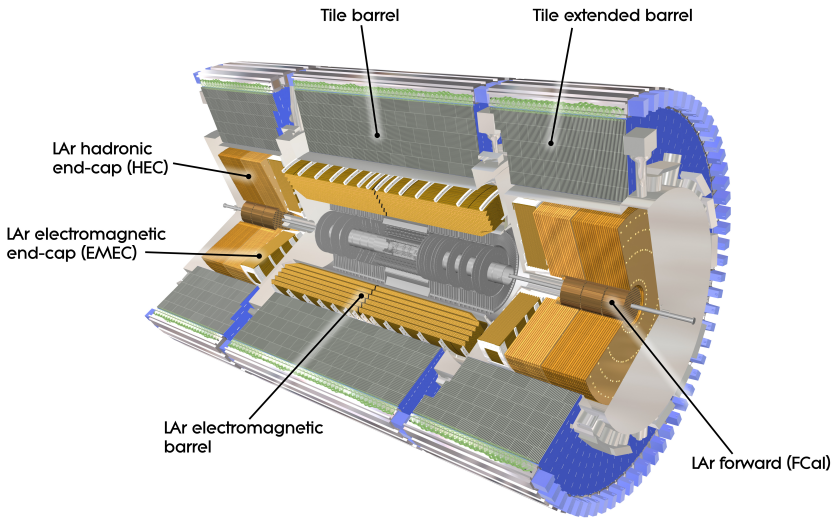

Figure 3.6.: Cut-away view of the calorimeter system of ATLAS, consisting of an electromagnetic and hadronic calorimeter [76].

Electromagnetic Calorimeter

The ECal [21, 77] is again divided into a barrel part and to end-caps, where an $|\eta| < 1.475$ and $1.375 < |\eta| < 3.2$ range is covered. To achieve the desired performance, the central solenoid and the ECal share a common vacuum vessel. The barrel part is composed of two half-barrels, separated by a gap of 4 mm at $z = 0$. The end-caps consist of two coaxial wheels, covering in total $1.375 < |\eta| < 3.2$. Lead plates are used as absorber material and are alternating with the active material arranged in an accordion shape in three layer. The size of the used cells increase from 0.003×0.1 (η-ϕ) in the first layer ($|\eta| < 1.4$) and

[1]The missing transverse energy E_T^{miss} is defined in Section 5.6.

0.05×0.025 (η-ϕ) in the third layer. A total of 22 radiation lengths[2] X_0 in the barrel and > 24 X_0 in the end-caps is reached. Additionally a presample detector is used in the region of $|\eta| < 1.8$ to correct for the energy loss of charge particles upstream of the ECal. The required resolution is $\sigma_E/E = 10\%/\sqrt{E} \oplus 0.7\%$

Hadronic Calorimeter

The energy of hadronic showers is measured by the Hadronic Calorimeter (HCal) [21, 78], which is composed of three main parts. The tile calorimeter, placed directly outside the ECal with radii from 2.28 m and 4.25 m, covering a η range of $|\eta| < 1.0$ (barrel) and $0.8 < |\eta| < 1.7$, respectively. In contrast to the ECal, it uses steel as absorber and scintillating tiles as active material with a total thickness of 9.7 interaction lengths[3] (λ) at $\eta = 0$. The second component, the end-caps (HEC), are composed of two independent wheels, with two layers each, built from 32 wedge-shaped modules using LAr as active material and copper as absorber material. It covers $1.5 < |\eta| < 3.2$, thus overlapping with the tile calorimeter and the forward calorimeter (FCal), the third part of the HCal. It is located close to the beam pipe ($3.1 < |\eta| < 4.9$) and at a distance of 4.7 m from the interaction point. The two end-caps consist of three modules each, with LAr as active material. However, the first modules absorber material is copper, optimised for electromagnetic measurement, whereas the absorber of the other modules consist of tungsten, triggering hadronic interactions.
The depth of the active calorimeter corresponds to 9.7 λ in the barrel and to 10 λ in end-cap. The system was designed to reach a resolution of $\sigma_E/E = 50\%/\sqrt{E} \oplus 3\%$ (barrel and end-cap) and $\sigma_E/E = 100\%/\sqrt{E} \oplus 10\%$ (FCal)

3.2.5. Muon Spectrometer

The outermost part of ATLAS is formed by the Muon Spectrometer [21, 79], which is designed to detect charged particles exiting the calorimeters and to measure their momentum in $|\eta| < 2.7$. Figure 3.7 provides a cut-away view of this system. Its design-driving performance goal is to reach an accuracy of $\sigma(p_T)/p_T = 10\%$ at $p_T = 1$ TeV. Furthermore,

[2] The radiation length is the mean distance over which an electron loses $\frac{1}{e}$ of its energy by bremsstrahlung in a given medium.
[3] The interaction length is the mean distance travelled by a hadron before undergoing an inelastic interaction in a given medium.

it is also designed to trigger on these particles (see below). The Muon Spectrometer is again divided into a barrel part and two end-caps. The precision-tracking chambers of the barrel part are located between and on the coils of the barrel toroid magnet, being arranged in three concentric cylindrical shells at radii of approximately 5 m, 7.5 m and 10 m. The end-cap chambers form large wheels, perpendicular to the z-axis and are located in front and behind the end-cap toroid magnets at distances of $|z| \approx 7.4$ m, 10.8 m, 14 m and 21.5 m from the interaction point.
To reach the performance goals, four different types of subdetectors are used in the Muon Spectrometer. To achieve the high accuracy in the momentum measurement, Monitored Drift Tube (MDT) chambers are used to cover the range $|\eta| < 2.7$, except in the innermost end-cap, where Cathode-Strip Chambers (CSC) are in the range of $2.0 < |\eta| < 2.7$. MDTs consist of three to eight layers of drift tubes, whereas CSCs are multiwire proportional chambers with cathode planes segmented into strips in orthogonal directions, which allows both coordinates to be measured. To provide the capability of muon triggering, in the barrel Resistive Plate Chambers (RPC) and in the end-caps Thin Gap Chambers (TGC) are used, which provide short readout times of a few tens of nanoseconds.

It should be noted that even though a good η coverage is achieved, there are several acceptance gaps due to service infrastructure.
Furthermore, the Muon Spectrometer is supplemented with a high-precision optical alignment system, monitoring the position and internal deformation of the MDT chambers.

3.2.6. Trigger System and Data Acquisition

The LHC provides proton–proton collision events with a rate of about 40 MHz to the ATLAS detector. Given the size of an event written to permanent storage in the MB region, this would result in EB recorded each day. However, given that the cross-sections of relevant processes are much smaller than the total *pp* cross-section (see Fig. 3.8), only a small fraction of events are of interest for physics analysis. To reduce the rate of recorded events while keeping relevant events, a trigger system [21, 81] is deployed.
In Run-1, this system had three distinct levels: Level-1 (L1), Level-2 (L2) and the Event Filter. However, due to the increased centre-of-mass energy from 8 to 13 TeV and the decreased bunch spacing from 50 ns to 25 ns, the trigger rates would have exceeded the

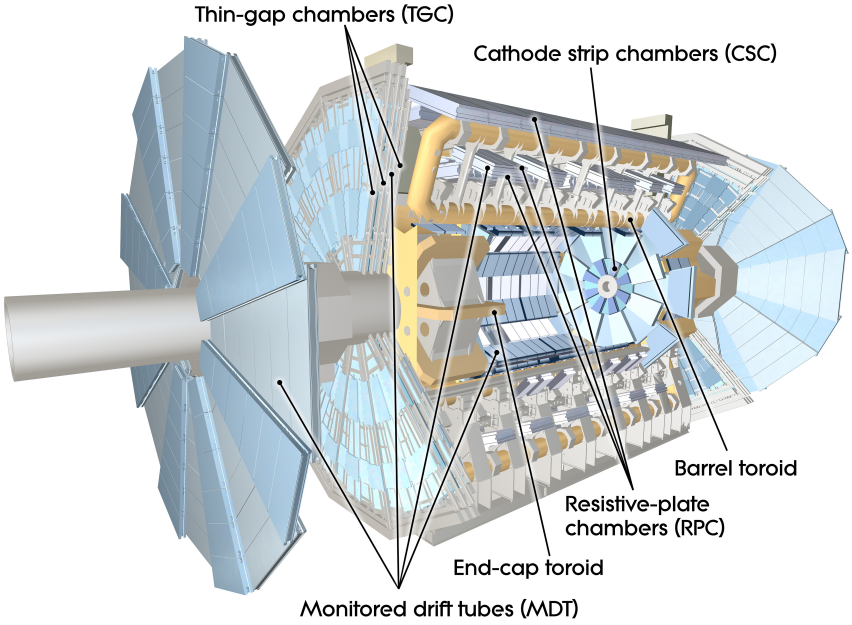

Figure 3.7.: The Muon Spectrometer of the ATLAS detector and its components [80].

allowed maximal rates in Run-2, which is the basis of this thesis. Therefore, the trigger system was significantly upgraded.

The upgraded system is composed of the L1 Trigger which in turn has three subtriggers: the Central Trigger, Level-1 Calo and the Level-1 Muon trigger, where the addition of a new topological trigger to the Central Trigger is the main change in comparison to Run-1. These systems are hardware based and define a region of interest (RoI) in η and ϕ coordinates based on high-p_T objects and high E_T^{miss}. In the next stage, the High Level Trigger (HLT), which is composed of two separated computing farms of L2 and the Event Filter, uses the RoI information as well as global event information for a software-based trigger decision based on several so-called trigger menus [82, 83].

In Run-2, the event rate is reduced from up to 40 MHz to 100 kHz at the L1 stage and events with a rate of about 1 kHz pass the HLT menus, thus are finally written to disk. Albeit this rate is still huge, it is manageable.

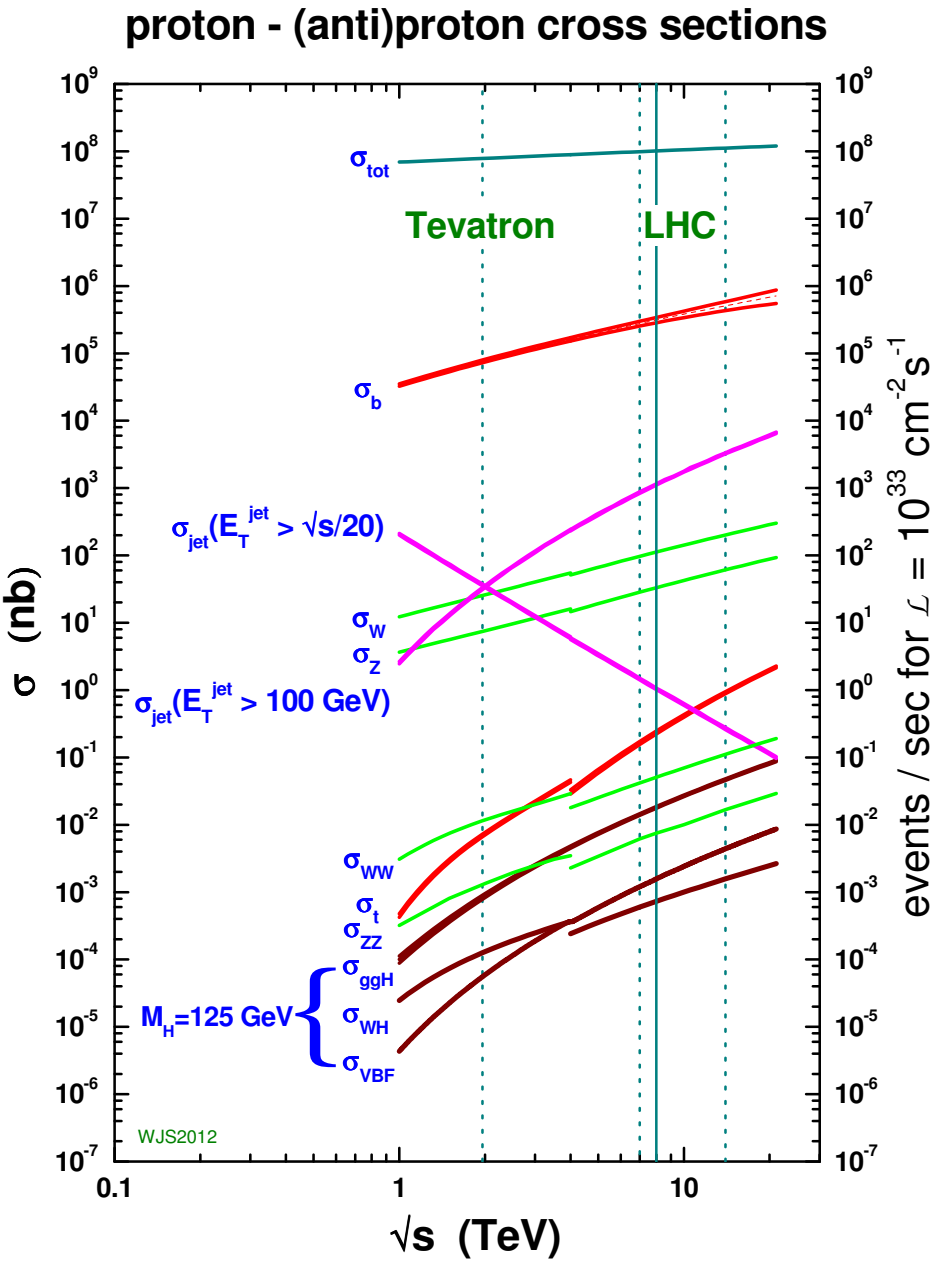

Figure 3.8.: Comparison of the cross-sections of several benchmark physics processes with the total proton–proton cross-section as a function of $\sqrt{s}$. The operating centre-of-mass energy of the LHC and Tevatron are indicated as well [84].

Chapter 4.

Modelling of Background and Signal Processes

To meet the goal of this thesis, an accurate prediction of the expected SM and alternative VLQ theories is of utmost importance, however, this alone is not an easy task. For this purpose, the relevant physics processes have to be generated and the response of the ATLAS detector has to be modelled, where for both sophisticated Monte Carlo (MC) methods are deployed.
In the following sections, the techniques and used MC samples relevant for this analysis are described.

4.1. Event Generation and Detector Simulation

The generation of physical final states of high-energy proton–proton collisions is an extremely difficult task and is described in detail in [32]. It involves the matrix element calculation which is only possible for a few orders in perturbation theory[1] and the formation of hadrons which is not accessible in perturbation theory at all. Thanks to the factorization theorem, it is possible to separate the event simulation into subtasks: the hard subprocess, parton showering and hadronisation (and detector simulation). These can now be solved individually according to the scale of the involved momentum transfer as it is indicated in Fig. 4.1.

[1] Only leading-order and next-to-leading order Feynman diagrams are considered for the simulation of the samples used in this analysis.

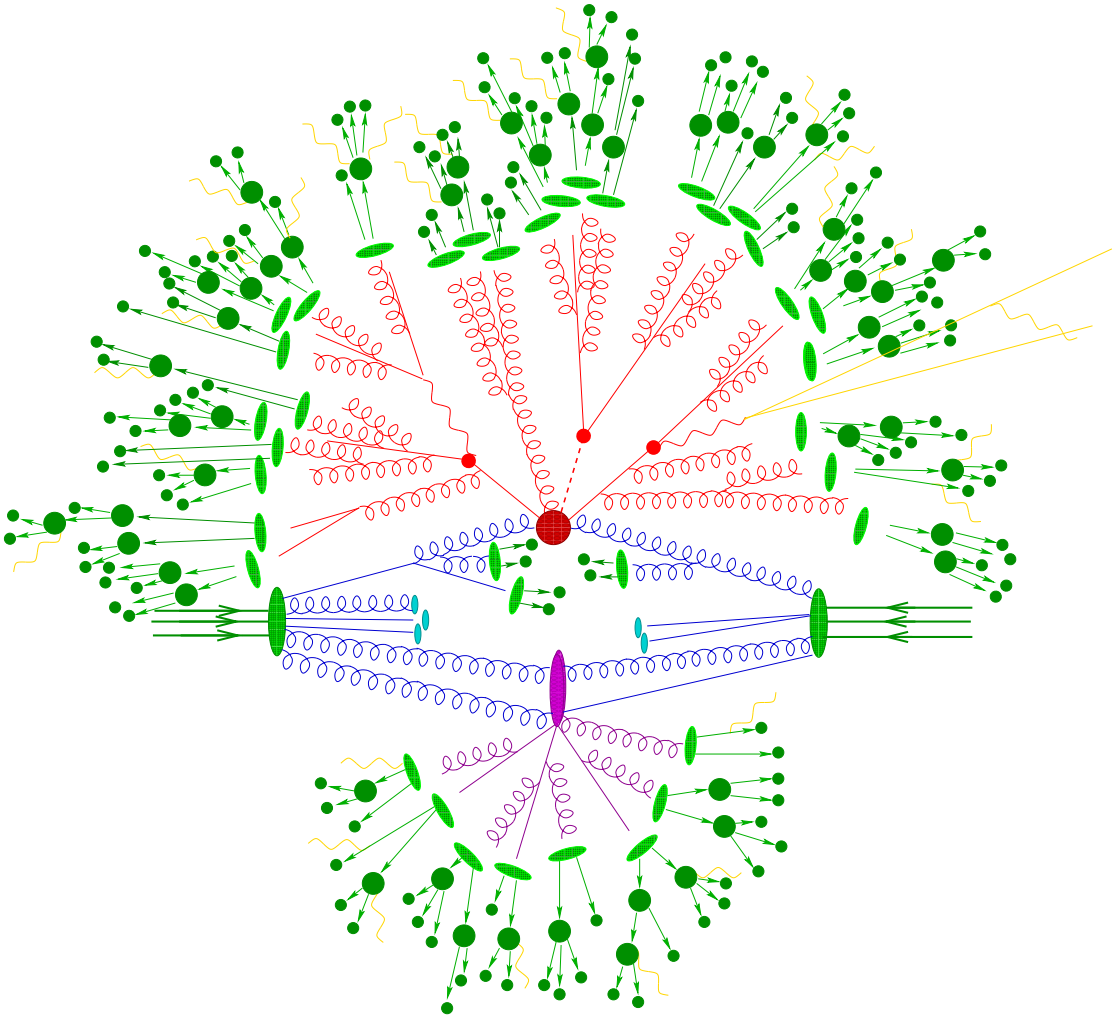

Figure 4.1.: Pictorial representation of a fully simulated pp collision event with a hard process of $qq \to t\bar{t}H$ (taken from [85]). The individual parts of the event generation are given in distinct colours: The hard interaction (big red ellipse), decays of produced particles (small red ellipses), additional QCD radiation (red lines), secondary interactions (purple ellipse), hadronisation (light green ellipses), hadronic decays (dark green ellipses), photon radiation (yellow lines).

Based on [32], each of the main steps of the event generation will be briefly discussed in the following.

4.1.1. Hard Subprocess

In many analyses, as for the search for heavy VLQs, events with large momentum transfer are of particular interest. Since at theses large scales the strong coupling constant α_s becomes small, a perturbative approach of the cross-section calculation using Equation 2.41 is applicable and a plethora of fully automated tools computing the relevant matrix elements is readily available. Due to the large dimension of the phase space and complexity of the processes, Monte Carlo sampling methods are the tools of choice for the phase space integration necessary for the evaluation of equation 2.41. Even though the relevant scales (μ_R, μ_F) are not fixed by first principles, the combination of the matrix element calculation and the subsequent parton shower simulation defines which choices are consistent.
Leading-order (LO) event generators typically provide reliable shapes of the kinematical distributions, whereas the overall normalisation, i.e. the total cross-section, is modelled rather badly due to the large next-to-leading order (NLO) effects. Therefore, the LO results are usually corrected by using a K-factor.

4.1.2. Parton Showering

For the hard subprocess, only a few orders in perturbation theory are considered (LO, NLO). However, initial state quarks and gluons will inevitably produce further quarks and gluons until they reach the scale at which non-perturbative confinement effects set in, typically below about 1 GeV. It is neither computationally nor theoretically possible to consider all of the relevant matrix elements since at the end of this showering low scales are reached. This in turn means that α_s becomes large and perturbation theory breaks down.
Nonetheless, these showers can be simulated as an evolution from the scale of the hard process down towards ≈ 1 GeV.

A common approach to model this evolution is the *Collinear final state evolution* (see e.g. [32] page 22 f.). Here, the cross-section of a hard process with cross-section σ_0 to radiate another parton of flavour j is considered, which can be approximated by

$$d\sigma \approx \sigma_0 \sum_{partons,i} \frac{\alpha_s}{2\pi} \frac{d\theta^2}{\theta^2} dz P_{ji}(z,\phi) d\phi, \tag{4.1}$$

where $P_{ji}(z, \phi)$ are the Altarelli-Parisi splitting functions [86]. The angle θ measures the opening angle between the emitted and the emitting parton whereas z represents the fraction of the energy of the emitted parton with respect to the energy of the emitting parton, ϕ the azimuth of particle j around the axis defined by particle i. The divergencies of this equation are removed by introducing a lower cutoff Q_0 on the transverse momentum of the daughter particle.
Using Eq. 4.1, it is possible to find an equation for the probability that there are no branchings giving virtualities larger than $q^2 = z(1-z)\theta^2 E^2$ (E is the energy of the radiated parton), given a maximal possible virtuality of Q^2, $\Delta_i(Q^2, q^2)$:

$$\frac{d\Delta_i(Q^2, q^2)}{dq^2} = \Delta_i(Q^2, q^2)\frac{d\mathcal{P}_i}{dq^2}, \tag{4.2}$$

where $\mathcal{P}$ is the total probability for all branchings of a parton of type i between q^2 and $q^2 + dq^2$. It has the solution

$$\Delta_i(Q^2, q^2) = \exp - \int_{q^2}^{Q^2} \frac{dk^2}{k^2}\frac{\alpha_s}{2\pi}\int_{Q_0^2/k^2}^{1-Q_0^2/k^2} dz P_{ji}(z). \tag{4.3}$$

This result is now used in an iterative procedure (Markov-Chain):
A splitting from the starting scale Q^2 is generated if $q^2 > Q_0^2$ holds for the solution q^2 of $\Delta_i(Q^2, q^2) = \rho$, with ρ a random number between 0 and 1. The result is afterwards considered as hard process and a new splitting is tested. This procedure results in an evolution of the particle transverse momenta starting from the highest p_T.
The initial state radiation is similarly simulated by starting from the hard process and use the shower evolution backwards to add additional radiation.

An alternative approach, the *Dipole approach* (see e.g. [32] page 41 f.), albeit following a similar strategy as the previous, makes use of the fact that in the large-N_c limit the colour structure of the initial hard process can be decomposed into colour lines starting from incoming quarks (colour flow). These colour lines are considered as radiating colour dipoles which are emitting independently.

Particles and particle showers which arise from interactions other than the hard process, e.g. from interactions of other proton constituents, are referred to as the *underlying event*.

These processes are also modelled in the showering step of the event simulation and make use of tuned phenomenological models.

4.1.3. Hadronisation

The result of the showering step of the simulation is considered as the *partonic final state*, i.e. no further partons are produced.
In the next step, the formation of colour singlet hadrons has to be modelled. The process of hadronisation takes place in an energy regime where α_s is large and thus it is not accessible from first principles. Hence, phenomenological models inspired by QCD with tunable parameters have to be deployed.
Currently, two main classes of hadronisation models are in use: the *string model* and the *cluster model*:

- The string model is based on the assumption of linear confinement, i.e. the potential between coloured particles grows linearly with distance r, $V(r) = \kappa r$, where $\kappa \approx 0.2$ GeV has to be tuned to data. This assumption justifies the connection of colored particles with massless colour strings storing the potential energy. A quark is defined as endpoint of a string, a gluon represents a kink and partons are ordered in colour along the string. As the partons move apart, the string breaks eventually at some maximal potential and a new $q\overline{q}$ pair is produced. This process is repeated until the string tensions are below a certain cutoff value and only ordinary colourless hadrons remain.
  The main weakness of this model are the many free parameters, which have to be tuned to data.

- The cluster model is based on the preconfinement property of parton showers, which means that the colour structure of a parton shower at any scale Q_0 in the evolution process is such that colour singlet clusters (combinations of partons) can be formed with an asymptotically ($Q \gg Q_0$) invariant mass distribution at low scales which depends only on Q_0 and the QCD scale Λ_{QCD}.
  Gluons, considered as colour line pairs (large-N_c limit), are splitted non-perturbatively into $q\overline{q}$ pairs and clusters are reformed from colour-connected pairs. The limited cluster mass spectrum leads to limited transverse momenta and heavy flavour suppression. Heavy clusters decay into lighter clusters until stable light clusters are formed.

The cluster model exhibits fewer free parameters but usually describes high-energy collider data less accurate than the string model.

After finalizing the formation of hadrons, the decay of unstable resonances is simulated based on a combination of experimental results and theoretically motivated assumptions. The parameter of the hadronisation model and the hadron decay model are closely connected and thus have to be re-evaluated if one of them is altered.

4.1.4. Detector Simulation

The final result of the event simulation is the true physics information (MC-truth) which an analysis would like to reconstruct. However, this is of course not the information which is provided by the ATLAS detector for real data. The produced particles propagate through the detector and interact with its various components, ionise and deposit energy, which in turn results in currents or voltages in the various subdetectors if a certain threshold is reached. Thus, to compare real data with MC data, it is crucial to simulate this detector interactions and digitise the result to obtain the final expected detector response. This process is described in details in [87].

Full Simulation

The full simulation (fullsim) of the interactions of the particles leaving the event generation, showering and hadronisation are performed using the GEANT4 simulation toolkit [88]. In this step a detailed model of the ATLAS detector is used which is stored in the *ATLAS Geometry Database* and is based on the GeoModel library [89]. Furthermore, the *ATLAS Conditions Database* allows modifications in the geometry which are necessary to account for the running conditions of the ATLAS detector, e.g. misalignments of detector components or dead channels. Given the information in these two databases, GEANT4 simulates all interactions of the traversing particles and the detector material as well as the decay of unstable particles.
Taking into account the full ATLAS geometry is very time consuming and it is not feasible to generate high-statistics samples for all required processes for any physics analysis. To

overcome this issue, fast detector simulations where developed.

Fast Simulation

Instead of using the detailed ATLAS model from the *ATLAS Geometry Database*, it is possible to substitute the full simulation by a parametrization of some detector parts, which is done by the commonly used fast simulation programs *Fast G4 Simulation* [90], *ATLFAST-I* [91] and *ATLFAST-II* (AFII) [92]. *ATLFAST-II*, which is used in this analysis, replaces the full by the fast calorimeter simulation (*FastCaloSim* [93]) and the full tracking simulation can be replaced by *Fatras* [94], a fast tracking simulation engine.
In general good performance of the fast simulations with respect to the full simulation is achieved. However, it is advisable to prove this for newly studied processes, which is done for the production of VLQ signals in Section 7.5.

Digitization

The result of the simulation of the interaction of detector and the traversing particles results in so-called *hits* in the various detector components, which have to be translated into the expected detector response, represented by currents and voltages of the readout channels (so-called *digits*). This process includes e.g. the simulation of electronics noise, the presence of additional primary proton–proton interactions (pile-up) or interactions with gas in the beam pipe.

4.2. Data, Signal and Background Processes

Given the topology of the processes of interest for this analysis and the applied event selection (see Chapter 6), of course not all SM processes have to be considered but only a small subset for which the contribution to the signal and control regions are not negligible. For the background estimation, this analysis makes use of officially produced MC samples as well as data-driven background estimation methods.
In the following, the simulated samples and the backgrounds determined by data-driven methods are described.

4.2.1. Simulated Samples

MC samples were processed either through the full ATLAS detector simulation based on GEANT4, or through the faster simulation *ATLFAST-II* making use of parametrised showers in the calorimeters both described in Section 4.1.4. Additional simulated pp collisions generated with PYTHIA 8.186 were overlaid to model the effects of both in- and out-of-time pileup, from collisions in the same and nearby bunch crossings, respectively. The pile-up distribution in the simulation is reweighed to reflect the mean number of additional interactions observed in data. All simulated events were processed using the same reconstruction algorithms and analysis chain as the data, and small corrections were applied to lepton trigger and reconstruction efficiencies to better model the response observed in data. All simulated samples use PHOTOS 3.22 [95] to simulate photon radiation, TAUOLA 2.7 [96] to simulate τ decays and EVTGEN [97] to model the decays of heavy-flavour hadrons.

Table 4.1 provides a summary of basic parameters of the MC samples used in the analysis which are discussed in the following. The list of the used data sets is given in Appendix VI.

Standard Model $t\bar{t}$ and Single Top Production

Simulated samples of $t\bar{t}$+jets events are generated with the NLO generator POWHEG 2.0 [98–101] using the CT10 PDF set [102]. All samples are generated assuming a top-quark mass (m_t) of 172.5 GeV and top-quark decays exclusively through $t \to Wb$. The Standard Model

Process	Generator + parton showering/hadronisation	Tuned parameters	PDF set	Inclusive cross-section order in pQCD
$\boldsymbol{Yqb}$	MADGRAPH5_aMC@NLO 2.2.3 + PYTHIA 8.210	A14	NNPDF2.3	NLO
$\boldsymbol{t\bar{t}}$	POWHEG-BOX 2.0 + PYTHIA 6.428	P2012	CT10	NNLO+NNLL
Single top	POWHEG-BOX 1.0 + PYTHIA 6.428	P2012	CT10	NNLO+NNLL
Dibosons WW, WZ, ZZ	SHERPA 2.1.1	Default	CT10	NLO
$\boldsymbol{W/Z}$ **+ jets**	SHERPA 2.2.0	Default	CT10	NNLO
$\boldsymbol{t\bar{t}V}$	MADGRAPH5_aMC@NLO 2.2.3 + PYTHIA 8.210	A14	NNPDF2.3	NLO
$\boldsymbol{t\bar{t}H}$	MADGRAPH5_aMC@NLO 2.2.3 + Herwig++ 2.7.1	CTEQ6L1	CT10	NLO

Table 4.1.: List of generators used to model the different background and signal processes. Information is given about the perturbative QCD (pQCD) highest-order accuracy used for the normalisation of the different samples, the underlying event tunes and PDF sets considered. All processes, except for Yqb signals, are generated at NLO in QCD.

expectation of 0.1082 was assumed for the $W \to l\nu$ branching ratio [103]. The POWHEG model parameter and resummation damping factor h_{damp}, which controls matrix element to parton-shower matching in POWHEG and effectively regulates the high-p_{T} radiation, was set to $m_t = 172.5$ GeV, a setting which was found to best describe the $t\bar{t}$ system p_{T} at $\sqrt{s} = 7$ TeV [104].

The nominal sample is interfaced to PYTHIA 6.428 [105] with the CTEQ6L PDF set [106] and the Perugia2012 (P2012) UE tune [107] for the simulation of the parton-shower and the hadronisation. Alternative $t\bar{t}$ simulation samples were generated using POWHEG interfaced to HERWIG++ [108] and aMC@NLO [109] interfaced to Herwig++.

The effects of initial- and final-state radiation (ISR/FSR) were explored using two alternative POWHEG+PYTHIA samples, one with h_{damp} set to $2m_t$, the renormalisation and factorisation scales set to half the nominal value and using the Perugia 2012 radHi UE tune, giving more radiation, and one with the Perugia 2012 radLo UE tune, $h_{\text{damp}} = m_t$

and the renormalisation and factorisation scales set to twice the nominal value, giving less radiation [110].
The alternative $t\bar{t}$ samples were produced using fast simulation and compared to a full simulation version of the baseline sample.
The $t\bar{t}$ samples are normalised to the next-to-next-to-leading-order (NNLO) cross-section using Top++ [111], including resummation of next-to-next-to-leading logarithmic (NNLL) soft gluon terms [112–116].
Theoretical uncertainties result from variations of the factorisation and renormalisation scales, as well as from uncertainties on the PDF and α_{S}. The latter two represent the largest contribution to the overall theoretical uncertainty on the cross-section and were calculated using the PDF4LHC prescription.

Samples of $t\bar{t} + V$ events ($V = W, Z$), including $t\bar{t}WW$, are generated with up to two additional partons using Madgraph5 and interfaced to Pythia 8 with the A14 NNPDF23LO UE tune. A sample of $t\bar{t}H$ events is generated with aMC@NLO generator using the CT10 PDF set. Showering is performed using Herwig++ and the UE-EE-5 [117] tune with the CTEQ6L1 PDF set. Inclusive decays of the Higgs boson are assumed in the generation of the $t\bar{t}H$ sample.

Samples of single top-quark backgrounds corresponding to the Wt and s-channel production mechanisms are generated with Powheg 2.0 [98–101] using the CT10 PDF set. Overlaps between the $t\bar{t}$ final states at LO and Wt final states at NLO are removed using the *diagram removal* (DR) scheme [118]. Samples of t-channel single top-quark events are generated using the Powheg (ST_tchan_4f) [119] NLO generator that uses the four-flavour scheme (4FS). The fixed four-flavour PDF set CT10f4 [102] is used for the matrix-element calculations. The single top-quark samples are normalised to the approximate NNLO theoretical cross-sections [120–122]. The parton shower, hadronisation and the underlying event are either modelled using Pythia 6 Perugia2012 tune [107] or Herwig++ [108] and the UE-EE-5 [117] tune.
An alternative single top-quark Powheg Wt sample was generated using the diagram subtraction (DS) scheme [123, 124] instead of DR, where a gauge-invariant subtraction term modifies the NLO Wt cross-section to locally cancel the double-resonant $t\bar{t}$ contribution [123, 125]. These additional Wt samples are used to estimate major systematic uncertainties.

W+jets, Z+jets and Diboson Productions

Samples of W/Z+jets events are generated with the SHERPA 2.2.0 [126] generator. The matrix-element calculation is performed up to two partons at NLO and up to four partons at LO using Comix [127] and OpenLoops [128]. The matrix element calculation is merged with the SHERPA parton shower [129] using the ME+PS@NLO prescription [130]. SHERPA models the hadronisation by its module AHADIC based on cluster-fragmentation [131–134]. The W/Z+jets samples have been produced with a simplified scale setting prescription in the multi-parton matrix elements, to improve the event generation speed. The PDF set used for the matrix-element calculation is CT10 with a dedicated parton shower tuning developed by the SHERPA authors. Both the W+jets and Z+jets samples are normalised to their respective inclusive NNLO theoretical cross-section calculated with FEWZ [135]. For the specific cases of W and Z+jets production, filters on vector-boson p_{T} and heavy-flavour content have been used to guarantee enough statistics in the full phase space. Samples are produced for each of the W+jets and Z+jets categories using filters for a b-jet (Wb or Zb+jets), a c-jet and no b-jet (Wc or Zc+jets), and with a veto on b- and c-jets (W or Z+light-jets).
It was observed that the Sherpa v2.2.0 V+jets samples predict too large cross-sections for large jet multiplicity at reconstruction level. This was traced back to an issue with the scale settings used in the central production samples. This problem is solved by reweighting the events with respect to the truth jet multiplicity using correction factors provided by the ATLAS Physics Modelling Group (PMG). Furthermore, it happens that Sherpa samples contain events with large Monte Carlo generator weights ($|w| > 100$). Such large weights occur if the differential cross-section in particular phase space regions is larger than the maximal weight which was estimated during the phase space optimisation. In this analysis, the weight of such events is set to unity manually as proposed by PMG.

Samples of diboson production $WW/WZ/ZZ$+jets are generated with the NLO generator SHERPA v2.1.1 and include processes containing up to four electroweak vertices. The matrix-element includes zero partons at NLO and up to three partons at LO using the same procedure as for the W/Z + jets. The final states simulated are 4ℓ, $\ell\ell\ell\nu$ with two different-flavour leptons and $\ell\ell\nu\nu$, and include off-shell Z-boson contributions. The diboson samples are normalised to their generator cross-sections (already at NLO).

Signal Samples

For the signal production, an implementation of the model described in [44] is deployed using MADGRAPH5 [136]. The signal events are generated in four-flavour scheme[2] with leading-order accuracy, with the NNPDF2.3 PDF sets [137] and are processed afterwards by Pythia 8 for the hadronisation modelling. The final limits are computed using Y signals, also for the singlet T interpretation[3]. This is justified due to the very similar kinematics of the decay products of the T and Y [23] as well as the negligible acceptance for the other decay modes of the T quark ($T \to Zt$, $T \to Ht$) (see Section 6.5.2). The signals are produced for different mass points: from 800 GeV to 1900 GeV, with 100 GeV steps for the coupling $\kappa = 0.5$ (for a relation to $c_{L/R}$, see Section 2.4.2), where the $Y \to Wb$ branching ratio is 100%. The signal samples corresponding to masses of 900 GeV, 1600 GeV, 1700 GeV, 1800 GeV and 1900 GeV are only available with the fast simulation, where the remaining samples are generated using the full ATLAS simulation. The differences between both simulations are evaluated in Section 7.5.
All signal samples are produced without considering interference and, since the kinematics of the final-state particles are again very similar for left-handed and right-handed particles [23], only left-handed signals are considered. To account for the interference effects, a reweighting procedure has to be applied, which is described in Section 4.3.
Further signal samples needed for the evaluation of systematic uncertainties, computation of the contamination of the signal region and control regions from other production and decay modes (see Section 6.5.2) are given in Appendix VI.

4.2.2. Data-Driven Backgrounds

For this analysis, the most important background estimation and modelling is driven by MC simulation. However, it is well known that not all backgrounds are well modelled in all phase space regions. Therefore, also data-driven background estimations and corrections, respectively, are utilised.

[2]The differences between four- and five-flavour schemes have been checked explicitly and only significant differences are found for the left-handed Y. The yields in the four- and five-flavour schemes differ by a factor of about two, while the m_{VLQ} distributions are very similar.
[3]The branching ratio of $\mathcal{B}(T \to Wb) \approx 0.5$ for the T-quark signals is taken into account.

Multijet Background

Several background sources which also contribute to events which are identified to contain a single lepton and jets final state are not mentioned so far. These comprise backgrounds with leptons not stemming from hard interactions (non-prompt), misidentified leptons or multijet production, in the following also referred to as fakes. The probability of these processes to occur is very small and thus the simulation of these backgrounds would be not very accurate. A more suited approach for their estimation is data-driven and the method used in this analysis is referred to as the *Matrix Method* [138].

The *Matrix Method* is based on the investigation of phase space regions with lepton candidates of lower reconstruction quality and used to disentangle the mixture of fakes found in the multijet background, and prompt leptons originating from the W/Z bosons to obtain a data-driven estimate of the fake lepton background component of the selected sample [138, 139].
The sample is divided into two overlapping subsamples based on the lepton identification:

- **Signal**
  Events in this category contain either an electron or muon candidate which satisfies the signal requirements given in Table 5.1 and 5.2, respectively.
- **Multijet**
  Events in this category have to contain a lepton which satisfies the multijet requirements in Table 5.1 and 5.2, i.e. the electron identification is loosened from TightLH to MediumLH with no isolation and muons are not forced to be isolated.

The number of events passing the multijet (N^{multijet}) and signal (N^{signal}) selection are decomposed into the sum of events with real leptons (high-p_{T} isolated leptons from W or Z decays) and fake leptons:

$$\text{N}^{\text{multijet}} = N^{\text{multijet}}_{\text{real}} + N^{\text{multijet}}_{\text{fake}}, \tag{4.4}$$

$$\text{N}^{\text{signal}} = \epsilon_{\text{real}} N^{\text{multijet}}_{\text{real}} + \epsilon_{\text{fake}} N^{\text{multijet}}_{\text{fake}} \tag{4.5}$$

where ϵ_{real} and ϵ_{fake} are the efficiencies for real and fake leptons to go from the multijet to the signal sample. These efficiencies are determined using control regions purified in real and fake leptons.

The actual number of fakes for the single lepton selection can be obtained from combining Equations 4.4 and 4.5, and solving for $N_{\text{fake}}^{\text{signal}} = \epsilon_{\text{fake}} N_{\text{fake}}^{\text{multijet}}$:

$$N_{\text{fake}}^{\text{signal}} = \frac{\epsilon_{\text{fake}}}{\epsilon_{\text{real}} - \epsilon_{\text{fake}}} (\epsilon_{\text{real}} N^{\text{multijet}} - N^{\text{signal}}). \tag{4.6}$$

The real and fake efficiencies ϵ_{fake} and ϵ_{real} are determined by the TopFakes group as a function of several kinematic variables such as p_T of the lepton (PT), η of the lepton (ETA), p_T of the leading jet (JETPT), $\Delta\phi(\vec{p}_{Tl}, \vec{p}_T^{\,\text{miss}})$ (DPHI) and the minimal $\Delta R(\vec{p}_l, \vec{p}(central\ jets))$, where all of these can be combined for the determination of the final efficiency. Beside this, all efficiency parameterisations are available with the requirement of more than one or exactly one jet. Furthermore, the parameterisation for the real and fake efficiencies could be chosen independently, however it was chosen to always use the same parametrisation for both. To obtain an estimate for the fake background using efficiencies with a particular parameterisation, Equation 4.6 is applied event-wise to data, where $N_{\text{fake}}^{\text{signal}}$ is used as a weight of the event.
To determine which parametrisation results in the most accurate estimate, a multijet enriched region is defined which is referred to as *multijet validation region* in the following. This region is equally defined as the pre-selection (see Section 6.2) except that the leading jet has to be b-tagged, the E_T^{miss} requirement is loosened to $E_T^{\text{miss}} > 20$ GeV and that $E_T^{\text{miss}} + m_T^W > 60$ GeV[4].
Different parametrisation have been tested in this region and the data is compared to the simulation for different kinematic distributions (see also Appendix III). It is found that the optimal choice is a parameterisation with respect to JETPT (leading jet p_{T}) for the electron channel and with respect to PT and DR for the muon channel (lepton p_{T} and minimal ΔR(lepton, central jets)). Figures 4.2, 4.3 and 4.4 show the lepton p_T, E_T^{miss} and

[4]The transverse W mass m_T^W is defined as $m_T^W = \sqrt{2p_T^l E_T^{\text{miss}}[1 - \cos\Delta\phi(p_T^l, E_T^{\text{miss}})]}$, where p_T^l is the transverse momentum of the lepton and $\Delta\phi(p_T^l, E_T^{\text{miss}})$ is the difference in ϕ of the lepton and the E_T^{miss} vector.

m_{VLQ} distribution in the multijet validation region.

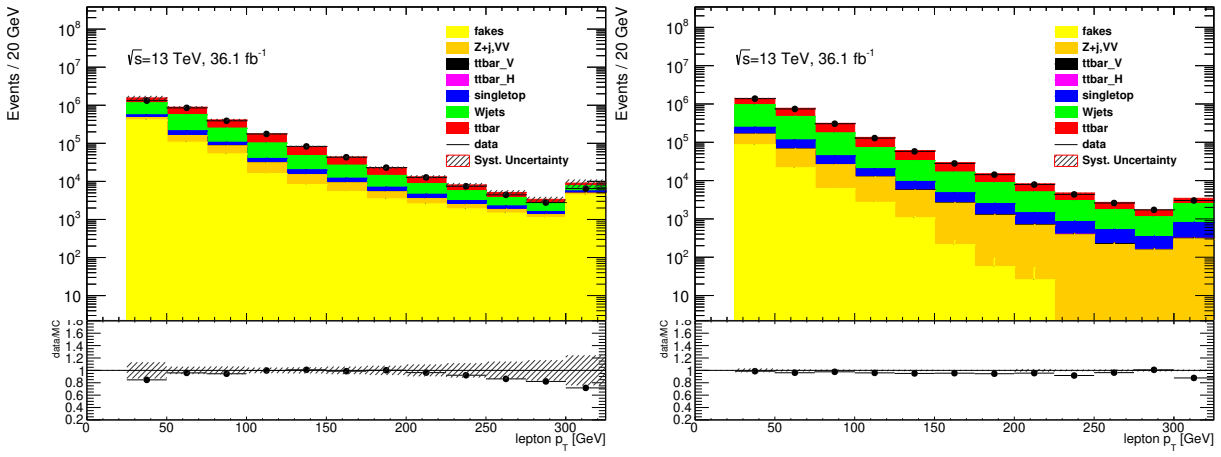

(a) (b)

Figure 4.2.: Lepton p_T distribution in the multijet validation region in the electron channel 4.2(a) and in the muon channel 4.2(b). The shaded band depicts the statistical uncertainty and a 50% normalisation uncertainty of the multijet estimate.

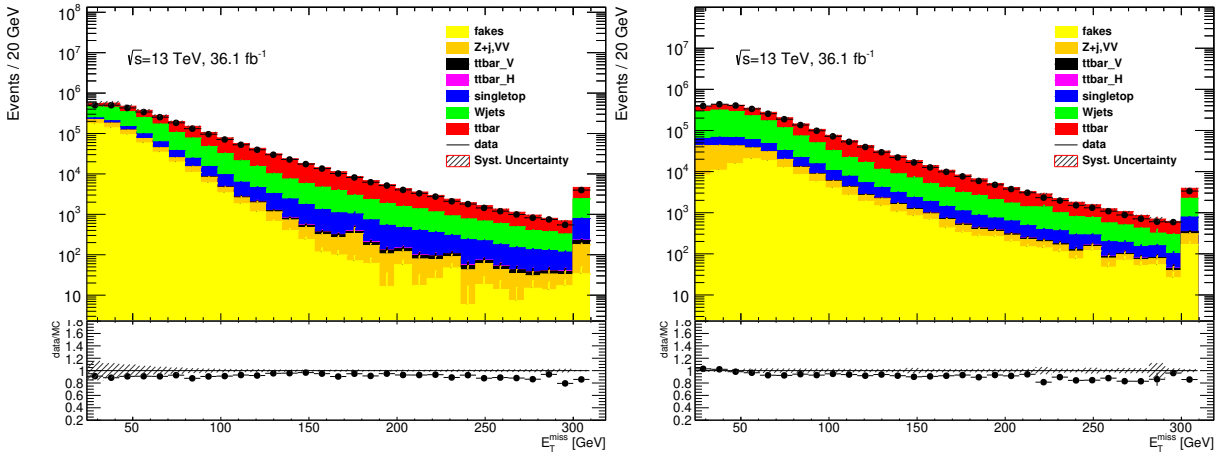

(a) (b)

Figure 4.3.: E_T^{miss} distribution in the multijet validation region in the electron channel 4.3(a) and in the muon channel 4.3(b). The shaded band depicts the statistical uncertainty and a 50% normalisation uncertainty of the multijet estimate.

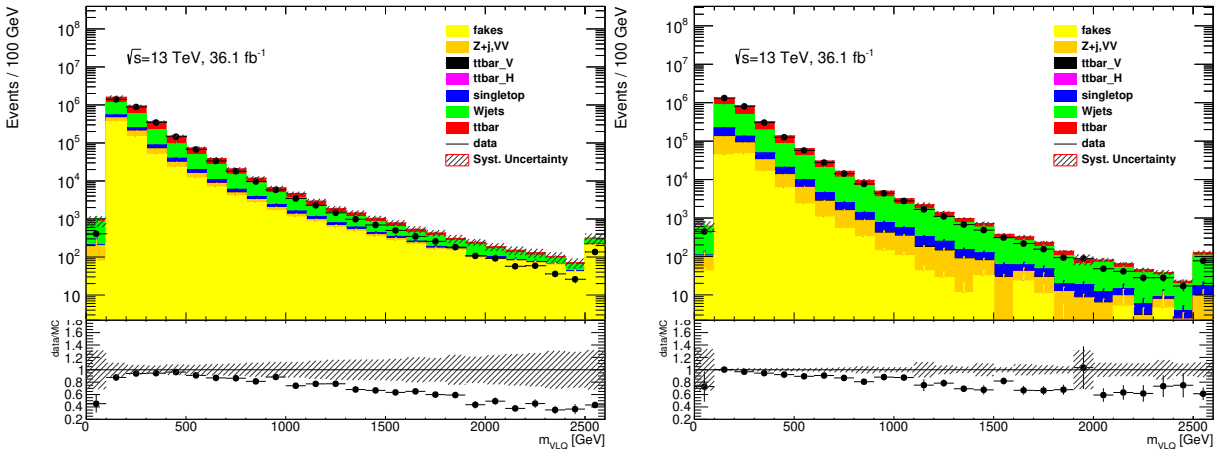

(a) (b)

Figure 4.4.: Mass distribution of vector-like quark candidate m_{VLQ} in the multijet validation region in the electron channel 4.4(a) and in the muon channel 4.4(b). The shaded band depicts the statistical uncertainty and a 50% normalisation uncertainty of the multijet estimate.

Background Correction with Control Regions

Any measured data excess over the background estimation would be interpreted as an indication for new physics, thus it is extremely important to make sure that the SM prediction is accurate. For this purpose event selections orthogonal to the signal region, referred to as *control regions* (CRs), are defined such that they are dominated by a particular background and suppress signal events as much as possible. Since these regions contain only events belonging to in principle well understood SM processes, any deviation is expected to be explainable by the uncertainties of the backgrounds. Therefore, especially these regions are used to correct the background prediction by pulling the nuisance parameter of the corresponding uncertainties (see Chapter 8).
The normalisation for $t\bar{t}$ and W+jets events is freely floating in the fit, since it is observed in other analyses in similar phase-space regions that $t\bar{t}$ and W+jets contributions in MC differ more from data than covered by the uncertainty on the inclusive cross-sections. There is no dedicated CR that allows to constrain well the background from single-top-quark production, since it is not possible to separate signal events from this background, given that single-top-quark production significantly results in the same final state as VLQ T production. As described above in Section 4.2.2, the multijets background is estimated on

data using the so-called matrix method. The SM dibosons and Z+jets background is very small and is well described by the simulation, consequently, no data-driven estimation is performed for these processes.

However, it is obvious that the quality of background modelling depends on the phase space region. Therefore and since the aim of control region is to check and correct the backgrounds in the signal region, the event selection for the control region needs to be as close as possible to the signal region.
For this reason and because the correction for the backgrounds is determined simultaneously in signal and control regions, the definition as well as the evaluation of the control regions is postponed to Section 6.4 after the signal region definition in Section 6.3.2.

4.2.3. Data Samples

The results described in this thesis are based on the full 13 TeV pp collision data sample collected in 2015 and 2016 by the ATLAS detector at the LHC, which belong to the *Main* physics stream[5]. The recorded peak luminosity was $L = 1.37 \times 10^{34} cm^{-2} s^{-1}$ with a bunch spacing of 25 ns and a mean number of additional pp interactions per bunch crossing (pileup) in the dataset of $\langle \mu \rangle = 25$.
To assure good data quality, all detector components are constantly monitored and with this informations so called *Good Run Lists* (GRL) are created, which allow to filter the recorded events on luminosity block[6] level to assure all necessary components operated as expected. The used GLRs are:
data16_13TeV.periodAllYear_DetStatus-v83-pro20-15_DQDefects-00-02-04_PHYS_StandardGRL_All_Good_25ns.xml,
data15_13TeV.periodAllYear_DetStatus-v79-repro20-02_DQDefects-00-02-02_PHYS_StandardGRL_All_Good_25ns.xml
for 2016 and 2015 data, respectively.
After the application of beam, detector and data quality requirements, the integrated luminosity considered in this analysis corresponds to 36.1 fb^{-1}.

[5]Events accepted by the HLT and used for physics analyses are written to single *Main* stream replacing the three separate physics streams (Egamma, Muons, JetTauEtMiss) used in Run-1.
[6]The luminosity block is a time interval defined by the ATLAS central trigger processor (CTP) for which it is assumed that the data recording took place under uniform conditions [140].

4.3. Signal Reweighting

In Section 2.4 it was demonstrated that not only the cross-section of VLQs but also the shape of the mass distribution, especially when interference effects are considered, is highly coupling dependent. Since the shape information is used in the statistical analysis (see Chapter 8), the results depend on the couplings used for the signal Monte Carlo production. To be more specific: The statistical analysis uses simulated signals produced with a coupling c^{Wb} and results in a 95% CL coupling limit c^{Wb}_{limit} where for instance $c^{Wb}_{limit} > c^{Wb}$ holds. However, if the signal with a coupling of c^{Wb}_{limit} actually exists, it would correspond to a larger VLQ width (considering interference the shape changes even more drastically). Thus, depending on the sensitivity of the analysis, it could be harder (the peak of the distribution becomes smaller) or easier (the tails become larger) to detect this signal in comparison to a simply scaled signal with coupling c^{Wb}. Therefore, a quoted coupling limit is only meaningful if the used signal distributions correspond to a coupling $c^{Wb'}$ where $c^{Wb'} = c^{Wb}_{limit}$. This is obviously a problem as the final limit is not known beforehand and since it is not possible to produce MC signal samples of every coupling. This is why a reweighting procedure was developed in close collaboration with Tobias Kupfer, Didier Alexandre and Ferdinand Schenck.

Reweighting Procedure

The reweighting procedure assigns each MC signal event a weight based on the truth VLQ mass, i.e. the invariant Wb mass m_{Wb}, according to

$$r(m_{Wb}; c^{Wb}, c_0^{Wb}) = \frac{K_{\mathrm{VLQ}} f_{\mathrm{VLQ}}(m_{Wb}; c^{Wb}) + \sqrt{K_{\mathrm{SM}} \cdot K_{\mathrm{VLQ}}} f_{\mathrm{I}}(m_{Wb}; c^{Wb})}{f_{\mathrm{VLQ}}(m_{Wb}; c_0^{Wb})}, \tag{4.7}$$

where the K-factors, K_{VLQ}, are taken from Ref. [43] and K_{SM} is set to unity [7]. The functions $f_{\mathrm{VLQ}}(m_{Wb}; c^{Wb})$, $f_{\mathrm{I}}(m_{Wb}; c^{Wb})$ and $f_{\mathrm{VLQ}}(m_{Wb}; c_0^{Wb})$ represent the distribution of m_{Wb} taken from high statistics MC samples of 10-20$\cdot 10^6$ events for each mass point, target coupling c^{Wb} and nominal coupling c_0^{Wb}. The values of $r(m_{Wb}; c^{Wb}, c_0^{Wb})$ are filled into a histogram,

[7] No NLO calculations for the interfering SM processes, t-channel single-top-quark production with far off-shell t-quarks and Wbq production, are available. The K-factor for on-shell t-channel single-top-quark production is close to one [141].

smoothed and fitted in order to obtain a continuous reweighting function.

It has been checked that samples generated at the target coupling c^{Wb} and reweighted samples from c_0^{Wb} to c^{Wb}, exhibit the same distributions of kinematic observables as it can be seen in Fig. 4.5. A systematic uncertainty on the total yield as well as on the shape of the distribution are assigned to this procedure (see Section 7.6.3).

Iterative Procedure

A priori it is not clear which coupling should be used as the target coupling for the reweighting procedure, since this obviously depends on the final results of the limit setting. Thus, an iterative procedure has to be performed: The default VLQ-only signal template is reweighted by applying the method described above to construct the signal-plus-interference template $h_{\mathrm{VLQ+I}}(m_Q; c^{Wb})$ containing the VLQ (σ_{VLQ}) and the interference contribution (σ_{I}). This reweighted template is used in the maximum-likelihood fit for signal-plus-background hypothesis (see Section 8.2.2) to determine an upper limit on $\sigma_{\mathrm{VLQ}}+\sigma_{\mathrm{I}}$. Now, the interference cross-section σ_{I} is subtracted and the result is used in Equation 2.55 and a corresponding coupling value $c^{Wb\prime}$ is calculated. Hereafter, a new signal template $h_{\mathrm{VLQ+I}}(m_Q; c^{Wb\prime})$ is constructed and the fit is repeated until convergence is observed in the coupling value $c^{Wb\prime}$. As mentioned in Section 2.4.2, the theoretical cross-sections are taken from Ref. [43], where the NLO Wb fusion cross-section is calculated using the NWA. However, the NWA is not valid for large masses and couplings. Therefore, cross-section correction factors are applied:

$$C_{\mathrm{NWA}} = \frac{\sigma_{\mathrm{LO,noNWA}}}{\sigma_{\mathrm{LO,NWA}}},$$

where $\sigma_{\mathrm{LO,noNWA}}$ is the LO cross-section without the NWA and $\sigma_{\mathrm{LO,NWA}}$ the LO cross-section with the NWA. Both cross-sections are computed with the MADGRAPH5_aMC@NLO 2.2.3 [109] generator (see Fig. 8.6 for a comparison of the cross-sections with and without NWA.).

It is explicitly checked that the result of the iterative procedure does not depend on the choice of starting value for c^{Wb}, by repeating the full iterative process with a lower or higher starting value than the one at convergence.

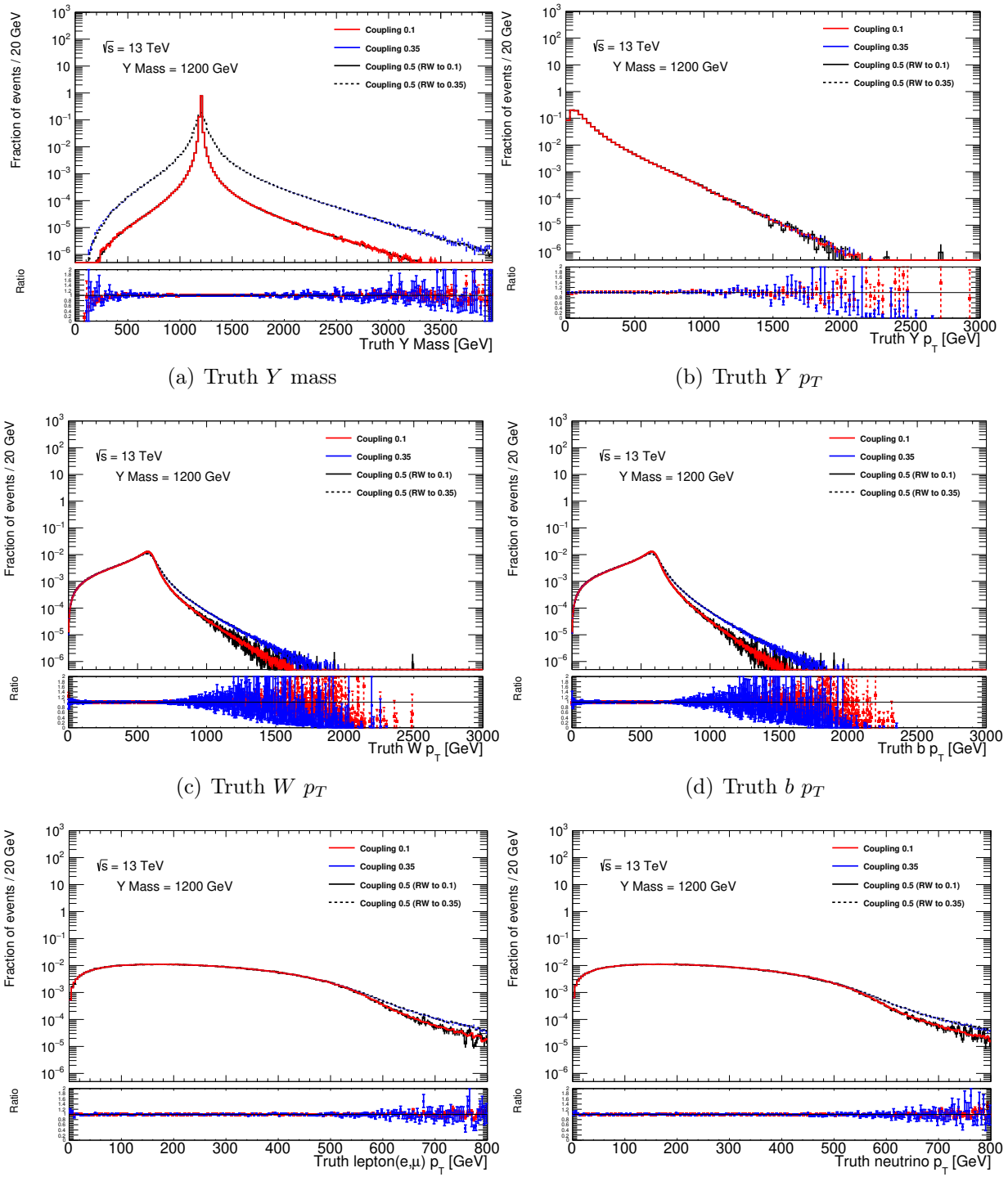

(a) Truth Y mass

(b) Truth Y p_T

(c) Truth W p_T

(d) Truth b p_T

(e) Truth ℓ p_T

(f) Truth ν p_T

Figure 4.5.: Kinematic distributions (4.5(a) : Y mass, 4.5(b) : Y p_T, 4.5(c) : W p_T, 4.5(d) : b p_T, 4.5(e) : ℓ p_T, 4.5(f) : ν p_T) are compared for truth samples, nominally produced with three different couplings κ (0.1, 0.35, 0.5) and two reweighted distributions (from 0.5 to 0.1 and from 0.5 to 0.35, respectively). The ratios are always the ratio between the nominal and reweighted distribution.

Chapter 5.

Object Reconstruction and Selection

The particles created in the *pp* collision traverse the detector components and the interactions with the detector material are recorded as currents and voltages. However, to perform physics analysis, physics objects have to be reconstructed from these raw informations. Naturally, this reconstruction is imperfect and several selection criteria have to be applied to achieve the desired quality. In this chapter, all relevant reconstruction techniques and applied quality criteria are described.

5.1. Interaction Vertices and Tracks

For the reconstruction of charged particle tracks, a combination of an Inside-out and Outside-in algorithm is applied [142, 143]. First, clusters are built from raw measurements in the pixel and SCT detectors from which so called space-points are created. Three of these space-points are used to form track seeds. From the chosen seeds, a combinatorial Kalman filter [144] is then used to build track candidates by incorporating additional space-points from the remaining layers of the pixel and SCT detectors. As this results in all realistic combinations of space-points, there are a number of track candidates where space-points overlap or have been incorrectly assigned, which necessitates an ambiguity-solving stage. The ambiguity solver relies on a track score definition that puts tracks into an order, since track candidates considered to create the reconstructed tracks are processed in descending order with respect to that score and tracks having a bad score are removed. Furthermore, Track candidates are rejected by the ambiguity solver if they do not meet any of the following criteria [143]:

- $p_T > 400$ MeV
- $|\eta| < 2.5$
- Minimum seven pixel and SCT clusters
- Maximum of either one shared pixel cluster or two shared SCT clusters on the same layer
- Not more than two holes in the combined pixel and SCT detectors
- $|d_0| < 2.0$ mm
- $|z_0 \sin\theta < 3.0$ mm$|$

where θ is the track polar angle, d_0 is the transverse impact parameter with respect to the beam line position and z_0 is the longitudinal difference along the beam line between the point where d_0 is measured and the primary vertex. For track candidates fulfilling these requirements, a high-resolution fit is performed using all available information. Fitted tracks which were not removed by the ambiguity solver are added to the final track collection and are extended into the TRT.
After this Inside-out sequence a reverse sequence is deployed (Outside-in) that starts a global pattern recognition in the TRT.

Interaction vertices from the proton–proton collisions are reconstructed from tracks in the Inner Detector. For this, a set of tracks satisfying an even tighter set of track selection criteria is used to find the primary vertices via an iterative procedure [145, 146]. Those fitted vertices having at least two tracks with $p_T > 0.4$ GeV and being consistent with the beam-collision region in the x-y plane are kept as primary vertices.
Due to multiple proton–proton collisions from the same or different bunch crossings (pile-up) in each recorded event usually more than one primary vertex is reconstructed. For objects which require an association to an primary vertex, the vertex with the largest quadratic sum of transverse momenta from associated tracks ($\sum |p_{T,\mathrm{track}}|^2$) is chosen.

5.2. Electrons

Electron candidate reconstruction [147–149] starts with the seed-cluster reconstruction from isolated energy deposits in the EM calorimeter within the fiducial region of $|\eta_{\text{cluster}}| < 2.47$, where η_{cluster} is the pseudorapidity of the calorimeter energy deposit associated with the electron candidate. An additional veto is placed on electrons in the calorimeter transition region between the barrel and end-cap electromagnetic calorimeters, $1.37 < |\eta_{\text{cluster}}| < 1.52$. The seeds are found with a sliding window with a size corresponding to the granularity of the EM calorimeter middle layer requiring a total transverse energy above 2.5 GeV. These seeds are finally matched to track candidates passing either the pion or electron hypothesis to form electron candidates for which the associated track has to be compatible with the primary vertex of the event. Candidates not fulfilling the quality requirements are removed. To determine whether the reconstructed electron candidates are signal-like objects or background-like objects, the likelihood identification criteria described in Ref. [149] are applied. It is a multivariate analysis (MVA) technique that simultaneously evaluates several properties of the electron candidates when making a selection decision. From the background and signal probabilities, a likelihood discriminant is constructed for which three levels of identification operating points are typically provided for electron identification. These are referred to as LooseLH, MediumLH and TightLH corresponding respectively to 96%, 94% and 88% identification efficiencies for signal electrons at $E_T = 100$ GeV.
In addition to the identification criteria, electrons are required to fulfil isolation requirements with respect to two isolation variables, to further discriminate between prompt signal and non-prompt or fake electrons. For this purpose, the calorimetric isolation is defined as the sum of transverse energies of topological clusters and track isolation defined as the sum of transverse momenta of all tracks, satisfying the quality requirements, within a cone of $\Delta R = \min(0.2, 10 \text{ GeV}/\text{E}_T)$.

In this thesis, TightLH electrons using a so-called Gradient isolation, relying on both isolation variables, are used for the signal processes and MediumLH electrons without isolation cuts are used for the data-driven estimate of the fake and real electron selection efficiency as discussed in Section 4.2.2.
The selection of the electrons used in this thesis is summarised in Table 5.1. The track selection mentioned in Table 5.1 is applied using the ElectronTrackVertexAssociationTool [150] performing both a cut on the d_0 significance of the transverse impact parameter

Electrons		
	Signal	Multijet
p_T threshold	25 GeV	
$\lvert\eta\rvert$	$< 2.47 \notin [1.37, 1.52]$	
Identification	TightLH	MediumLH
Isolation	Gradient	none
$\lvert d_0/\sigma(d_0)\rvert$	< 5	
$\lvert z_0 \sin\theta\rvert$	< 0.5 mm	

Table 5.1.: Selection for electron candidates used in the analysis.

of the track with respect to the measured beam line position and on the $|z_0 \sin\theta|$ with respect to the primary vertex of the event. Electron and muon tracks are matched to the primary vertex of the event by requiring the longitudinal impact parameter z_0 to satisfy $|z_0 \sin\theta| < 0.5$ mm, where θ is the polar angle of the track. The d_0 significance of the transverse impact parameter of the track is required to satisfy $|d_0/\sigma(d_0)| < 5$ for electrons, where $\sigma(d_0)$ is the uncertainty on d_0.

To match the simulated electron scale and resolution to the measurement, corrections are applied. Additionally, scale factors are applied to account for the differences of the identification, isolation and trigger efficiencies between simulation and measurement.

5.3. Muons

Muons are reconstructed first independently in the ID and MS. These candidates from the subdetectors are then combined to form the muon tracks that are used in physics analyses [151].
The muon track reconstruction in the ID is performed like for any other charged particles as described in Section 5.1. Muon reconstruction in the MS starts with a search for hit patterns inside each muon chamber to form segments combining the measurements in the

MDT chambers, CSC, RPC and TGC, whereas the algorithm requires a loose compatibility of the track with the interaction region. Muon track candidates are then built by a fit using the hits from segments in different layers. The hits associated with each track candidate are fitted using a global χ^2 fit and accepted if the selection criteria are satisfied.

The combination of the independently reconstructed muon candidates from the ID and MS is performed according to various algorithms based on the information provided by the ID, MS, and calorimeters. Depending on which subdetectors are used in reconstruction, four muon types are defined:

- Combined (CB) muon: From the independently reconstructed tracks in the ID and MS a combined track is formed by a global refit using hits from the ID as well as the MS subdetectors.
- Segment-tagged (ST) muons: If at least one local track segment in the MDT or CSC chambers is associated with a extrapolated track from the ID, this track is classified as a muon.
- Calorimeter-tagged (CT) muons: If an ID track can be matched to an energy deposit in the calorimeter compatible with a minimum-ionizing particle, it is identified as muon.
- Extrapolated (ME) muons: The muon trajectory is reconstructed using the MS track only and a loose compatibility with originating from the vertex is required.

For the mentioned track-to-vertex association, certain thresholds of the d_0 significance $|d_0/\sigma(d_0)|$ of the track with respect to the beam line with uncertainty $\sigma(d_0)$ and the longitudinal impact parameter $|z_0 \sin\theta|$ with respect to the primary vertex of the event are defined.
It happens that the candidates for the different types overlap, which is resolved before producing the collection of muons used in physics analyses: If muons share an ID track, CB muons are preferred over ST as well as CT muons and ST muons are preferred over CT muons. Overlap with ME muons is resolved by selecting the track with higher fit quality and a larger number of hits.

Muons		
	Signal	Multijet
p_T threshold	25 GeV	
$\|\eta\|$	< 2.5	
Identification	Medium	
Isolation	Gradient	none
$\|d_0/\sigma(d_0)\|$	< 3	
$\|z_0 \sin\theta\|$	< 0.5 mm	

Table 5.2.: Selection for muon candidates used in the analysis.

As for the electrons, the muon identification is performed by applying quality requirements that suppress background from non-prompt muons while selecting prompt muons with high efficiency and/or guaranteeing a robust momentum measurement. There are four different identification selections: Loose, Medium (default), Tight and High-p_{T} muons. They differ in the q/p significance (absolute difference of charge/momentum ratio measured in the ID and MS divided by the squared sum of uncertainties), ρ' (absolute difference p_{T} measured in ID and MS divided by p_{T} of the combined track), χ^2 of the combined fit, allowed muon types as well as the number of required/allowed hits and holes, respectively. As for electrons, the same isolation requirements are applied for muons as well as the corresponding correction and scale factors are applied.

5.4. Jets

In the primary interaction as well as in subsequent decays not only leptons but also quarks and gluons are produced. However, even stable coloured particles can not be observed unbound, since they are quickly bound in colourless states, as described in Section 2.1.1. During this process of hadronisation, additional particles are produced which finally appear as spray or bundle of particles, so called jets.

The jet finding and reconstruction is separated into several stages, which are discussed in the following subsections.

5.4.1. Topo-Clusters

Jets are reconstructed from three-dimensional clusters consisting of topologically connected calorimeter cell signals [152]. The collection of signals into topo-clusters follows spatial signal-significance patterns generated by particle showers controlled by the signal significance which is defined as the ratio of the cell signal to the average (expected) noise in this cell $\zeta_{\text{cell}}^{\text{EM}} = \frac{E_{\text{cell}}^{\text{EM}}}{\sigma_{\text{noise,cell}}^{\text{EM}}}$. Both the cell signal $E_{\text{cell}}^{\text{EM}}$ and the noise $\sigma_{\text{noise,cell}}^{\text{EM}}$ are measured at the electromagnetic (EM) energy scale, meaning that they correctly reconstruct the activity of an electromagnetic shower but do not include any corrections for the loss of signal for hadrons. However, during the calibration of the reconstructed jet, this effect is corrected.
Topo-clusters are formed by a growing-volume algorithm starting from a calorimeter cell with a highly significant seed signal. The seeding, growth, and boundary features of topo-clusters are in this algorithm controlled by the parameters S, N and P, defining signal significance thresholds. Hereby, S defines the primary seed threshold (default S= 4), N is the threshold for growth control (default N= 2) and P represents the principal cell filter (default P= 0). The formation starts from primary seeds with $\zeta_{\text{cell}}^{\text{EM}} > S$ and collecting cells with $\zeta_{\text{cell}}^{\text{EM}} > N$ until in the last step cells with $N > \zeta_{\text{cell}}^{\text{EM}} > P$ are added.
The resulting proto-clusters can be too large to provide a good measurement of the energy flow and therefore proto-clusters with two or more local maxima (see definition in [152]) are split in all three spatial dimensions
The energy and direction of a topo-cluster are taken from a weighted mean of all its contributing cells.

5.4.2. Anti-k_t Algorithm

A jet is not a real physical object in the sense of a muon or electron, they are rather defined by the algorithm which reconstructs them. Thus, there are different possible definitions of a jet.
One of the most widely used algorithms is the Anti-k_t algorithm [153, 154], which is both infrared and collinear safe and is also deployed in this thesis.

The algorithm considers all topo-clusters as pseudojets and creates an ordered list with respect to p_T of the quantities

$$\begin{aligned} d_{ij} &= \min(p_{Ti}^{-2}, p_{Tj}^{-2}) \frac{\Delta R_{ij}^2}{R^2}, \\ d_{iB} &= p_{Ti}^{-2}, \end{aligned} \tag{5.1}$$

where i and j run over all topo-clusters with $j \neq i$ and R is a predefined parameter (typically 0.2, 0.4 or 1.0). Here, d_{ij} can be interpreted as the distance between the objects i and j in $\eta - \phi$ space and d_{iB} represents the squared transverse momentum with respect to the beam pipe. If the smallest value in the list is a d_{iB}, the object i is considered as final and removed from the list of pseudojets. If not, the objects (initially individual topo-clusters) i and j are merged and the list is recalculated. This procedure is repeated until all objects are removed and thus all jets are considered as final.

5.4.3. Jet Calibration

To account for the imperfect energy reconstruction, especially for hadronic jets, the reconstructed jets undergo a calibration procedure. The methods of the jet calibration are described in [155] and consist of several sequential steps as depicted in Fig. 5.1.
As a first step, the origin correction recomputes the jet four-momentum to point to the primary vertex, while keeping the jet energy constant, rather than the centre of the detector, which improves the η resolution of the jets. Since pile-up increases the activity in the calorimeter and spoils the jet energy measurement, a pile-up correction is applied. This correction has two components: an area-based p_T density subtraction, applied at the per-event level, and a residual correction derived from the MC simulation. As a next step, the jet energy scale (JES) calibration correct the four-momentum to the particle-level energy scale which was derived from truth jets in dijet MC events. A global sequential calibration further improves the reconstructed energy through the use of calorimeter, MS and track-based variables. As the last step, jets in data are corrected with a residual in situ calibration which uses well-measured reference objects, such as photons, Z bosons and

calibrated jets.

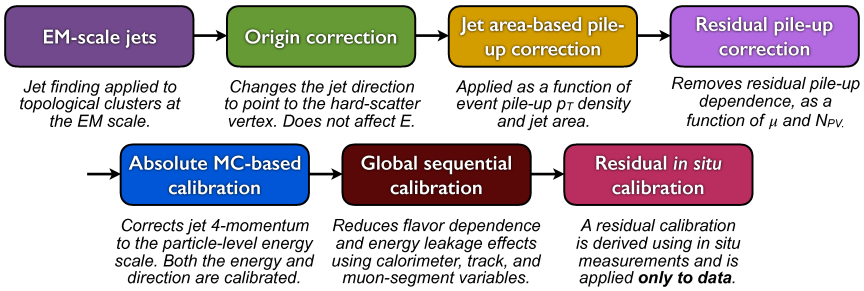

Figure 5.1.: Step sequence applied for the jet energy calibration [155].

5.4.4. Jet Vertex Tagging

To suppress jets originating from pile-up interactions, only jets which are associated with the primary vertex of the interaction are considered. To achieve this, the jet vertex tagger discriminant (JVT) [156] is deployed.
This variable is based on the k-nearest neighbour (kNN) algorithm and uses a two-dimensional likelihood based on R_{p_T} and corrJVF using simulated dijet events. Hereby, R_{p_T} is defined as the ratio of the scalar sum of the transverse momenta of all tracks of the jet originating from the hard-scatter vertex and the fully calibrated jet p_T (corrected for pile-up). The variable corrJVF is similarly defined as JVF but it is corrected for the dependence of the number of reconstructed vertices. The JVF in turn is the scalar p_T sum of matched tracks originating from a given vertex divided by the sum of p_T of all matched tracks of the jet.

5.4.5. *b*-Tagging

The decay of vector-like T and Y quarks is characterised by a high-p_T b quark which will, as usual, hadronise as a jet. The number of b quarks in the event provide a good handle to suppress background events and thus the identification of jets containing b hadrons (b-tagging) [157, 158] is an important ingredient in this analysis.

There are several b-tagging algorithms used in physics analysis in ATLAS but all rely on the trajectories of charged particles reconstructed in the ID as inputs. Most of them make use of the fact that hadrons containing b quarks (b hadrons) have a relatively long lifetime τ, which is of the order of 1.5 ps. This results in a decay length of $\langle L_{xy} \rangle = \beta\gamma c\tau = 6.4$ mm in the transverse plane before the decay for b hadrons with $p_T = 70$ GeV, which gives rise to a secondary vertex as depicted in Fig. 5.2.
The algorithm used for this thesis, MV2 [159, 160] is a multivariate discriminant, a Boosted Decision Tree (BDT), and is constructed from three variables:

- Impact parameter based: IP2D and IP3D
- Secondary vertex finding algorithm: SV
- The decay chain multi-vertex reconstruction algorithm: JetFitter

There are three variants of MV2 available, differing in the used training sets. The MV2c20 (the naming scheme has historical reasons) algorithm is defined as the output of such a BDT with the training performed by assigning b-jets as signal and a mixture of 85% light-flavour jets and 15% c-jets as background. MV2c10 and MV2c00 have 7% and 0% c-jet admixture in the background jets, respectively. There are 24 input variables used to train the BDT: 2 kinematics (p_T, η), 3 constructed from IP2D and IP3D output each, 8 from SV and 8 from JetFitter.
Jets are considered as being b-tagged if the value of the multivariate discriminant is larger than a certain threshold (operating point). These thresholds are chosen to provide a defined b-jet efficiency on a $t\bar{t}$ sample (see Table 5.3 for examples).

The difference in the response of b-tagging between data and simulation is taken into account by applying a corresponding correction factor [161].

5.4.6. Jet Quality

It is possible to identify objects other than collimated hadrons originating from the proton–proton collision as jets, e.g. muons from beam induced backgrounds, cosmic-ray showers or calorimeter noise. These misidentifications must be suppressed as much as possible while keeping the efficiency for *real* jets as high as possible. Therefore, jets have to satisfy several

BDT Cut Value	b-jet Efficiency [%]
0.9349	60
0.8244	70
0.6459	77
0.1758	85

Table 5.3.: MVc10 BDT cut values and corresponding b-jet efficiencies [160].

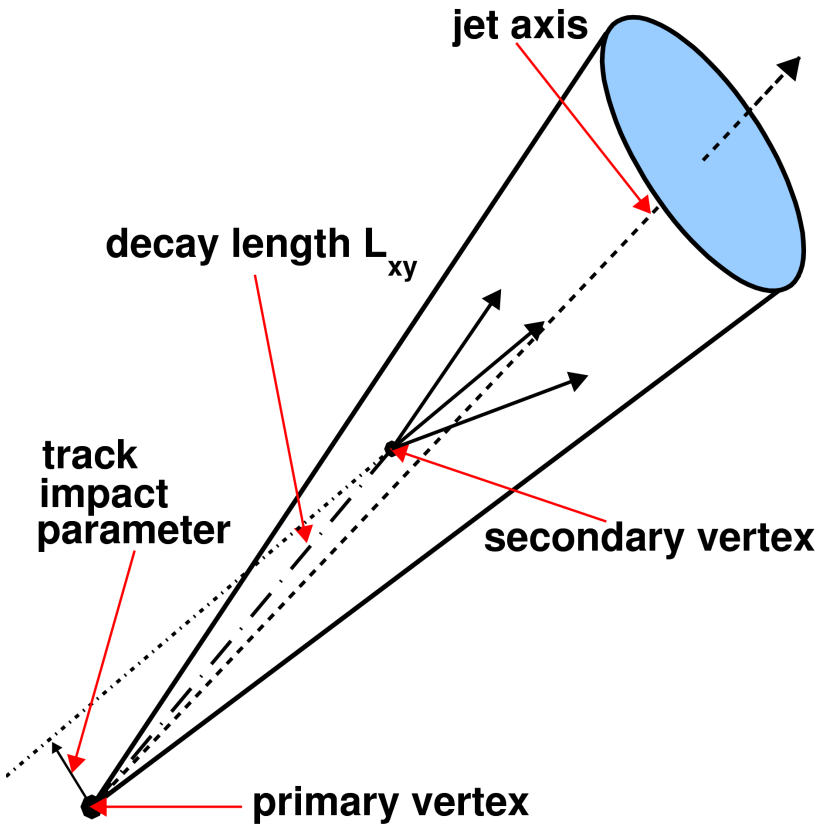

Figure 5.2.: Visualization of the parameters relevant for the b-tagging algorithm [157].

quality criteria to be kept in the jet collection, where two kind of selections of bad jets are defined by the JetEtMiss group [162, 163]: *LooseBad* and *TightBad*.
If a jet satisfies one of the following criteria, it is identified as LooseBad [162]:

- $f_{\mathrm{HEC}} > 0.5$ and $|f_Q^{\mathrm{HEC}}| > 0.5$ and $\langle Q \rangle > 0.8$
- $|E_{\mathrm{neg}}| > 60$ GeV
- $f_{\mathrm{EM}} > 0.95$ and $f_Q^{\mathrm{LAr}} > 0.8$ and $\langle Q \rangle > 0.8$ and $|\eta| < 2.8$
- $f_{\mathrm{max}} > 0.99$ and $|\eta| < 2$
- $f_{\mathrm{EM}} < 0.05$ and $f_{\mathrm{ch}} < 0.05$ and $|\eta| < 2.8$
- $f_{\mathrm{EM}} < 0.05$ and $|\eta| \geq 2$

where $\langle Q \rangle$ is the energy-squared weighted average of the pulse quality of the calorimeter cells in the jet, f_Q^{LAr} and f_Q^{HEC} are the energy fractions in the liquid-argon and hadronic calorimeter cells of a jet with poor signal shape quality, respectively, E_{neg} is the sum of negative energies (as measured by the calorimeter cells), f_{HEC} and f_{EM} is the fraction of energy deposited in the handronic and electro-magnetic calorimeter, respectively, f_{ch} is the ratio of the scalar sum of the p_T of the tracks coming from the primary vertex associated to the jet and the total jet p_T, f_{max} is the jet energy fraction in the layer with maximum energy deposit and η denotes the azimuthal angle of the jet.

5.4.7. Jet Requirements in this Thesis

This thesis exclusively makes use of jets reconstructed with the anti-k$_T$ algorithm with $R = 0.4$. Central jets are required to have $p_T > 25$ GeV and for their pseudo rapidity $|\eta| < 2.5$ is required. For forward jets, the p_T requirement is tightened to $p_T > 40$ GeV[1] and the allowed η region is $2.5 < |\eta| < 4.5$.
Furthermore, to select jets that originate from the hard scattering and to reduce the effect of in-time pileup, jets with $p_T < 60$ GeV and $|\eta| < 2.4$ are required to satisfy the criteria implemented in the jet vertex tagger algorithm (JVT) [156].
The jet requirements are summarised in Tab. 5.4. It should be noted that several other jet collections, especially designed for analysis concerned with heavy objects, are available, such as anti-k$_T$ jets with large-R (e.g. $R = 1.0$) or reclustered jets [164].

[1]The enhanced p_T cut on the forward jet reduces the background from single top production

Signal Small-R Jets	
Algorithm	anti-k_T
p_T threshold	25 GeV
$\|\eta\|$	< 4.5
Quality	not LooseBad
Pile-up Removal	JVT > 0.59 if $\|\eta\| < 2.4$, $p_T < 60$ GeV
b-tagging (if applied)	MV2c10, 85% efficiency, $\|\eta\| < 2.5$

Table 5.4.: Selection for small-R jets with distance parameter $R = 0.4$.

5.5. Overlap Removal

To avoid counting a single detector response as two objects, an overlap removal (OR) procedure following the recommendations of the ATLAS physics objects and analysis harmonisation study group [165] is used.
The applied OR consists of four steps:

- An electron candidate is removed if it shares the track with a muon
- Jet candidates overlapping with an electron candidate (within $\Delta R < 0.2$) are removed
- Electron candidates overlapping with surviving jet candidates are removed if $\Delta R < 0.4$
- Muon candidates are removed if they are within $\Delta R < 0.4$ of any jet. However, if this jet has fewer than three associated tracks, the muon is kept and the jet is removed instead

5.6. Missing Transverse Energy

Momentum conservation implies in collider experiments that the momenta transverse to the beam axis of the collision products should sum to zero. However, due to particles escaping the detector undetected, primarily weakly-interacting, stable particles in the final state, this might not be the case. The imbalance is referred to as *missing transverse momentum/energy*,

or E_T^{miss} [166]. In the SM, only neutrinos should contribute to the E_T^{miss} but fake E_T^{miss} can also result from interacting Standard Model particles which escape the acceptance of the detector, are badly reconstructed, or fail to be reconstructed altogether.
The E_T^{miss} used in this thesis is reconstructed with a track-based soft term (TST E_T^{miss}), which means that TST E_T^{miss} comprises contributions from the "hard term", containing selected reconstructed and fully calibrated physics objects and the (ID track-based) "soft term", containing reconstructed tracks associated with the hard-scatter vertex that are not associated to the physics objects. Jets used in the E_T^{miss} calculation are reconstructed from clusters of calorimeter cells with $|\eta| < 5$ using the anti-k_T algorithm with a radius parameter of 0.4. They are required to have a $p_T > 20$ GeV.
From the components $E_{x(y)}^{\text{miss}}$, the azimuthal angle ϕ^{miss} and the magnitude of E_T^{miss} are calculated as:

$$\begin{aligned} E_T^{\text{miss}} &= \sqrt{(E_x^{\text{miss}})^2 + (E_y^{\text{miss}})^2} \\ \phi^{\text{miss}} &= \arctan \frac{E_y^{\text{miss}}}{E_x^{\text{miss}}}. \end{aligned} \tag{5.2}$$

A major difficulty in the E_T^{miss} determination is its sensitivity to pile-up. The hard term is already pile-up corrected, however, for the soft term, several correction methods have been developed in ATLAS to mitigate the effect of pile-up.

Chapter 6.

Event Selection

The cross-sections of the VLQ production is many orders of magnitude smaller (compare Figure 3.8 and Table 2.1) than the total proton–proton cross-section and thus the difference of the outcome of the measurement with or without VLQs would not differ significantly if all pp collisions would be taken into account. Therefore, an event selection has to be deployed which enriches signal processes over background processes. To achieve this goal, the signal process has to be analysed (Section 6.1) and appropriate kinematic variables have to be studied with respect to their discriminating power (Section 6.3.1), resulting in a final event selection (Section 6.3.2).

6.1. Analysis Strategy

The analysis strategy exploited in this thesis, is cut-based, i.e. a sequence of requirements (cuts) on certain kinematic variables is applied for each event. If the event passes all cuts, the event is considered to be signal-like and kept or, if not, it is background-like and discarded.
The development of the strategy is of course tightly bound to the signal process under consideration: The single production of a Y or T with subsequent decay to Wb, where the W decays leptonically (see Fig. 6.1). Thus, the event topology is characterised by a light-flavour jet, originating from the u or d quark, a b-jet from the gluon splitting, the lepton and missing transverse energy from the escaping neutrino, and a b-jet from the VLQ decay. Typically, the b-jet is high energetic and leading in p_T (leading jet).
The light-flavour jet has typically a small η and is therefore called *forward jet* whereas the

b-jet from the gluon splitting is typically soft, i.e. has small momentum. If the Y or T VLQs exist, their mass should be relatively large (see Section 2.4) and therefore their decay products should have large momentum (and typically high p_T). The lepton and the b quark from the VLQ decay are preferentially produced with opposite momenta ($\vec{p}_l \approx -\vec{p}_b$, with $\vec{p}_l$ the lepton momentum and $\vec{p}_b$ the b-quark momentum) in the rest frame of the VLQ and the VLQ momentum in the laboratory frame is expected to be small. Thus, the b-tagged jet and the lepton should exhibit a large separation in ϕ. Furthermore, from Fig. 6.1 it is obvious that signal-like events contain relatively less hard-jet[1] activity, but in principle the forward jet as well as the second b-jet could be hard-jets as well. Thus, vetoing all hard jets in addition to the leading jet might be to strict. Therefore, an additional hard central jet veto within certain ΔR distances to the leading jet is considered to be more appropriate. However, it is a priori not obvious which exact cut values should be used for the optimal event selection and an optimization procedure is applied (see Section 6.3.1).

As described in Chapter 8, a binned maximum likelihood fit is performed to test the background-only and signal hypothesis. For this purpose, a signal-to-background discriminant has to be chosen whose distribution is exploited in the final fit. Here, a good candidate is the invariant mass of the heavy quark, called VLQ mass m_{VLQ} in the following. Hence, the four-momentum of the VLQ candidate is required, which can be computed from the four-momenta of the b quark, expected to show up as a b-tagged jet[2], the lepton and the neutrino. The components of the four-momentum of the neutrino perpendicular to the beam axis are expected to be equal to E_T^{miss}. To obtain the z-component of the neutrino momentum, the invariant lepton-neutrino mass is set to the W-boson mass of 80.4 GeV and the resulting quadratic equation is solved. If no real-valued solution exists, the E_T^{miss} vector is varied by the minimum amount required to produce exactly one real-valued solution. If two real-valued solutions are found, the one with the smallest $|p_z|$ is used. Additional methods to determine analytically the four-momentum-vector of the neutrino were studied for Run-1 [167], however the described method was the most efficient one.
The sum of the four-momenta of the neutrino candidate, the lepton and the (leading) b-tagged jet is considered as the four-momentum of the VLQ candidate and its invariant

[1] Jets with large (transverse) momentum are referred to as *hard jets*. In this analysis, hard jets are jets with $p_T > 75$ GeV.
[2] In case no (more than one) b-tagged jet is required in the selection, the leading (b-tagged) jet is used to reconstruct the invariant mass of the heavy quark.

mass is the final discriminant m_{VLQ}.

Other approaches beside the sketched analysis strategy are also possible, relying on large-R jets or reclustered jets, respectively, in contrast to anti-k_T R=0.4 jets. Vetoing events with large-mass large-R jets or reclustered jets, could significantly remove $t\bar{t}$ background events and possibly increase the sensitivity of the analysis. However, it has been shown that the presented strategy is superior to the others, especially due to the smaller systematic uncertainties of small-R jets. Furthermore, it was also tested if an alternative discriminating variable, H_T[3], should be preferred instead of m_{VLQ}, which is not the case.

It should be noted that for all figures in this section, the Y signal with a mass of 1200 GeV and a coupling of $\sqrt{c_L^{Wb2} + c_R^{Wb2}} = 1/\sqrt{2}$ is presented and all numbers are calculated for this coupling which is the coupling used for the signal sample production. Furthermore, the last bin in all distributions includes always the overflow.

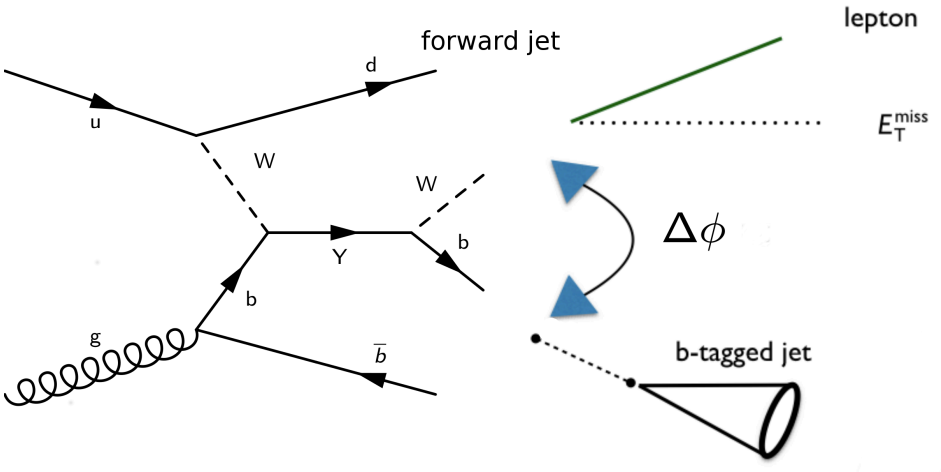

Figure 6.1.: Leading-order Feynman diagram and resulting physics objects/quantities for single Y/T production with subsequent decay into Wb.

[3] H_T is defined as the scalar sum of the transverse momenta of jets and leptons.

6.2. Pre-selection

Considering all possible physics processes and running the cut optimization on all available events would be computationally too expensive and unnecessary. Therefore, several basic selection cuts and event quality requirements are applied beforehand, referred to as pre-selection, which will be described in the following.

Event Quality Cuts

To assure that the quality of the recorded events is high, several basic event quality cuts are applied as a part of the pre-selection to each considered event. They are as follows:

- **Good Runs List (GRL):** To assure a good data quality, only events corresponding to the GRLs given in Section 4.2.3.
- **Primary vertex:** The existence of a primary vertex as described in Section 5.1 is required.
- **Good Calorimeter:** Events are rejected if either the tile of LAr calorimeter are flagged to be in *error* state.
- **Jet Quality:** Events are rejected if they contain *bad* jets (see Section 5.4.6).

Trigger Selection

As mentioned in Section 3.2.6, so called triggers have to be applied to reduce the event rate to an acceptable order of magnitude. The ATLAS collaboration provides readily available Trigger-Menus with different combinations of L1 and HLT trigger requirements. Since the decay of VLQs will inevitably result in exactly one lepton, this analysis combines different single-electron as well as single-muon triggers [82, 83] with different p_{T} thresholds and in order to increase the overall efficiency. The triggers used for this analysis are given in Table 6.1. Due to isolation requirements on the candidate lepton, the triggers with lower p_{T} threshold show inefficiencies for high-p_{T} leptons, which is compensated by the combination with high-p_{T} triggers without isolation requirements.

	Electrons	Muons
2015 data	HLT_e24_lhmedium_L1EM20VH HLT_e60_lhmedium HLT_e120_lhloose	HLT_mu20_iloose_L1MU15 HLT_mu50
2016 data	HLT_e26_lhtight_nod0_ivarloose HLT_e60_lhmedium_nod0 HLT_e140_lhloose_nod0	HLT_mu26_ivarmedium HLT_mu50

Table 6.1.: Trigger menus for 2015 and 2016 data used in this analysis.

In order to avoid double counting of the events, an offline dilepton veto was applied: events that fired the electron triggers are required to have no further signal muon (see Tab. 5.2) that fired the muon trigger and events that fired the muon triggers are required to have no signal electrons (see Tab. 5.1) that fired the electron trigger.

Additional Pre-selection Cuts

After the event quality and trigger requirements, the event is required to contain exactly one lepton with $p_{\mathrm{T}} > 28$ GeV, which has to be matched to the triggered electron or muon, respectively. Here, the p_T requirement is increased since the trigger plateau is reached at $p_{\mathrm{T}} \approx 27$ GeV. Furthermore, it needs to have at least two jets with $p_{\mathrm{T}} > 25$ GeV where the jet with the largest p_T has to be central ($|\eta| < 2.5$) and forward jets ($2.5 < |\eta| < 4.5$) are only taken into account if their transverse momentum (p_T) is larger than 40 GeV. The missing transverse energy E_T^{miss} is required to be larger than 120 GeV in order to suppress SM diboson and multijet events. However, the cut on E_T^{miss} was part of the optimization.

After requiring the pre-selection cuts, data-to-SM disagreement was found in some kinematic distributions for events with high-p_T jets which can be interpreted as a not well modelled W+jets background (see Section 7.6.1). The W+jets mismodelling is affecting lepton, jets and E_T^{miss} and therefore has a significant influence on the reconstructed mass of the VLQ candidate. A jet-p_T-reweighting method which is discussed in Section 7.6.1 is developed to improve the results. In the final analysis, an alternative m_{VLQ} distribution for the W+jets background obtained by this jet-p_T reweighting is used in order to quantify a systematic uncertainty in the m_{VLQ} shape of W+jets events.

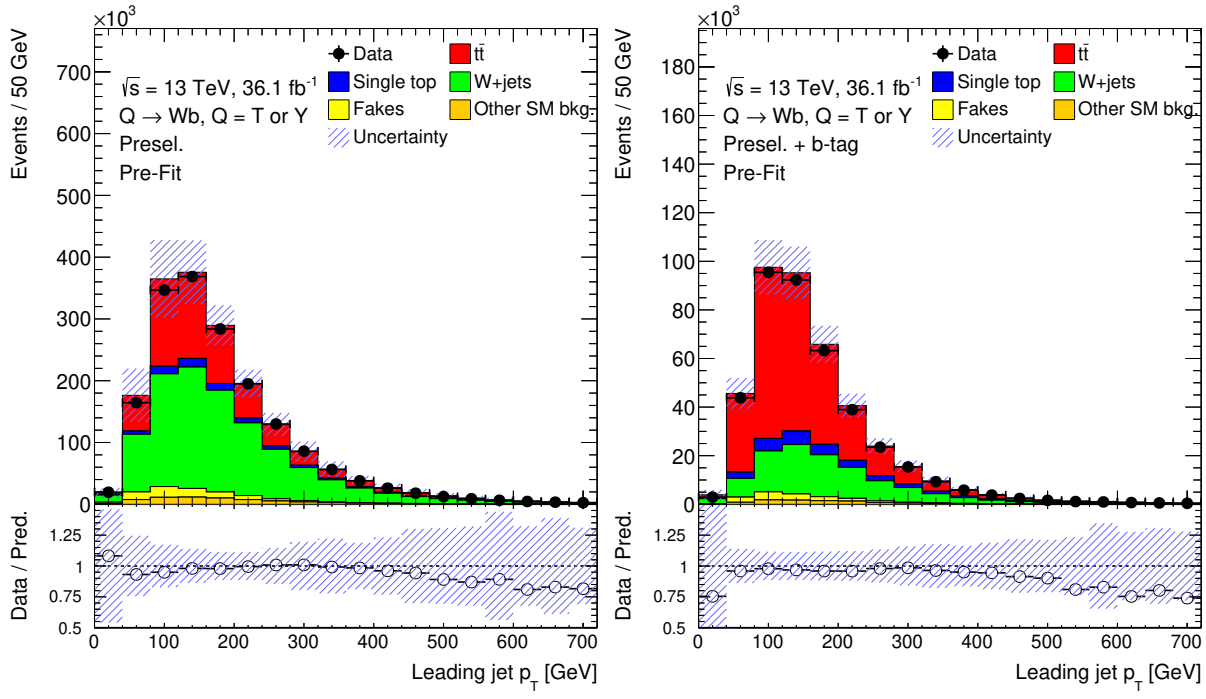

(a) (b)

Figure 6.2.: Distribution of the transverse momentum of the leading jet after applying preselection cuts (left figure) and requiring that the leading jet is b-tagged (right figure). The shaded error band depicts the statistical and systematic uncertainty of the SM prediction as listed in Chapter 7, taken as fully uncorrelated. The error attached to the data points is the corresponding statistical uncertainty.

6.3. Signal Region

6.3.1. Optimization of the Signal Region Requirements

Optimization for 2015 data set

To find the optimal sequence, the values for the applied cuts on the different kinematic variables of the objects defined in Chapter 5 are considered and varied independently. The ratio of the number of passing events of a 900 GeV Y signal and the square root of passing background events $S/\sqrt{B}$ was evaluated, without taking into account any systematic uncertainties. Correlations between the different cut criteria have been considered and the combination of all cut criteria resulting in the largest $S/\sqrt{B}$ was selected. The considered values are given in Table 6.2.

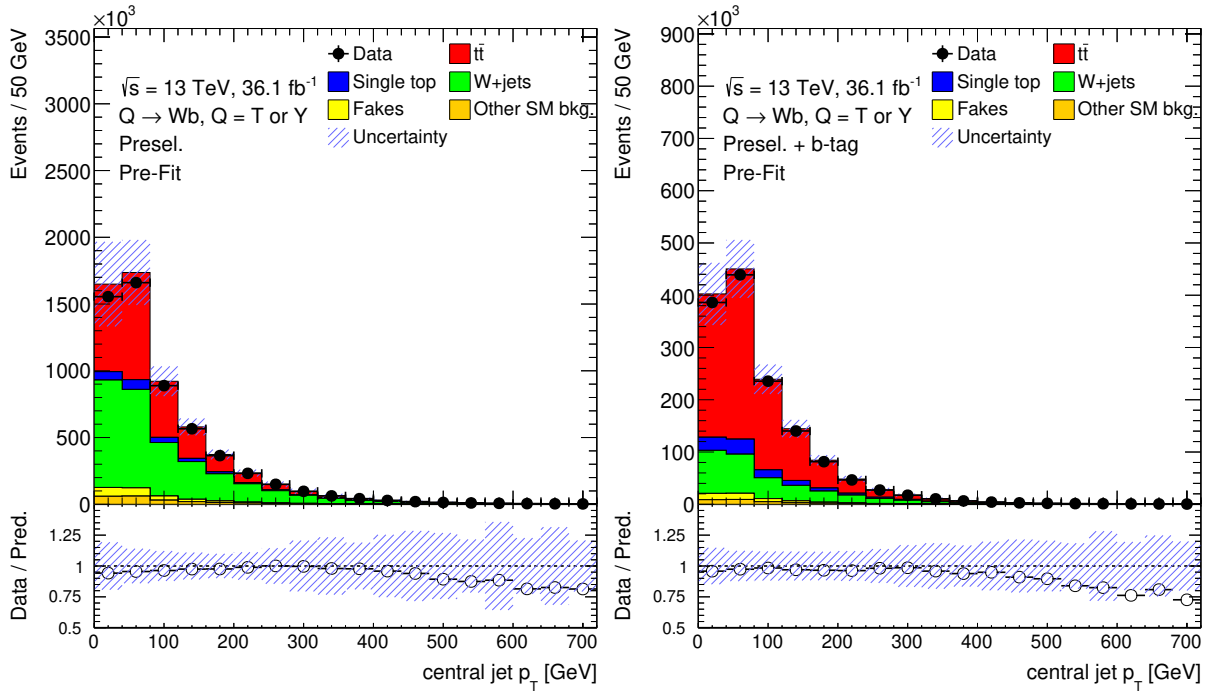

(a) (b)

Figure 6.3.: Data and SM MC distribution of the transverse momentum of all central jets after pre-selection (Figure (a)) and after pre-selection and requiring that the leading jet is b-tagged (Figure (b)). The error bands are analogous to those in Figure 6.2.

leading-jet p_T	200 GeV to 450 GeV, 50 GeV steps
leading jet is b-tagged	is b-tagged / is not b-tagged
veto additional hard central jets maximal allowed ΔR (jet, leading jet)	0 to 2.7, 0.3 steps
veto additional hard central jets minimal allowed ΔR (jet, leading jet)	0 to 2.7, 0.3 steps
$\Delta\phi$ between leading jet and lepton	0 to 3, 0.5 steps
number of forward jets	0, 1, 2
E_T^{miss}	60 GeV to 150 GeV, 10 GeV steps

Table 6.2.: Considered cut values corresponding to the studied physics objects used for the signal region optimization.

Additionally, the definition of p_T threshold which qualifies a jet to be considered as hard was changed to 65 and 85 GeV, respectively, but none resulted in improved sensitivity. The

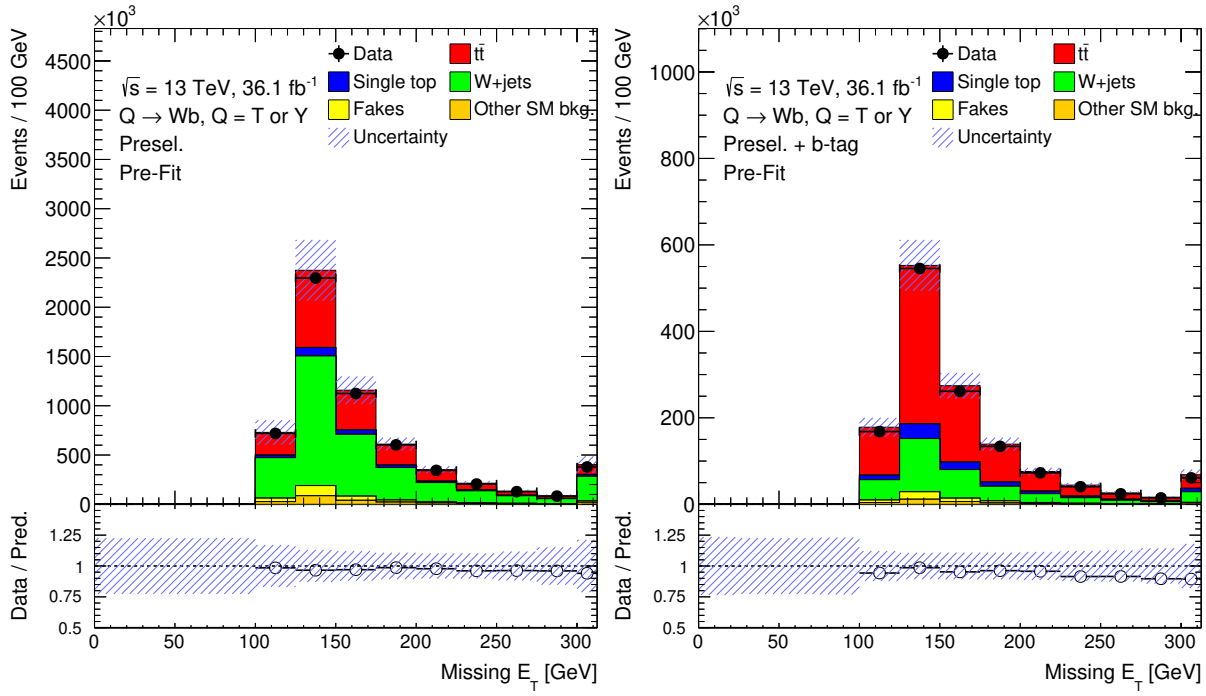

(a) (b)

Figure 6.4.: Data and SM MC distribution of the missing transverse energy after pre-selection (Figure (a)) and after pre-selection and requiring that the leading jet is b-tagged (b). The errors bands are analogous to those in Figure 6.2.

analysis using the outcome of this optimization is published in [23], using the 2015 data set. However, the presented version of the analysis aims for the search of VLQs using the data recorded in 2015 and 2016. Given the improved mass limits, the optimization has to be adjusted to increase the signal discovery reach for a higher VLQ mass ($\approx$ 1200 GeV).

Selection Adjustments

It has been found that the 85% b-tagging working point is superior to the 77% working point for a higher VLQ mass of 1200 GeV. Furthermore, the p_T requirement of the leading jet has been increased to $p_T > 350$ GeV instead of $p_T > 250$ GeV. Also, it was discovered that an additional cut on the minimal $\Delta R_{\text{min}}(\text{lepton}, \text{cent. jets})$ between the lepton and any central jet further improves the signal significance, as can be seen below.

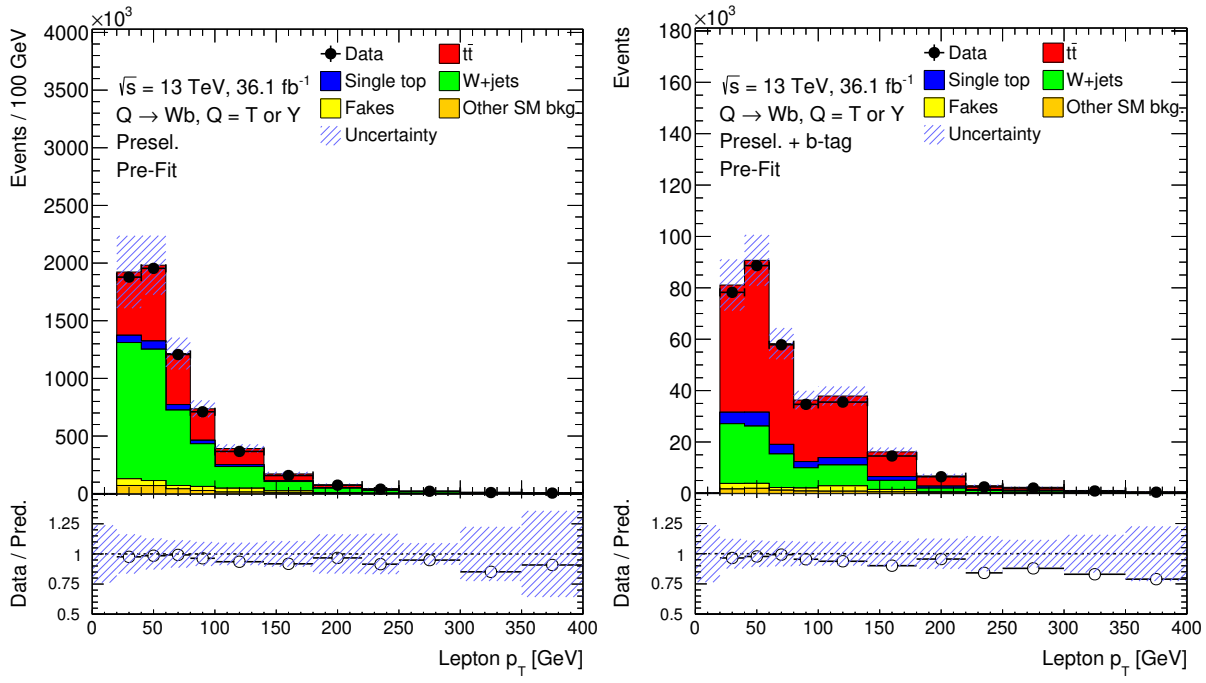

(a) (b)

Figure 6.5.: Data and SM MC distribution of the transverse momentum of the lepton after pre-selection (Figure (a)) and after pre-selection and requiring that the leading jet is b-tagged (Figure (b)). The errors bands are analogous to those in Figure 6.2.

6.3.2. Final Signal Region Cuts

The sequence of the final event selection is illustrated in Figures 6.7–6.12, for the combined e+jets and μ+jets channels, following the order in which each criterion is applied[4]. The plots on the left side always show a comparison between the distributions of the SM prediction and the VLQ Y quark with a coupling of $\sqrt{c_L^{Wb2} + c_R^{Wb2}} = 1/\sqrt{2}$ and its lower part provides the per bin distribution of $S/\sqrt{B}$, which serves as a proxy for the total $S/\sqrt{B}$. The plots on the right-hand side show only the SM prediction but with the full systematic uncertainty.

Figure 6.7 shows the number of events passing the event pre-selection for which the leading jet is not b-tagged (first bin) and for which the leading jet is b-tagged (second bin). It can be seen that requiring the leading jet to be identified as a jet stemming from a b quark enables a large background suppression, especially originating from W+jets processes.

[4]The figures show always the distributions of the variables on which cuts are applied.

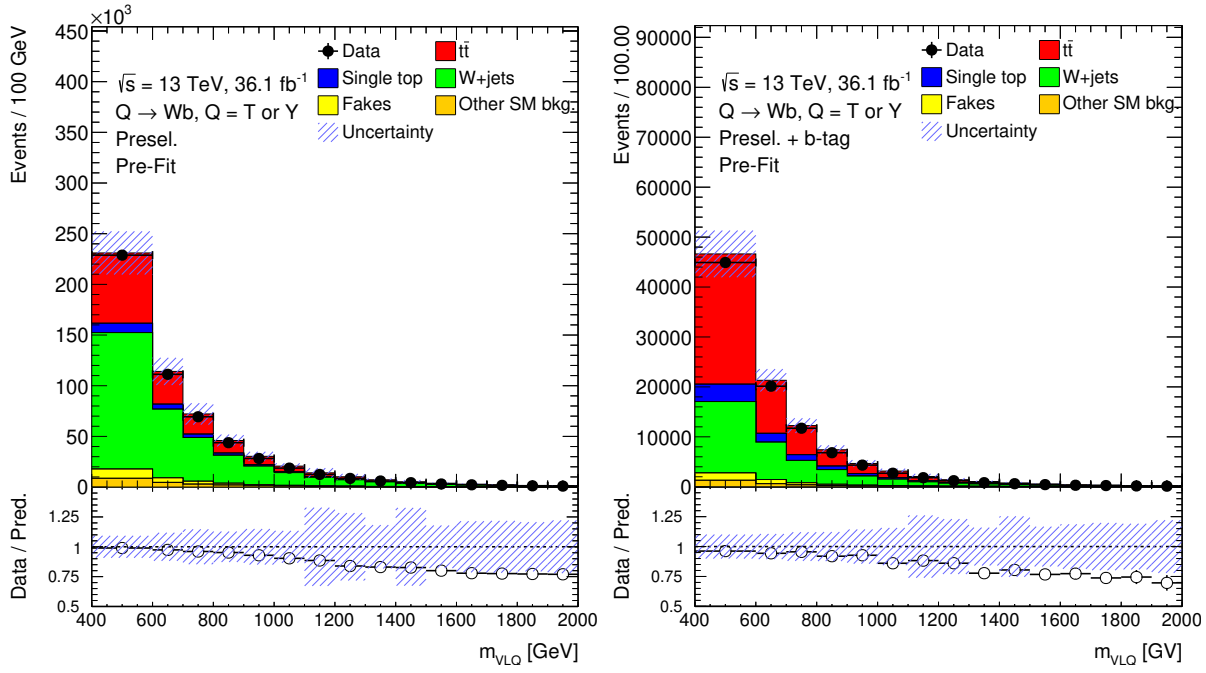

(a) (b)

Figure 6.6.: Data and SM MC distribution of the mass of the VLQ candidate after pre-selection (Figure (a)) and after pre-selection and requiring that the leading jet is b-tagged (Figure (b)). The errors bands are analogous to those in Figure 6.2.

Figure 6.8 shows a signal-to-SM background comparison of the distribution of the leading-jet p_T, for events passing the event pre-selection and the b-tagging requirement. Here, the corresponding distributions of all background processes peak between 100 and 200 GeV and show a more or less steeply falling behaviour afterwards. The signal distribution peaks at around 550 GeV – 600 GeV for a Y VLQ signal with a mass of 1200 GeV, as it would be roughly expected for a decaying particle with this mass. Thus, a cut on the minimum leading-jet p_T is beneficial and the optimal value is found to be 350 GeV.
As suggested above and inferred from Fig. 6.1, signal events tend to have a low hard-jet multiplicity and background processes, especially $t\bar{t}$ events show a higher hard-jet multiplicity. This can be seen in Fig. 6.9, where the number of hard central jets after applying the leading-jet p_T cut is depicted. However, since it happens that also signal events exhibit more than one hard jet, a strict veto is unnecessarily harsh. Fig. 6.10 provides the distribution of ΔR(leading jet, hard cent. jets), the angular distance between the leading jet and any additional hard central jet. Note that one event with more than one additional hard central jet occurs more than once in the figure. The stacked background distributions show a

double peak structure, with a peak at ≈ 0.8 and another at ≈ 3.0, mainly induced by $t\bar{t}$ events. Therefore, these peaks can be understood as mainly originating from the two top quarks emitted back to back. The signal peaks between ≈ 1.5 and ≈ 2.5. It has been found that vetoing central jets with ΔR (leading jet, hard cent. jets) < 1.2 or ΔR (leading jet, hard cent. jets) > 2.7 improves the signal-to-SM background ratio.
As in the signal decay process $T/Y \rightarrow Wb$ the b quark recoils against the W boson a large separation in the azimuthal angle ϕ between the b quark identified as the b-tagged leading jet and the lepton from the subsequent W-boson decay is expected. This can be clearly seen in Fig. 6.11, which depicts $|\Delta\phi$ (lepton, leading jet)| after the additional hard central jet veto and a cut value of 2.5 proves to be optimal.
Figure 6.12 shows the signal and background comparison of the number of forward jets, for events passing the previous selection. Signal events mostly have at least one forward jet, which is a characteristic feature of singly produced VLQs as can be inferred from Fig. 6.1. In contrast, the majority of the background events have no such jet. Therefore, in this analysis events are required to have at least one jet with $2.4 < |\eta| < 4.5$ and $p_T > 40$ GeV[5]. The isolation arguments above with respect to the leading jet, can also be extended to the lepton. Therefore, the signal distribution of the minimal angular distance between the lepton and any central jet ΔR_{min} (lep, cent. jet) is expected to peak at large ΔR_{min} (lep, cent. jet). This can be clearly seen in Fig. 6.13, which shows a signal-to-background comparison in this variable after all of the previous mentioned cuts were applied. A cut of min ΔR_{min}(lep, cent. jets) > 2 removes again a significant part of the background, resulting in an improved $S/\sqrt{B}$.

To summarise, after the pre-selection, the final sequence of requirements is:

(a) The leading jet is b-tagged.

(b) The leading-jet p_T is larger than 350 GeV.

(c) Events with any jet with p_T above 75 GeV and with $|\eta| < 2.5$ excluding the leading jet are rejected if ΔR (leading jet, hard cent. jets)< 1.2 or ΔR (leading jet, hard cent. jets) > 2.7.

(d) The azimuthal separation between the lepton and the b-tagged jet (absolute value) is required to be larger than $|\Delta\phi$ (lepton, leading jet)| > 2.5.

[5]The enhanced p_T cut on the forward jet reduces the background from single top production

(e) At least one forward jet ($p_T > 40$ GeV and $2.5 < |\eta| < 4.5$) is required in the event.

(f) It is required that the minimal angular distance between the lepton and any central jet ΔR_{min} (lepton, cent. jets) > 2.0.

In Fig. 6.14, the final discriminant, the mass of the reconstructed VLQ candidate, after all cuts is presented and Figure 6.15 shows the VLQ candidate mass for three different signal masses in this region.
For the MC signal sample $m(Y) = 1.2$ TeV with a coupling of $\sqrt{c_L^{Wb2} + c_R^{Wb2}} = 1/\sqrt{2}$, the combined acceptance times efficiency after applying all analysis selection cuts (in the SR) is about 1%, the signal over background S/B = 286/440 = 0.65 and the $S/\sqrt{B}$ value about 13.7.

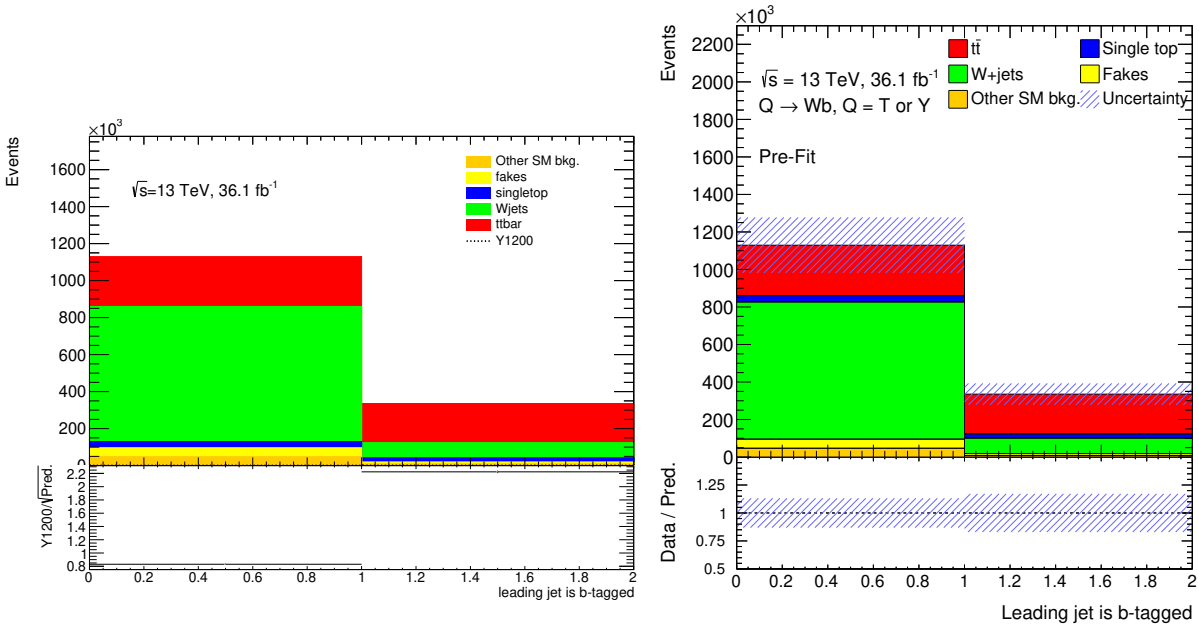

(a) (b)

Figure 6.7.: Illustration of the requirement that the leading jet is a b-tagged jet after the pre-selection. (Left) Simulated SM background prediction (Pred.) and Y signal with a mass of 1200 GeV (Y1200) setting $\sqrt{c_L^{Wb2} + c_R^{Wb2}}$ to $1/\sqrt{2}$. In the bottom plot, $Y1200/\sqrt{Pred.}$ is shown per bin. (Right) Simulated SM background prediction with the shaded error band in the upper part of the plots depicts the statistical and systematic error on the SM prediction as listed in Chapter 7, taken as fully uncorrelated. In the bottom part of the plot, the shaded band is the relative systematic uncertainty adding in quadrature the systematic and statistical error on the SM prediction.

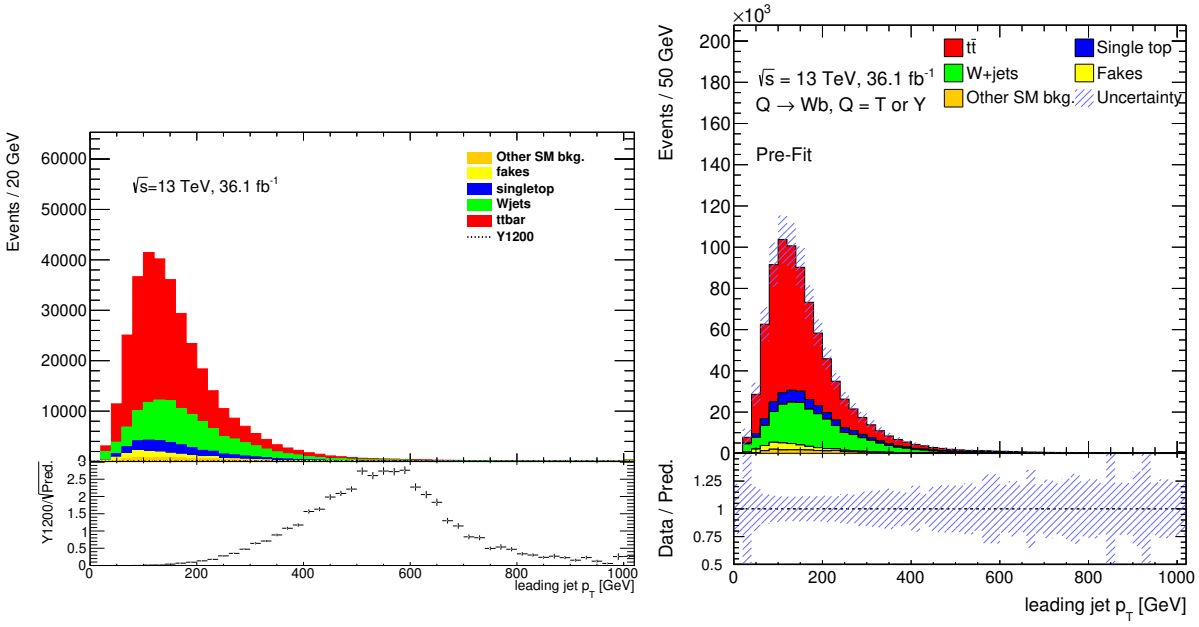

(a) (b)

Figure 6.8.: Distribution of transverse momentum of leading jet after the pre-selection and requiring that the leading jet is a b-tagged jet (cut (a)). (Left) Simulated SM background prediction (Pred.) and Y signal with a mass of 1200 GeV (Y1200) setting $\sqrt{c_L^{Wb2} + c_R^{Wb2}}$ to $1/\sqrt{2}$. In the bottom plot, $S/\sqrt{B}$ is shown per bin. (Right) Simulated SM background with the shaded error band in the upper part of the plots depicts the statistical and systematic error on the SM prediction as listed in Chapter 7, taken as fully uncorrelated. In the bottom part of the plots, the shaded band is the relative systematic uncertainty adding in quadrature the systematic and statistical error on the SM prediction.

6.4. Control Regions

The result of this analysis highly depends on the accurate prediction of the SM background processes. Though the event simulation provides astonishingly good results, it is not certain that the predictions are precise in all phase space regions. Thus, it is desirable to check and correct, if necessary, the MC distributions in a data-driven manner. For this purpose so called *control regions* (CRs) are used.

For this analysis, two control regions orthogonal to the signal region are defined, one for each of the dominant background processes, $t\bar{t}$ and W+jets production. These regions are such that they are highly dominated by the respective background process and the signal contribution is negligible. Thus, with the assumption that no other BSM physics is present (which

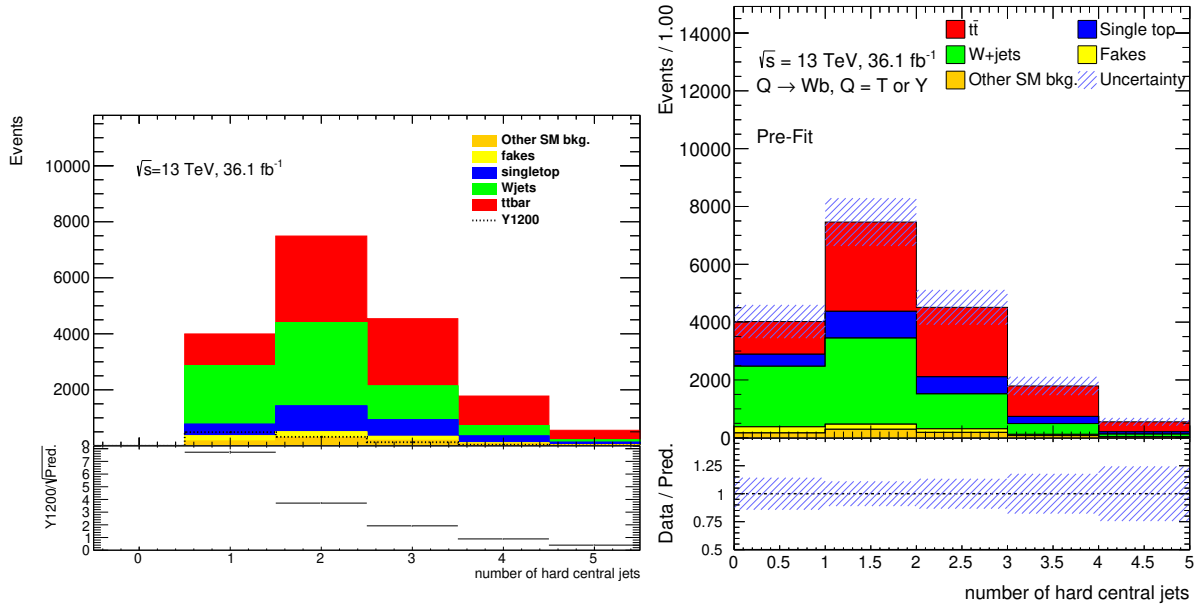

(a) (b)

Figure 6.9.: Distribution of number of hard jets with a $p_T > 75$ GeV after the pre-selection and cuts (a) and (b) described in the text. (Left) Simulated SM background prediction (Pred.) and Y signal with a mass of 1200 GeV (Y1200) setting $\sqrt{c_L^{Wb2} + c_R^{Wb2}}$ to $1/\sqrt{2}$. In the bottom plot, $S/\sqrt{B}$ is shown per bin. (Right) Simulated SM background with the shaded error band in the upper part of the plots depicts the statistical and systematic error on the SM prediction as listed in Chapter 7, taken as fully uncorrelated. In the bottom part of the plots, the shaded band is the relative systematic uncertainty adding in quadrature the systematic and statistical error on the SM prediction.

is generally a necessary assumption), the prediction from the simulation of SM processes and the measured data should exactly match within uncertainties. If deviations are observed, the prediction can be corrected accordingly and this correction can be propagated to the signal region. However, this is only meaningful if the control regions and the signal region do belong to close phase space regions, such that the assumption of similar mismodeling is valid.

For the $t\bar{t}$ CR, the minimal leading-jet p_{T} requirement is loosened to 200 GeV in comparison to the SR, since the invariant mass of a top quark is much smaller than the expected mass of a VLQ. To further enhance the $t\bar{t}$ contribution, the large jet multiplicity is exploited: at least one hard jet with ΔR (leading jet, hard cent. jets)< 1.2 or ΔR (leading jet, hard cent. jets) > 2.7) is required, i.e. this requirement is reversed with respect to the SR

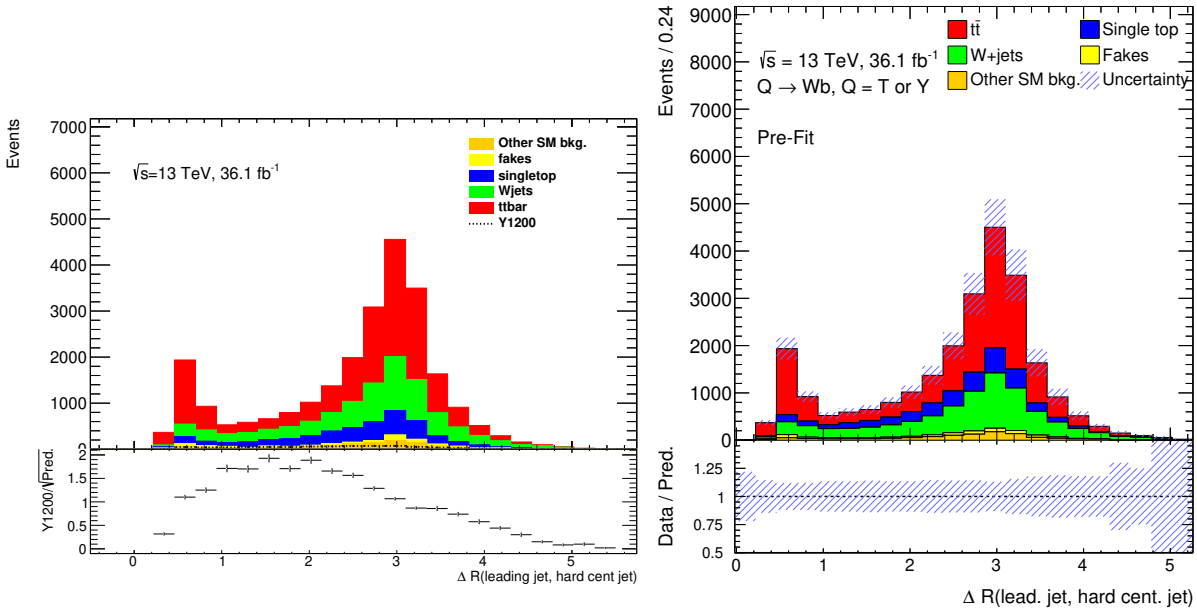

(a) (b)

Figure 6.10.: Distribution of ΔR (leading jet, hard cent. jets) between the leading jet and any hard ($p_T > 75$ GeV) jet after the pre-selection and cuts (a) and (b) as described in the text. The errors bands in the top part of the plot are analogous to those in Figure 6.2. (Left) Simulated SM background prediction (Pred.) and Y signal with a mass of 1200 GeV (Y1200) setting $\sqrt{c_L^{Wb2} + c_R^{Wb2}}$ to $1/\sqrt{2}$. In the bottom plot, $S/\sqrt{B}$ is shown per bin. (Right) Simulated SM background with the shaded error band in the upper part of the plots depicts the statistical and systematic error on the SM prediction as listed in Chapter 7, taken as fully uncorrelated. In the bottom part of the plots, the shaded band is the relative systematic uncertainty adding in quadrature the systematic and statistical error on the SM prediction.

requirement. To avoid further suppression of this background source, no ΔR_{min} (lepton, cent. jets) cut is applied.

For the W+jets control region, also the leading-jet p_T cut is lowered, in this case to 250 GeV. As can be seen in Fig. 6.12, a significant amount of W+jets events are removed due to the forward jet requirement, thus this cut is removed. The requirement of the azimuthal separation between the lepton and the leading jet (absolute value) is reversed compared to the SR, that is, it is required to be $|\Delta\phi$ (lepton, leading jet)$| < 2.5$. Though, a hard central jet veto could increase the amount of W+jets events in comparison to events from $t\bar{t}$ production, this veto is not applied to keep the statistics reasonably large.

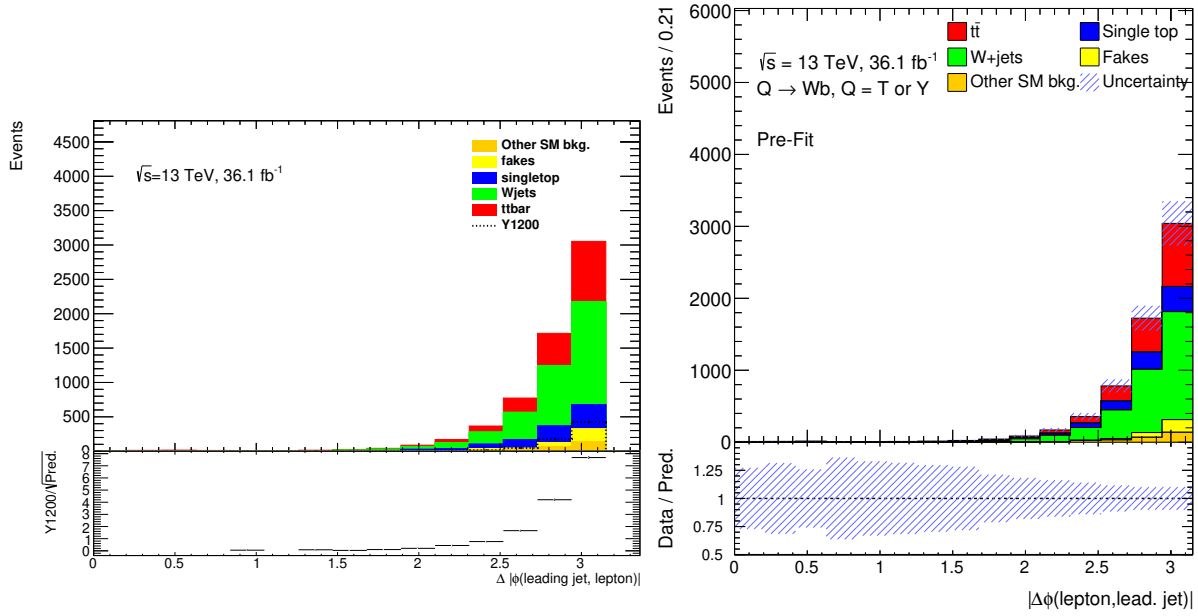

(a) (b)

Figure 6.11.: Distribution of $|\Delta\phi$ (lepton, leading jet)| between the leading jet and lepton after the pre-selection and cuts (a)–(c) as described in the text. (Left) Simulated SM background prediction (Pred.) and Y signal with a mass of 1200 GeV (Y1200) setting $\sqrt{c_L^{Wb2} + c_R^{Wb2}}$ to $1/\sqrt{2}$. In the bottom plot, $S/\sqrt{B}$ is shown per bin. (Right) Simulated SM background with the shaded error band in the upper part of the plots depicts the statistical and systematic error on the SM prediction as listed in Chapter 7, taken as fully uncorrelated. In the bottom part of the plots, the shaded band is the relative systematic uncertainty adding in quadrature the systematic and statistical error on the SM prediction.

It should be noted that this CR differs from the W+jets CR in [23]. The most important difference is that the leading jet is required to be b-tagged as it is the case in the SR. This change is mostly inspired by the fact that it is desirable to keep the ratio of W+jets processes with jets originating from light (LF) and those originating from heavy flavour (HF) quarks in the CR and in the SR as close as possible. In Fig. 6.16, which shows the m_{VLQ} distribution for W+jets separated in LF and HF processes in the SR and in the W+jets CR, it can be seen that this is actually the case.

There is no dedicated CR that allows to constrain the background from single top-quark production, though this background source is significant and a CR would be desirable. The

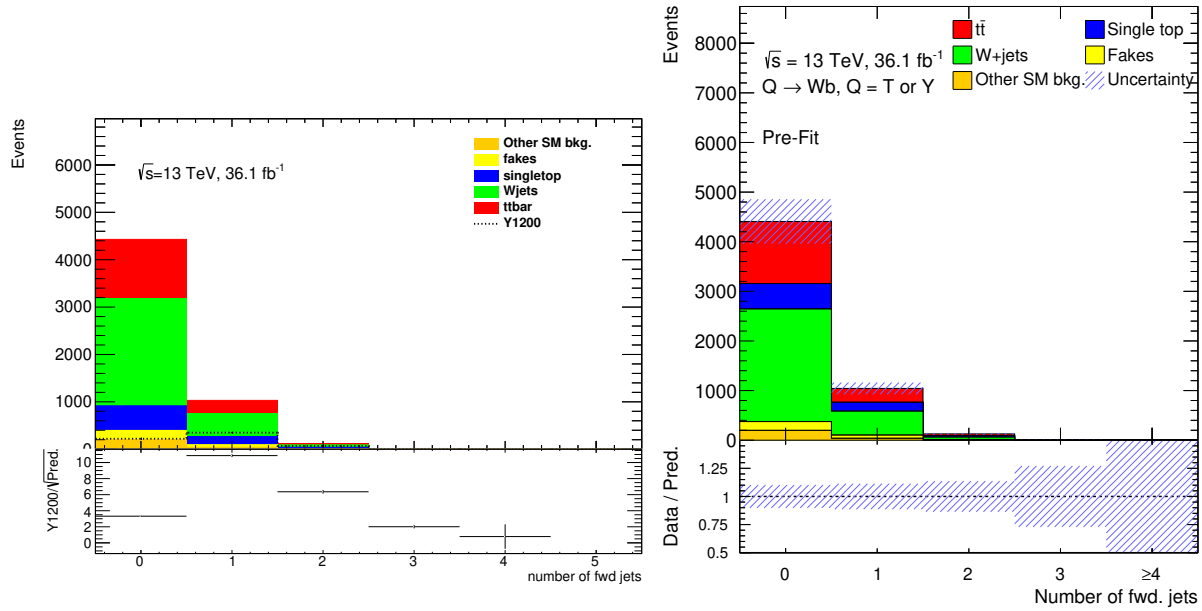

(a) (b)

Figure 6.12.: Distribution of number of forward jets after the pre-selection and cuts (a)–(d) as described in the text. (Left) Simulated SM background prediction (Pred.) and Y signal with a mass of 1200 GeV (Y1200) setting $\sqrt{c_L^{Wb2} + c_R^{Wb2}}$ to $1/\sqrt{2}$. In the bottom plot, $S/\sqrt{B}$ is shown per bin. (Right) Simulated SM background with the shaded error band in the upper part of the plots depicts the statistical and systematic error on the SM prediction as listed in Chapter 7, taken as fully uncorrelated. In the bottom part of the plots, the shaded band is the relative systematic uncertainty adding in quadrature the systematic and statistical error on the SM prediction.

Wt production process of single top and VLQ T production can result in the same final state except for the higher mass of the T. Thus, a region orthogonal to the signal region but still *close* in terms of phase space but with negligible signal contribution can not be found.

The multijets background is already estimated on data using the matrix method as described in Section 4.2.2 and thus no CR is needed. The SM dibosons background is very small and is well described by the simulation, consequently, no data-driven estimation using control regions is performed.

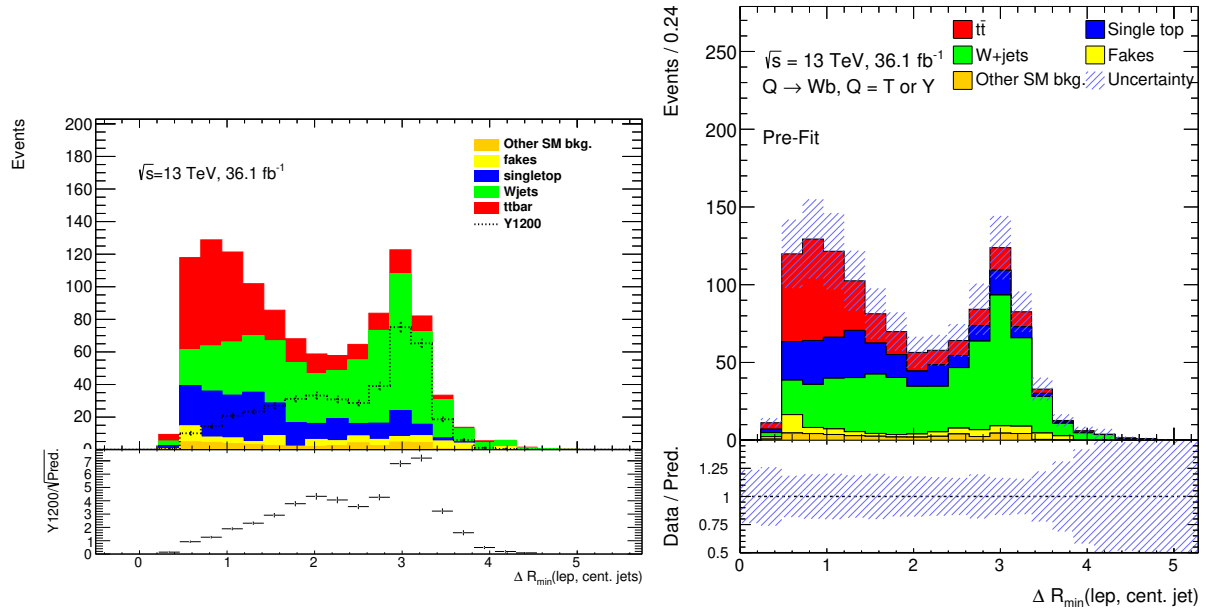

(a) (b)

Figure 6.13.: Distribution of ΔR_{min} (lepton, cent. jets) after the pre-selection and cuts (a)–(e) as described in the text. (Left) Simulated SM background prediction (Pred.) and Y signal with a mass of 1200 GeV (Y1200) setting $\sqrt{c_L^{Wb2} + c_R^{Wb2}}$ to $1/\sqrt{2}$. In the bottom plot, $S/\sqrt{B}$ is shown per bin. (Right) Simulated SM background with the shaded error band in the upper part of the plots depicts the statistical and systematic error on the SM prediction as listed in Chapter 7, taken as fully uncorrelated. In the bottom part of the plots, the shaded band is the relative systematic uncertainty adding in quadrature the systematic and statistical error on the SM prediction.

6.5. Event Yields and Contaminations

6.5.1. Signal Contamination in Control Regions

Table 6.4 presents the Y/T signal contamination given the theoretical cross-section (not considering interference) in the $t\bar{t}$ and W+jets control regions, respectively, corresponding to a coupling of $\sqrt{c_L^{Wb2} + c_R^{Wb2}} = 1/\sqrt{2}$. While $S/\sqrt{B}$ is quite high especially for the lowest mass points, the signal fraction shows that this is not worrisome, especially because this behaviour is most pronounced for the lowest signal mass points, for which the model is already excluded for high couplings and also from pair-production searches (see Section 2.4). The maximal signal contamination per bin has been checked for a 1200 GeV vector-like Y

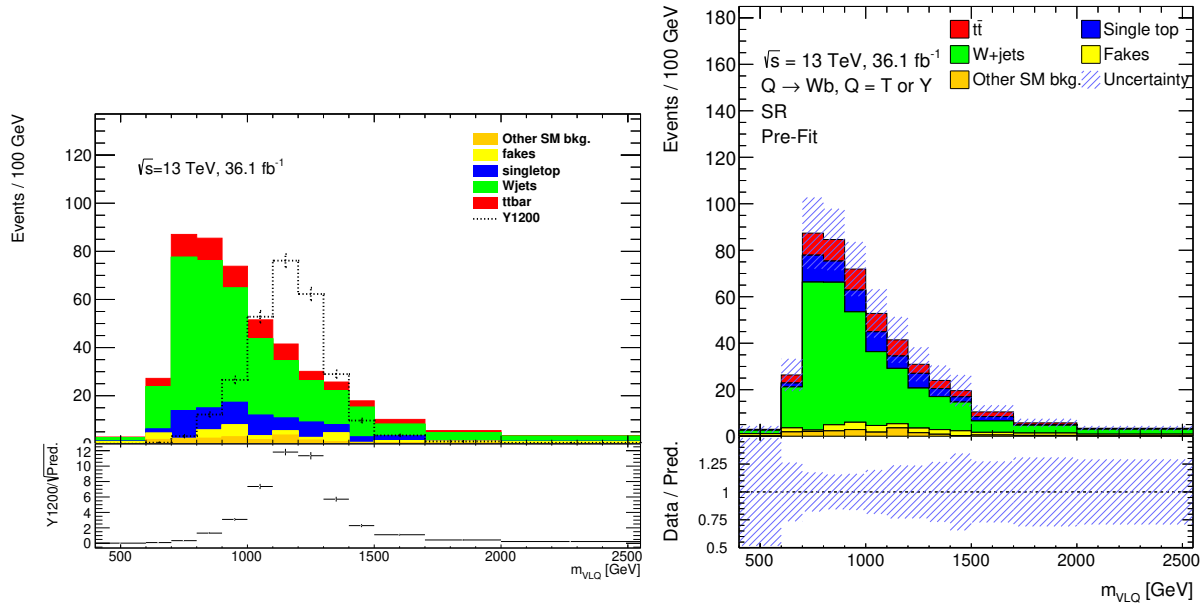

(a) (b)

Figure 6.14.: Distribution of VLQ candidate mass after the pre-selection and cuts (a)–(f) as described in the text. (Left) Simulated SM background prediction (Pred.) and Y signal with a mass of 1200 GeV (Y1200) setting $\sqrt{c_L^{Wb2} + c_R^{Wb2}}$ to $1/\sqrt{2}$. In the bottom plot, $S/\sqrt{B}$ is shown per bin. (Right) Simulated SM background with the shaded error band in the upper part of the plots depicts the statistical and systematic error on the SM prediction as listed in Chapter 7, taken as fully uncorrelated. In the bottom part of the plots, the shaded band is the relative systematic uncertainty adding in quadrature the systematic and statistical error on the SM prediction.

quark with a coupling of $\sqrt{c_L^{Wb2} + c_R^{Wb2}} = 1/\sqrt{2}$. The maximal contamination for the $t\bar{t}$ control region is found in the 1000–1250 GeV bin and is 20% whereas the uncertainty of the Standard Model background in this particular bin is 25%. The maximal contamination for the W+jets control region is found in the 1100–1200 GeV bin and is 7% whereas the corresponding uncertainty of the SM prediction in this particular bin is 30%.
It should be noted that the selected coupling for the different Y is rather large, so less signal events are expected in the different CRs for smaller couplings (cross-sections).

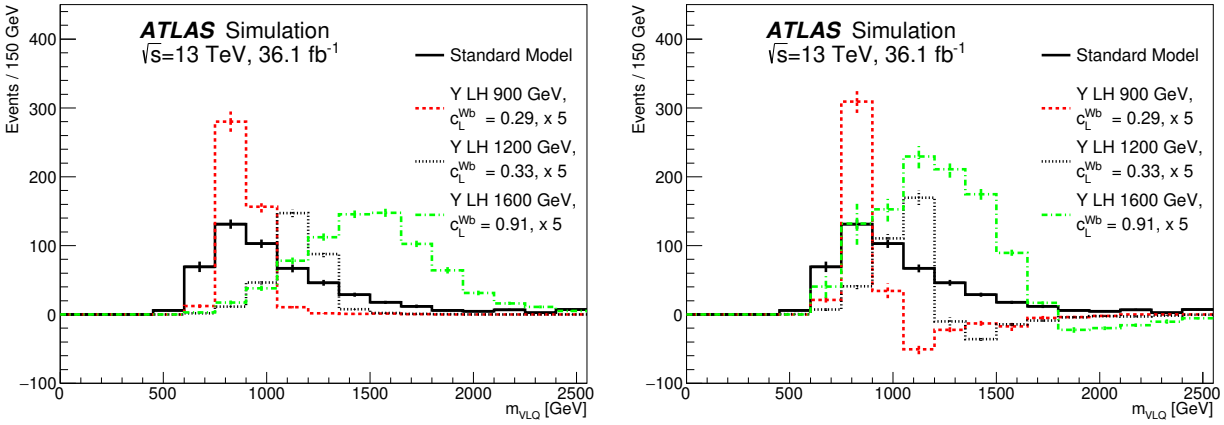

(a) (b)

Figure 6.15.: Distribution of VLQ candidate mass m_{VLQ} in the SR for a left-handed Y signal with a mass of 900 GeV (dashed line), 1200 GeV (dotted) and 1600 GeV (dash-dotted line) and a coupling of $c_L^{Wb} \approx 0.29$, ≈ 0.33 and ≈ 0.91 respectively, without (a) and with (b) interference effects. The signal yield is scaled by factor of 5 and only statistical uncertainties are shown.

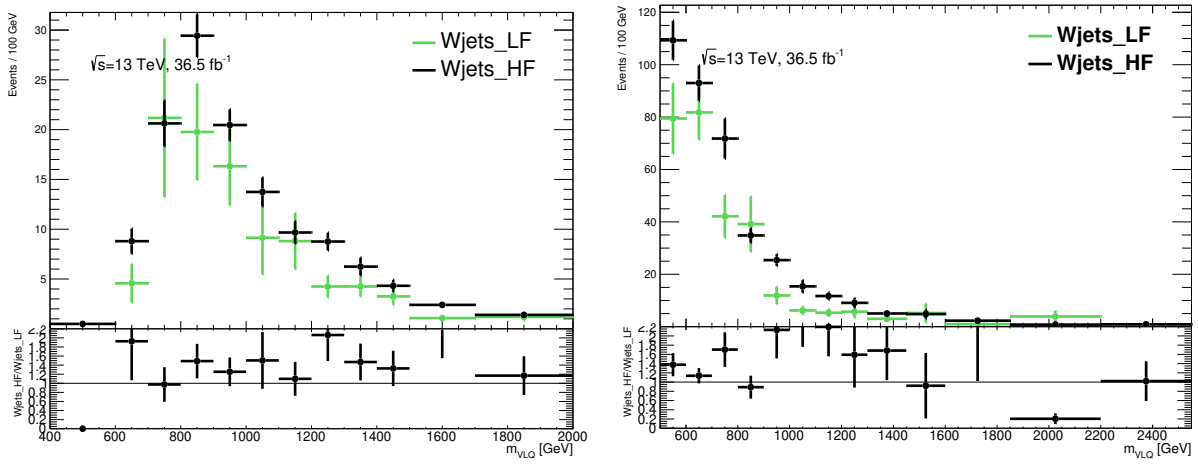

(a) (b)

Figure 6.16.: Distribution of VLQ candidate mass for W+jets separated in LF and HF in the SR 6.16(a) and in the W+jets CR 6.16(b). The bottom part of the plots, the ratio of Wjets_HF and Wjets_LF is given.

Requirement \ Region	SR	$t\bar{t}$ CR	W+jets CR
Preselection			
Leptons	1		
$E_{\mathrm{T}}^{\mathrm{miss}}$	> 120 GeV		
Central jets ($p_{\mathrm{T}} > 25$ GeV)	≥ 1		
Selection			
b-tagged jets	≥ 1	≥ 1	1
Leading jet p_{T}	> 350 GeV	> 200 GeV	> 250 GeV
Leading jet is b-tagged	Yes	Yes	Yes
$\lvert\Delta\phi$(lepton, leading jet)$\rvert$	> 2.5	> 2.5	≤ 2.5
Jets ($p_{\mathrm{T}} > 75$ GeV) with ΔR (jet, leading jet) < 1.2 or ΔR (jet, leading jet) > 2.7	0	≥ 1	–
ΔR (lepton, cent. jets)	> 2.0	–	> 2.0
Forward jets ($p_{\mathrm{T}} > 40$ GeV)	≥ 1	≥ 1	–

Table 6.3.: Summary of most important pre-selection, signal region as well as $t\bar{t}$ and W+jets CRs requirements.

6.5.2. Contamination from VLQ Pair-Production and Other Single-Production Processes

The contamination from VLQ pair production of Y quarks was checked in the SR, and the $t\bar{t}$ and W+jets CRs. In all regions, the contamination was found to be below the 1% level. The efficiency of single-production VLQ $T \to Tt$ and $T \to Ht$ events is a factor of 15 to 30 smaller than for the studied $T/Y \to Wb$ signals and was found to be below the 1% level. For example, for a T-Singlet signal with a mass of 1.2 TeV and with a of BR($T \to Wb$) = 0.5 and BR($T \to Zt$) = BR($T \to Ht$)= 0.25 produced via Wb fusion the signal contamination is about 0.3% (0.8%) and 0.02% (0.01%) in the $t\bar{t}$ and W+jets control region and about 0.3% (0.4%) in the signal region for decays via $T \to Zt$ ($T \to Ht$). Therefore decays via $T \to Zt$ and $T \to Ht$ can be neglected for the final limits.

	Y 800 GeV		Y 1000 GeV		Y 1200 GeV		Y 1400 GeV		Y 1600 GeV	
$t\bar{t}$ CR	S/B	$S/\sqrt{B}$	S/B	$S/\sqrt{B}$	S/B	$S/\sqrt{B}$	S/B	$S/\sqrt{B}$	S/B	$S/\sqrt{B}$
	0.08	5.7	0.06	4.2	0.04	2.7	0.02	1.7	0.01	0.93
	Y 800 GeV		Y 1000 GeV		Y 1200 GeV		Y 1400 GeV		Y 1600 GeV	
W+jets CR	S/B	$S/\sqrt{B}$	S/B	$S/\sqrt{B}$	S/B	$S/\sqrt{B}$	S/B	$S/\sqrt{B}$	S/B	$S/\sqrt{B}$
	0.05	1.9	0.02	0.82	0.01	0.35	0.004	0.14	0.002	0.08

Table 6.4.: Signal contamination in the $t\bar{t}$ and W+jets control region for signals with coupling of $\sqrt{c_L^{Wb2} + c_R^{Wb2}} = 1/\sqrt{2}$. Signals are normalised to the theoretical cross-section. Higher values for $S/\sqrt{B}$ are only observed for the lowest mass points that are already excluded.

6.5.3. Event Yields in the Signal and Control Regions

The event yields in the signal and control regions are summarised in Table 6.5. The acceptance × efficiency for three different Y signal masses are given in Table 6.6 and the yield for each step of the cut-sequence for the same signals is given in Table 6.7.

Source	SR	$t\bar{t}$ CR	W+jets CR
$t\bar{t}$	65 ± 48	2983 ± 907	111 ± 40
Single top	63 ± 56	520 ± 408	68 ± 57
W+jets	324 ± 66	909 ± 168	923 ± 125
Multijet e	22 ± 25	35 ± 40	0 ± 0
Multijet μ	7 ± 7	93 ± 95	26 ± 27
Z+jets,VV	20 ± 5	105 ± 19	50 ± 7
$t\bar{t}$V	0.3 ± 0.1	22 ± 2	1.6 ± 0.2
$t\bar{t}$H	0 ± 0	7.4 ± 1.2	0.2 ± 0.1
Total	501 ± 106	4672 ± 1089	1179 ± 155
Data	497	4227	1274

Table 6.5.: Pre-fit event yields in the SR and the $t\bar{t}$ and W+jets CRs. The uncertainties include statistical and systematic uncertainties. Due to correlations among the SM backgrounds the uncertainties of the sum of the individual components can be larger than the uncertainty on the total background.

Q signal mass [GeV]	Acceptance × efficiency [%]
800	0.70 ± 0.03
900	1.08 ± 0.05
1000	1.29 ± 0.06
1100	1.45 ± 0.08
1200	1.61 ± 0.10
1300	1.68 ± 0.12
1400	1.67 ± 0.14
1500	1.73 ± 0.17
1600	1.75 ± 0.20
1700	1.54 ± 0.22
1800	1.68 ± 0.27
1900	1.59 ± 0.29

Table 6.6.: Signal acceptance times efficiency in percent for the Y signal in the SR. The uncertainty includes the statistical uncertainty in the Monte Carlo predictions.

Selection/mass [GeV]	900	1200	1600
Preselection	4925 ± 39	2166 ± 15	793 ± 5
Leading jet is b-tagged	3329 ± 31	1286 ± 11	405 ± 4
Leading jet $p_{\mathrm{T}} > 350$ GeV	1857 ± 23	986 ± 10	351 ± 3
Veto events with jets with ΔR (jet, leading jet) < 1.2 or ΔR (jet, leading jet) > 2.7	1340 ± 19	666 ± 8	227 ± 3
$\lvert\Delta\phi$(lepton, leading jet)$\rvert > 2.5$	1280 ± 19	645 ± 8	221 ± 3
# forward jets > 0	792 ± 15	425 ± 6	141 ± 2
ΔR (lepton, cent. jets) > 2.0	530 ± 12	286 ± 5	96 ± 2

Table 6.7.: Signal event yields after the different selection steps for a Y signal with a mass of 900 GeV, 1200 GeV and 1600 GeV and a coupling strength of $c_{\mathrm{L}}^{Wb} = c_{\mathrm{R}}^{Wb} \approx 0.5$ ($\sqrt{c_{\mathrm{L}}^{Wb\,2} + c_{\mathrm{R}}^{Wb\,2}} \approx 0.7$) without considering interference. The signal cross-sections are calculated at NLO accuracy and an integrated luminosity of 36.1 fb^{-1} is used. Only statistical uncertainties are given.

Chapter 7.

Systematic Uncertainties

As for every measurement, also in this analysis it is only possible to test the agreement of the prediction with the observed data within uncertainties. Thus, to judge if signs of new physics have been detected, the evaluation of the relevant sources of uncertainties is of utmost importance. This chapter describes the sources of systematic uncertainties in this thesis, which are divided in three categories: experimental uncertainties, uncertainties on the modelling of background processes and theoretical uncertainties on the signal processes. For most of the uncertainties, the effect is evaluated by rerunning the full analysis chain for each uncertainty separately, where the corresponding parameters are varied accordingly. In the statistical analysis the effects on the final discriminant, the reconstructed mass of the VLQ candidate, are taken into account as individual nuisance parameters. Wherever possible, the latest available recommendations from the combined performance (CP) groups are followed. The leading experimental uncertainties are the uncertainty on the b-tagging efficiency and the jet energy scale (JES).

7.1. Luminosity, Pileup and JVT

For the correct prediction of the number of background and signal events, the luminosity has to be known as precise as possible. However, the uncertainty in the combined 2015+2016 integrated luminosity is 2.1%, which is derived following the same methodology as that detailed in [140, 168, 169]. This normalisation uncertainty is applied to all background and signal samples.

The performance of several deployed algorithms as well as the efficiency of the cut-sequence depend on the number of primary interactions and thus it is crucial that the simulated signal and background events exhibit the same distribution of simultaneous interactions. To account for differences in the pileup distributions in the MC samples and data, the simulated events are reweighted. The uncertainties of this weight are taken into account via an up and down variation of the applied corrections for all MC samples.

The efficiency of the JVT in the simulated events does not perfectly match the efficiency in data, which is measured in $Z \to \mu\mu + \text{jets}$ events [170]. The ratio of the measured efficiency and the efficiency in simulation is used as a scale factor and applied to each MC event, whereas the corresponding uncertainties are propagated to the scale factors and used as an up and down variation [171].

7.2. Muons and Electrons

Uncertainties associated with leptons arise from the trigger, reconstruction, identification, and isolation efficiencies, as well as the lepton momentum scale and resolution.

Since the reconstruction, identification and isolation efficiency as well as the trigger efficiency of the leptons differ between data and simulation, scale factors are applied to match the measured efficiencies in $Z \to l^+l^-$ ($l = e, \mu$) events using tag-and-probe techniques [149, 172]. The lepton efficiencies as well as their uncertainties are determined in bins of transverse momentum and rapidity from data and MC. The lepton scale factors are then calculated by taking the ratio of the determined data efficiency to the MC efficiency and are applied to the MC lepton efficiencies to be able to reproduce the efficiencies seen in data. To account for the imperfect measurements, the scale factors are varied within their uncertainties.

The impact of the lepton energy scale and resolution uncertainty are measured in $Z \to ee$ as well as $J/\psi \to ee$ for electrons [173] and in $Z \to \mu\mu$ as well as $J/\psi \to \mu\mu$ events for muons [172]. The impact of the lepton energy scale and resolution uncertainty on the

distribution of the final discriminant is evaluated by scaling the p_T of all leptons up or down by 1σ.

7.2.1. Missing Transverse Energy

The *hard term* of the missing transverse energy is calculated using reconstructed physics objects as described in Section 5.6 and, thus, its uncertainties are stemming mostly directly from the uncertainties of these objects. These are the dominant sources of uncertainty on E_T^{miss} [174]. During their evaluation, the effects are also propagated to E_T^{miss} and thus are included under the corresponding per-object uncertainty category.
However, there are also uncertainties affecting the *soft term*[1], from the unassociated inner detector tracks: The resolution and scale of the soft term are varied within their errors to evaluate their contribution to the total uncertainty. The METSystematicsTool is used to determine all systematic variations following the 2017 recommendations [175].

7.3. Jet Systematics

7.3.1. Jet Energy Scale and Resolution Uncertainty

The calibration of jets and the applied corrections described in Section 5.4 have associated uncertainties as well. Theses uncertainties arise from the jet identification efficiency based on the jet energy scale and resolution. The jet energy scale (JES) and resolution (JER) as well as their uncertainties are measured in-situ by calculating the difference between MC and test-beam and LHC data in various bins of kinematic phase space [176].

The JES uncertainty depends on the pseudo-rapidity and transverse momentum of the reconstructed jet. They were derived by combining information from test-beam data, LHC collision data and simulation [176]. These uncertainties contain contributions originating from the in-situ analysis, η intercalibration, the behaviour of high-p_{T} jets in propagation of single hadron uncertainties to jets and pile-up [177]. The (correlated) JES uncertainties are

[1] Small uncertainties associated with the modelling of the underlying event, in particular its impact on the p_T scale and resolution of unclustered energy.

combined into 21 nuisance parameters, such that they can be varied independently.
The JES uncertainty is about 6% for jets with $p_T = 25$ GeV and quickly decreasing with increasing jet p_{T}. It is below 1% for central jets with p_T in the range of $\simeq 100$ GeV $- 1.5$ TeV and increasing again to 3% for jets of higher p_T, for the average pile-up conditions during the 2015 data-taking period. The JES uncertainty represents one of the leading sources of uncertainty associated with reconstructed objects [176].

The detector resolution of the jet energy (JER) measurement is used for smearing the energy of the simulated jets. Thus, it may affect the selection efficiency of the jet, hence resulting in changes in the multiplicity distribution due to the migration of events from one jet bin to another. It was measured in Run-1 data and simulation as a function of jet p_T and rapidity using dijet events. They were found to agree within 10% [178]. Additional uncertainties are coming from the extrapolation from Run-1 to Run-2 conditions [176].
All JER uncertainties are combined into one nuisance parameter, where only the "up" variation is provided by the ATLAS Jet E_T^{miss} group, resulting in a one-sided uncertainty which is symmetrised in the final fit (see Section 8.1).

In total, this analysis uses 22 jet systematic variations provided by the ATLAS Jet E_T^{miss} group.

7.3.2. *b*-Tagging Systematics

As every classifier, the used b-tagging algorithm described in Section 5.4.5 is subject to a certain amount of misclassification, which results in a systematic uncertainty. This uncertainty can be separated into contributions from the tagging efficiencies from b-jets, c-jets and jets originating from light-flavour quarks, thus leading to three uncorrelated systematic uncertainties. They are evaluated by varying the η, p_T and flavour-dependent scale factors applied to each jet in the simulation within a range that reflects the systematic uncertainty on the measured tagging efficiency and mistag rates. As these scale factors are only determined up to a jet p_T of 300 GeV and to 750 GeV for light-flavour jets, the uncertainty on the extrapolation to higher p_T ranges is retrieved based on the values in the last bin below that cutoff.
In total, there are 16 eigenvector variations describing light-jet mistagging uncertainties,

three variations related to b-jet tagging, six variations related to c-jet tagging, one variation describing extrapolations to high p_T, and one variation related to the application of c-jet scale factors to τ-jets.

7.4. Modelling Systematics

The prediction of the background and signal processes are determined using Monte Carlo simulations and subject to a certain modelling decision as detailed in Chapter 4. This modelling gives rise to several important systematic uncertainties as described in the following.

7.4.1. Parton Distribution Function

The predictions of the parton distribution functions (PDFs) are also subject to uncertainties and that may cause acceptance variations in both signal and background. Therefore, the uncertainty has been estimated by reweighting the $t\bar{t}$, W+jets, and signal MC samples according to the x and Q^2 of each colliding parton to model the effect of different PDFs. The effects are evaluated using the PDF4LHC15 prescription [179] and the recommendations of the ATLAS MC group [180]: The reconstructed VLQ mass distribution is reweighted to a collection of 31 different PDF sets (including the nominal), named PDF4LHC15 that represents an a-posteriori statistical combination of global PDF sets. The differences are considered as individual nuisance parameter in the statistical analysis.

For $t\bar{t}$ and for the W+jets, no direct reweighting of the nominal samples was possible. Instead, PDF systematics were evaluated for aMC@NLO+Herwig samples and Madgraph+Pythia sample, respectively. The relative difference to the respective sample is propagated to the nominal sample used in this analysis.

7.4.2. Uncertainties from Event Generation

The simulation of physics processes, as described in Section 4.1, can be separated in three main steps (excluding the detector simulation) and thus each of them is a source of modelling uncertainties.

These uncertainties are taken into account for the main background sources due to comparing different MC samples and using the corresponding difference as an additional systematic uncertainty.

$t\bar{t}$

The modelling uncertainty for the simulated $t\bar{t}$ events from the choice of the showering algorithm is evaluated by comparing the nominal $POWHEG + PYTHIA$ sample with an alternative $POWHEG + HERWIG$ sample. The uncertainty arising from the MC generator choice is estimated by comparing a sample generated and showered, respectively, by $MC@NLO + HERWIG$ with a sample where $POWHEG + HERWIG$ was used. The difference is propagated to the nominal sample. Additionally, the uncertainty connected to the choice of the h_{damp} parameter, which determines the amount of initial and final state radiation, is taken into account by comparing the nominal sample with two samples where this parameter was varied.

Single Top

To determine the uncertainties due to the event generation of single top events, the same approach as for the $t\bar{t}$ was pursued, however, each of the contributing processes (s-channel, t-channel, Wt) has to be treated individually.
The generator uncertainty was evaluated by a comparison of $MC@NLO + HERWIG$ and $POWHEG + HERWIG$ samples, whereas the difference is propagated to the nominal $POWHEG + PYTHIA$ sample (t-channel).
The systematic uncertainty connected to the fragmentation algorithm is determined by the difference of the nominal $POWHEG + PYTHIA$ and the alternative $POWHEG + HERWIG$ samples (t-channel, Wt).
It has to be noted that, due to the small statistics of the $MC@NLO + HERWIG$ and $POWHEG{+}HERWIG$ samples in the signal and control regions, both of these systematics are evaluated at the pre-selection+b-tag level (see Chapter 6).
The uncertainty of the choice of the h_{damp} parameter is evaluated for the t-channel, s-channel and for Wt-production.

Furthermore, differences between single top-quark Wt samples produced with using the diagram subtraction scheme and Wt samples produced using the diagram removal scheme are also considered as additional systematic uncertainty. The DR scheme is used as default.

W+jets

As an alternative generator, MADGRAPH+Pythia 8 samples are used for W+jets. Since the statistics of the MADGRAPH+Pythia 8 samples in the signal region is rather small, the comparison is done at the pre-selection plus b-tagged jet level and is propagated to the signal region.

The light- and heavy-flavour components of the W+jets Sherpa samples show a similar but not identical distribution of the reconstructed mass of the VLQ candidate in the SR and CR. However, since W+jets events are the dominant background, special care must be taken. Therefore, to account for a possible mispredicted shape of the m_{VLQ} distribution due to an incorrect flavour composition, a template with HF-only is used instead of the LF+HF template while keeping the LF+HF cross-section constant.

7.4.3. Cross-section Uncertainties

The normalisation of the single-top background has an uncertainty of 6.8% [121]. For the Z+jets background, a 5% uncertainty of the theoretical NNLO cross sections [181] is considered. This uncertainty is applied to the sum of the predicted Z+jets+ diboson background processes. An uncorrelated normalisation uncertainty of 100% is considered for e-channel and μ-channel multijet processes (see Section 7.6.2). Since the contributions from $t\bar{t} + H/V$ are tiny, no additional cross-section uncertainty is applied.
The normalisation of $t\bar{t}$ and W+jets is a free parameter in the analysis.

7.5. Fastsim-Fullsim Comparison

As mentioned in Section 4.2.1, some of the signal MC samples used in this analysis were processed with a faster detector simulation making use of parameterised showers in the calorimeters but were not produced with the full detector simulation.

To check if the prediction using samples generated with AFII differs from the prediction using fully simulated samples, the m_{VLQ} distributions are compared at four different VLQ mass points: 900 GeV, 1500 GeV, 1600 GeV, and 1800 GeV, which is given in Fig. 7.1. Whereby the shape difference is not significant, a small efficiency difference is observed,

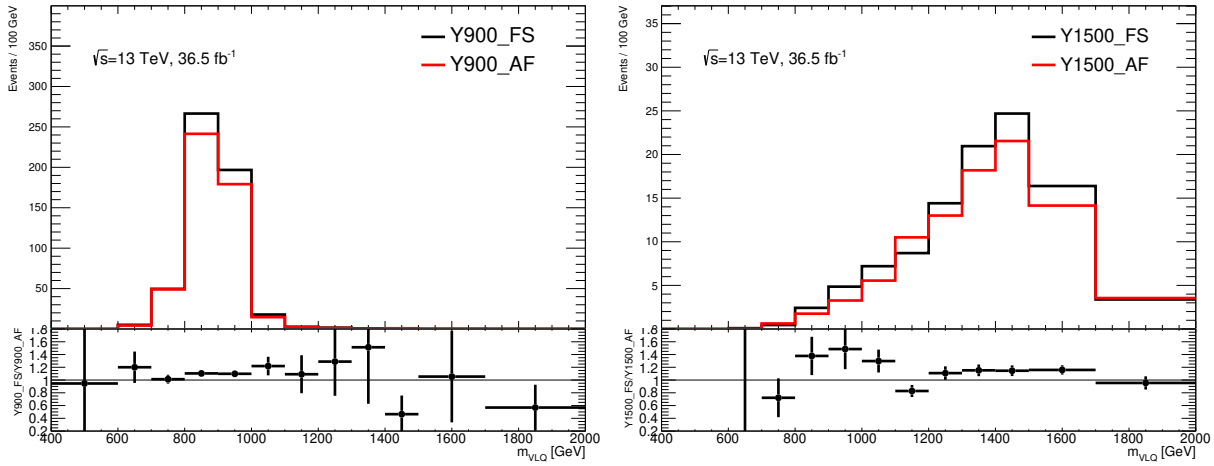

(a)

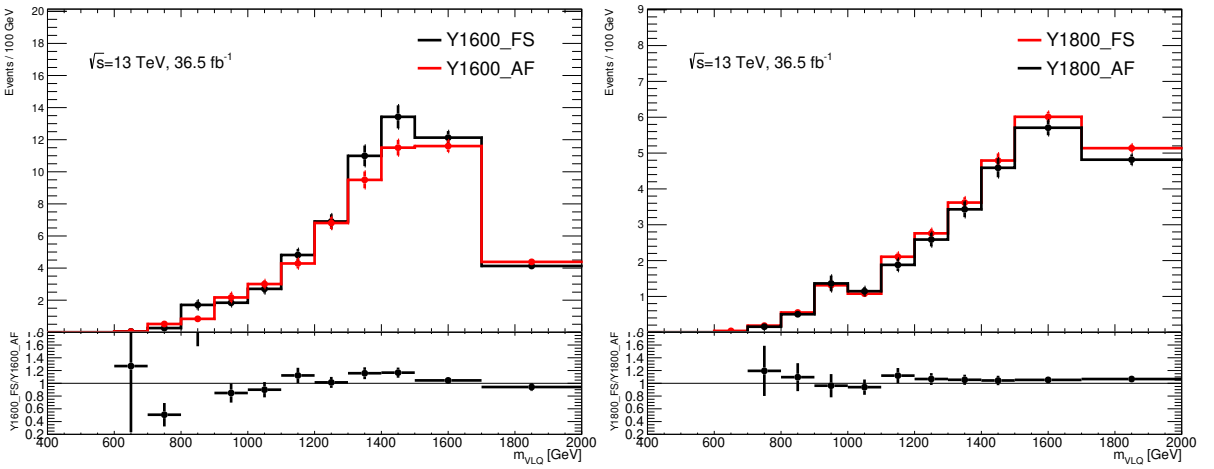

(b)

Figure 7.1.: Comparison of the distribution of the VLQ candidate mass for signal samples using the full ATLAS simulation (FS) and AFII (AF), respectively, for generated signal masses of 900 GeV, 1500 GeV, 1600 GeV and 1800 GeV in the SR. In the bottom part of the plots, the ratio of the prediction using the full ATLAS simulation sample and the AFII sample is given.

which is mainly driven by the requirement of at least one forward jet in the event. A cutflow fullsim and AFII comparison in the m_{VLQ} distribution is presented for a Y signal samples

with a mass of 1800 GeV in Appendix II.
Fitting a constant to the ratio fullsim/AFII allows to quantify the relative difference in efficiency. The AFII and fullsim samples differ only in the detector simulation and, thus, are highly correlated. Therefore, a fit using the statistical bin uncertainties in an uncorrelated fashion, would result in an incorrect estimation of the uncertainty of the fitted constant. On the other hand, if the uncertainties would be correctly estimated, the expectation value of χ^2 of the fit divided by the number of degrees of freedom ($NDoF$) is one. Therefore, the following procedure is applied: The constant is first fitted without considering correlations. Afterwards, each bin uncertainty is multiplied by $\sqrt{\chi^2/NDoF}$ and the fit is repeated, where by definition $\chi'^2/NDoF = 1$ for the second fit. This procedure results in the following efficiency differences: $5.5\% \pm 1.2\%$ (900 GeV), $9.9\% \pm 3.4\%$ (1500 GeV), $4.7\% \pm 3.4\%$ (1600 GeV), and $8.8\% \pm 1.3\%$ (1800 GeV).
To account for this efficiency difference, AFII samples are scaled by the average of these values and the standard deviation of the mean is used as additional systematic uncertainty: $7.2\% \pm 2.5\%$.

7.6. Reweighting Systematics

7.6.1. W+jets Leading Jet p_T Modelling and Reweighting

Studying various distributions of the physics objects used in this analysis for events passing the event pre-selection and pre-selection plus requiring that the leading jet is b-tagged in Figures 6.2–6.6, a mismodelling of the MC prediction is observed. Especially, in Fig. 6.2 a slope in the data/MC ratio is visible. Since the mismodelling increases with increasing jet p_T and the dominance of W+jets processes is also increasing with jet p_T (see Fig. 7.2(a)), it is assumed that this effect comes from a mismodelling of jet p_T distribution of W+jets. The W+jets mismodelling at high-p_T, affecting lepton, jets and $E_{\mathrm{T}}^{\mathrm{miss}}$, is a feature observed already by other analyses at 8 TeV [167] and 13 TeV [182].

To improve the modelling of the W+jets SM background, a reweighting procedure with respect to the leading jet transverse momentum is established and used as a systematic uncertainty. To derive the correction factors for this leading-jet-p_T reweighting, the following method is deployed: First, all predicted SM backgrounds different from W+jets are subtracted from the number of observed data events in the leading jet p_T distribution after

applying pre-selection cuts and requiring that the leading jet is b-tagged (see Fig. 7.2(a)). This region is chosen and not the pre-selection for the determination of the reweighting factors since it is closer to the SR in terms of phase space. Afterwards the remaining data as well as the W+jets distribution are normalised and then the ratio of each bin is used as a weight to be applied for each event where the leading jet p_T corresponds to that particular bin. The effect of this procedure can be seen in Fig. 7.2 for the leading jet p_T distribution and in Fig. 7.3 for the m_{VLQ} distribution, respectively. In Table 7.1 the derived correction factors are listed. With this approach, statistical fluctuations in each bin enter directly into the correction factor and therefore may have an undesired influence on other physical observables. The bin size has been chosen such that the uncertainty is smaller than 10% to keep this effect small. However, to minimise the influence of statistical fluctuations the correction factors could be smoothed by a fit to a polynomial. It has been shown (see Ref. [183]) that using smoothed correction factors has a negligible effect on the observables in comparison to using non-smoothed correction factors. Therefore, the raw (not smoothed) correction factors are used.

It should be stressed that this W+jets background leading-jet-p_T-reweighting method is not applied to the nominal distributions, but instead it is used as an additional systematic uncertainty in the fit (see Section 8.1 for the treatment of systematics).

7.6.2. Fake Electron p_T Reweighting

Uncertainties on the data-driven multijet background estimate receive contributions from the limited sample size in data as well as from the uncertainty on the rate of fake leptons, estimated in different control regions. In Figures 4.2-4.4, a combined normalisation uncertainty of 50% due to all of these effects is assigned. No explicit shape uncertainty is assigned since the large statistical uncertainties associated with the multijet background prediction effectively cover all possible shape uncertainties and the fit results do not change. Especially from Figure 4.4 it becomes obvious that the disagreement between data and the Standard Model prediction is not covered with this choice of the assigned uncertainty. Additionally in Figure 4.2 it is visible that the electron p_T is mismodelled.
Therefore, the electron p_T distribution is used to obtain correction factors such that the Standard Model prediction matches exactly the observed data in the multijet validation region. However, to consider also the electron $|\eta|$, different correction factors for $|\eta| > 1.2$

Leading jet p_T interval [GeV]	Correction factor
$[0, 100]$	0.942863 ± 0.087497
$[100, 120]$	0.976492 ± 0.0573165
$[120, 140]$	1.03943 ± 0.0433686
$[140, 160]$	0.933849 ± 0.0422482
$[160, 180]$	0.97981 ± 0.0410025
$[180, 200]$	0.963376 ± 0.0387254
$[200, 220]$	1.01447 ± 0.0382805
$[220, 240]$	0.998375 ± 0.0637117
$[240, 260]$	1.08998 ± 0.044946
$[260, 280]$	1.10032 ± 0.0453289
$[280, 300]$	1.08203 ± 0.0464115
$[300, 320]$	1.06803 ± 0.0498211
$[320, 340]$	0.978013 ± 0.0552648
$[340, 360]$	1.08423 ± 0.067327
$[360, 380]$	1.04203 ± 0.0725794
$[380, 400]$	0.902079 ± 0.0799135
$[400, 420]$	0.926421 ± 0.0915929
$[420, 460]$	0.972516 ± 0.0796357
$[460, 520]$	0.801356 ± 0.0862193
> 520	0.436806 ± 0.0479317

Table 7.1.: Correction factors for different leading jet p_T intervals for the W+jets prediction applied on event level. The calculation is described in the text. The uncertainty includes the statistical uncertainty on the Monte Carlo predictions.

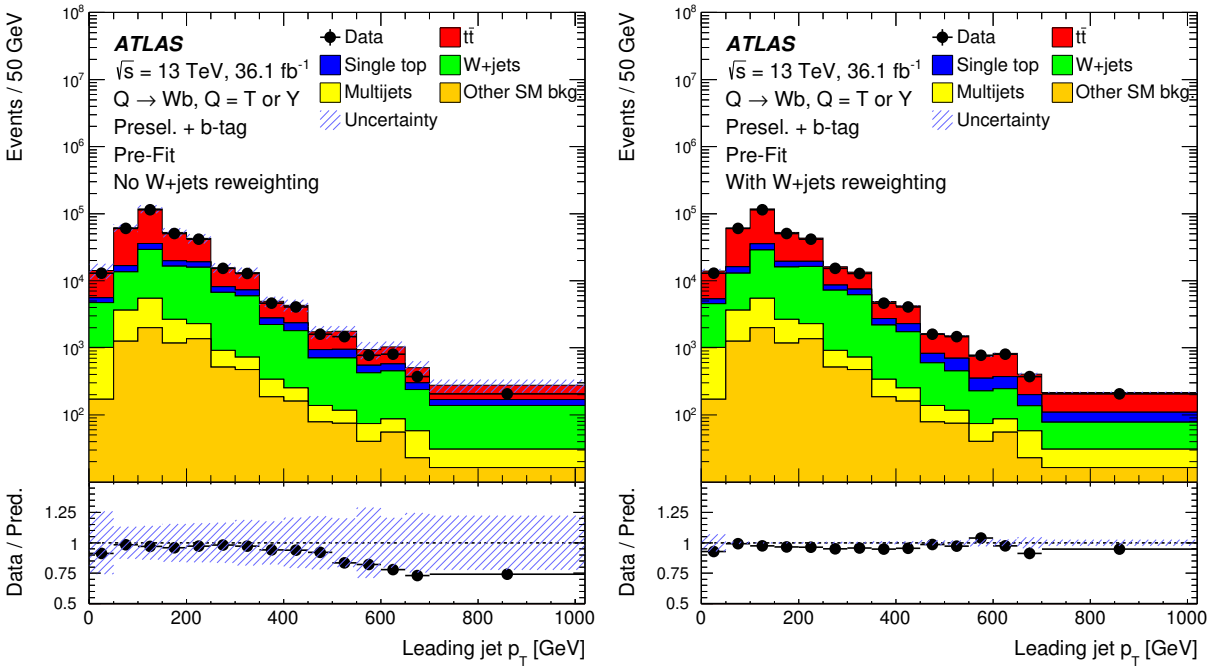

(a) (b)

Figure 7.2.: Distribution of the leading jet p_T after the pre-selection and requiring that the leading jet is b-tagged, before (Fig. (a)) and after (Fig. (b)) applying the W+jets reweighting described in the text. In Fig. (a) the shaded band depicts the uncorrelated sum of the statistical and systematic uncertainty of the SM prediction, whereas in Fig. (b) only statistical uncertainties are included. The error bars of the data points show the corresponding statistical uncertainty.

and $|\eta| < 1.2$ are calculated. To derive these corrections all SM backgrounds are subtracted from the observed data distribution. The ratios of each bin of the remaining distribution (data - SM background) and the multijet estimate are used as correction factors. These weights are applied to each event of the electron channel of the multijet estimate and the resulting distribution is used as an additional systematic variation. Figure 7.4 shows the effect of this reweighting for the m_{VLQ} and electron p_T distribution.

To fully cover the discrepancies between the observed data and the SM prediction in multijet enriched regions of the phase space the normalisation uncertainty of the multijet estimate is increased to 100%. In Figure 7.5 the invariant mass distribution of the vector-like quark candidate m_{VLQ} in the multijet validation region in the electron channel and in the muon channel is presented. The shaded band depicts the statistical uncertainty and a 100% normalisation uncertainty of the multijet estimate as well as the electron-p_T-reweighting sys-

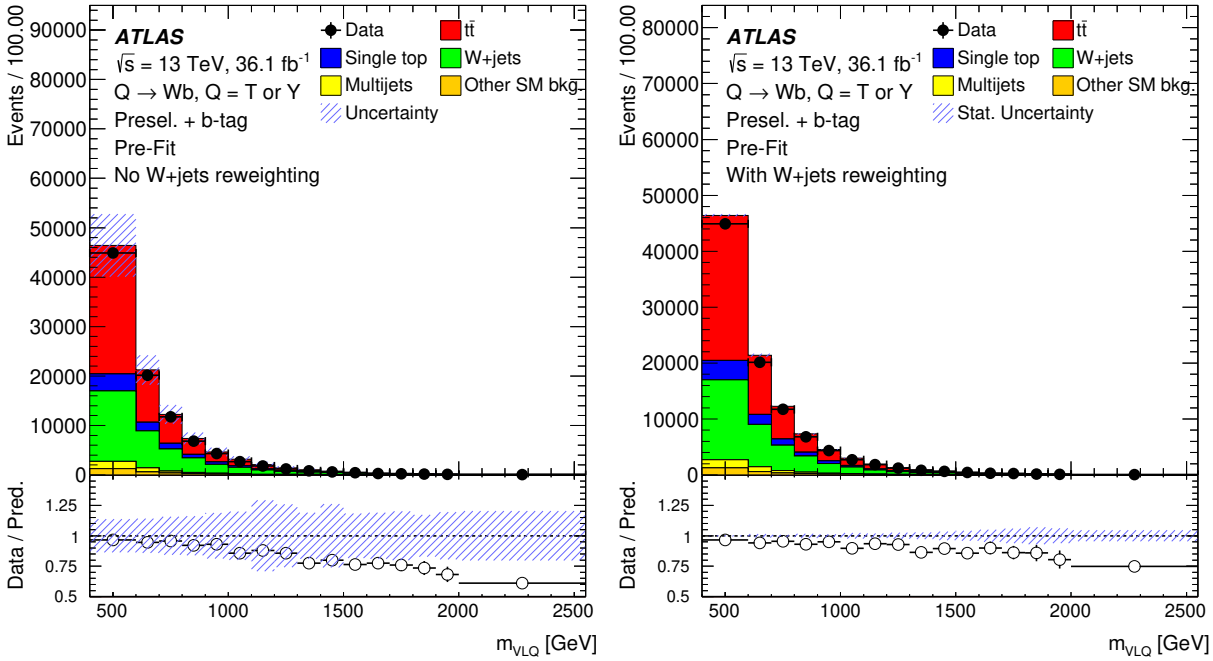

(a) (b)

Figure 7.3.: Distributions of the reconstructed VLQ mass after the pre-selection and requiring that the leading jet is b-tagged, before (Fig. (a)) and after (Fig. (b)) applying the W+jets reweighting described in the text. In Fig. (a) the shaded band depicts the uncorrelated sum of the statistical and systematic uncertainty of the SM prediction, whereas in Fig. (b) only statistical uncertainties are included. The error bars of the data points show the corresponding statistical uncertainty.

tematic applied to the fake estimate and the leading-jet-p_T-reweighting systematic applied to W+jets background.

7.6.3. Signal Reweighting

The uncertainty of the reweighting procedure is taken into account in two ways:

- The ratios of the nominal and target distribution are smeared by a Gaussian (bin-wise and uncorrelated), where the mean is equal to the nominal and the standard deviation equals the corresponding statistical uncertainty. An up and down variation of the reweighting function is determined using these smeared ratios.

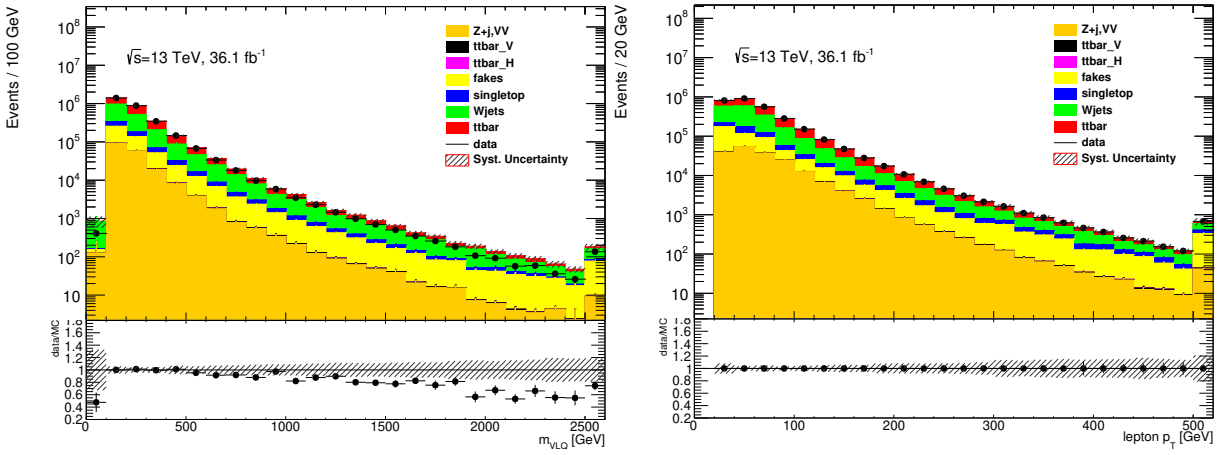

(a) (b)

Figure 7.4.: Mass distribution of vector-like quark candidate m_{VLQ} (electron channel) 7.4(a) and electron p_T distribution 7.4(b) in the multijet validation region with reweighted multijet estimate. The shaded band depicts the statistical uncertainty and a 50% normalisation uncertainty of the multijet estimate.

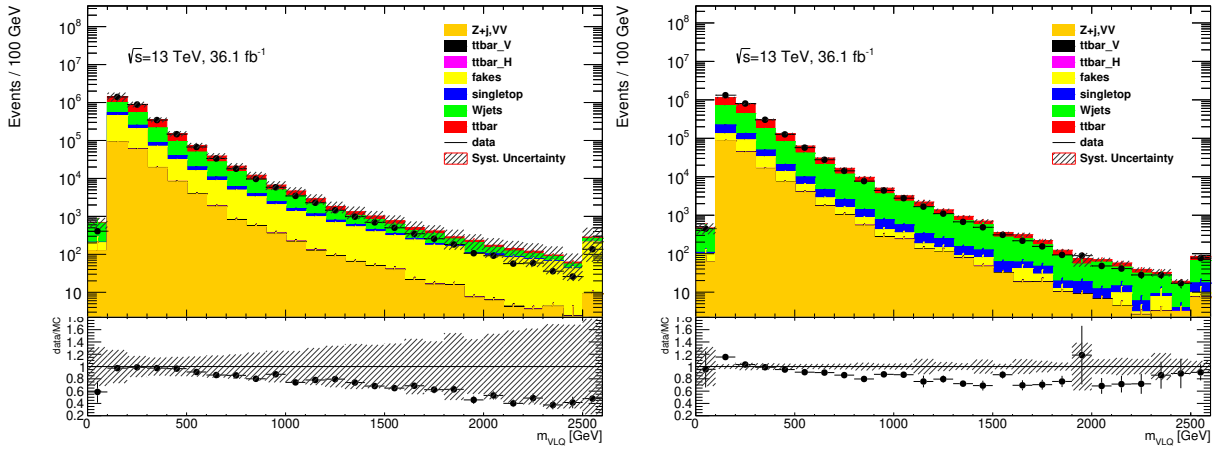

(a) (b)

Figure 7.5.: Mass distribution of vector-like quark candidate m_{VLQ} in the multijet validation region in the electron channel 7.5(a) and in the muon channel 7.5(b). The shaded band depicts the statistical uncertainty and a 100% normalisation uncertainty of the multijet estimate as well as the electron-p_T-reweighting systematic applied to the fake estimate and the leading jet p_T reweighting systematic applied to W+jets background.

- The performance of the reweighting is tested using fully reconstructed VLQ Y signal samples produced with a coupling of $\kappa = 0.1$ and $\kappa = 0.5$, where each sample is

reweighted to the other coupling. An 2.5% offset in the reweighted event yields compared to the ones taken from the nominal samples are observed and, thus, 2.5% is used as an additional normalisation uncertainty.

7.7. Interfering SM Background

The ATLAS MC production used in this analysis does not contain simulated events from the SM contributions that lead to interference with the VLQ signal. For the VLQ T the interfering background is t-channel single-top-quark production where the top quark is far off-shell. However, in the ATLAS MC production, top quarks are only simulated with a mass in a rather small window around the on-shell mass. Even if they were simulated, the statistics would be much too small. The relevant process for the VLQ Y, is electroweak Wbq production and the diagrams relevant for the interference are not contained in SHERPA for the simulation of W+jets events. Therefore, these SM contributions can not be explicitly considered in the background modelling of the fit.
A recent MC production of the interfering background at reconstruction level using the four-flavour scheme[2] shows that the corresponding m_{VLQ} distribution in the SR is similar but not identical to that of the other background contributions (W+jets, $t\bar{t}$, single top), as shown in Fig. 7.6. Since the shape of the m_{VLQ} distribution of the interfering background is most similar to the shape of the m_{VLQ} distribution of $t\bar{t}$, an additional shape uncertainty is applied to the $t\bar{t}$ m_{VLQ} template to account for the presence of the interfering SM contributions in the fit. This leads to an uncertainty of 0.2% in the $t\bar{t}$ yield in the signal region.

7.8. Summary of Systematics

The Table 7.2 provides an overview of the systematic and its relative size with respect to the Standard Model prediction.

[2]MadGraph studies have shown that the predicted size of the interfering background differs significantly between five- and four-flavour scheme, e.g. by a factor or two for the background interfering with Y. However, the shapes are consistent.

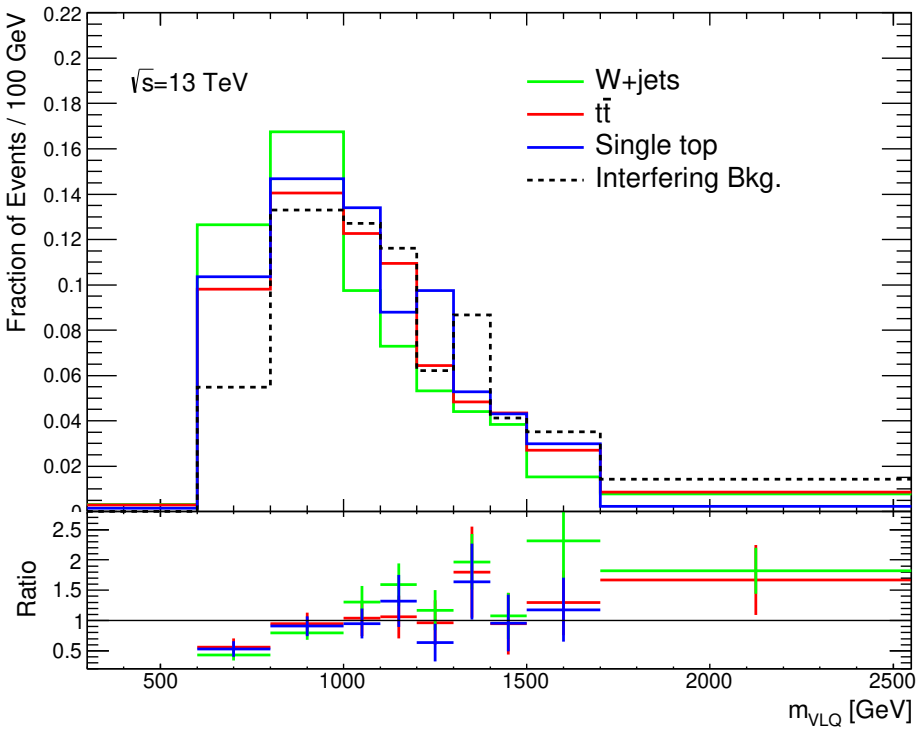

Figure 7.6.: The top part of the figure shows a comparison of the normalised m_{VLQ} distribution of the interfering background (black dashed line) with the corresponding distribution of W+jets (green solid line), $t\bar{t}$ (red solid line) and single top (blue solid line), respectively, in the SR. The bottom part of the figure shows the ratio of the interfering background with W+jets (green), $t\bar{t}$ (red) and single top (blue), respectively.

Systematic uncertainty	Type	SM background [%]
Luminosity	N	2.1
Pile-up	SN	0.3
Reconstructed objects:		
Electron efficiency, energy scale, resolution	SN	0.9
Muon efficiency, momentum scale, resolution	SN	0.7
Jet vertex tagger	SN	0.1
Jet energy scale	SN	6.4
Jet energy resolution	SN	2.7
Missing transverse momentum	SN	0.3
b-tagging efficiency for b-jets	SN	0.8
b-tagging efficiency for c-jets	SN	1.8
b-tagging efficiency for light-flavour jets	SN	8.4
Background model:		
$t\bar{t}$ modelling: ISR/FSR	SN	0.2
$t\bar{t}$ modelling: generator	SN	3.8
$t\bar{t}$ modelling: parton shower/hadronisation	SN	4.5
$t\bar{t}$ modelling: interfering background shape	S	0.3
Single-top cross-section	N	0.4
Single-top modelling: ISR/FSR	SN	0.04
Single-top modelling: generator	SN	0.3
Single-top modelling: DS/DR	SN	3.1
Single-top modelling: parton shower/hadronisation	SN	1.6
W+jets modelling: generator	SN	0.8
W+jets modelling: reweighting	S	4.6
W+jets heavy flavour	S	0.04
Diboson + Z+jets normalisation	N	0.2
Multijet normalisation	N	3.8
Multijet reweighting	S	2.1
$t\bar{t}$ background scaling factor	F	26
W+jets background scaling factor	F	19

Table 7.2.: Systematic uncertainties of the SM prediction considered in this analysis, where "S" denotes a systematic affecting the shape of the prediction, "N" affects only the normalisation and "F" corresponds to a floating normalisation uncertainty. The effect on the total SM prediction after the fit to the background-only hypothesis (see Chapter 8) is given in the last column in percent. Except for the $t\bar{t}$ and W+jets background scaling-factors, where the the relative uncertainty for the respective background prediction is given.

Chapter 8.

Statistical Analysis

The discovery of a VLQ T or Y signal is only possible on a statistical basis, thus dedicated tools and methods have to be exploited.
This chapter gives a short introduction and overview of the used statistical methods (based on [184]) and afterwards presents the results of the limit setting procedure[1].

8.1. Methods

A binned maximum-likelihood (ML) fit is performed on the reconstructed VLQ mass m_{VLQ} using histogram templates derived from MC and data-driven estimates using the package `TRexFitter` [185] which uses the `RooStats` [186, 187] framework to perform the fit. In the following, this method is sketched.

Maximum-Likelihood Fit

In order to search for new physics, the compatibility of the observed data with the alternative hypothesis H_1 (new physics exists, i.e. VLQ+SM) has to be compared with the compatibility with the default hypothesis H_0 (no new physics exists, i.e. SM only). This is done by quantifying the outcome of an experiment with an appropriate *test statistic* q, which translates the observations into a single number. This can be done using the definition of

[1] The limits and corresponding plots were kindly provided by Anjishnu Bandyopadhyay from the University of Bonn

the so-called p-value, which gives the probability p_{H_1} to observe a q at least as large as the measured q_{obs} given the probability distribution $f(q|H_1)$ of q given H_1

$$p_{H_1} = \int_{q_{obs}}^{\infty} f(q|H_1)dq. \tag{8.1}$$

Now, a certain threshold $p_{H_1,t}$ could be defined above which the hypothesis H_1 would be rejected. However, this could lead to a hypothesis rejection even if the analysis is not sensitive enough or due to a downward fluctuation in data. Therefore, the $\mathrm{CL_s}$ is defined as

$$\mathrm{CL_s} = \frac{p_{H_1}}{p_{H_0}}, \tag{8.2}$$

where usually $\mathrm{CL_s} < 0.05$ is required for an exclusion of H_1, as it is the case in this analysis. The next crucial point is the definition of a suitable *test statistic* q, which can be constructed using the number of events n_i in bin i of the binned invariant mass distribution m_{VLQ} of the VLQ candidates. This number receives contributions not only from the hypothetical signal events but also from the mentioned backgrounds:

$$n_i = \mu n_i^{sig}(\vec{\alpha}) + \sum_{j}^{N_{Bkgs}} \mu_j n_i^j(\vec{\alpha}), \tag{8.3}$$

with $n_i^{sig}(\vec{\alpha})$ the number of signal events in bin i, N_{Bkgs} is the number of contributing background processes and $n_i^j(\vec{\alpha})$ the number of events in bin i from background source j. Furthermore, $\vec{\alpha}$ denotes the set of *nuisance parameters* which measure the size of the corresponding systematic variation, μ_j the (potential) background scale factors and μ is the parameter of interest, the *signal strength*. The total number of events in each bin is Poisson distributed $P(n_i|\lambda)$ with expectation value λ and the impact of the nuisance parameter α_j is encoded by a Normal distribution $G(0|\alpha_j)$. This is used to construct the likelihood function

$$\mathcal{L}(\mu, \vec{\mu_{bkg}}, \vec{\alpha}) = \prod_{i \in bins} P(n_i|\lambda(\mu, \vec{\mu}_{bkg}), \vec{\alpha}) \prod_{j \in sys} G(0|\alpha_j), \tag{8.4}$$

where *bins* include all bins of the signal and control regions. Statistical uncertainties in each bin of the discriminant distributions are also taken into account via dedicated parameters

in the fit.
Now, the maximum of this distribution with respect to all parameters $\mathcal{L}(\hat{\mu}, \hat{\vec{\mu}}_{bkg}, \hat{\vec{\alpha}})$ and the maximum given a fixed μ, corresponding to the hypothesis being tested, $L(\mu, \hat{\hat{\vec{\mu}}}_{bkg}, \hat{\hat{\vec{\alpha}}})$, are used to construct the *profile likelihood ratio*:

$$\Lambda = \frac{\mathcal{L}(\mu, \hat{\hat{\vec{\mu}}}_{bkg}, \hat{\hat{\vec{\alpha}}})}{\mathcal{L}(\hat{\mu}, \hat{\vec{\mu}}_{bkg}, \hat{\vec{\alpha}})}. \tag{8.5}$$

This analysis uses $q_\mu = -2 \ln \Lambda$ as test statistic.
The test statistic q_μ is implemented in the RooFit package [187, 188] and is used to measure the compatibility of the observed data with the background-only hypothesis (i.e. the discovery test) setting $\mu = 0$ in the profile likelihood ratio: $q_0 = -2 \ln(\mathcal{L}(0, \hat{\hat{\alpha}}_0)/\mathcal{L}(\hat{\mu}, \hat{\alpha}))$. The background-only hypothesis is estimated by integrating the distribution of q_0 from background-only pseudo-experiments, approximated using the asymptotic formulae given in Ref. [189, 190], above the observed value of q_0.
In the absence of any significant excess above the background expectation, upper limits on the signal production cross-section for each of the signal scenarios considered are derived by using q_μ in the CL_s method [191, 192]. For a given signal scenario, values of the production cross-section (parameterised by μ) yielding $CL_s < 0.05$, where CL_s is computed using the asymptotic approximation [189, 190], are excluded at $\geq 95\%$ confidence level.
The fit of the signal-plus-background hypothesis to data yields the observed limit and the result of the fit to the nominal background predictions represents the expected limit, which is obtained using Asimov data. The Asimov dataset is defined such that the "true" values of the parameters are obtained, when it is used in the fit (see [184]). This means that the nuisance parameters are set to zero and the content of bin i is set to the value of n_i (see Eq. 8.3) predicted by the MC simulation, where μ is set to the desired value (e.g. 0 for the background-only hypothesis).

Treatment of Systematics

Fitting the nuisance parameters to the values which maximise $\mathcal{L}$ in the likelihood fit allows a reduction of the impact of systematic uncertainties on the search sensitivity especially by taking advantage of the highly populated background-dominated control regions. To verify the improved background prediction, fits are performed under the background-only hypothesis. Differences between the data and the background prediction are checked relative

to the smaller post-fit uncertainties in kinematic variables other than the ones used in the fit.
The different systematics are taken into account within the fit and limit setting by using related alternative histograms of the invariant mass distributions in the signal and control regions.
In case of one-sided systematics k (for example the jet energy resolution), the given variation is defined to be the *up* variation histogram h_k^+. The effect of the *down* systematic variation is then symmetrised by defining the down variation h_k^- as

$$h_k^- = h^0 - (h_k^+ - h^0), \tag{8.6}$$

with the nominal histogram h^0. To avoid bad behaviour of the fit, also two-sided systematics are symmetrised using:

$$\begin{aligned} h_k^+ &= h^0 + 0.5 \times (h_k'^+ - h_k^-), \\ h_k^- &= h^0 - 0.5 \times (h_k'^+ - h_k^-). \end{aligned} \tag{8.7}$$

Then, the nominal histogram and the systematic variations are combined using the nuisance parameter α_j as:

$$h_k = \begin{cases} h^0 + \alpha \left(h_k^+ - h^0\right), & \alpha \geq 0. \\ h^0 - \alpha \left(h_k^- - h^0\right), & \alpha < 0. \end{cases} \tag{8.8}$$

As mentioned above, a Gaussian constraint with mean 0 and width 1 is applied to each of the α_j.

The statistical MC errors per bin are analogously symmetrised and nuisance parameters are introduced using the so-called Barlow-Beeston "lite" method [193]. One nuisance parameter is used for each histogram bin in each channel; the nuisance parameter represents the statistical MC errors in that bin from each of the components added in quadrature.
In order to speed up the fit, systematic uncertainties that have a very small effect on normalisation are pruned for a given process and a given category: the pruning algorithm removes systematic uncertainties that have an $\leq 1\%$ impact on the normalisation[2]. If there is at least one bin that is above this pruning threshold, all bins are kept. For systematic

[2]If the change of the total rate is less than 1.0%, then this uncertainty does not act anymore on the rate.

uncertainties that have an impact on the shape of the final discriminant, the pruning algorithm removes shape systematics if the differences between the highest and lowest variation in a single histogram are smaller than 1%. A pruning threshold is also applied for MC statistical uncertainties. If the MC statistical uncertainty associated with a given bin is less than 5%, no extra nuisance parameter is introduced for that bin.

Binning

As could be seen in Section 2.4.3, considering interference effects leads to partially negative signal distributions. Since `TRexFitter` can not handle negative bin entries, all bins for all channels used in the fit need to have non-negative entries and thus the binning of the histograms has to be chosen accordingly (at least 5 events per bin). However, since the shape of the signal is highly mass- and coupling-dependent, a dedicated binning for each mass point was chosen.
In the T singlet case, the overall integral of the signal distribution becomes negative for masses above 1200 GeV and thus no limits could be determined for $m_Q \geq 1300$ GeV.
The binning given in Table 8.1 is used for the limit determination.

Signal	Mass in [GeV]	Binning in [GeV]
Y LH	800	[600,650,700,750,2550]
Y LH	900	[600,650,700,800,850,2550]
Y LH	1000	[600,650,700,750,800,850,900,950,2550]
Y LH	1100	[600,650,700,750,800,850,900,950,1000,2550]
Y LH	1200	[600,650,700,750,800,850,900,950,1000,1050,1100,1150,2550]
Y LH	1300	[600,650,700,750,800,850,900,950,1000,1050,1100,1150,1200,2550]
Y LH	1400	[600,650,700,750,800,850,900,950,1000,1050,1100,1150,1200,1250,1300,2550]
Y LH	1500	[600,650,700,750,800,850,900,950,1000,1050,1100,1150,1200,1250,1300,1350,1400,2550]
Y LH	1600	[600,650,700,750,800,850,900,950,1000,1050, 1100,1150,1200,1250,1300,1350,1400,1450,1500,2550]
T	800	[600,800,900,1000,1500,2550]
T	900	[600,900,1000,1200,1500,2550]
T	1000	[600,1000,1100,1400,2550]
T	1100	[600,1150,1250,1600,2550]
T	1200	[600,1250,1350,1500,1650,2550]
Y RH		[600,800,1000,1100,1200,1300,1400,1500,1700,2550]

Table 8.1.: Signal region binning for different Y/T mass points that is used to determine limits for signals where interference with the SM is also considered. For the right-handed Y, the binning is always the same and this binning is also used for the background-only hypothesis.

8.2. Fit Results

In the following section, the fit results for the two hypotheses are presented. First, it is tested if the Standard Model could be ruled out given the observed data, thus the background-only hypothesis is tested. As a second step, it is tested if the alternative VLQ hypothesis, i.e. the signal-plus-background hypothesis, can explain the data or if certain parts of the parameter space could be excluded for various benchmark scenarios.

8.2.1. Background-Only Hypothesis

The resulting invariant mass distribution of a combined fit to data in both the signal region and the control regions under the background-only hypothesis is given in Fig. 8.2. Additionally, the corresponding pre-fit distributions are given in Fig. 8.1. As can be clearly seen, already at pre-fit level no significant deviation from the Standard Model prediction is observed. At post-fit level, the agreement of the data with the prediction is improved and the uncertainties are reduced, as expected. The fitted values of the free-floating $t\bar{t}$ and W+jets normalisation parameters are 0.99 ± 0.25 and 1.15 ± 0.16, respectively.

Also the pre- and post-fit yields in each of the regions considered are given in Figure 8.1 and Figure 8.2, respectively, and further post-fit kinematic variables are presented in Fig. 8.3. It should be noted that the enhanced uncertainties in the bins around 1450-1600 GeV and 1850-2200 GeV in the W+jets CR are due to lower statistics in these bins, but the total uncertainties on the SM background do not increase. The corresponding observed and expected event yields broken down to the individual processes can be found in Table 6.5 and Table 8.2, respectively.

Given that the prediction and the data agree well in all considered regions in yields and in shape, the Standard Model was not successfully excluded. Therefore, the next step is to test whether the alternative hypothesis can be excluded at 95% confidence level (CL) for several benchmark scenarios.

Source	SR	$t\bar{t}$ CR	W+jets CR
$t\bar{t}$	58 ± 21	2715 ± 295	100 ± 29
Single top	29 ± 15	271 ± 118	34 ± 18
W+jets	373 ± 45	1052 ± 143	1077 ± 84
Multijet e	22 ± 20	35 ± 40	0 ± 4
Multijet μ	7 ± 7	92 ± 71	26 ± 20
Z+jets, diboson	20 ± 5	102 ± 20	50 ± 8
$t\bar{t}V$	0.3 ± 0.1	21 ± 3	1.6 ± 0.3
$t\bar{t}H$	0 ± 0	7 ± 1	0.2 ± 0.1
Total	500 ± 30	4300 ± 210	1290 ± 70
Data	497	4227	1274

Table 8.2.: Post-fit (background-only hypothesis) event yields in the SR and the $t\bar{t}$ and W+jets CRs. The uncertainties include statistical and systematic uncertainties. Due to correlations among the SM backgrounds, summing the uncertainties of the individual components in quadrature can be larger than the uncertainty on the total background.

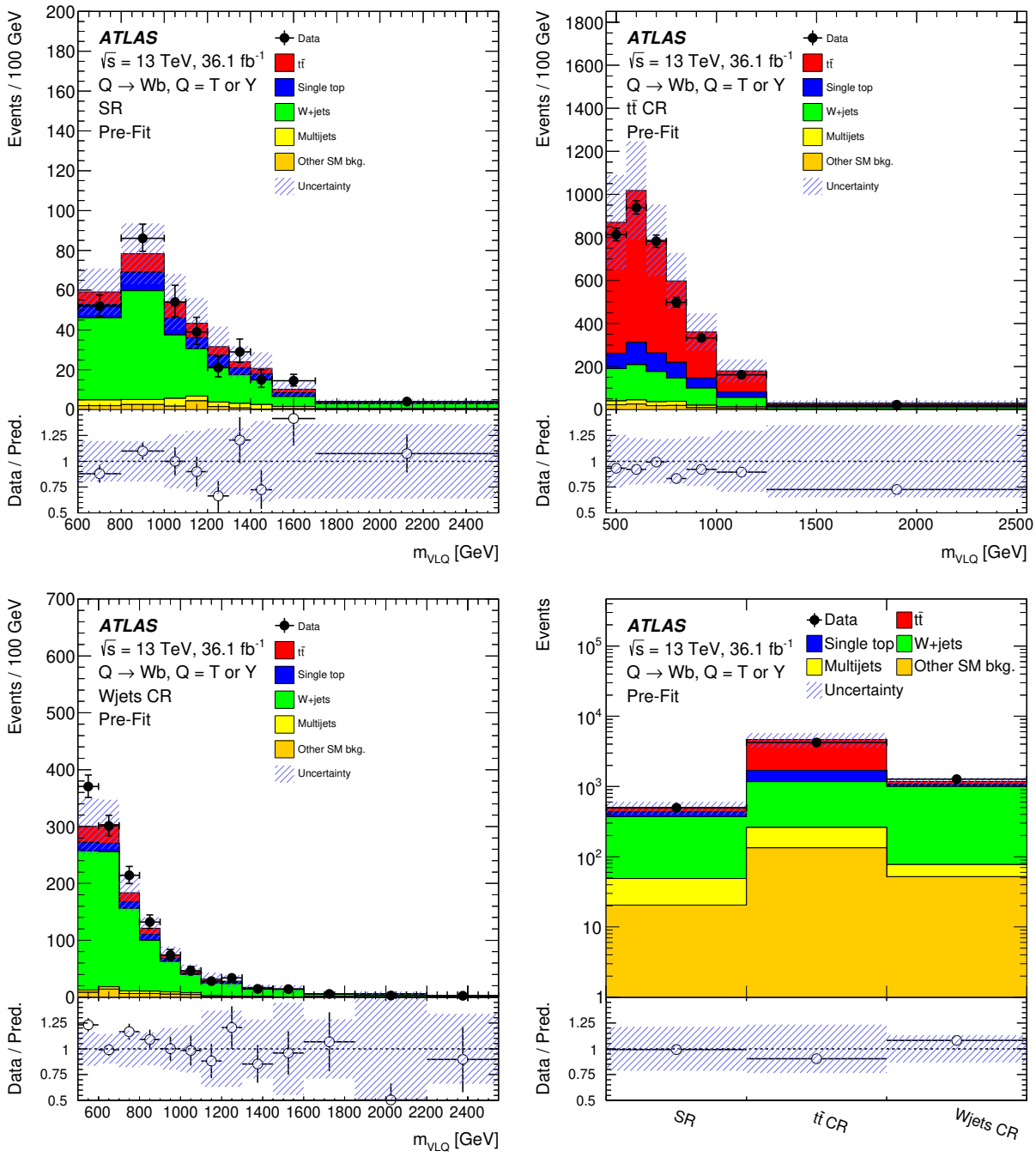

Figure 8.1.: Pre-fit VLQ mass distribution for the signal region, $t\bar{t}$ and W+jets control regions. The bottom right figure shows a data-MC comparison of the integral in the signal and control regions. The uncertainties correspond to statistical and systematic uncertainties.

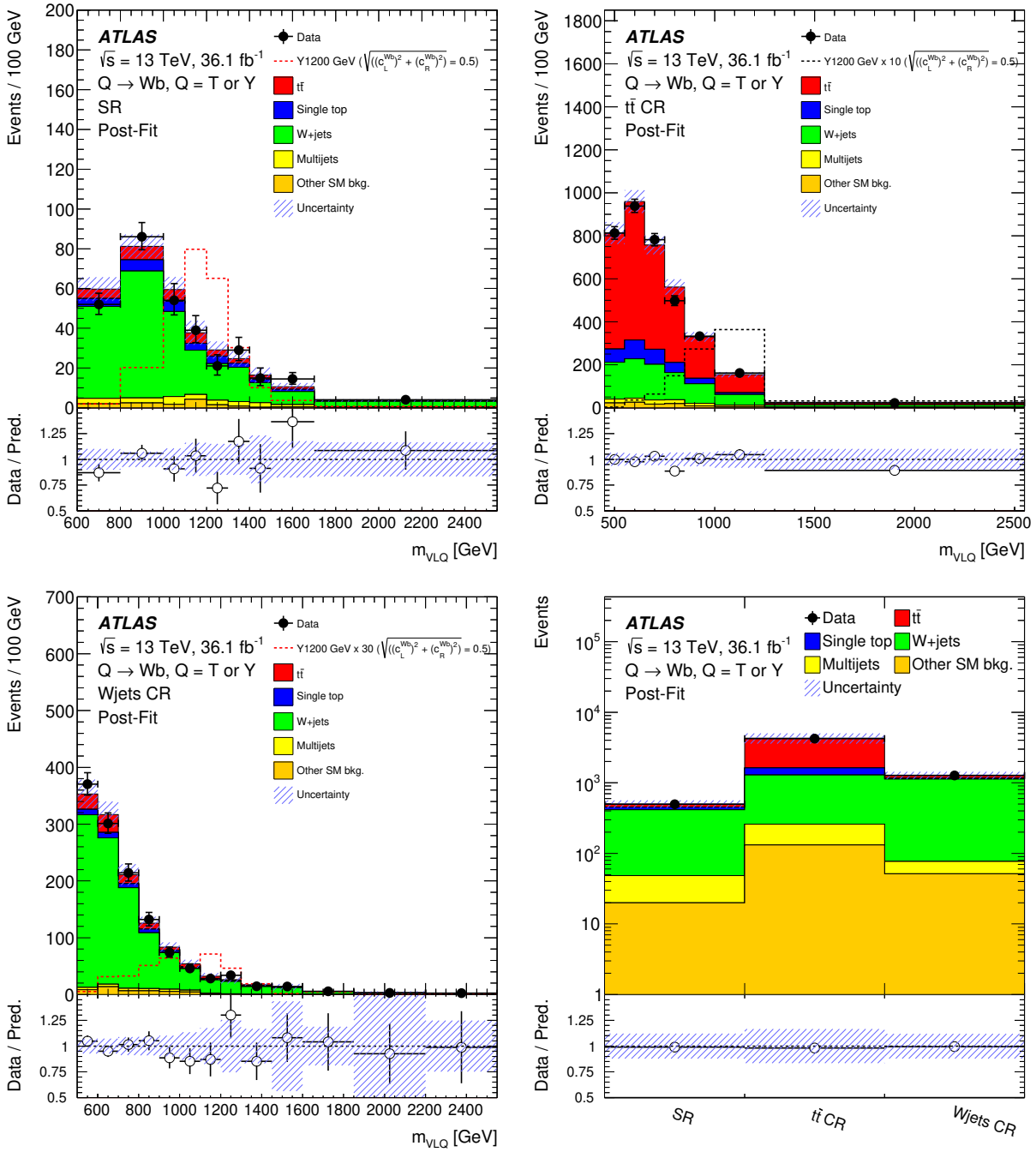

Figure 8.2.: Post-fit VLQ mass distribution for the signal region, $t\bar{t}$ and W+jets control regions after performing a fit to the signal and control regions for the background-only hypothesis. The bottom right figure shows a data-MC comparison of the integral in these regions. The uncertainties correspond to statistical and systematic uncertainties. An example distribution for a Y signal without considering interference effects with a coupling of $\sqrt{c_{\mathrm{L}}^{Wb\,2} + c_{\mathrm{R}}^{Wb\,2}} \approx 0.5$ is overlaid. For better visibility, the signal distribution is multiplied by a factor of 30 in the W+jets CR and by a factor of 10 in the $t\bar{t}$ CR.

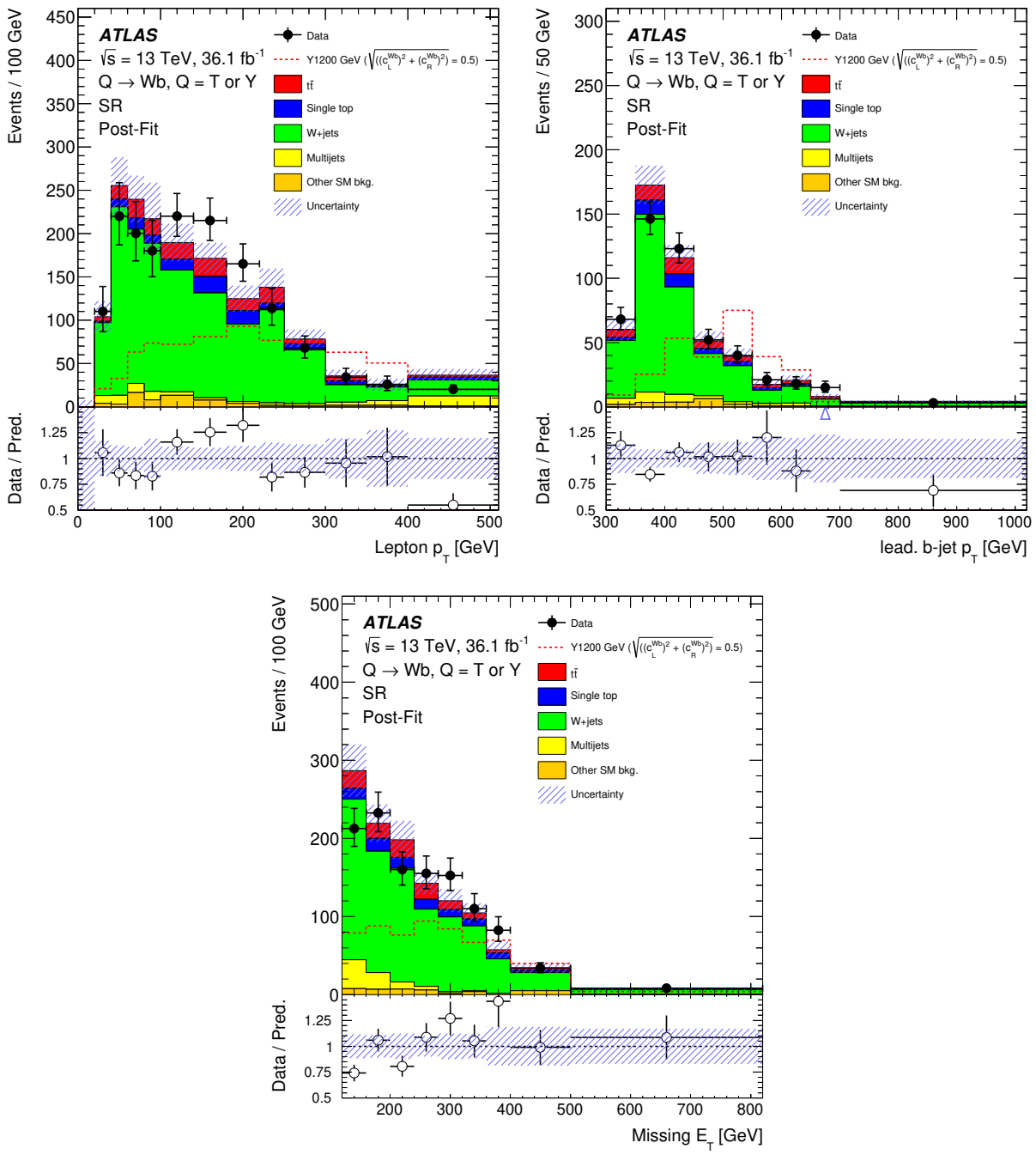

Figure 8.3.: Post-fit lepton p_T, leading jet p_T and E_T^{miss} distributions for the signal region region after performing a fit to the signal and control regions for the background-only hypothesis. The uncertainties correspond to statistical and systematic uncertainties. An example distribution for a Y signal without considering interference effects with a coupling of $\sqrt{c_{\text{L}}^{Wb\,2} + c_{\text{R}}^{Wb\,2}} \approx 0.5$ is overlaid.

8.2.2. Signal-plus-Background Hypothesis and Limits

In Section 2.4, it was found that interference between the signal and SM processes has a significant effect on the distribution of the invariant mass of the VLQ candidate. As in explained in Section 4.3, a reweighting procedure is applied to achieve meaningful results and that this approach implies that the final limits for the signal-plus-background hypothesis have to be determined in an iterative way until convergence is achieved. The chosen convergence criterion is defined as $|c_{\text{limit}} - c| < 0.015$. As outlined in Section 2.4, the results are interpreted in terms of VLQ Y in a (B, Y) doublet and (T, B, Y) triplet, where, according to Equation 2.51, the left-handed and the right-handed component is dominant, respectively. Additionally, the interpretation is done with respect to a T singlet, where only the left-handed coupling and mixing angle, respectively, are relevant. The sub-dominant components are neglected. The final κ values of the iterative process that are used as input parameter for the signal masses for the right-handed Y, left-handed Y and T template production, can be found in the Appendix I in Table I.1.
Corresponding distributions of the final discriminant in the signal region for some example mass points are depicted in Fig. 8.4.

The final expected and observed 95% CL upper limits on the coupling value and on the mixing angle as a function of vector-like quark mass for the left- and right-handed Y as well as for the left-handed T (assuming $\mathcal{B}(T \to Wb) = 0.5$) are summarised in Tables 8.5, 8.4 and 8.3. These results are visualised in the plots in Figure 8.5 where always both limits of the mixing angle and the limits of the coupling are given in the same plot, since these parameterisations can be easily translated to the other (see Section 2.4.2).
For the T-singlet model, the best (smallest) upper exclusion limit on $|\sin\theta_{\text{L}}|$ (c_{L}^{Wb}) is found for a mass of 800 GeV and are as small as 0.18 (0.25). The worst (largest) result of 0.35 (0.49) is observed for a T-singlet quark with a mass of 1200 GeV. In a (B, Y) doublet, the upper exclusion limit on $|\sin\theta_{\text{R}}|$ (c_{R}^{Wb}) range from 0.17 (0.24) for a mass of 800 GeV to 0.55 (0.77) for Y quarks with a mass of 1800 GeV. The upper exclusion limits on $|\sin\theta_{\text{L}}|$ (c_{L}^{Wb}) in a (T, B, Y) triplet vary between 0.16 (0.31) and 0.39 (0.78) for Y-signal masses between 800 GeV and 1600 GeV. No significant deviations between the expected and observed upper exclusion limits are found, however the observed limit shows a "kinky" shape, especially for the left-handed Y. This effect can be traced back to different binnings for the various mass points.
The embedding of the VLQs in $SU(2)$ multiplets allows the determination of indirect

bounds inferred from electroweak precision variables, as mentioned in Section 2.4. Figure 8.5 therefore also provides these indirect bounds taken from Ref. [41], assuming that there is no other multiplet than the multiplet under consideration. Notably, the observed limits of the mixing angle of this analysis are competitive with these indirect bounds in a mass range of 800 GeV to 1250 GeV for the (B, Y) doublet model.

T mass [GeV]	Observed limit on $\lvert\sin\theta_{\mathrm{L}}\rvert$	Expected limit on $\lvert\sin\theta_{\mathrm{L}}\rvert^{+1\sigma/+2\sigma}_{-1\sigma/-2\sigma}$	Observed limit on c_{L}^{Wb}	Expected limit on $c_{\mathrm{L}}^{Wb\,+1\sigma/+2\sigma}_{\quad-1\sigma/-2\sigma}$
800	0.18	$0.19\,^{0.04/0.08}_{0.03/0.06}$	0.25	$0.27\,^{0.06/0.11}_{0.05/0.08}$
900	0.24	$0.20\,^{0.05/0.09}_{0.05/0.07}$	0.34	$0.29\,^{0.07/0.13}_{0.07/0.10}$
1000	0.20	$0.21\,^{0.06/0.08}_{0.07/0.09}$	0.29	$0.30\,^{0.08/0.12}_{0.10/0.12}$
1100	0.25	$0.27\,^{0.09/0.11}_{0.13/0.15}$	0.36	$0.38\,^{0.12/0.15}_{0.18/0.21}$
1200	0.35	$0.35\,^{0.13/0.14}_{0.22/0.23}$	0.49	$0.49\,^{0.18/0.20}_{0.31/0.33}$

Table 8.3.: Observed and expected 95% CL upper limits on $\lvert\sin\theta_{\mathrm{L}}\rvert$ and c_{L}^{Wb} for a left-handed T quark in a T-singlet model with masses of 800 GeV to 1200 GeV assuming $\mathcal{B}(T \to Wb) = 0.5$ with $\pm1\sigma$ and $\pm2\sigma$ uncertainties in the expected limits.

Y mass [GeV]	Observed limit on $\lvert\sin\theta_{\mathrm{R}}\rvert$	Expected limit on $\lvert\sin\theta_{\mathrm{R}}\rvert^{+1\sigma/+2\sigma}_{-1\sigma/-2\sigma}$	Observed limit on c_{R}^{Wb}	Expected limit on $c_{\mathrm{R}}^{Wb\,+1\sigma/+2\sigma}_{\quad -1\sigma/-2\sigma}$
800	0.17	$0.20\,^{0.04/0.08}_{0.03/0.05}$	0.24	$0.28\,^{0.05/0.12}_{0.04/0.07}$
900	0.18	$0.19\,^{0.04/0.08}_{0.03/0.05}$	0.26	$0.27\,^{0.05/0.11}_{0.04/0.07}$
1000	0.17	$0.17\,^{0.03/0.07}_{0.03/0.05}$	0.25	$0.25\,^{0.04/0.10}_{0.04/0.07}$
1100	0.17	$0.18\,^{0.03/0.07}_{0.03/0.05}$	0.24	$0.25\,^{0.05/0.10}_{0.04/0.07}$
1200	0.17	$0.20\,^{0.04/0.08}_{0.03/0.05}$	0.25	$0.28\,^{0.05/0.11}_{0.04/0.08}$
1300	0.19	$0.22\,^{0.04/0.09}_{0.03/0.06}$	0.27	$0.31\,^{0.06/0.12}_{0.05/0.08}$
1400	0.24	$0.25\,^{0.05/0.10}_{0.04/0.07}$	0.35	$0.36\,^{0.06/0.14}_{0.05/0.10}$
1500	0.31	$0.28\,^{0.05/0.11}_{0.04/0.07}$	0.44	$0.39\,^{0.07/0.15}_{0.06/0.11}$
1600	0.45	$0.37\,^{0.08/0.19}_{0.06/0.10}$	0.64	$0.53\,^{0.11/0.27}_{0.08/0.14}$
1700	0.59	$0.46\,^{0.10/0.25}_{0.08/0.13}$	0.83	$0.65\,^{0.15/0.36}_{0.11/0.18}$
1800	0.55	$0.43\,^{0.09/0.22}_{0.07/0.12}$	0.77	$0.61\,^{0.13/0.32}_{0.10/0.17}$

Table 8.4.: Observed and expected 95% CL upper limits on $\lvert\sin\theta_{\mathrm{R}}\rvert$ and c_{R}^{Wb} for a right-handed Y quark in a (B, Y) doublet model with masses of 800 GeV to 1800 GeV with the $\pm1\sigma$ and $\pm2\sigma$ uncertainties in the expected limits.

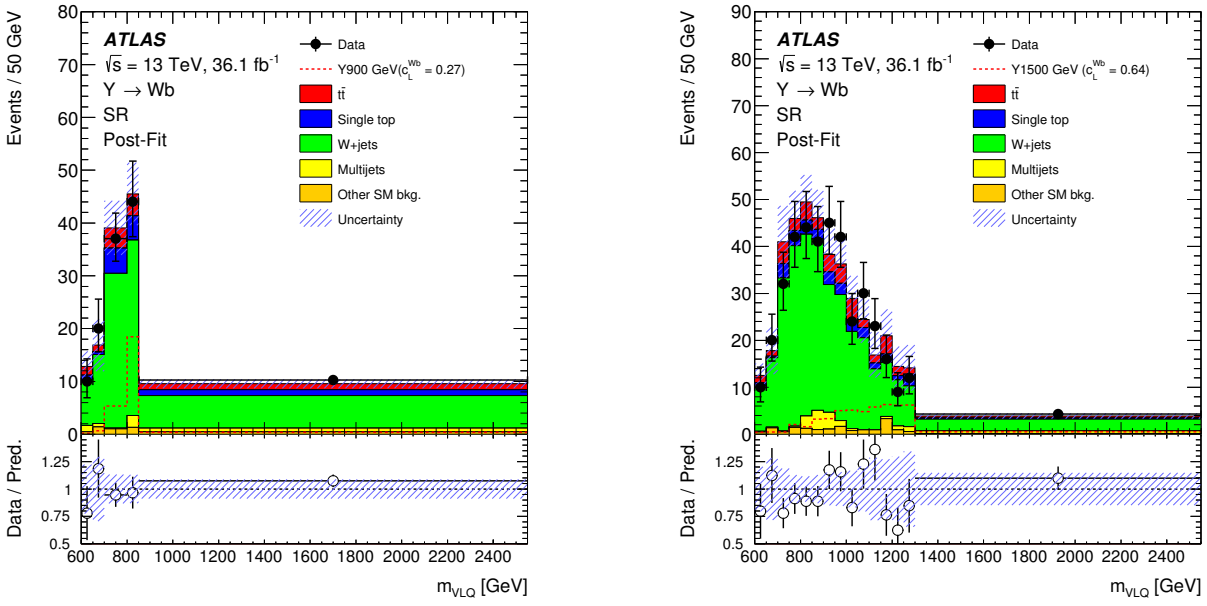

(a)

(b)

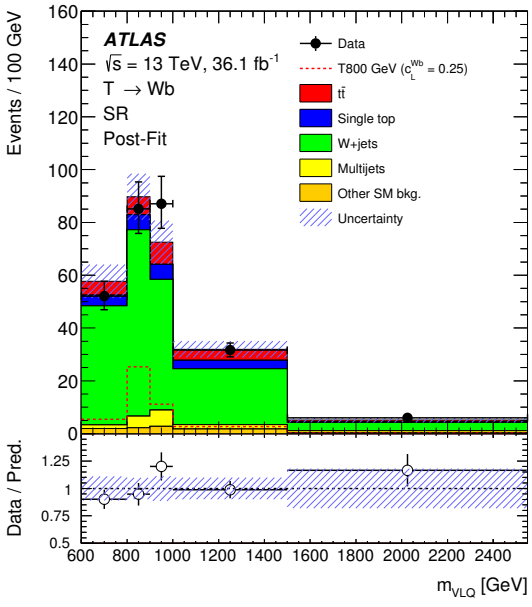

(c)

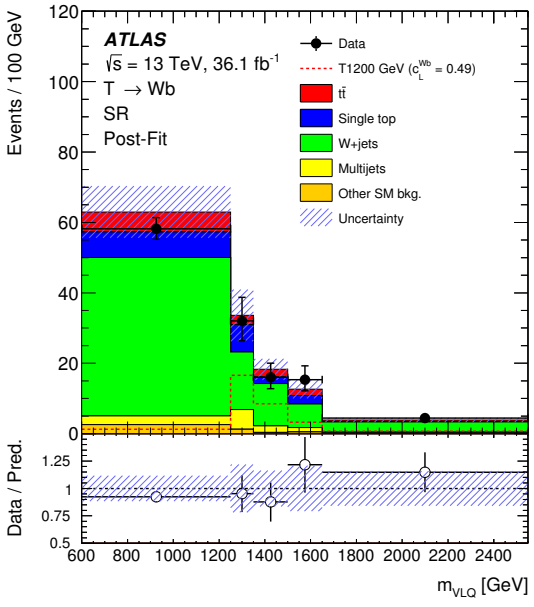

(d)

Figure 8.4.: Post-fit VLQ candidate mass distribution, m_{VLQ}, of the SM prediction for four different binning as given in Table 8.1 with the corresponding signal distribution. In Fig. (a) a left-handed Y signal with mass 900 GeV and coupling $c_{\mathrm{L}}^{Wb} = 0.27$, in (b) a left-handed Y signal with mass 1500 GeV and coupling $c_{\mathrm{L}}^{Wb} = 0.64$, in Fig. (c) a left-handed T signal with mass of 800 GeV and coupling $c_{\mathrm{L}}^{Wb} = 0.25$ and in Fig. (d) a left-handed T signal with mass 1200 GeV and coupling $c_{\mathrm{L}}^{Wb} = 0.49$ are shown, where always interference is considered. The lower panels show the ratio of data to the fitted background yields. The error bars represent the statistical uncertainty in the data, whereas the band represents the total post-fit systematic uncertainty.

Y mass [GeV]	Observed limit on $\lvert\sin\theta_{\mathrm{L}}\rvert$	Expected limit on $\lvert\sin\theta_{\mathrm{L}}\rvert^{+1\sigma/+2\sigma}_{-1\sigma/-2\sigma}$	Observed limit on c_{L}^{Wb}	Expected limit on $c_{\mathrm{L}}^{Wb\,+1\sigma/+2\sigma}_{\quad -1\sigma/-2\sigma}$
800	0.16	$0.20\,^{0.04/0.09}_{0.03/0.05}$	0.31	$0.40\,^{0.08/0.19}_{0.06/0.11}$
900	0.14	$0.15\,^{0.03/0.07}_{0.02/0.04}$	0.28	$0.30\,^{0.06/0.13}_{0.05/0.08}$
1000	0.16	$0.15\,^{0.03/0.06}_{0.02/0.04}$	0.32	$0.29\,^{0.05/0.12}_{0.04/0.08}$
1100	0.23	$0.22\,^{0.03/0.08}_{0.03/0.06}$	0.47	$0.43\,^{0.07/0.15}_{0.07/0.12}$
1200	0.20	$0.16\,^{0.03/0.07}_{0.02/0.04}$	0.40	$0.33\,^{0.06/0.13}_{0.05/0.09}$
1300	0.25	$0.21\,^{0.04/0.08}_{0.03/0.06}$	0.49	$0.43\,^{0.08/0.16}_{0.07/0.12}$
1400	0.18	$0.25\,^{0.05/0.10}_{0.04/0.07}$	0.36	$0.51\,^{0.09/0.20}_{0.08/0.14}$
1500	0.32	$0.35\,^{0.08/0.18}_{0.06/0.10}$	0.64	$0.70\,^{0.16/0.37}_{0.12/0.20}$
1600	0.39	$0.40\,^{0.11/0.28}_{0.07/0.12}$	0.78	$0.80\,^{0.21/0.56}_{0.14/0.24}$

Table 8.5.: Observed and expected 95% CL upper limits on $\lvert\sin\theta_{\mathrm{L}}\rvert$ and c_{L}^{Wb} for a left-handed Y quark in a (T, B, Y) triplet model with masses of 800 GeV to 1600 GeV with the $\pm1\sigma$ and $\pm2\sigma$ uncertainties in the expected limits.

Interference effects for the Y quark in a (B, Y) doublet model are very small. This means that the difference between the signal+interference template and the template without considering interference is very small. Thus, a signal interpretation as a pure VLQ resonance is meaningful in this case and therefore a limit on $\sigma_{\mathrm{VLQ}} + \sigma_{\mathrm{I}}$ times branching ratio is presented in Figure 8.6, which correspond to the $|\sin\theta_{\mathrm{R}}|$ and c_{R}^{Wb} presented in Figure 8.5(c). From this, it is also possible to compute a observed (expected) lower mass limit, which is found to be about 1.64 TeV (1.80 TeV) for a right-handed coupling value of $c_{\mathrm{R}}^{Wb} = 1/\sqrt{2}$.

To see from which systematic uncertainties this analysis suffers most and, thus, to evaluate where future improvements would be most promising, in Figs. 8.7 and 8.8, ranking plots of the uncertainties are presented for right-handed Y signals with a mass of 1200 GeV and 900 GeV respectively. The most important systematics stem from the modelling of the background samples, especially the generator choice. Furthermore, the fit was repeated with statistical uncertainties only, which revealed that the remaining uncertainty of the signal strength μ is significantly smaller than with considering systematic uncertainties. Therefore, it can be concluded that this search is dominated by systematic uncertainties.

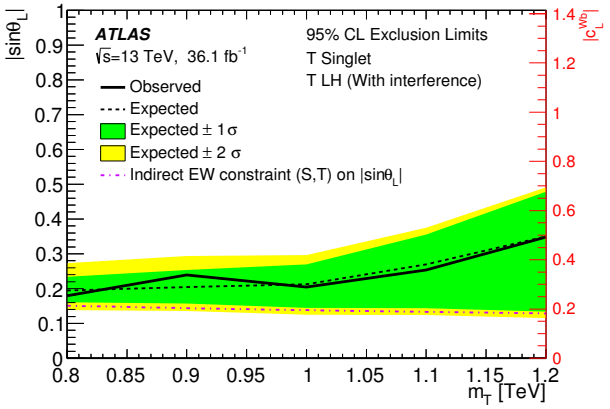

(a)

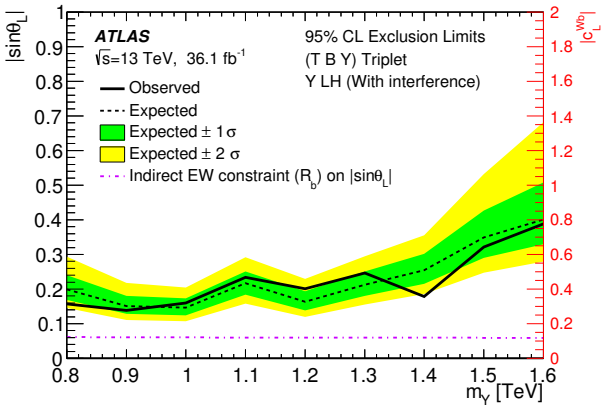

(b)

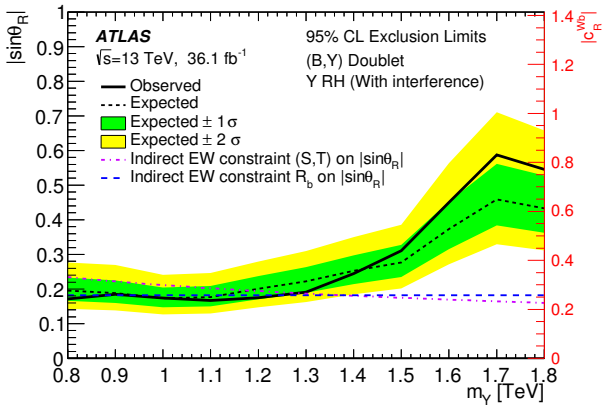

(c)

Figure 8.5.: Observed (solid line) and expected (short-dashed line) 95% CL limits on the mixing angle $|\sin\theta_{\mathrm{L}}|$ and the coupling c_{L}^{Wb} for a singlet T-quark model (a), $|\sin\theta_{\mathrm{L}}|$ and c_{L}^{Wb} for a (T, B, Y) triplet model (b) and $|\sin\theta_{\mathrm{R}}|$ and c_{R}^{Wb} for a (B, Y) doublet model (c), as a function of the VLQ mass, where the corresponding excluded region is given by the area above. The green and yellow band correspond to ± 1 and ± 2, respectively, standard deviations around the expected limit. Constraints for the mixing angles from electroweak precision observables from either the S and T parameters (dashed-dotted line) or from the R_b values (long-dashed line) taken from Ref. [41] are also shown.

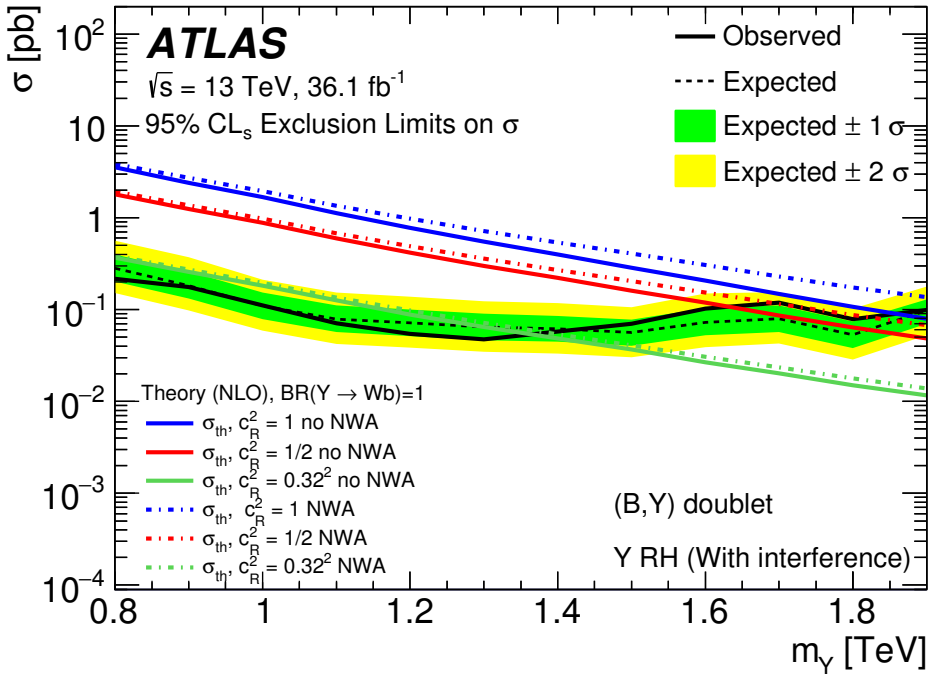

Figure 8.6.: Observed (solid line) and expected (short-dashed line) 95% CL limits on cross-section times branching ratio for a right-handed Y quark in a (B, Y) doublet model as a function of VLQ mass. The theoretical NLO cross-sections predictions for $c_R^2 = 1$ (blue), $c_R^2 = 1/2$ (red) and $c_R^2 = 0.32^2$ (green) using the narrow-width approximation (dashed-dotted lines) and using no narrow-width approximation (solid lines) are given as well.

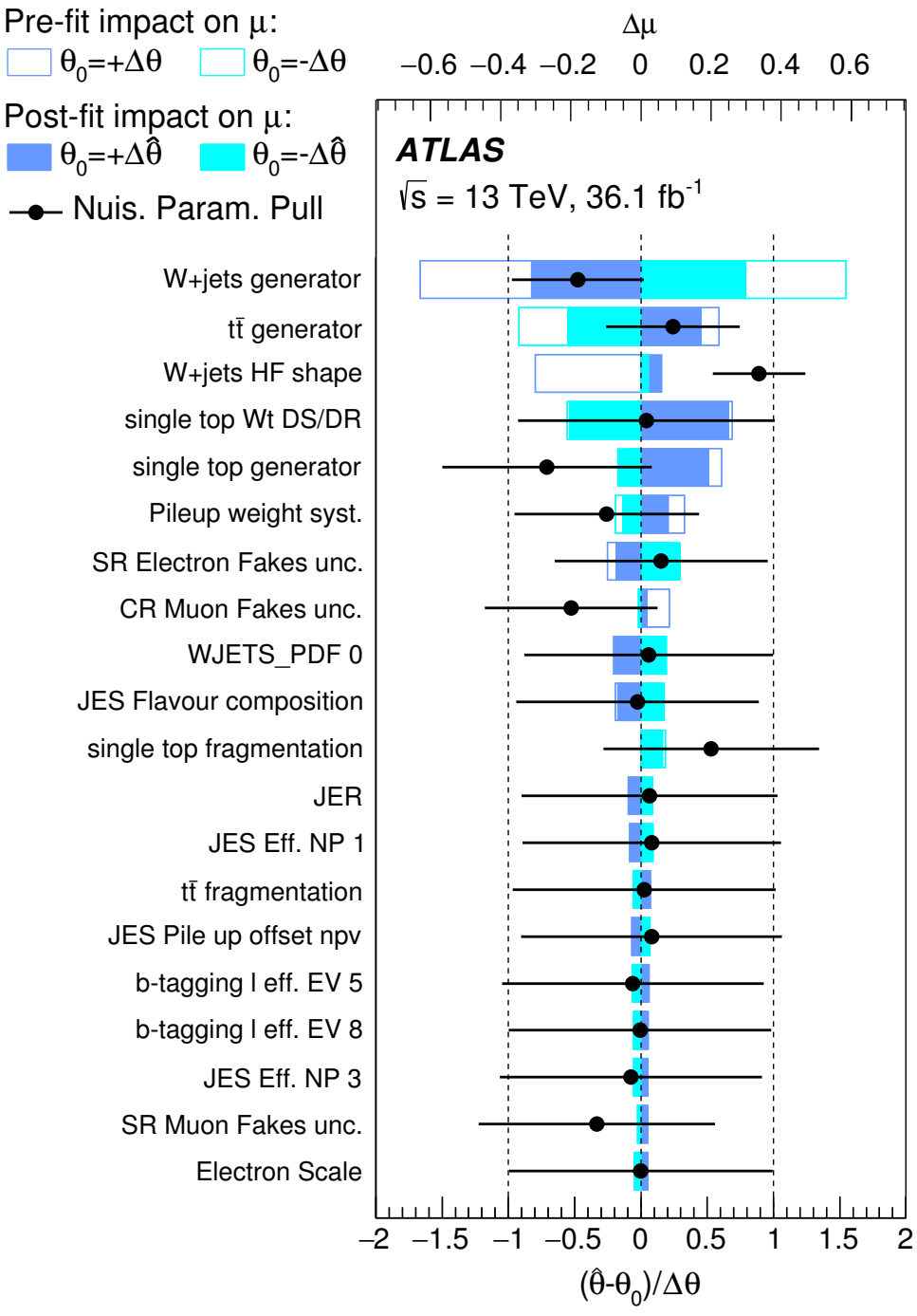

Figure 8.7.: Ranking plot corresponding to a signal-plus-background fit on data for a right-handed Y signal of mass 1200 GeV with interference and with coupling of $c_R^{\mathrm{Wb}} \approx 0.28$ where the signal was injected. The fitted signal strength μ for a fit including both systematic and statistical uncertainties and only statistical uncertainties for the aforementioned signal is $\mu = -0.50 \pm 0.70$ and $\mu = -0.10 \pm 0.42$, respectively.

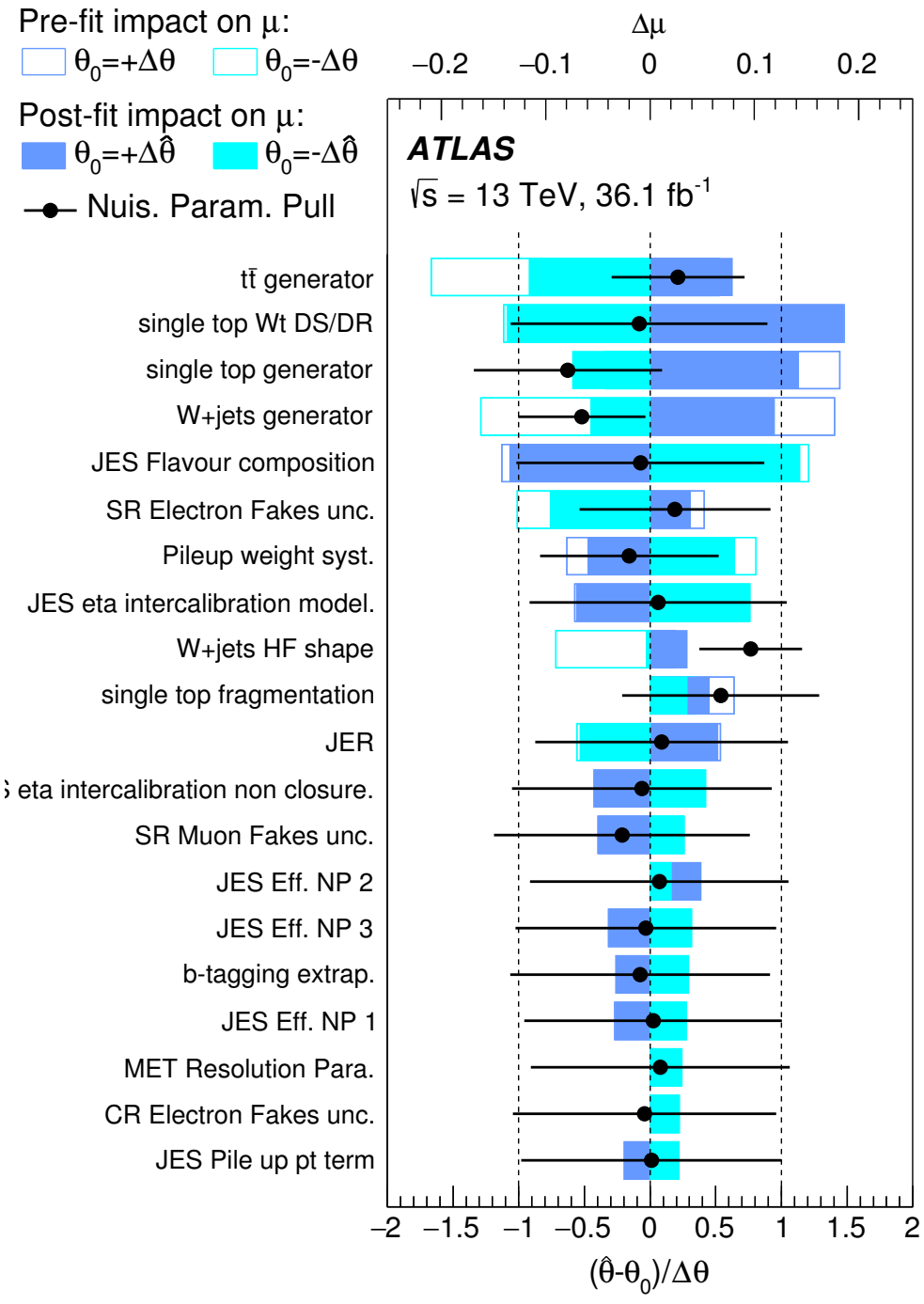

Figure 8.8.: Ranking plot corresponding to a signal-plus-background fit on data for a right-handed Y signal of mass 900 GeV with interference and with coupling of $c_R^{\mathrm{Wb}} \approx 0.27$ where the signal was injected. The fitted signal strength μ for a fit including both systematic and statistical uncertainties and only statistical uncertainties for the aforementioned signal is $\mu = -0.11 \pm 0.48$ and $\mu = -0.12 \pm 0.28$, respectively.

Chapter 9.

Summary

This thesis presents a search for the production of a single vector-like quark Y or T with the ATLAS detector at the LHC. Vector-like quarks are fermionic colour triplets predicted by several BSM theories such as little Higgs models or composite Higgs models. These particles couple via a vector-current to the W bosons and are thus not forced to acquire their mass by the Higgs mechanism. There have been several other VLQ searches carried out by the ATLAS and CMS collaborations, which have set upper limits on the VLQ masses, thus VLQs are known to be heavy, if they exist.

The presented analysis corresponds to the 36.1 fb^{-1} of proton–proton collisions data set recorded in 2015 and 2016 by ATLAS. The event selection is designed for VLQ t-channel production and $Y/T \to Wb$ decays with subsequently leptonically decaying W boson. Thus, the signal region selection requires exactly one isolated electron or muon, a high p_{T} b-tagged jet, missing transverse momentum and at least one forward jet. The modelling of the main backgrounds, W+jets and $t\bar{t}$ production, is checked and improved in dedicated control regions and the final results are obtained with a maximum-likelihood fit in the binned distribution of the reconstructed mass of the vector-like quark candidate. Since the observed data distributions are compatible with the Standard Model background prediction and no significant excess is observed, upper 95% CL limits on the mixing angle as well as coupling strength for several benchmark interpretations are determined with the CL_{s} method. The interpretation is done in terms of a T-singlet model as well as in terms of a (B, Y) doublet and (T, B, Y) triplet model, respectively. Hereby, interference effects with the Standard Model background are taken into account.

For the T-singlet model, the best upper exclusion limits on $|\sin\theta_{\text{L}}|$ (c_{L}^{Wb}) are found for a mass of 800 GeV and are as small as 0.18 (0.25). In a (B, Y) doublet, the upper exclusion

limit on $|\sin\theta_{\mathrm{R}}|$ (c_{R}^{Wb}) range from 0.17 (0.24) for a mass of 800 GeV to 0.55 (0.77) for Y quarks with a mass of 1800 GeV. The upper exclusion limits on $|\sin\theta_{\mathrm{L}}|$ (c_{L}^{Wb}) in a (T, B, Y) triplet vary between 0.16 (0.31) and 0.39 (0.78) for Y-signal masses between 800 GeV and 1600 GeV. The observed limits of the mixing angle for the (B, Y) doublet model are competitive with indirect bounds from electro-weak precision observables in the mass range of 800 GeV to 1250 GeV. Since in the (B, Y) doublet case interference effects are very small, also observed (expected) lower mass limits are determined and found to be about 1.64 TeV (1.80 TeV) for a right-handed coupling value of $c_{\mathrm{R}}^{Wb} = 1/\sqrt{2}$.

Even though no BSM effects are observed, this thesis represents a significant progress in narrowing down the phase-space for new physics. If the theories predicting VLQs should provide any insight to the mechanism of electro-weak symmetry breaking, not too large masses are required as described in Section 2.4. As mass exclusion limits approach the two TeV region, their discovery should be right around the corner, perhaps in the upcoming LHC Run-3.

Appendix

Appendix I.

Additional Information about the Reweighting Procedure

As mentioned in Section 4.3, the final target couplings used in the reweighting procedure need to be determined iteratively until convergence is reached. The final coupling values used for the limit determination are given in Table I.1.
A comparison of signal distributions using different settings for the reweighting can be found in Fig. I.1 and Fig. I.2.

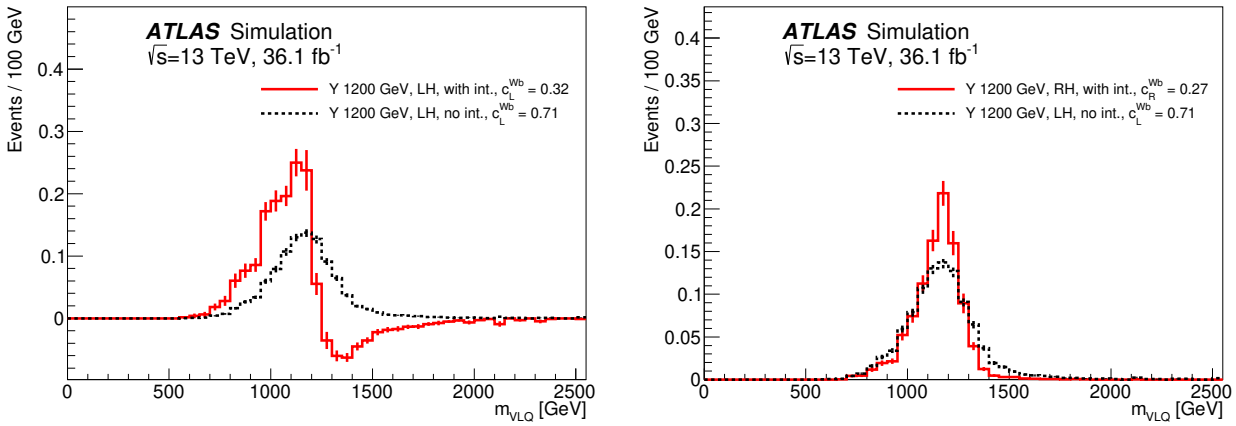

(a) (b)

Figure I.1.: In Fig. (a) a comparison between m_{VLQ} in the SR for a Y signal with $c_{\mathrm{L}}^{Wb} \approx 0.71$ without considering interference effects (dashed black line) with a Y signal with $c_{\mathrm{L}}^{Wb} \approx 0.32$ with considering interference (solid red line), both with $m = 1.2$ TeV is presented. In Fig. (b) the shape of a Y signal with coupling $c_{\mathrm{L}}^{Wb} \approx 0.71$ (dashed black line) is compared with a Y signal with $c_{\mathrm{R}}^{Wb} \approx 0.27$ (solid red line), both with a mass of 1.2 TeV and with considering interference effects. The distributions for a right- and left-handed Y signal without considering interference effects are identical.

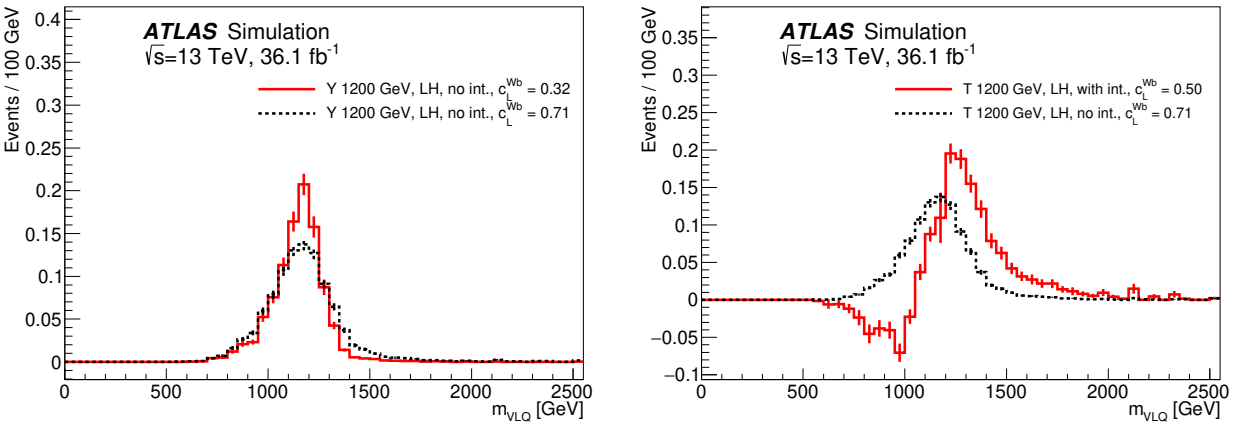

(a) (b)

Figure I.2.: In Fig. (a) a comparison between m_{VLQ} in the SR for a Y signal with $c_{\mathrm{L}}^{Wb} \approx 0.71$ (dashed black line) with a Y signal with $c_{\mathrm{L}}^{Wb} \approx 0.32$ (solid red line), both with $m = 1.2$ TeV and without considering interference effects, is presented. In Fig. (b) the shape of a T signal with coupling $c_{\mathrm{L}}^{Wb} \approx 0.71$ without considering interfernce (dashed black line) is compared with a T signal with $c_{\mathrm{L}}^{Wb} \approx 0.5$ with interference (solid red line), both with a mass of 1.2 TeV.

Q Signal	mass in [GeV]	κ
T	800 GeV	0.275
T	900 GeV	0.285
T	1000 GeV	0.298
T	1100 GeV	0.377
T	1200 GeV	0.495
Y LH	800 GeV	0.272
Y LH	900 GeV	0.213
Y LH	1000 GeV	0.204
Y LH	1100 GeV	0.296
Y LH	1200 GeV	0.227
Y LH	1300 GeV	0.295
Y LH	1400 GeV	0.333
Y LH	1500 GeV	0.477
Y LH	1600 GeV	0.554
Y RH	800 GeV	0.194
Y RH	900 GeV	0.187
Y RH	1000 GeV	0.171
Y RH	1100 GeV	0.173
Y RH	1200 GeV	0.194
Y RH	1300 GeV	0.221
Y RH	1400 GeV	0.252
Y RH	1500 GeV	0.276
Y RH	1600 GeV	0.368
Y RH	1700 GeV	0.532
Y RH	1800 GeV	0.468
Y RH	1900 GeV	0.767

Table I.1.: Summary of the coupling results of the iterative process: couplings κ used for the right-handed (RH) Y, left-handed (LH) Y and T template production.

Appendix II.

Fastsim-Fullsim Comparison for a Y Signal-Cutflow

Some of the signal MC samples were processed with a faster detector simulation (fastsim) making use of parameterised showers in the calorimeters. Figure II.1 till II.4 compare the m_{VLQ} distribution for a Y-signal sample of mass 1800 GeV simulated with AFII (black line) to the corresponding fullsim sample (red line) after applying the analysis selection cuts as discussed in Section 6.1.

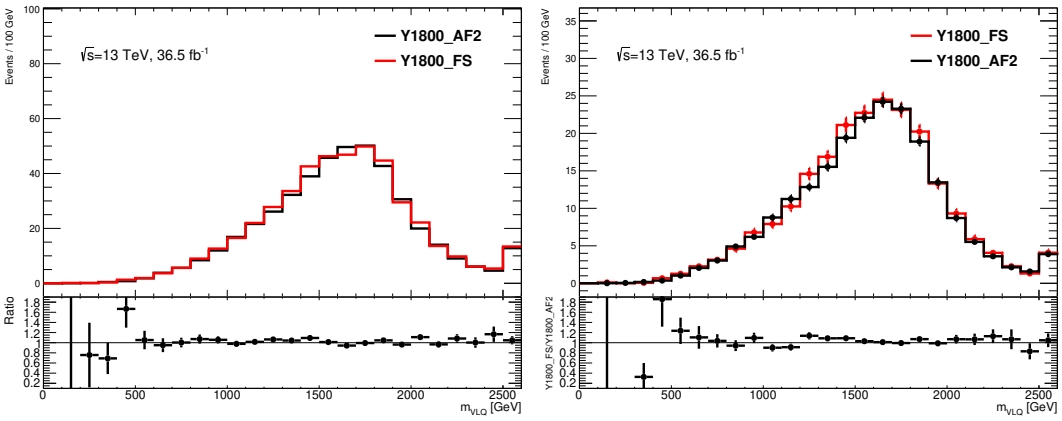

Figure II.1.: Distribution of the invariant mass m_{VLQ} for a Y-signal sample of mass 1800 GeV simulated with AFII (black line) and the corresponding Fullsim sample (red line) after the pre-selection (left plot) and requiring that the leading jet is a b-tagged jet (right plot). The errors attached to the points in the bottom plot are the corresponding statistical errors.

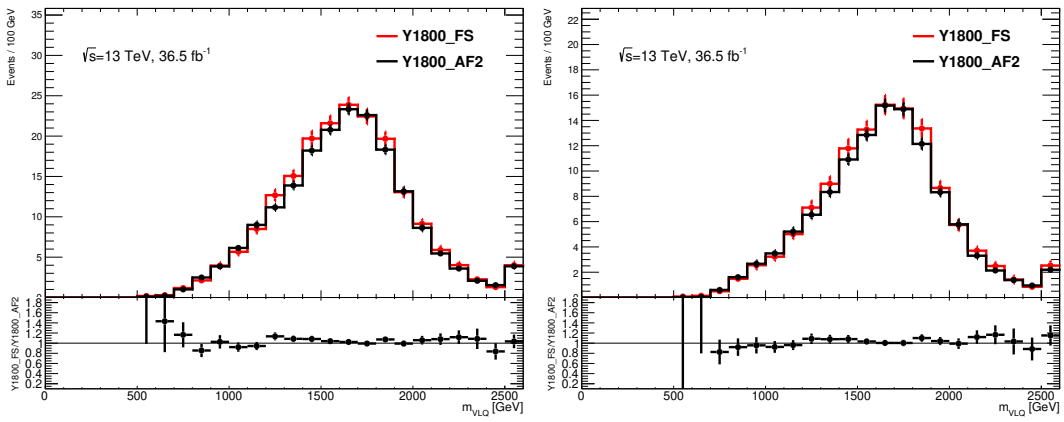

Figure II.2.: Distribution of the invariant mass m_{VLQ} for a Y-signal sample of mass 1800 GeV simulated with AFII (black line) and the corresponding fullsim sample (red line) after the pre-selection and cuts (a) and (b) (left plot) and after the pre-selection and cuts (a)–(c). The errors attached to the points in the bottom plot are the corresponding statistical errors.

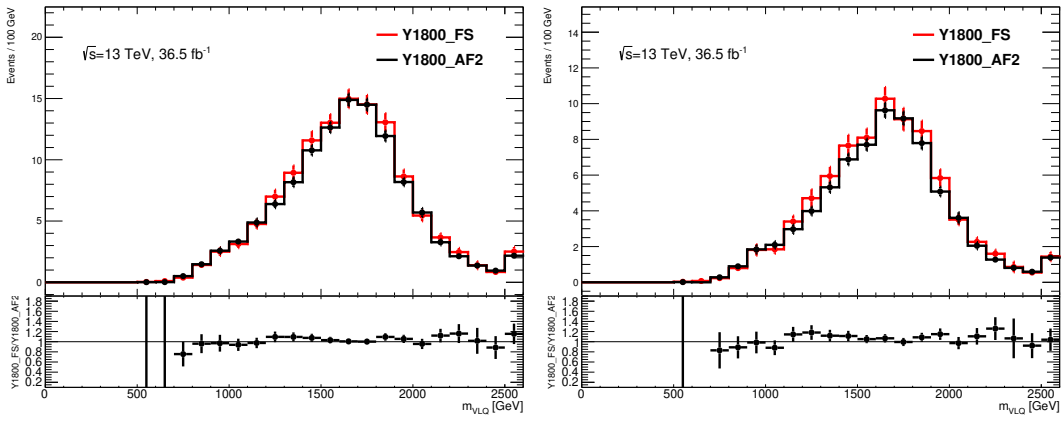

Figure II.3.: Distribution of the invariant mass m_{VLQ} for a Y-signal sample of mass 1800 GeV simulated with AFII (black line) and the corresponding fullsim sample (red line) after the pre-selection and cuts (a)–(d) (left plot) and after the pre-selection and cuts (a)–(e) (right plot). The errors attached to the points in the bottom plot are the corresponding statistical errors.

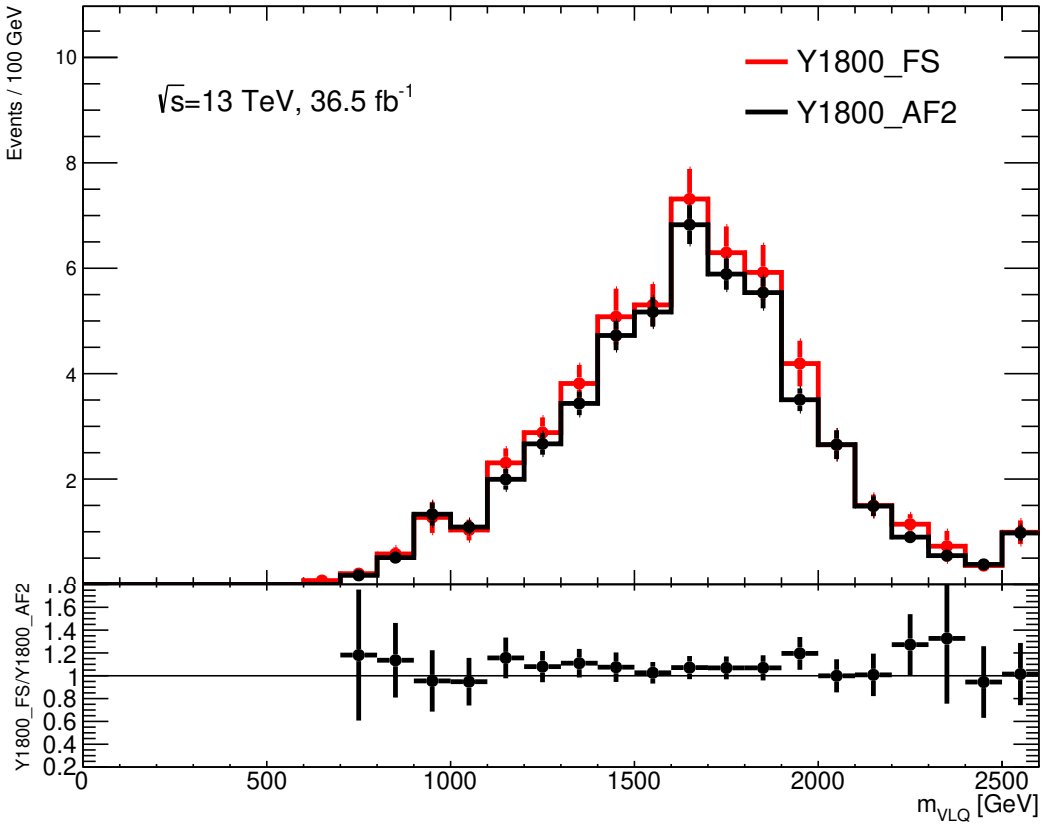

Figure II.4.: Distribution of the invariant mass m_{VLQ} for a Y-signal sample of mass 1800 GeV simulated with AFII (black line) and the corresponding fullsim sample (red line) in the signal region. The errors attached to the points in the bottom plot are the corresponding statistical errors.

Appendix III.

Additional Figures for the Multijet Background Estimate

Different parameterisation have been tested in the multijet validation region and the data is compared to the simulation for different kinematic distributions. As an example, in Figure III.1, III.2, III.3 and III.4 the lepton transverse momentum p_T, missing transverse energy E_T^{miss}, transverse W-boson mass $m_T(\ell, E_{\text{T}}^{\text{miss}})$ and invariant mass m_{VLQ} distribution of the vector-like quark candidate in the multijet validation region using the lepton p_T parameterisation are shown. Comparing the same distributions where the jet p_T parameterisation was used (see Figure 4.2 till Figure 4.4) it can be seen that the data-MC disagreement is much worse using the lepton p_T parametrisation.

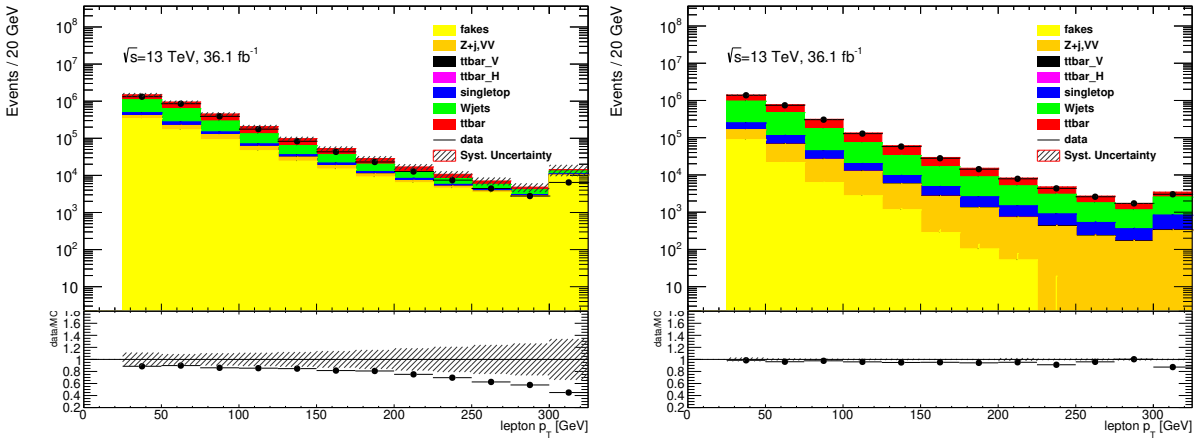

(a) (b)

Figure III.1.: Lepton p_T distribution in the multijet validation region in the electron channel V.2(a) and in the muon channel V.2(b). The shaded band depicts the statistical uncertainty and a 50% normalisation uncertainty of the multijet estimate.

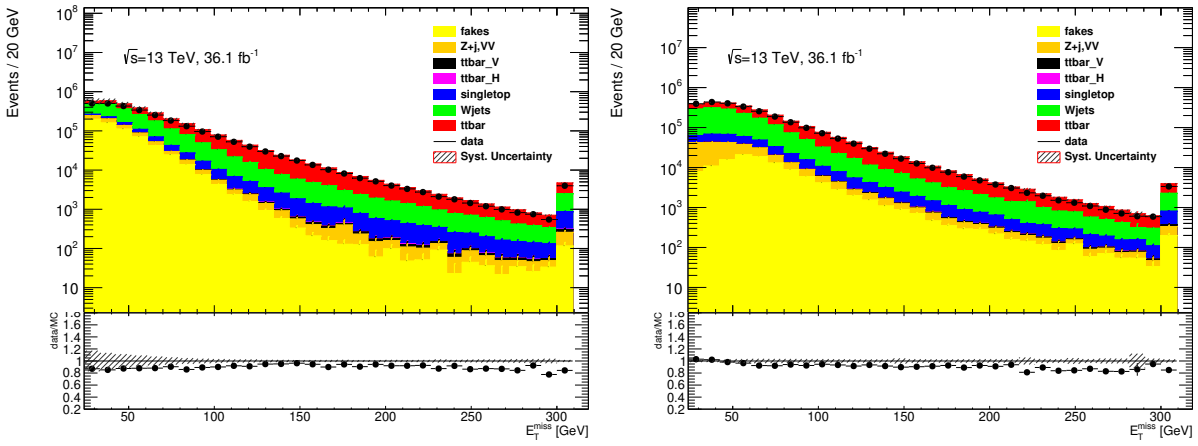

(a) (b)

Figure III.2.: E_T^{miss} distribution in the multijet validation region in the electron channel III.2(a) and in the muon channel III.2(b). The shaded band depicts the statistical uncertainty and a 50% normalisation uncertainty of the multijet estimate.

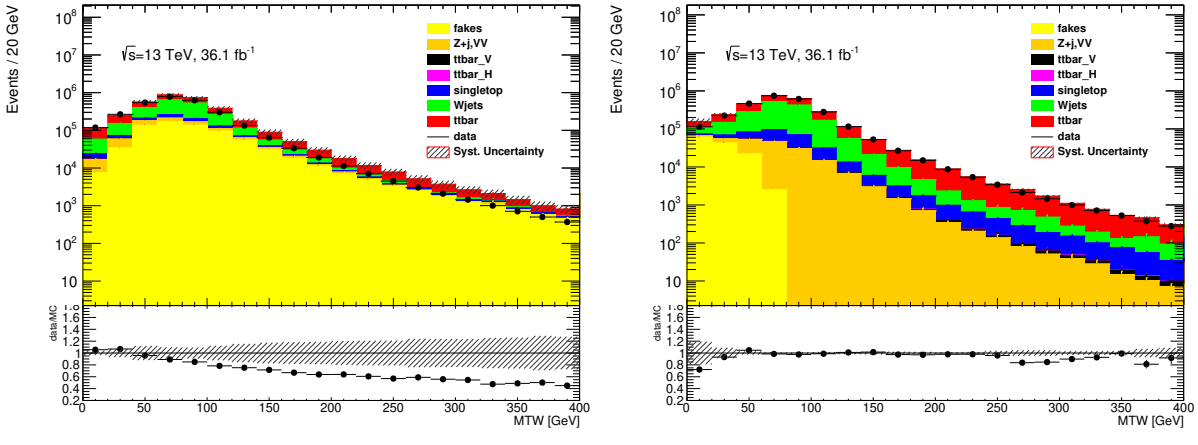

(a) (b)

Figure III.3.: Transverse W mass $m_T(\ell, E_{\text{T}}^{\text{miss}})$ distribution in the multijet validation region in the electron channel III.3(a) and in the muon channel III.3(b). The shaded band depicts the statistical uncertainty and a 50% normalisation uncertainty of the multijet estimate.

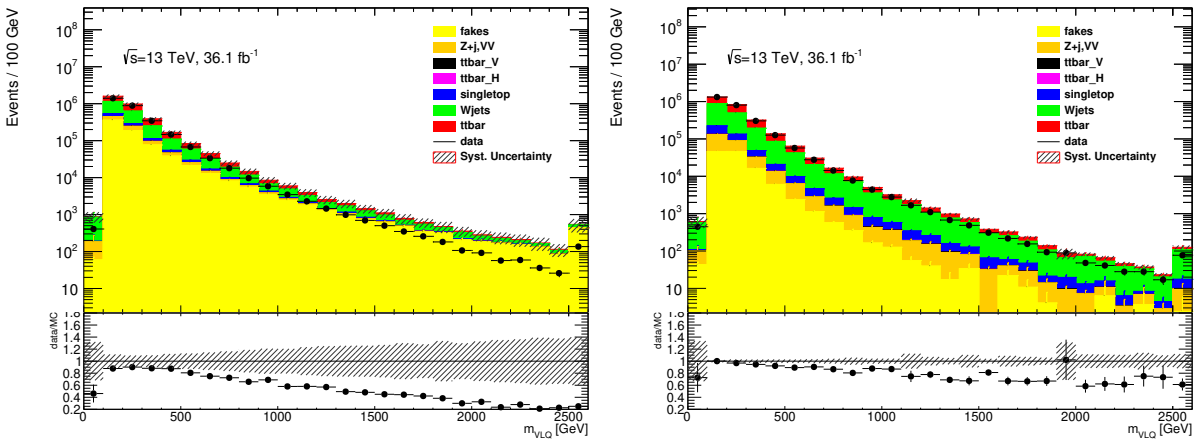

(a) (b)

Figure III.4.: Invariant mass distribution of vector-like quark candidate m_{VLQ} in the multijet validation region in the electron channel III.4(a) and in the muon channel III.4(b). The shaded band depicts the statistical uncertainty and a 50% normalisation uncertainty of the multijet estimate.

Appendix IV.

Limits without Interference

The cross-section limits for a Y quark without considering interference effects in comparison with three theoretical benchmark predictions with and without using the narrow-width approximation are depicted in Fig. IV.1 and the corresponding numbers are given in Table IV.1.

Q Signal	Observed limit on $\sigma \times$ BR [pb]	-2σ	-1σ	Expected limit on $\sigma \times$ BR [pb]	+1σ	+2σ
800 GeV	0.19	0.11	0.07	0.24	0.10	0.22
900 GeV	0.18	0.09	0.06	0.20	0.09	0.21
1000 GeV	0.14	0.06	0.03	0.12	0.05	0.11
1100 GeV	0.08	0.04	0.03	0.09	0.04	0.09
1200 GeV	0.07	0.04	0.02	0.09	0.04	0.08
1300 GeV	0.08	0.04	0.03	0.09	0.04	0.08
1400 GeV	0.09	0.04	0.02	0.09	0.03	0.07
1500 GeV	0.10	0.03	0.02	0.08	0.03	0.07
1600 GeV	0.12	0.04	0.03	0.09	0.04	0.09
1700 GeV	0.09	0.03	0.02	0.06	0.03	0.06
1800 GeV	0.06	0.03	0.02	0.06	0.03	0.06
1900 GeV	0.08	0.03	0.02	0.06	0.03	0.06
2000 GeV	0.07	0.03	0.02	0.08	0.03	0.06

Table IV.1.: Observed and expected 95% CL upper limits on the production cross-section times branching ratio ($\sigma \times$ BR) for various Q signals with masses of 800 GeV to 2000 GeVwithout considering interference effects. The 68% and 95% confidence intervals around the expected limits under are also provided, denoted by $\pm 1\sigma$ and $\pm 2\sigma$, respectively.

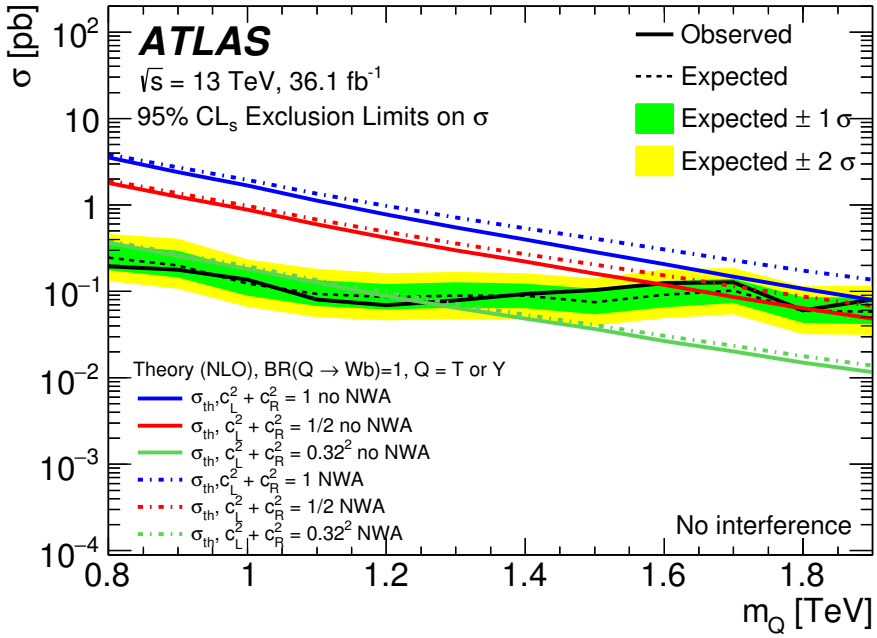

Figure IV.1.: Expected (dashed black line) and observed (solid black line) 95% limits on cross-section times branching fraction for a vector-like Y or T quark without considering interference. The blue, red and green lines show the theoretical cross-section predictions for a coupling of $\sqrt{c_L^2 + c_R^2} = 1$ (blue), $1/\sqrt{2}$ (red) and 0.32 (green), respectively, where the branching ratio was set to one. For the dotted theory lines no correction for a narrow-width approximation has been applied. The surrounding shaded bands correspond to ± 1 and ± 2 standard deviations around the expected limit.

Figure IV.2 compares the expected (dashed orange and black line) and observed (solid orange and black line) 95% CL cross-section times branching ratio limits for the case of the right-handed Y (orange line) where interference was considered and for a VLQ Q (black line) as a function of VLQ mass for a no-interference case. The theoretical NLO cross sections for different coupling values are shown for the calculation using narrow-width approximation (blue, red and green dashed-dotted lines) and without using narrow-width approximation (blue, red and green solid lines)

However, it should be noted that results without considering interference are not physically meaningful and are only presented for a comparison with results of other analyses.

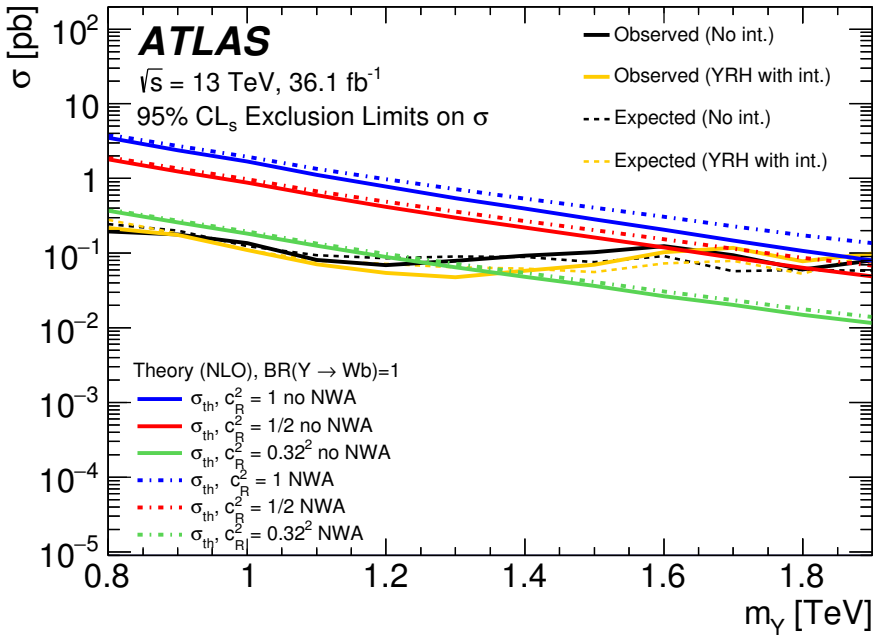

Figure IV.2.: Expected (dashed orange and black line) and observed (solid orange and black line) 95% CL cross-section times branching ratio limits for the case of the right-handed Y (red line) with considering interference and for a VLQ Q quark (black line) without considering interference as a function of m_{VLQ}. The theoretical NLO cross sections for different coupling values with (blue, red and green dashed-dotted lines) and without (blue, red and green solid lines) using narrow-width approximation are given as well.

Appendix V.

Additional Information about the Fit

Figure V.1 ($t\bar{t}$ and W+jets normalisation factors) and V.2 (nuisance parameter) compare the results of a fit to data in the control regions (black lines) to the results of a fit to data in the signal and control regions (red lines) for the background-only hypothesis. The results are consistent in pulls and constraints. The post-fit scale factors for the $t\bar{t}$ and W+jets backgrounds agree well within their uncertainties. For the nuisance parameter there is a small difference for the jet p_{T} W+jet reweighting parameter which is expected, because for a fit to the control region only the W+jet background is mainly constraint by the W+jets control region only.
Figure V.3 shows the correlation matrix among the nuisance for the fit to data in the signal and control regions for the background-only hypothesis.

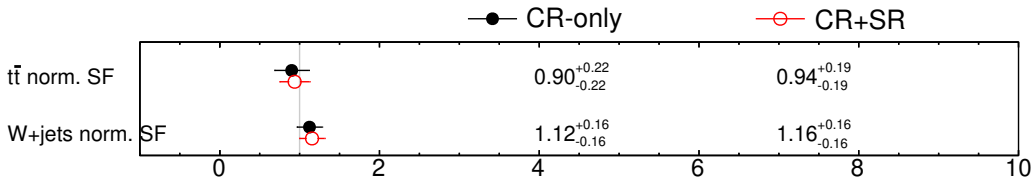

Figure V.1.: Comparison of the post-fit scale factors of all major backgrounds extracted from a fit to data in the control regions only (black line) with the factors from a fit to data in the signal and control regions (red line) for the background-only hypothesis.

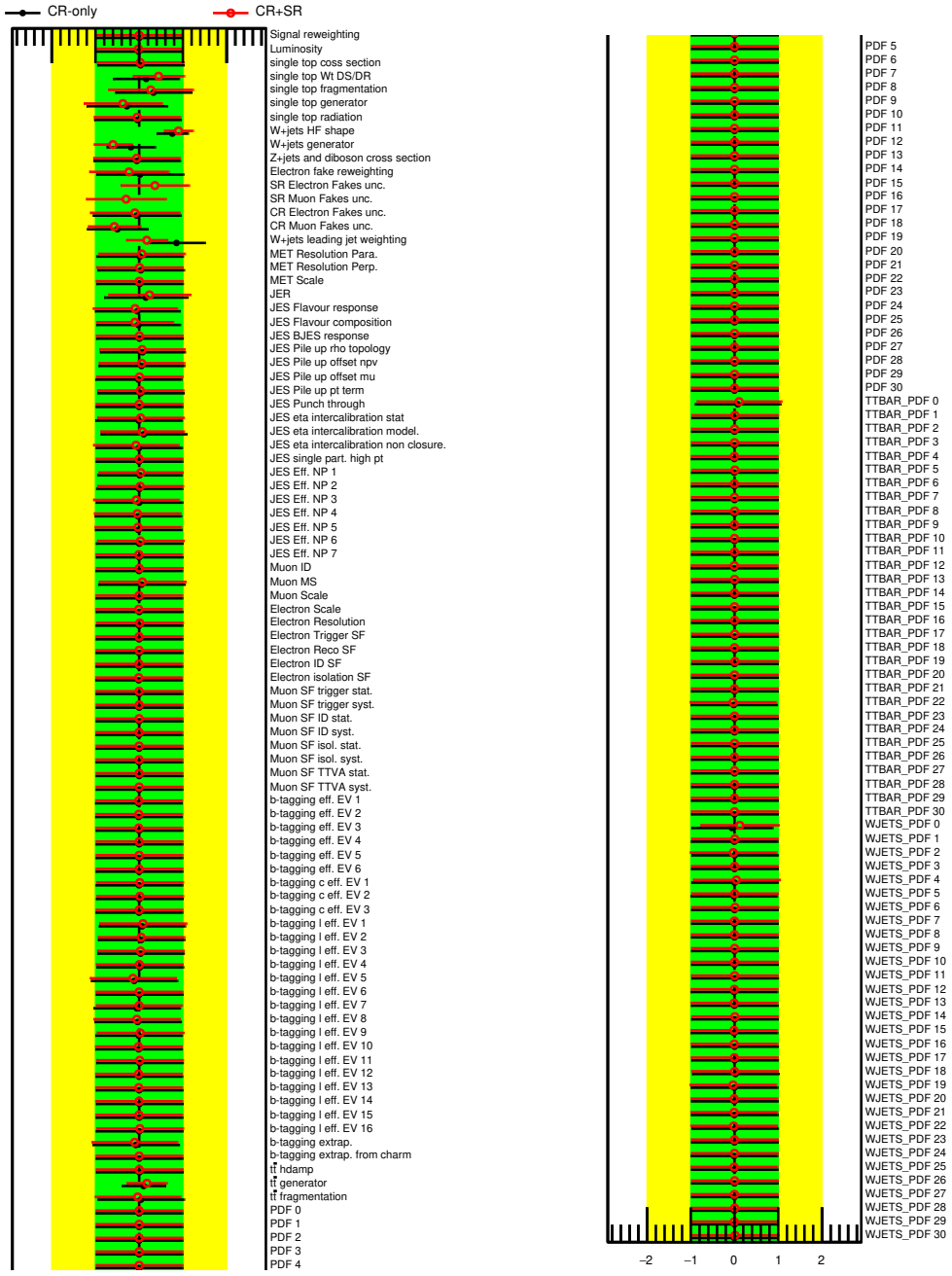

(a) (b)

Figure V.2.: Comparison of the fitted nuisance parameters for a fit to data in the control regions only (black line) with the nuisance parameters for a fit to data in the signal and control regions (red line) for the background-only hypothesis. The scale-factor of $t\bar{t}$ and W+jets backgrounds are used as free-parameters.

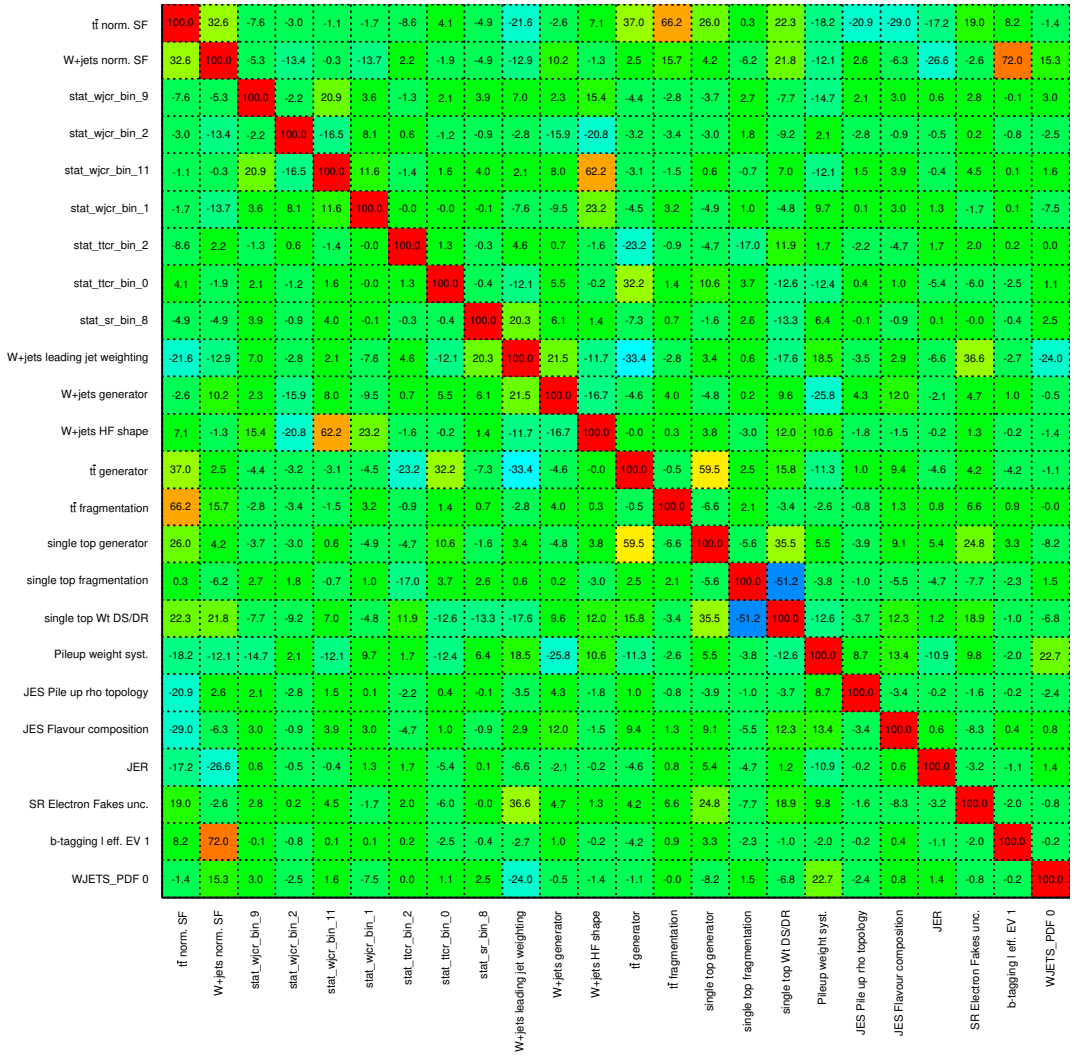

Figure V.3.: Correlation matrix among the nuisance parameters for a fit to data in the signal and control regions for the background-only hypothesis.

Appendix VI.

List of the Datasets used in the Analysis

Table VI.1.: List of MC15 datasets used for the background and signal estimates.

Sample	Name
data samples	data15_13TeV.periodD.physics_Main.PhysCont.DAOD_{}.grp15_v01_p2950
	data15_13TeV.periodE.physics_Main.PhysCont.DAOD_{}.grp15_v01_p2950
	data15_13TeV.periodF.physics_Main.PhysCont.DAOD_{}.grp15_v01_p2950
	data15_13TeV.periodG.physics_Main.PhysCont.DAOD_{}.grp15_v01_p2950
	data15_13TeV.periodH.physics_Main.PhysCont.DAOD_{}.grp15_v01_p2950
	data15_13TeV.periodJ.physics_Main.PhysCont.DAOD_{}.grp15_v01_p2950
	data16_13TeV.periodA.physics_Main.PhysCont.DAOD_{}.grp16_v01_p2950
	data16_13TeV.periodB.physics_Main.PhysCont.DAOD_{}.grp16_v01_p2950
	data16_13TeV.periodC.physics_Main.PhysCont.DAOD_{}.grp16_v01_p2950
	data16_13TeV.periodD.physics_Main.PhysCont.DAOD_{}.grp16_v01_p2950
	data16_13TeV.periodE.physics_Main.PhysCont.DAOD_{}.grp16_v01_p2950
	data16_13TeV.periodF.physics_Main.PhysCont.DAOD_{}.grp16_v01_p2950
	data16_13TeV.periodG.physics_Main.PhysCont.DAOD_{}.grp16_v01_p2950
	data16_13TeV.periodI.physics_Main.PhysCont.DAOD_{}.grp16_v01_p2950
	data16_13TeV.periodK.physics_Main.PhysCont.DAOD_{}.grp16_v01_p2950
	data16_13TeV.periodL.physics_Main.PhysCont.DAOD_{}.grp16_v01_p2950
$t\bar{t}$	mc15_13TeV.410000.PowhegPythiaEvtGen_P2012_ttbar_hdamp172p5_nonallhad.merge.DAOD_TOPQ1.e3698_s2608_s2183_r7725_r7676_p2952
	mc15_13TeV.410001.PowhegPythiaEvtGen_P2012radHi_ttbar_hdamp345_down_nonallhad.merge.DAOD_TOPQ1.e3783_s2608_r7725_r7676_p2952
	mc15_13TeV.410002.PowhegPythiaEvtGen_P2012radLo_ttbar_hdamp172_up_nonallhad.merge.DAOD_TOPQ1.e3783_s2608_r7725_r7676_p2952
	mc15_13TeV.410003.aMcAtNloHerwigppEvtGen_ttbar_nonallhad.merge.DAOD_TOPQ1.e4441_s2726_r7772_r7676_p2952
	mc15_13TeV.410004.PowhegHerwigppEvtGen_UEEE5_ttbar_hdamp172p5_nonallhad.merge.DAOD_TOPQ1.e3836_a766_a821_r7676_p2952
Single top	mc15_13TeV.410011.PowhegPythiaEvtGen_P2012_singletop_tchan_lept_top.merge.DAOD_TOPQ1.e3824_s2608_s2183_r7725_r7676_p2952
	mc15_13TeV.410012.PowhegPythiaEvtGen_P2012_singletop_tchan_lept_antitop.merge.DAOD_TOPQ1.e3824_s2608_s2183_r7725_r7676_p2952
	mc15_13TeV.410013.PowhegPythiaEvtGen_P2012_Wt_inclusive_top.merge.DAOD_TOPQ1.e3753_s2608_s2183_r7725_r7676_p2952
	mc15_13TeV.410014.PowhegPythiaEvtGen_P2012_Wt_inclusive_antitop.merge.DAOD_TOPQ1.e3753_s2608_s2183_r7725_r7676_p2952
	mc15_13TeV.410025.PowhegPythiaEvtGen_P2012_SingleTopSchan_noAllHad_top.merge.DAOD_TOPQ1.e3998_s2608_s2183_r7725_r7676_p2952
	mc15_13TeV.410026.PowhegPythiaEvtGen_P2012_SingleTopSchan_noAllHad_antitop.merge.DAOD_TOPQ1.e3998_s2608_s2183_r7725_r7676_p2952
	mc15_13TeV.410017.PowhegPythiaEvtGen_P2012radLo_singletop_tchan_lept_top.merge.DAOD_TOPQ1.e3978_a766_a818_r7676_p2952
	mc15_13TeV.410018.PowhegPythiaEvtGen_P2012radHi_singletop_tchan_lept_top.merge.DAOD_TOPQ1.e3978_a766_a818_r7676_p2952
	mc15_13TeV.410019.PowhegPythiaEvtGen_P2012radLo_singletop_tchan_lept_antitop.merge.DAOD_TOPQ1.e3978_a766_a818_r7676_p2952
	mc15_13TeV.410020.PowhegPythiaEvtGen_P2012radHi_singletop_tchan_lept_antitop.merge.DAOD_TOPQ1.e3978_a766_a818_r7676_p2952
	mc15_13TeV.410047.PowhegHerwigppEvtGen_UEEE5_singletop_tchan_lept_top.merge.DAOD_TOPQ1.e4775_a766_a818_r7676_p2952
	mc15_13TeV.410048.PowhegHerwigppEvtGen_UEEE5_singletop_tchan_lept_antitop.merge.DAOD_TOPQ1.e4775_a766_a818_r7676_p2952
	mc15_13TeV.410099.PowhegPythiaEvtGen_P2012radHi_Wt_inclusive_top.merge.DAOD_TOPQ1.e4403_a766_a818_r7676_p2952
	mc15_13TeV.410100.PowhegPythiaEvtGen_P2012radLo_Wt_inclusive_top.merge.DAOD_TOPQ1.e4403_a766_a818_r7676_p2952
	mc15_13TeV.410101.PowhegPythiaEvtGen_P2012radHi_Wt_inclusive_antitop.merge.DAOD_TOPQ1.e4403_a766_a818_r7676_p2952
	mc15_13TeV.410102.PowhegPythiaEvtGen_P2012radLo_Wt_inclusive_antitop.merge.DAOD_TOPQ1.e4403_a766_a818_r7676_p2952
	mc15_13TeV.410103.PowhegPythiaEvtGen_P2012radHi_Wt_dilepton_top.merge.DAOD_TOPQ1.e4403_a766_a818_r7676_p2952
	mc15_13TeV.410104.PowhegPythiaEvtGen_P2012radLo_Wt_dilepton_top.merge.DAOD_TOPQ1.e4403_a766_a818_r7676_p2952
	mc15_13TeV.410105.PowhegPythiaEvtGen_P2012radHi_Wt_dilepton_antitop.merge.DAOD_TOPQ1.e4403_a766_a818_r7676_p2952
	mc15_13TeV.410106.PowhegPythiaEvtGen_P2012radLo_Wt_dilepton_antitop.merge.DAOD_TOPQ1.e4403_a766_a818_r7676_p2952
	mc15_13TeV.410107.PowhegPythiaEvtGen_P2012radHi_SingleTopSchan_lept_top.merge.DAOD_TOPQ1.e4403_a766_a818_r7676_p2952
	mc15_13TeV.410108.PowhegPythiaEvtGen_P2012radLo_SingleTopSchan_lept_top.merge.DAOD_TOPQ1.e4403_a766_a818_r7676_p2952
	mc15_13TeV.410109.PowhegPythiaEvtGen_P2012radHi_SingleTopSchan_lept_antitop.merge.DAOD_TOPQ1.e4403_a766_a818_r7676_p2952
	mc15_13TeV.410110.PowhegPythiaEvtGen_P2012radLo_SingleTopSchan_lept_antitop.merge.DAOD_TOPQ1.e4403_a766_a818_r7676_p2952
	mc15_13TeV.410064.PowhegPythiaEvtGen_P2012_Wt_DS_dilepton_top.merge.DAOD_TOPQ1.e4132_s2608_s2183_r7725_r7676_p2952
	mc15_13TeV.410063.PowhegPythiaEvtGen_P2012_Wt_DS_inclusive_antitop.merge.DAOD_TOPQ1.e4132_s2608_s2183_r7725_r7676_p2952

Continued on next page

Table VI.1 – *Continued from previous page*

Sample	Name
	mc15_13TeV.410065.PowhegPythiaEvtGen_P2012_Wt_DS_dilepton_antitop.merge.DAOD_TOPQ1.e4132_s2608_s2183_r7725_r7676_p2952
	mc15_13TeV.410062.PowhegPythiaEvtGen_P2012_Wt_DS_inclusive_top.merge.DAOD_TOPQ1.e4132_s2608_s2183_r7725_r7676_p2952
W+jets	mc15_13TeV.363331.Sherpa_NNPDF30NNLO_Wtaunu_Pt0_70_CVetoBVeto.merge.DAOD_TOPQ1.e4709_s2726_r7725_r7676_p2952
	mc15_13TeV.363332.Sherpa_NNPDF30NNLO_Wtaunu_Pt0_70_CFilterBVeto.merge.DAOD_TOPQ1.e4709_s2726_r7725_r7676_p2952
	mc15_13TeV.363333.Sherpa_NNPDF30NNLO_Wtaunu_Pt0_70_BFilter.merge.DAOD_TOPQ1.e4709_s2726_r7725_r7676_p2952
	mc15_13TeV.363334.Sherpa_NNPDF30NNLO_Wtaunu_Pt70_140_CVetoBVeto.merge.DAOD_TOPQ1.e4709_s2726_r7725_r7676_p2952
	mc15_13TeV.363335.Sherpa_NNPDF30NNLO_Wtaunu_Pt70_140_CFilterBVeto.merge.DAOD_TOPQ1.e4709_s2726_r7725_r7676_p2952
	mc15_13TeV.363336.Sherpa_NNPDF30NNLO_Wtaunu_Pt70_140_BFilter.merge.DAOD_TOPQ1.e4779_s2726_r7725_r7676_p2952
	mc15_13TeV.363337.Sherpa_NNPDF30NNLO_Wtaunu_Pt140_280_CVetoBVeto.merge.DAOD_TOPQ1.e4709_s2726_r7725_r7676_p2952
	mc15_13TeV.363338.Sherpa_NNPDF30NNLO_Wtaunu_Pt140_280_CFilterBVeto.merge.DAOD_TOPQ1.e4709_s2726_r7725_r7676_p2952
	mc15_13TeV.363339.Sherpa_NNPDF30NNLO_Wtaunu_Pt140_280_BFilter.merge.DAOD_TOPQ1.e4709_s2726_r7725_r7676_p2952
	mc15_13TeV.363340.Sherpa_NNPDF30NNLO_Wtaunu_Pt280_500_CVetoBVeto.merge.DAOD_TOPQ1.e4709_s2726_r7725_r7676_p2952
	mc15_13TeV.363341.Sherpa_NNPDF30NNLO_Wtaunu_Pt280_500_CFilterBVeto.merge.DAOD_TOPQ1.e4779_s2726_r7725_r7676_p2952
	mc15_13TeV.363342.Sherpa_NNPDF30NNLO_Wtaunu_Pt280_500_BFilter.merge.DAOD_TOPQ1.e4779_s2726_r7725_r7676_p2952
	mc15_13TeV.363343.Sherpa_NNPDF30NNLO_Wtaunu_Pt500_700_CVetoBVeto.merge.DAOD_TOPQ1.e4709_s2726_r7725_r7676_p2952
	mc15_13TeV.363344.Sherpa_NNPDF30NNLO_Wtaunu_Pt500_700_CFilterBVeto.merge.DAOD_TOPQ1.e4709_s2726_r7725_r7676_p2952
	mc15_13TeV.363345.Sherpa_NNPDF30NNLO_Wtaunu_Pt500_700_BFilter.merge.DAOD_TOPQ1.e4779_s2726_r7725_r7676_p2952
	mc15_13TeV.363346.Sherpa_NNPDF30NNLO_Wtaunu_Pt700_1000_CVetoBVeto.merge.DAOD_TOPQ1.e4709_s2726_r7725_r7676_p2952
	mc15_13TeV.363347.Sherpa_NNPDF30NNLO_Wtaunu_Pt700_1000_CFilterBVeto.merge.DAOD_TOPQ1.e4709_s2726_r7725_r7676_p2952
	mc15_13TeV.363348.Sherpa_NNPDF30NNLO_Wtaunu_Pt700_1000_BFilter.merge.DAOD_TOPQ1.e4779_s2726_r7725_r7676_p2952
	mc15_13TeV.363349.Sherpa_NNPDF30NNLO_Wtaunu_Pt1000_2000_CVetoBVeto.merge.DAOD_TOPQ1.e4709_s2726_r7725_r7676_p2952
	mc15_13TeV.363350.Sherpa_NNPDF30NNLO_Wtaunu_Pt1000_2000_CFilterBVeto.merge.DAOD_TOPQ1.e4709_s2726_r7725_r7676_p2952
	mc15_13TeV.363351.Sherpa_NNPDF30NNLO_Wtaunu_Pt1000_2000_BFilter.merge.DAOD_TOPQ1.e4779_s2726_r7725_r7676_p2952
	mc15_13TeV.363352.Sherpa_NNPDF30NNLO_Wtaunu_Pt2000_E_CMS_CVetoBVeto.merge.DAOD_TOPQ1.e4709_s2726_r7725_r7676_p2952
	mc15_13TeV.363353.Sherpa_NNPDF30NNLO_Wtaunu_Pt2000_E_CMS_CFilterBVeto.merge.DAOD_TOPQ1.e4709_s2726_r7725_r7676_p2952
	mc15_13TeV.363354.Sherpa_NNPDF30NNLO_Wtaunu_Pt2000_E_CMS_BFilter.merge.DAOD_TOPQ1.e4709_s2726_r7725_r7676_p2952
	mc15_13TeV.363436.Sherpa_NNPDF30NNLO_Wmunu_Pt0_70_CVetoBVeto.merge.DAOD_TOPQ1.e4715_s2726_r7725_r7676_p2952
	mc15_13TeV.363437.Sherpa_NNPDF30NNLO_Wmunu_Pt0_70_CFilterBVeto.merge.DAOD_TOPQ1.e4715_s2726_r7725_r7676_p2952
	mc15_13TeV.363438.Sherpa_NNPDF30NNLO_Wmunu_Pt0_70_BFilter.merge.DAOD_TOPQ1.e4715_s2726_r7725_r7676_p2952
	mc15_13TeV.363439.Sherpa_NNPDF30NNLO_Wmunu_Pt70_140_CVetoBVeto.merge.DAOD_TOPQ1.e4715_s2726_r7725_r7676_p2952
	mc15_13TeV.363440.Sherpa_NNPDF30NNLO_Wmunu_Pt70_140_CFilterBVeto.merge.DAOD_TOPQ1.e4715_s2726_r7725_r7676_p2952
	mc15_13TeV.363441.Sherpa_NNPDF30NNLO_Wmunu_Pt70_140_BFilter.merge.DAOD_TOPQ1.e4771_s2726_r7725_r7676_p2952
	mc15_13TeV.363442.Sherpa_NNPDF30NNLO_Wmunu_Pt140_280_CVetoBVeto.merge.DAOD_TOPQ1.e4715_s2726_r7725_r7676_p2952
	mc15_13TeV.363443.Sherpa_NNPDF30NNLO_Wmunu_Pt140_280_CFilterBVeto.merge.DAOD_TOPQ1.e4715_s2726_r7725_r7676_p2952
	mc15_13TeV.363444.Sherpa_NNPDF30NNLO_Wmunu_Pt140_280_BFilter.merge.DAOD_TOPQ1.e4715_s2726_r7725_r7676_p2952
	mc15_13TeV.363445.Sherpa_NNPDF30NNLO_Wmunu_Pt280_500_CVetoBVeto.merge.DAOD_TOPQ1.e4715_s2726_r7725_r7676_p2952
	mc15_13TeV.363446.Sherpa_NNPDF30NNLO_Wmunu_Pt280_500_CFilterBVeto.merge.DAOD_TOPQ1.e4715_s2726_r7725_r7676_p2952
	mc15_13TeV.363447.Sherpa_NNPDF30NNLO_Wmunu_Pt280_500_BFilter.merge.DAOD_TOPQ1.e4715_s2726_r7725_r7676_p2952
	mc15_13TeV.363448.Sherpa_NNPDF30NNLO_Wmunu_Pt500_700_CVetoBVeto.merge.DAOD_TOPQ1.e4715_s2726_r7725_r7676_p2952
	mc15_13TeV.363449.Sherpa_NNPDF30NNLO_Wmunu_Pt500_700_CFilterBVeto.merge.DAOD_TOPQ1.e4715_s2726_r7725_r7676_p2952
	mc15_13TeV.363450.Sherpa_NNPDF30NNLO_Wmunu_Pt500_700_BFilter.merge.DAOD_TOPQ1.e4715_s2726_r7725_r7676_p2952
	mc15_13TeV.363451.Sherpa_NNPDF30NNLO_Wmunu_Pt700_1000_CVetoBVeto.merge.DAOD_TOPQ1.e4715_s2726_r7725_r7676_p2952
	mc15_13TeV.363452.Sherpa_NNPDF30NNLO_Wmunu_Pt700_1000_CFilterBVeto.merge.DAOD_TOPQ1.e4715_s2726_r7725_r7676_p2952
	mc15_13TeV.363453.Sherpa_NNPDF30NNLO_Wmunu_Pt700_1000_BFilter.merge.DAOD_TOPQ1.e4715_s2726_r7725_r7676_p2952
	mc15_13TeV.363454.Sherpa_NNPDF30NNLO_Wmunu_Pt1000_2000_CVetoBVeto.merge.DAOD_TOPQ1.e4715_s2726_r7725_r7676_p2952
	mc15_13TeV.363455.Sherpa_NNPDF30NNLO_Wmunu_Pt1000_2000_CFilterBVeto.merge.DAOD_TOPQ1.e4715_s2726_r7725_r7676_p2952
	mc15_13TeV.363456.Sherpa_NNPDF30NNLO_Wmunu_Pt1000_2000_BFilter.merge.DAOD_TOPQ1.e4715_s2726_r7725_r7676_p2952
	mc15_13TeV.363457.Sherpa_NNPDF30NNLO_Wmunu_Pt2000_E_CMS_CVetoBVeto.merge.DAOD_TOPQ1.e4715_s2726_r7725_r7676_p2952
	mc15_13TeV.363458.Sherpa_NNPDF30NNLO_Wmunu_Pt2000_E_CMS_CFilterBVeto.merge.DAOD_TOPQ1.e4715_s2726_r7725_r7676_p2952
	mc15_13TeV.363459.Sherpa_NNPDF30NNLO_Wmunu_Pt2000_E_CMS_BFilter.merge.DAOD_TOPQ1.e4715_s2726_r7725_r7676_p2952
	mc15_13TeV.363460.Sherpa_NNPDF30NNLO_Wenu_Pt0_70_CVetoBVeto.merge.DAOD_TOPQ1.e4715_s2726_r7725_r7676_p2952
	mc15_13TeV.363461.Sherpa_NNPDF30NNLO_Wenu_Pt0_70_CFilterBVeto.merge.DAOD_TOPQ1.e4715_s2726_r7725_r7676_p2952
	mc15_13TeV.363462.Sherpa_NNPDF30NNLO_Wenu_Pt0_70_BFilter.merge.DAOD_TOPQ1.e4715_s2726_r7725_r7676_p2952
	mc15_13TeV.363463.Sherpa_NNPDF30NNLO_Wenu_Pt70_140_CVetoBVeto.merge.DAOD_TOPQ1.e4715_s2726_r7725_r7676_p2952
	mc15_13TeV.363464.Sherpa_NNPDF30NNLO_Wenu_Pt70_140_CFilterBVeto.merge.DAOD_TOPQ1.e4715_s2726_r7725_r7676_p2952
	mc15_13TeV.363465.Sherpa_NNPDF30NNLO_Wenu_Pt70_140_BFilter.merge.DAOD_TOPQ1.e4715_s2726_r7725_r7676_p2952
W+jets	mc15_13TeV.363466.Sherpa_NNPDF30NNLO_Wenu_Pt140_280_CVetoBVeto.merge.DAOD_TOPQ1.e4715_s2726_r7725_r7676_p2952
	mc15_13TeV.363467.Sherpa_NNPDF30NNLO_Wenu_Pt140_280_CFilterBVeto.merge.DAOD_TOPQ1.e4715_s2726_r7725_r7676_p2952
	mc15_13TeV.363468.Sherpa_NNPDF30NNLO_Wenu_Pt140_280_BFilter.merge.DAOD_TOPQ1.e4715_s2726_r7725_r7676_p2952
	mc15_13TeV.363469.Sherpa_NNPDF30NNLO_Wenu_Pt280_500_CVetoBVeto.merge.DAOD_TOPQ1.e4715_s2726_r7725_r7676_p2952
	mc15_13TeV.363470.Sherpa_NNPDF30NNLO_Wenu_Pt280_500_CFilterBVeto.merge.DAOD_TOPQ1.e4715_s2726_r7725_r7676_p2952
	mc15_13TeV.363471.Sherpa_NNPDF30NNLO_Wenu_Pt280_500_BFilter.merge.DAOD_TOPQ1.e4715_s2726_r7725_r7676_p2952
	mc15_13TeV.363472.Sherpa_NNPDF30NNLO_Wenu_Pt500_700_CVetoBVeto.merge.DAOD_TOPQ1.e4715_s2726_r7725_r7676_p2952
	mc15_13TeV.363473.Sherpa_NNPDF30NNLO_Wenu_Pt500_700_CFilterBVeto.merge.DAOD_TOPQ1.e4715_s2726_r7725_r7676_p2952
	mc15_13TeV.363474.Sherpa_NNPDF30NNLO_Wenu_Pt500_700_BFilter.merge.DAOD_TOPQ1.e4771_s2726_r7725_r7676_p2952
	mc15_13TeV.363475.Sherpa_NNPDF30NNLO_Wenu_Pt700_1000_CVetoBVeto.merge.DAOD_TOPQ1.e4715_s2726_r7725_r7676_p2952
	mc15_13TeV.363476.Sherpa_NNPDF30NNLO_Wenu_Pt700_1000_CFilterBVeto.merge.DAOD_TOPQ1.e4715_s2726_r7725_r7676_p2952
	mc15_13TeV.363477.Sherpa_NNPDF30NNLO_Wenu_Pt700_1000_BFilter.merge.DAOD_TOPQ1.e4715_s2726_r7725_r7676_p2952

Continued on next page

Table VI.1 – *Continued from previous page*

Sample	Name
	mc15_13TeV.363478.Sherpa_NNPDF30NNLO_Wenu_Pt1000_2000_CVetoBVeto.merge.DAOD_TOPQ1.e4715_s2726_r7725_r7676_p2952
	mc15_13TeV.363479.Sherpa_NNPDF30NNLO_Wenu_Pt1000_2000_CFilterBVeto.merge.DAOD_TOPQ1.e4715_s2726_r7725_r7676_p2952
	mc15_13TeV.363480.Sherpa_NNPDF30NNLO_Wenu_Pt1000_2000_BFilter.merge.DAOD_TOPQ1.e4715_s2726_r7725_r7676_p2952
	mc15_13TeV.363481.Sherpa_NNPDF30NNLO_Wenu_Pt2000_E_CMS_CVetoBVeto.merge.DAOD_TOPQ1.e4715_s2726_r7725_r7676_p2952
	mc15_13TeV.363482.Sherpa_NNPDF30NNLO_Wenu_Pt2000_E_CMS_CFilterBVeto.merge.DAOD_TOPQ1.e4715_s2726_r7772_r7676_p2952
	mc15_13TeV.363483.Sherpa_NNPDF30NNLO_Wenu_Pt2000_E_CMS_BFilter.merge.DAOD_TOPQ1.e4715_s2726_r7725_r7676_p2952
	mc15_13TeV.361520.MadGraphPythia8EvtGen_A14NNPDF23LO_Wenu_Np0.merge.DAOD_TOPQ1.e3898_s2608_s2183_r7725_r7676_p2669
	mc15_13TeV.361521.MadGraphPythia8EvtGen_A14NNPDF23LO_Wenu_Np1.merge.DAOD_TOPQ1.e3898_s2608_s2183_r7725_r7676_p2669
	mc15_13TeV.361522.MadGraphPythia8EvtGen_A14NNPDF23LO_Wenu_Np2.merge.DAOD_TOPQ1.e3898_s2608_s2183_r7772_r7676_p2669
	mc15_13TeV.361523.MadGraphPythia8EvtGen_A14NNPDF23LO_Wenu_Np3.merge.DAOD_TOPQ1.e3898_s2608_s2183_r7725_r7676_p2669
	mc15_13TeV.361524.MadGraphPythia8EvtGen_A14NNPDF23LO_Wenu_Np4.merge.DAOD_TOPQ1.e3898_s2608_s2183_r7772_r7676_p2669
	mc15_13TeV.361525.MadGraphPythia8EvtGen_A14NNPDF23LO_Wmunu_Np0.merge.DAOD_TOPQ1.e3898_s2608_s2183_r7725_r7676_p2669
	mc15_13TeV.361526.MadGraphPythia8EvtGen_A14NNPDF23LO_Wmunu_Np1.merge.DAOD_TOPQ1.e3898_s2608_s2183_r7725_r7676_p2669
	mc15_13TeV.361527.MadGraphPythia8EvtGen_A14NNPDF23LO_Wmunu_Np2.merge.DAOD_TOPQ1.e3898_s2608_s2183_r7772_r7676_p2669
	mc15_13TeV.361528.MadGraphPythia8EvtGen_A14NNPDF23LO_Wmunu_Np3.merge.DAOD_TOPQ1.e3898_s2608_s2183_r7725_r7676_p2669
	mc15_13TeV.361529.MadGraphPythia8EvtGen_A14NNPDF23LO_Wmunu_Np4.merge.DAOD_TOPQ1.e3898_s2608_s2183_r7725_r7676_p2669
	mc15_13TeV.361530.MadGraphPythia8EvtGen_A14NNPDF23LO_Wtaunu_Np0.merge.DAOD_TOPQ1.e3898_s2608_s2183_r7772_r7676_p2669
	mc15_13TeV.361531.MadGraphPythia8EvtGen_A14NNPDF23LO_Wtaunu_Np1.merge.DAOD_TOPQ1.e3898_s2608_s2183_r7725_r7676_p2669
	mc15_13TeV.361532.MadGraphPythia8EvtGen_A14NNPDF23LO_Wtaunu_Np2.merge.DAOD_TOPQ1.e3898_s2608_s2183_r7772_r7676_p2669
	mc15_13TeV.361533.MadGraphPythia8EvtGen_A14NNPDF23LO_Wtaunu_Np3.merge.DAOD_TOPQ1.e3898_s2608_s2183_r7725_r7676_p2669
	mc15_13TeV.361534.MadGraphPythia8EvtGen_A14NNPDF23LO_Wtaunu_Np4.merge.DAOD_TOPQ1.e3898_s2608_s2183_r7725_r7676_p2669
Z+jets	mc15_13TeV.363102.Sherpa_NNPDF30NNLO_Ztautau_Pt70_140_CVetoBVeto.merge.DAOD_TOPQ1.e4742_s2726_r7725_r7676_p2952
	mc15_13TeV.363103.Sherpa_NNPDF30NNLO_Ztautau_Pt70_140_CFilterBVeto.merge.DAOD_TOPQ1.e4742_s2726_r7725_r7676_p2952
	mc15_13TeV.363104.Sherpa_NNPDF30NNLO_Ztautau_Pt70_140_BFilter.merge.DAOD_TOPQ1.e4792_s2726_r7725_r7676_p2952
	mc15_13TeV.363105.Sherpa_NNPDF30NNLO_Ztautau_Pt140_280_CVetoBVeto.merge.DAOD_TOPQ1.e4666_s2726_r7725_r7676_p2952
	mc15_13TeV.363106.Sherpa_NNPDF30NNLO_Ztautau_Pt140_280_CFilterBVeto.merge.DAOD_TOPQ1.e4666_s2726_r7725_r7676_p2952
	mc15_13TeV.363107.Sherpa_NNPDF30NNLO_Ztautau_Pt140_280_BFilter.merge.DAOD_TOPQ1.e4742_s2726_r7725_r7676_p2952
	mc15_13TeV.363108.Sherpa_NNPDF30NNLO_Ztautau_Pt280_500_CVetoBVeto.merge.DAOD_TOPQ1.e4666_s2726_r7725_r7676_p2952
	mc15_13TeV.363109.Sherpa_NNPDF30NNLO_Ztautau_Pt280_500_CFilterBVeto.merge.DAOD_TOPQ1.e4792_s2726_r7725_r7676_p2952
	mc15_13TeV.363110.Sherpa_NNPDF30NNLO_Ztautau_Pt280_500_BFilter.merge.DAOD_TOPQ1.e4792_s2726_r7725_r7676_p2952
	mc15_13TeV.363111.Sherpa_NNPDF30NNLO_Ztautau_Pt500_700_CVetoBVeto.merge.DAOD_TOPQ1.e4666_s2726_r7725_r7676_p2952
	mc15_13TeV.363112.Sherpa_NNPDF30NNLO_Ztautau_Pt500_700_CFilterBVeto.merge.DAOD_TOPQ1.e4742_s2726_r7725_r7676_p2952
	mc15_13TeV.363113.Sherpa_NNPDF30NNLO_Ztautau_Pt500_700_BFilter.merge.DAOD_TOPQ1.e4742_s2726_r7725_r7676_p2952
	mc15_13TeV.363114.Sherpa_NNPDF30NNLO_Ztautau_Pt700_1000_CVetoBVeto.merge.DAOD_TOPQ1.e4742_s2726_r7725_r7676_p2952
	mc15_13TeV.363115.Sherpa_NNPDF30NNLO_Ztautau_Pt700_1000_CFilterBVeto.merge.DAOD_TOPQ1.e4792_s2726_r7725_r7676_p2952
	mc15_13TeV.363116.Sherpa_NNPDF30NNLO_Ztautau_Pt700_1000_BFilter.merge.DAOD_TOPQ1.e4742_s2726_r7725_r7676_p2952
	mc15_13TeV.363117.Sherpa_NNPDF30NNLO_Ztautau_Pt1000_2000_CVetoBVeto.merge.DAOD_TOPQ1.e4666_s2726_r7725_r7676_p2952
	mc15_13TeV.363118.Sherpa_NNPDF30NNLO_Ztautau_Pt1000_2000_CFilterBVeto.merge.DAOD_TOPQ1.e4666_s2726_r7725_r7676_p2952
	mc15_13TeV.363119.Sherpa_NNPDF30NNLO_Ztautau_Pt1000_2000_BFilter.merge.DAOD_TOPQ1.e4666_s2726_r7725_r7676_p2952
	mc15_13TeV.363120.Sherpa_NNPDF30NNLO_Ztautau_Pt2000_E_CMS_CVetoBVeto.merge.DAOD_TOPQ1.e4690_s2726_r7725_r7676_p2952
	mc15_13TeV.363121.Sherpa_NNPDF30NNLO_Ztautau_Pt2000_E_CMS_CFilterBVeto.merge.DAOD_TOPQ1.e4690_s2726_r7725_r7676_p2952
	mc15_13TeV.363122.Sherpa_NNPDF30NNLO_Ztautau_Pt2000_E_CMS_BFilter.merge.DAOD_TOPQ1.e4792_s2726_r7725_r7676_p2952
	mc15_13TeV.363361.Sherpa_NNPDF30NNLO_Ztautau_Pt0_70_CVetoBVeto.merge.DAOD_TOPQ1.e4689_s2726_r7725_r7676_p2952
	mc15_13TeV.363362.Sherpa_NNPDF30NNLO_Ztautau_Pt0_70_CFilterBVeto.merge.DAOD_TOPQ1.e4689_s2726_r7725_r7676_p2952
	mc15_13TeV.363363.Sherpa_NNPDF30NNLO_Ztautau_Pt0_70_BFilter.merge.DAOD_TOPQ1.e4743_s2726_r7725_r7676_p2952
	mc15_13TeV.363364.Sherpa_NNPDF30NNLO_Zmumu_Pt0_70_CVetoBVeto.merge.DAOD_TOPQ1.e4716_s2726_r7725_r7676_p2952
	mc15_13TeV.363365.Sherpa_NNPDF30NNLO_Zmumu_Pt0_70_CFilterBVeto.merge.DAOD_TOPQ1.e4716_s2726_r7725_r7676_p2952
	mc15_13TeV.363366.Sherpa_NNPDF30NNLO_Zmumu_Pt0_70_BFilter.merge.DAOD_TOPQ1.e4716_s2726_r7725_r7676_p2952
	mc15_13TeV.363367.Sherpa_NNPDF30NNLO_Zmumu_Pt70_140_CVetoBVeto.merge.DAOD_TOPQ1.e4716_s2726_r7725_r7676_p2952
	mc15_13TeV.363368.Sherpa_NNPDF30NNLO_Zmumu_Pt70_140_CFilterBVeto.merge.DAOD_TOPQ1.e4716_s2726_r7725_r7676_p2952
	mc15_13TeV.363369.Sherpa_NNPDF30NNLO_Zmumu_Pt70_140_BFilter.merge.DAOD_TOPQ1.e4716_s2726_r7725_r7676_p2952
	mc15_13TeV.363370.Sherpa_NNPDF30NNLO_Zmumu_Pt140_280_CVetoBVeto.merge.DAOD_TOPQ1.e4716_s2726_r7725_r7676_p2952
	mc15_13TeV.363371.Sherpa_NNPDF30NNLO_Zmumu_Pt140_280_CFilterBVeto.merge.DAOD_TOPQ1.e4716_s2726_r7725_r7676_p2952
	mc15_13TeV.363372.Sherpa_NNPDF30NNLO_Zmumu_Pt140_280_BFilter.merge.DAOD_TOPQ1.e4716_s2726_r7725_r7676_p2952
	mc15_13TeV.363373.Sherpa_NNPDF30NNLO_Zmumu_Pt280_500_CVetoBVeto.merge.DAOD_TOPQ1.e4716_s2726_r7725_r7676_p2952
	mc15_13TeV.363374.Sherpa_NNPDF30NNLO_Zmumu_Pt280_500_CFilterBVeto.merge.DAOD_TOPQ1.e4716_s2726_r7725_r7676_p2952
	mc15_13TeV.363375.Sherpa_NNPDF30NNLO_Zmumu_Pt280_500_BFilter.merge.DAOD_TOPQ1.e4772_s2726_r7725_r7676_p2952
	mc15_13TeV.363376.Sherpa_NNPDF30NNLO_Zmumu_Pt500_700_CVetoBVeto.merge.DAOD_TOPQ1.e4716_s2726_r7725_r7676_p2952
	mc15_13TeV.363377.Sherpa_NNPDF30NNLO_Zmumu_Pt500_700_CFilterBVeto.merge.DAOD_TOPQ1.e4716_s2726_r7725_r7676_p2952
	mc15_13TeV.363378.Sherpa_NNPDF30NNLO_Zmumu_Pt500_700_BFilter.merge.DAOD_TOPQ1.e4772_s2726_r7725_r7676_p2952
	mc15_13TeV.363379.Sherpa_NNPDF30NNLO_Zmumu_Pt700_1000_CVetoBVeto.merge.DAOD_TOPQ1.e4716_s2726_r7725_r7676_p2952
	mc15_13TeV.363380.Sherpa_NNPDF30NNLO_Zmumu_Pt700_1000_CFilterBVeto.merge.DAOD_TOPQ1.e4716_s2726_r7725_r7676_p2952
	mc15_13TeV.363381.Sherpa_NNPDF30NNLO_Zmumu_Pt700_1000_BFilter.merge.DAOD_TOPQ1.e4716_s2726_r7725_r7676_p2952
	mc15_13TeV.363382.Sherpa_NNPDF30NNLO_Zmumu_Pt1000_2000_CVetoBVeto.merge.DAOD_TOPQ1.e4716_s2726_r7725_r7676_p2952
	mc15_13TeV.363383.Sherpa_NNPDF30NNLO_Zmumu_Pt1000_2000_CFilterBVeto.merge.DAOD_TOPQ1.e4716_s2726_r7725_r7676_p2952
	mc15_13TeV.363384.Sherpa_NNPDF30NNLO_Zmumu_Pt1000_2000_BFilter.merge.DAOD_TOPQ1.e4716_s2726_r7725_r7676_p2952
	mc15_13TeV.363385.Sherpa_NNPDF30NNLO_Zmumu_Pt2000_E_CMS_CVetoBVeto.merge.DAOD_TOPQ1.e4716_s2726_r7725_r7676_p2952
	mc15_13TeV.363386.Sherpa_NNPDF30NNLO_Zmumu_Pt2000_E_CMS_CFilterBVeto.merge.DAOD_TOPQ1.e4716_s2726_r7725_r7676_p2952

Continued on next page

Table VI.1 – *Continued from previous page*

Sample	Name
	mc15_13TeV.363387.Sherpa_NNPDF30NNLO_Zmumu_Pt2000_E_CMS_BFilter.merge.DAOD_TOPQ1.e4716_s2726_r7725_r7676_p2952
	mc15_13TeV.363388.Sherpa_NNPDF30NNLO_Zee_Pt0_70_CVetoBVeto.merge.DAOD_TOPQ1.e4716_s2726_r7725_r7676_p2952
	mc15_13TeV.363389.Sherpa_NNPDF30NNLO_Zee_Pt0_70_CFilterBVeto.merge.DAOD_TOPQ1.e4716_s2726_r7725_r7676_p2952
	mc15_13TeV.363390.Sherpa_NNPDF30NNLO_Zee_Pt0_70_BFilter.merge.DAOD_TOPQ1.e4716_s2726_r7725_r7676_p2952
	mc15_13TeV.363391.Sherpa_NNPDF30NNLO_Zee_Pt70_140_CVetoBVeto.merge.DAOD_TOPQ1.e4716_s2726_r7725_r7676_p2952
	mc15_13TeV.363392.Sherpa_NNPDF30NNLO_Zee_Pt70_140_CFilterBVeto.merge.DAOD_TOPQ1.e4772_s2726_r7725_r7676_p2952
	mc15_13TeV.363393.Sherpa_NNPDF30NNLO_Zee_Pt70_140_BFilter.merge.DAOD_TOPQ1.e4716_s2726_r7725_r7676_p2952
	mc15_13TeV.363394.Sherpa_NNPDF30NNLO_Zee_Pt140_280_CVetoBVeto.merge.DAOD_TOPQ1.e4716_s2726_r7725_r7676_p2952
	mc15_13TeV.363395.Sherpa_NNPDF30NNLO_Zee_Pt140_280_CFilterBVeto.merge.DAOD_TOPQ1.e4716_s2726_r7725_r7676_p2952
	mc15_13TeV.363396.Sherpa_NNPDF30NNLO_Zee_Pt140_280_BFilter.merge.DAOD_TOPQ1.e4772_s2726_r7725_r7676_p2952
	mc15_13TeV.363397.Sherpa_NNPDF30NNLO_Zee_Pt280_500_CVetoBVeto.merge.DAOD_TOPQ1.e4716_s2726_r7725_r7676_p2952
	mc15_13TeV.363398.Sherpa_NNPDF30NNLO_Zee_Pt280_500_CFilterBVeto.merge.DAOD_TOPQ1.e4716_s2726_r7725_r7676_p2952
	mc15_13TeV.363399.Sherpa_NNPDF30NNLO_Zee_Pt280_500_BFilter.merge.DAOD_TOPQ1.e4772_s2726_r7725_r7676_p2952
	mc15_13TeV.363400.Sherpa_NNPDF30NNLO_Zee_Pt500_700_CVetoBVeto.merge.DAOD_TOPQ1.e4716_s2726_r7725_r7676_p2952
	mc15_13TeV.363401.Sherpa_NNPDF30NNLO_Zee_Pt500_700_CFilterBVeto.merge.DAOD_TOPQ1.e4716_s2726_r7725_r7676_p2952
	mc15_13TeV.363402.Sherpa_NNPDF30NNLO_Zee_Pt500_700_BFilter.merge.DAOD_TOPQ1.e4716_s2726_r7725_r7676_p2952
	mc15_13TeV.363403.Sherpa_NNPDF30NNLO_Zee_Pt700_1000_CVetoBVeto.merge.DAOD_TOPQ1.e4716_s2726_r7725_r7676_p2952
	mc15_13TeV.363404.Sherpa_NNPDF30NNLO_Zee_Pt700_1000_CFilterBVeto.merge.DAOD_TOPQ1.e4716_s2726_r7725_r7676_p2952
	mc15_13TeV.363405.Sherpa_NNPDF30NNLO_Zee_Pt700_1000_BFilter.merge.DAOD_TOPQ1.e4716_s2726_r7725_r7676_p2952
	mc15_13TeV.363406.Sherpa_NNPDF30NNLO_Zee_Pt1000_2000_CVetoBVeto.merge.DAOD_TOPQ1.e4716_s2726_r7725_r7676_p2952
	mc15_13TeV.363407.Sherpa_NNPDF30NNLO_Zee_Pt1000_2000_CFilterBVeto.merge.DAOD_TOPQ1.e4716_s2726_r7725_r7676_p2952
	mc15_13TeV.363408.Sherpa_NNPDF30NNLO_Zee_Pt1000_2000_BFilter.merge.DAOD_TOPQ1.e4772_s2726_r7725_r7676_p2952
	mc15_13TeV.363409.Sherpa_NNPDF30NNLO_Zee_Pt2000_E_CMS_CVetoBVeto.merge.DAOD_TOPQ1.e4716_s2726_r7725_r7676_p2952
	mc15_13TeV.363410.Sherpa_NNPDF30NNLO_Zee_Pt2000_E_CMS_CFilterBVeto.merge.DAOD_TOPQ1.e4716_s2726_r7725_r7676_p2952
	mc15_13TeV.363411.Sherpa_NNPDF30NNLO_Zee_Pt2000_E_CMS_BFilter.merge.DAOD_TOPQ1.e4772_s2726_r7725_r7676_p2952
Dibosons	mc15_13TeV.361063.Sherpa_CT10_llll.merge.DAOD_TOPQ1.e3836_s2608_s2183_r7725_r7676_p2952
	mc15_13TeV.361064.Sherpa_CT10_lllvSFMinus.merge.DAOD_TOPQ1.e3836_s2608_s2183_r7725_r7676_p2952
	mc15_13TeV.361065.Sherpa_CT10_lllvOFMinus.merge.DAOD_TOPQ1.e3836_s2608_s2183_r7725_r7676_p2952
	mc15_13TeV.361066.Sherpa_CT10_lllvSFPlus.merge.DAOD_TOPQ1.e3836_s2608_s2183_r7725_r7676_p2952
	mc15_13TeV.361067.Sherpa_CT10_lllvOFPlus.merge.DAOD_TOPQ1.e3836_s2608_s2183_r7725_r7676_p2952
	mc15_13TeV.361068.Sherpa_CT10_llvv.merge.DAOD_TOPQ1.e3836_s2608_s2183_r7725_r7676_p2952
	mc15_13TeV.361070.Sherpa_CT10_llvvjj_ss_EW6.merge.DAOD_TOPQ1.e3836_s2608_s2183_r7725_r7676_p2952
	mc15_13TeV.361071.Sherpa_CT10_lllvjj_EW6.merge.DAOD_TOPQ1.e3836_s2608_s2183_r7772_r7676_p2952
	mc15_13TeV.361072.Sherpa_CT10_lllljj_EW6.merge.DAOD_TOPQ1.e3836_s2608_s2183_r7772_r7676_p2952
$t\bar{t}H$	mc15_13TeV.341177.aMcAtNloHerwigppEvtGen_UEEE5_CTEQ6L1_CT10ME_ttH125_dil.merge.DAOD_TOPQ1.e4277_s2608_s2183_r7772_r7676_p2952
	mc15_13TeV.341270.aMcAtNloHerwigppEvtGen_UEEE5_CTEQ6L1_CT10ME_ttH125_semilep.merge.DAOD_TOPQ1.e4277_s2608_s2183_r7772_r7676_p2952
	mc15_13TeV.341271.aMcAtNloHerwigppEvtGen_UEEE5_CTEQ6L1_CT10ME_ttH125_allhad.merge.DAOD_TOPQ1.e4277_s2608_s2183_r7772_r7676_p2952
$t\bar{t}V$	mc15_13TeV.410155.aMcAtNloPythia8EvtGen_MEN30NLO_A14N23LO_ttW.merge.DAOD_TOPQ1.e5070_s2726_r7772_r7676_p3045
	mc15_13TeV.410156.aMcAtNloPythia8EvtGen_MEN30NLO_A14N23LO_ttZnunu.merge.DAOD_TOPQ1.e5070_s2726_r7772_r7676_p2952
	mc15_13TeV.410157.aMcAtNloPythia8EvtGen_MEN30NLO_A14N23LO_ttZqq.merge.DAOD_TOPQ1.e5070_s2726_r7772_r7676_p2952
	mc15_13TeV.410218.aMcAtNloPythia8EvtGen_MEN30NLO_A14N23LO_ttee.merge.DAOD_TOPQ1.e5070_s2726_r7772_r7676_p3045
	mc15_13TeV.410219.aMcAtNloPythia8EvtGen_MEN30NLO_A14N23LO_ttmumu.merge.DAOD_TOPQ1.e5070_s2726_r7772_r7676_p3045
	mc15_13TeV.410220.aMcAtNloPythia8EvtGen_MEN30NLO_A14N23LO_tttautau.merge.DAOD_TOPQ1.e5070_s2726_r7772_r7676_p3045
	mc15_13TeV.410215.aMcAtNloPythia8EvtGen_A14_NNPDF23LO_260000_tWZDR.merge.DAOD_TOPQ1.e4851_s2726_r7725_r7676_p2952
	mc15_13TeV.410217.aMcAtNloHerwigppEvtGen_UEEE5_CTEQ6L1_CT10ME_260000_tWZDR.merge.DAOD_TOPQ1.e4851_s2726_r7725_r7676_p2952
signal samples	mc15_13TeV.303343.MadGraphPythia8EvtGen_NNPDF30LO_A14NNPDF23LO_WYWb500GeV01.merge.DAOD_TOPQ1.e4352_s2608_r7772_r7676_p2771
	mc15_13TeV.303344.MadGraphPythia8EvtGen_NNPDF30LO_A14NNPDF23LO_WYWb900GeV01.merge.DAOD_TOPQ1.e4352_s2608_r7772_r7676_p2771
	mc15_13TeV.303345.MadGraphPythia8EvtGen_NNPDF30LO_A14NNPDF23LO_WYWb1200GeV01.merge.DAOD_TOPQ1.e4352_s2608_r7772_r7676_p2771
	mc15_13TeV.305124.MGPy8EG_NNPDF30LO_A14NNPDF23LO_WYWb700LH05.merge.DAOD_TOPQ1.e4871_s2726_r7772_r7676_p2771
	mc15_13TeV.305125.MGPy8EG_NNPDF30LO_A14NNPDF23LO_WYWb800LH05.merge.DAOD_TOPQ1.e4871_s2726_r7772_r7676_p2771
	mc15_13TeV.305126.MGPy8EG_NNPDF30LO_A14NNPDF23LO_WYWb1000LH05.merge.DAOD_TOPQ1.e4871_s2726_r7772_r7676_p2771
	mc15_13TeV.305127.MGPy8EG_NNPDF30LO_A14NNPDF23LO_WYWb1100LH05.merge.DAOD_TOPQ1.e4871_s2726_r7772_r7676_p2771
	mc15_13TeV.305128.MGPy8EG_NNPDF30LO_A14NNPDF23LO_WYWb1200LH05.merge.DAOD_TOPQ1.e4871_s2726_r7772_r7676_p2771
	mc15_13TeV.305129.MGPy8EG_NNPDF30LO_A14NNPDF23LO_WYWb1300LH05.merge.DAOD_TOPQ1.e4871_s2726_r7772_r7676_p2771
	mc15_13TeV.305130.MGPy8EG_NNPDF30LO_A14NNPDF23LO_WYWb1400LH05.merge.DAOD_TOPQ1.e4871_s2726_r7772_r7676_p2771
	mc15_13TeV.305131.MGPy8EG_NNPDF30LO_A14NNPDF23LO_WYWb1500LH05.merge.DAOD_TOPQ1.e4871_s2726_r7772_r7676_p2771
	mc15_13TeV.305009.MGPy8EG_NNPDF30LO_A14NNPDF23LO_WYWb900LH05.merge.DAOD_TOPQ1.e4813_a766_a821_r7676_p2842
	mc15_13TeV.305010.MGPy8EG_NNPDF30LO_A14NNPDF23LO_WYWb1600LH05.merge.DAOD_TOPQ1.e4813_a766_a821_r7676_p2842
	mc15_13TeV.302468.ProtosLHEFPythia8EvtGen_A14NNPDF23LO_TTS_M500.merge.DAOD_TOPQ1.e4112_s2608_r7772_r7676_p2952
	mc15_13TeV.302469.ProtosLHEFPythia8EvtGen_A14NNPDF23LO_TTS_M600.merge.DAOD_TOPQ1.e4112_s2608_r7772_r7676_p2952
	mc15_13TeV.302470.ProtosLHEFPythia8EvtGen_A14NNPDF23LO_TTS_M700.merge.DAOD_TOPQ1.e4112_s2608_r7772_r7676_p2952
	mc15_13TeV.302471.ProtosLHEFPythia8EvtGen_A14NNPDF23LO_TTS_M750.merge.DAOD_TOPQ1.e4112_s2608_r7772_r7676_p2952
	mc15_13TeV.302472.ProtosLHEFPythia8EvtGen_A14NNPDF23LO_TTS_M800.merge.DAOD_TOPQ1.e4112_s2608_r7772_r7676_p2952
	mc15_13TeV.302473.ProtosLHEFPythia8EvtGen_A14NNPDF23LO_TTS_M850.merge.DAOD_TOPQ1.e4112_s2608_r7772_r7676_p2952
	mc15_13TeV.302474.ProtosLHEFPythia8EvtGen_A14NNPDF23LO_TTS_M900.merge.DAOD_TOPQ1.e4112_s2608_r7772_r7676_p2952
	mc15_13TeV.302475.ProtosLHEFPythia8EvtGen_A14NNPDF23LO_TTS_M950.merge.DAOD_TOPQ1.e4112_s2608_r7772_r7676_p2952
	mc15_13TeV.302476.ProtosLHEFPythia8EvtGen_A14NNPDF23LO_TTS_M1000.merge.DAOD_TOPQ1.e4112_s2608_r7772_r7676_p2952

Continued on next page

Table VI.1 – *Continued from previous page*

Sample	Name
	mc15_13TeV.302477.ProtosLHEFPythia8EvtGen_A14NNPDF23LO_TTS_M1050.merge.DAOD_TOPQ1.e4112_s2608_r7772_r7676_p2952
	mc15_13TeV.302478.ProtosLHEFPythia8EvtGen_A14NNPDF23LO_TTS_M1100.merge.DAOD_TOPQ1.e4112_s2608_r7772_r7676_p2952
	mc15_13TeV.302479.ProtosLHEFPythia8EvtGen_A14NNPDF23LO_TTS_M1150.merge.DAOD_TOPQ1.e4112_s2608_r7772_r7676_p2952
	mc15_13TeV.302480.ProtosLHEFPythia8EvtGen_A14NNPDF23LO_TTS_M1200.merge.DAOD_TOPQ1.e4112_s2608_r7772_r7676_p2952
	mc15_13TeV.302481.ProtosLHEFPythia8EvtGen_A14NNPDF23LO_TTS_M1300.merge.DAOD_TOPQ1.e4112_s2608_r7772_r7676_p2952
	mc15_13TeV.302482.ProtosLHEFPythia8EvtGen_A14NNPDF23LO_TTS_M1400.merge.DAOD_TOPQ1.e4112_s2608_r7772_r7676_p2952
	mc15_13TeV.302483.ProtosLHEFPythia8EvtGen_A14NNPDF23LO_TTD_M700.merge.DAOD_TOPQ1.e4112_s2608_r7772_r7676_p2952
	mc15_13TeV.302484.ProtosLHEFPythia8EvtGen_A14NNPDF23LO_TTD_M950.merge.DAOD_TOPQ1.e4112_s2608_r7772_r7676_p2952
	mc15_13TeV.302485.ProtosLHEFPythia8EvtGen_A14NNPDF23LO_TTD_M1200.merge.DAOD_TOPQ1.e4112_s2608_r7772_r7676_p2952
	mc15_13TeV.302486.ProtosLHEFPythia8EvtGen_A14NNPDF23LO_BBS_M500.merge.DAOD_TOPQ1.e4112_s2608_r7772_r7676_p2952
	mc15_13TeV.302487.ProtosLHEFPythia8EvtGen_A14NNPDF23LO_BBS_M600.merge.DAOD_TOPQ1.e4112_s2608_r7772_r7676_p2952
	mc15_13TeV.302488.ProtosLHEFPythia8EvtGen_A14NNPDF23LO_BBS_M700.merge.DAOD_TOPQ1.e4141_s2608_r7772_r7676_p2952
	mc15_13TeV.302489.ProtosLHEFPythia8EvtGen_A14NNPDF23LO_BBS_M750.merge.DAOD_TOPQ1.e4112_s2608_r7772_r7676_p2952
	mc15_13TeV.302490.ProtosLHEFPythia8EvtGen_A14NNPDF23LO_BBS_M800.merge.DAOD_TOPQ1.e4112_s2608_r7772_r7676_p2952
	mc15_13TeV.302491.ProtosLHEFPythia8EvtGen_A14NNPDF23LO_BBS_M850.merge.DAOD_TOPQ1.e4112_s2608_r7772_r7676_p2952
	mc15_13TeV.302492.ProtosLHEFPythia8EvtGen_A14NNPDF23LO_BBS_M900.merge.DAOD_TOPQ1.e4112_s2608_r7772_r7676_p2952
	mc15_13TeV.302493.ProtosLHEFPythia8EvtGen_A14NNPDF23LO_BBS_M950.merge.DAOD_TOPQ1.e4112_s2608_r7772_r7676_p2952
	mc15_13TeV.302494.ProtosLHEFPythia8EvtGen_A14NNPDF23LO_BBS_M1000.merge.DAOD_TOPQ1.e4112_s2608_r7772_r7676_p2952
	mc15_13TeV.302495.ProtosLHEFPythia8EvtGen_A14NNPDF23LO_BBS_M1050.merge.DAOD_TOPQ1.e4112_s2608_r7772_r7676_p2952
	mc15_13TeV.302496.ProtosLHEFPythia8EvtGen_A14NNPDF23LO_BBS_M1100.merge.DAOD_TOPQ1.e4112_s2608_r7772_r7676_p2952
	mc15_13TeV.302497.ProtosLHEFPythia8EvtGen_A14NNPDF23LO_BBS_M1150.merge.DAOD_TOPQ1.e4112_s2608_r7772_r7676_p2952
	mc15_13TeV.302498.ProtosLHEFPythia8EvtGen_A14NNPDF23LO_BBS_M1200.merge.DAOD_TOPQ1.e4112_s2608_r7772_r7676_p2952
	mc15_13TeV.302499.ProtosLHEFPythia8EvtGen_A14NNPDF23LO_BBS_M1300.merge.DAOD_TOPQ1.e4112_s2608_r7772_r7676_p2952
	mc15_13TeV.302500.ProtosLHEFPythia8EvtGen_A14NNPDF23LO_BBS_M1400.merge.DAOD_TOPQ1.e4112_s2608_r7772_r7676_p2952
	mc15_13TeV.302501.ProtosLHEFPythia8EvtGen_A14NNPDF23LO_BBD_M700.merge.DAOD_TOPQ1.e4112_s2608_r7772_r7676_p2952
	mc15_13TeV.302502.ProtosLHEFPythia8EvtGen_A14NNPDF23LO_BBD_M950.merge.DAOD_TOPQ1.e4112_s2608_r7772_r7676_p2952
	mc15_13TeV.302503.ProtosLHEFPythia8EvtGen_A14NNPDF23LO_BBD_M1200.merge.DAOD_TOPQ1.e4112_s2608_r7772_r7676_p2952
signal pair-production samples	mc15_13TeV.302504.ProtosLHEFPythia8EvtGen_A14NNPDF23LO_XX_M500.merge.DAOD_TOPQ1.e4112_s2608_r7772_r7676_p2952
	mc15_13TeV.302505.ProtosLHEFPythia8EvtGen_A14NNPDF23LO_XX_M700.merge.DAOD_TOPQ1.e4112_s2608_r7772_r7676_p2952
	mc15_13TeV.302506.ProtosLHEFPythia8EvtGen_A14NNPDF23LO_XX_M800.merge.DAOD_TOPQ1.e4112_s2608_r7772_r7676_p2952
	mc15_13TeV.302507.ProtosLHEFPythia8EvtGen_A14NNPDF23LO_XX_M900.merge.DAOD_TOPQ1.e4112_s2608_r7772_r7676_p2952
	mc15_13TeV.302508.ProtosLHEFPythia8EvtGen_A14NNPDF23LO_XX_M1000.merge.DAOD_TOPQ1.e4112_s2608_r7772_r7676_p2952
	mc15_13TeV.302509.ProtosLHEFPythia8EvtGen_A14NNPDF23LO_XX_M1100.merge.DAOD_TOPQ1.e4112_s2608_r7772_r7676_p2952
	mc15_13TeV.302510.ProtosLHEFPythia8EvtGen_A14NNPDF23LO_XX_M1200.merge.DAOD_TOPQ1.e4112_s2608_r7772_r7676_p2952
	mc15_13TeV.302511.ProtosLHEFPythia8EvtGen_A14NNPDF23LO_XX_M1400.merge.DAOD_TOPQ1.e4112_s2608_r7772_r7676_p2952
	mc15_13TeV.302512.ProtosLHEFPythia8EvtGen_A14NNPDF23LO_YY_M500.merge.DAOD_TOPQ1.e4112_s2608_r7772_r7676_p2952
	mc15_13TeV.302513.ProtosLHEFPythia8EvtGen_A14NNPDF23LO_YY_M700.merge.DAOD_TOPQ1.e4112_s2608_r7772_r7676_p2952
	mc15_13TeV.302514.ProtosLHEFPythia8EvtGen_A14NNPDF23LO_YY_M800.merge.DAOD_TOPQ1.e4112_s2608_r7772_r7676_p2952
	mc15_13TeV.302515.ProtosLHEFPythia8EvtGen_A14NNPDF23LO_YY_M900.merge.DAOD_TOPQ1.e4112_s2608_r7772_r7676_p2952
	mc15_13TeV.302516.ProtosLHEFPythia8EvtGen_A14NNPDF23LO_YY_M1000.merge.DAOD_TOPQ1.e4112_s2608_r7772_r7676_p2952
	mc15_13TeV.302517.ProtosLHEFPythia8EvtGen_A14NNPDF23LO_YY_M1100.merge.DAOD_TOPQ1.e4112_s2608_r7772_r7676_p2952
	mc15_13TeV.302518.ProtosLHEFPythia8EvtGen_A14NNPDF23LO_YY_M1200.merge.DAOD_TOPQ1.e4112_s2608_r7772_r7676_p2952
	mc15_13TeV.302519.ProtosLHEFPythia8EvtGen_A14NNPDF23LO_YY_M1400.merge.DAOD_TOPQ1.e4141_s2608_r7772_r7676_p2952

Bibliography

[1] M. D. Schartz. *Quantum Field Theory and the Standard Model.* Cambridge University Press, 2014.

[2] M. E. Peskin and D. V. Schroeder. *An Introduction to Quantum Field Theory.* Westview Press, 1995.

[3] ATLAS Collaboration. *Search for resonances decaying to photon pairs in 3.2 fb^{-1} of pp collisions at $\sqrt{s}$ = 13 TeV with the ATLAS detector.* Tech. rep. ATLAS-CONF-2015-081. Geneva: CERN, 2015. URL: https://cds.cern.ch/record/2114853.

[4] ATLAS Collaboration. " Search for new phenomena in high-mass diphoton final states using 37 fb^{-1} of proton–proton collisions collected at $\sqrt{s} = 13$ **TeV** with the ATLAS detector". In: *Phys. Lett. B* 775 (2017), p. 34. DOI: 10.1016/j.physletb.2017.10.039. arXiv: 1707.04147 [hep-ex].

[5] CMS Collaboration. "Search for high-mass diphoton resonances in proton–proton collisions at 13 TeV and combination with 8 TeV search". In: *Phys. Lett. B* 767 (2017), p. 147. DOI: 10.1016/j.physletb.2017.01.027. arXiv: 1609.02507 [hep-ex].

[6] J. H. Oort. "The force exerted by the stellar system in the direction perpendicular to the galactic plane and some related problems". In: *Bull. Astron. Inst. Netherlands* 6 (1932), pp. 249–287. URL: http://cds.cern.ch/record/436532.

[7] F. Zwicky. "Die Rotverschiebung von extragalaktischen Nebeln". In: *Helv. Phys. Acta* 6 (1933). [Gen. Rel. Grav.41,207(2009)], pp. 110–127. DOI: 10.1007/s10714-008-0707-4.

[8] E. Komatsu et al. "Results from the Wilkinson Microwave Anisotropy Probe". In: *Progress of Theoretical and Experimental Physics* 2014.6 (June 2014). ISSN: 2050-3911. DOI: 10.1093/ptep/ptu083. eprint: http://oup.prod.sis.lan/ptep/article-pdf/2014/6/06B102/4452879/ptu083.pdf. URL: https://dx.doi.org/10.1093/ptep/ptu083.

[9] Alves, Joao et al. "Planck 2015 results". In: *A&A* 594 (2016), E1. DOI: 10.1051/0004-6361/201629543. URL: https://doi.org/10.1051/0004-6361/201629543.

[10] A. A. Petrov and A. E. Blechman. *Effective Field Theories*. World Scientific Publishing Co. Pte. Ltd., 2016.

[11] S. Dimopoulos and L. Susskind. "Mass without scalars". In: *Nuclear Physics B* 155.1 (1979), pp. 237 –252. ISSN: 0550-3213. DOI: https://doi.org/10.1016/0550-3213(79)90364-X. URL: http://www.sciencedirect.com/science/article/pii/055032137990364X.

[12] L. Susskind. "Dynamics of spontaneous symmetry breaking in the Weinberg-Salam theory". In: *Phys. Rev. D* 20 (10 1979), pp. 2619–2625. DOI: 10.1103/PhysRevD.20.2619. URL: https://link.aps.org/doi/10.1103/PhysRevD.20.2619.

[13] G. 't Hooft. "Naturalness, chiral symmetry, and spontaneous chiral symmetry breaking". In: *NATO Sci. Ser. B* 59 (1980), pp. 135–157. DOI: 10.1007/978-1-4684-7571-5_9.

[14] M. Schmaltz and D. Tucker-Smith. "Little Higgs review". In: *Ann.Rev.Nucl.Part.Sci.* 55 (2005), pp. 229–270. DOI: 10.1146/annurev.nucl.55.090704.151502. arXiv: hep-ph/0502182 [hep-ph].

[15] D. B. Kaplan, H. Georgi, and S. Dimopoulos. "Composite Higgs Scalars". In: *Phys.Lett.* B136 (1984), p. 187. DOI: 10.1016/0370-2693(84)91178-X.

[16] N. Vignaroli. "Discovering the composite Higgs through the decay of a heavy fermion". In: *JHEP* 1207 (2012), p. 158. DOI: 10.1007/JHEP07(2012)158. arXiv: 1204.0468 [hep-ph].

[17] ATLAS Collaboration. "Observation of a new particle in the search for the Standard Model Higgs boson with the ATLAS detector at the LHC". In: *Phys. Lett. B* 716 (2012), p. 1. DOI: 10.1016/j.physletb.2012.08.020. arXiv: 1207.7214 [hep-ex].

[18] CMS Collaboration. "Observation of a new boson at a mass of 125 GeV with the CMS experiment at the LHC". In: *Phys. Lett. B* 716 (2012), p. 30. DOI: 10.1016/j.physletb.2012.08.021. arXiv: 1207.7235 [hep-ex].

[19] O. Eberhardt et al. "Impact of a Higgs boson at a mass of 126 GeV on the standard model with three and four fermion generations". In: *Phys. Rev. Lett.* 109 (2012), p. 241802. DOI: 10.1103/PhysRevLett.109.241802. arXiv: 1209.1101 [hep-ph].

[20] L. Evans and P. Bryant. "LHC Machine". In: *Journal of Instrumentation* 3.08 (2008), S08001. URL: http://stacks.iop.org/1748-0221/3/i=08/a=S08001.

[21] ATLAS Collaboration.
"The ATLAS Experiment at the CERN Large Hadron Collider".
In: *JINST* 3 (2008), S08003. DOI: 10.1088/1748-0221/3/08/S08003.

[22] ATLAS Collaboration. "Search for single production of vector-like quarks decaying into Wb in pp collisions at $\sqrt{s} = 13$ TeV with the ATLAS detector".
In: *Journal of High Energy Physics* 2019.5 (2019), p. 164.

[23] ATLAS Collaboration. *Search for single production of vector-like quarks decaying into Wb in pp collisions at $\sqrt{s} = 13$ TeV with the ATLAS detector*.
ATLAS-CONF-2016-072. 2016. URL: https://cds.cern.ch/record/2206226.

[24] A. Purcell. "Go on a particle quest at the first CERN webfest. Le premier webfest du CERN se lance a la conquete des particules".
In: BUL-NA-2012-269. 35/2012 (2012), p. 10.
URL: https://cds.cern.ch/record/1473657.

[25] S. Weinberg. "A Model of Leptons".
In: *Phys. Rev. Lett.* 19 (21 1967), pp. 1264–1266.
DOI: 10.1103/PhysRevLett.19.1264.
URL: https://link.aps.org/doi/10.1103/PhysRevLett.19.1264.

[26] A. Salam. "Weak and Electromagnetic Interactions".
In: *Conf. Proc.* C680519 (1968), pp. 367–377.

[27] S. L. Glashow. "Partial-symmetries of weak interactions".
In: *Nuclear Physics* 22.4 (1961), pp. 579 –588. ISSN: 0029-5582.
DOI: https://doi.org/10.1016/0029-5582(61)90469-2. URL:
http://www.sciencedirect.com/science/article/pii/0029558261904692.

[28] F. Englert and R. Brout.
"Broken Symmetry and the Mass of Gauge Vector Mesons".
In: *Phys. Rev. Lett.* 13 (9 1964), pp. 321–323. DOI: 10.1103/PhysRevLett.13.321.
URL: https://link.aps.org/doi/10.1103/PhysRevLett.13.321.

[29] P. W. Higgs. "Broken Symmetries and the Masses of Gauge Bosons".
In: *Phys. Rev. Lett.* 13 (16 1964), pp. 508–509. DOI: 10.1103/PhysRevLett.13.508.
URL: https://link.aps.org/doi/10.1103/PhysRevLett.13.508.

[30] G. S. Guralnik, C. R. Hagen, and T. W. B. Kibble.
"Global Conservation Laws and Massless Particles".
In: *Phys. Rev. Lett.* 13 (20 1964), pp. 585–587. DOI: 10.1103/PhysRevLett.13.585.
URL: https://link.aps.org/doi/10.1103/PhysRevLett.13.585.

[31] R. K. Ellis, W. J. Stirling, and B. R. Webber. "QCD and collider physics".
In: *Camb. Monogr. Part. Phys. Nucl. Phys. Cosmol.* 8 (1996), pp. 1–435.

[32] A. Buckley et al. “General-purpose event generators for LHC physics”. In: *Physics Reports* 504.5 (2011), pp. 145 –233. ISSN: 0370-1573. DOI: https://doi.org/10.1016/j.physrep.2011.03.005. URL: http://www.sciencedirect.com/science/article/pii/S0370157311000846.

[33] G. L. Fogli et al. “Global analysis of neutrino masses, mixings, and phases: Entering the era of leptonic CP violation searches”. In: *Phys. Rev. D* 86 (1 2012), p. 013012. DOI: 10.1103/PhysRevD.86.013012. URL: https://link.aps.org/doi/10.1103/PhysRevD.86.013012.

[34] S. Troitsky. “Unsolved problems in particle physics”. In: *arXiv:1112.4515* (2011).

[35] K. Arun, S. Gudennavar, and C. Sivaram. “Dark matter, dark energy, and alternate models: A review”. In: *Advances in Space Research* 60.1 (2017), pp. 166 –186. ISSN: 0273-1177. DOI: https://doi.org/10.1016/j.asr.2017.03.043. URL: http://www.sciencedirect.com/science/article/pii/S027311771730248X.

[36] K G. Begeman. “H I rotation curves of spiral galaxies. I - NGC 3198”. In: *Astronomy and Astrophysics* 223 (Sept. 1989), pp. 47–60.

[37] P. Schneider. *Extragalaktische Astronomie und Kosmologie*. Springer, 2008.

[38] G. Panico and A. Wulzer. *The Composite Nambu-Goldstone Higgs*. Lecture Notes in Physics. Springer International Publishing Switzerland, 2016.

[39] The ALEPH Collaboration and the DELPHI Collaboration and the L3 Collaboration and the OPAL Collaboration and the SLD Collaboration and the LEP Electroweak Working Group and the SLD electroweak and heavy flavour groups. “Precision Electroweak Measurements on the Z Resonance”. In: *Phys. Rep.* 427 (2005), pp. 257–454. DOI: 10.1016/j.physrep.2005.12.006. arXiv: 1305.4172 [hep-ph].

[40] L. Randall and R. Sundrum. “A Large mass hierarchy from a small extra dimension”. In: *Phys.Rev.Lett.* 83 (1999), pp. 3370–3373. DOI: 10.1103/PhysRevLett.83.3370. arXiv: hep-ph/9905221 [hep-ph].

[41] J. Aguilar-Saavedra et al. “Handbook of vectorlike quarks: Mixing and single production”. In: *Phys.Rev.* D88.9 (2013), p. 094010. DOI: 10.1103/PhysRevD.88.094010. arXiv: 1306.0572 [hep-ph].

[42] A. De Simone et al. “A First Top Partner Hunter’s Guide”. In: *JHEP* 04 (2013), p. 004. arXiv: 1211.5663 [hep-ph].

[43] O. Matsedonskyi, G. Panico, and A. Wulzer. “On the Interpretation of Top Partners Searches”. In: *JHEP* 12 (2014), p. 097. arXiv: 1409.0100 [hep-ph].

[44] M. Buchkremer et al. "Model Independent Framework for Searches of Top Partners". In: *Nucl. Phys.* B876 (2013), pp. 376–417. DOI: 10.1016/j.nuclphysb.2013.08.010. arXiv: 1305.4172 [hep-ph].

[45] M. E. Peskin and T. Takeuchi. "A New constraint on a strongly interacting Higgs sector". In: *Phys. Rev. Lett.* 65 (1990), pp. 964–967.

[46] ATLAS Collaboration. "Search for production of vector-like quark pairs and of four top quarks in the lepton-plus-jets final state in pp collisions at $\sqrt{s} = 8$ TeV with the ATLAS detector". In: *JHEP* 08 (2015), p. 105. DOI: 10.1007/JHEP08(2015)105. arXiv: 1505.04306 [hep-ex].

[47] ATLAS Collaboration. "Search for pair production of vector-like top quarks in events with one lepton, jets, and missing transverse momentum in $\sqrt{s} = 13$ TeV pp collisions with the ATLAS detector". In: *JHEP* 08 (2017), p. 052. DOI: 10.1007/JHEP08(2017)052. arXiv: 1705.10751 [hep-ex].

[48] CMS Collaboration. "Search for vector-like T quarks decaying to top quarks and Higgs bosons in the all-hadronic channel using jet substructure". In: *JHEP* 06 (2015), p. 080. DOI: 10.1007/JHEP06(2015)080. arXiv: 1503.01952 [hep-ex].

[49] CMS Collaboration. "Inclusive search for a vector-like T quark with charge $\frac{2}{3}$ in pp collisions at $\sqrt{s} = 8$ TeV". In: *Phys. Lett. B* 729 (2014), p. 149. DOI: 10.1016/j.physletb.2014.01.006. arXiv: 1311.7667 [hep-ex].

[50] *Search for vector-like quark pair production* $\mathrm{T\bar{T}(Y\bar{Y})} \to \mathrm{bWbW}$ *using kinematic reconstruction in lepton+jets final states at* $\sqrt{s}$*=13 TeV.* Tech. rep. CMS-PAS-B2G-17-003. Geneva: CERN, 2017. URL: https://cds.cern.ch/record/2264685.

[51] ATLAS Collaboration. "Analysis of events with b-jets and a pair of leptons of the same charge in pp collisions at $\sqrt{s} = 8$ TeV with the ATLAS detector". In: *JHEP* 10 (2015), p. 150. DOI: 10.1007/JHEP10(2015)150. arXiv: 1504.04605 [hep-ex].

[52] ATLAS Collaboration. "Search for single production of vector-like quarks decaying into Wb in pp collisions at $\sqrt{s} = 8$ TeV with the ATLAS detector". In: *Eur. Phys. J. C* 76 (2016), p. 442. DOI: 10.1140/epjc/s10052-016-4281-8. arXiv: 1602.05606 [hep-ex].

[53] ATLAS Collaboration. "Search for pair production of up-type vector-like quarks and for four-top-quark events in final states with multiple b-jets with the ATLAS detector". In: *JHEP* 07 (2018), p. 089. DOI: 10.1007/JHEP07(2018)089. arXiv: 1803.09678 [hep-ex].

[54] CMS Collaboration.
"Search for pair production of vector-like T and B quarks in single-lepton final states using boosted jet substructure in proton-proton collisions at $\sqrt{s} = 13$ TeV". In: *JHEP* 11 (2017), p. 085. DOI: 10.1007/JHEP11(2017)085. arXiv: 1706.03408 [hep-ex].

[55] CMS Collaboration. *Search for single production of vector-like quarks decaying into final states with a Z boson and a top or a bottom quark*. CMS-PAS-B2G-16-001. Geneva, 2016. URL: https://cds.cern.ch/record/2199567.

[56] ATLAS Collaboration. "Search for pair production of heavy vector-like quarks decaying to high-p_T W bosons and b quarks in the lepton-plus-jets final state in pp collisions at $\sqrt{s}$=13 TeV with the ATLAS detector". In: *JHEP* 10 (2017), p. 141. DOI: 10.1007/JHEP10(2017)141. arXiv: 1707.03347 [hep-ex].

[57] CMS Collaboration. "Search for vector-like T and B quark pairs in final states with leptons at $\sqrt{s} = 13$ TeV". In: *JHEP* 08 (2018), p. 177. DOI: 10.1007/JHEP08(2018)177. arXiv: 1805.04758 [hep-ex].

[58] CMS Collaboration. "Search for single production of a heavy vector-like T quark decaying to a Higgs boson and a top quark with a lepton and jets in the final state". In: *Phys. Lett. B* (2016). arXiv: 1612.00999 [hep-ex].

[59] CMS Collaboration. "Search for single production of vector-like quarks decaying into a b quark and a W boson in proton–proton collisions at $\sqrt{s} = 13$ TeV". In: (2017). arXiv: 1701.08328 [hep-ex].

[60] CMS Collaboration. "Search for single production of a vector-like T quark decaying to a Z boson and a top quark in proton-proton collisions at $\sqrt{s} = 13$ TeV". In: *Phys. Lett.* B781 (2018), pp. 574–600. DOI: 10.1016/j.physletb.2018.04.036. arXiv: 1708.01062 [hep-ex].

[61] ATLAS Collaboration. "Search for pair and single production of new heavy quarks that decay to a Z boson and a third-generation quark in pp collisions at $\sqrt{s} = 8$ TeV with the ATLAS detector". In: *JHEP* 11 (2014), p. 104. DOI: 10.1007/JHEP11(2014)104. arXiv: 1409.5500 [hep-ex].

[62] CMS Collaboration. *Search for a vectorlike top partner produced through electroweak interaction and decaying to a top quark and a Higgs boson using boosted topologies in the all-hadronic final state*. CMS-PAS-B2G-16-005. Geneva, 2016. URL: https://cds.cern.ch/record/2160371.

[63] ATLAS Collaboration. "Search for pair- and single-production of vector-like quarks in final states with at least one Z boson decaying into a pair of electrons or muons in pp collision data collected with the ATLAS detector". In: (2018). arXiv: 1806.10555 [hep-ex].

[64] ATLAS Collaboration. "Combination of the searches for pair-produced vector-like partners of the third-generation quarks at $\sqrt{s} = 13$ TeV with the ATLAS detector". In: *Phys. Rev. Lett.* 121.21 (2018), p. 211801. DOI: 10.1103/PhysRevLett.121.211801. arXiv: 1808.02343 [hep-ex].

[65] J. A. Aguilar-Saavedra. "Effects of mixing with quark singlets". In: *Phys. Rev. D* 67 (3 2003), p. 035003. DOI: 10.1103/PhysRevD.67.035003. URL: https://link.aps.org/doi/10.1103/PhysRevD.67.035003.

[66] O. Matsedonskyi, G. Panico, and A. Wulzer. "On the Interpretation of Top Partners Searches". In: *JHEP* 12 (2014), p. 097. DOI: 10.1007/JHEP12(2014)097. arXiv: 1409.0100 [hep-ph].

[67] ATLAS Collaboration. "Searches for Heavy Quark States at ATLAS". In: *Journal of Physics: Conference Series* 770.1 (2016), p. 012008. URL: http://stacks.iop.org/1742-6596/770/i=1/a=012008.

[68] E. A. Mobs. "The CERN accelerator complex. Complexe des accélérateurs du CERN". In: (2016). General Photo. URL: https://cds.cern.ch/record/2225847.

[69] ATLAS Collaboration. "Improved luminosity determination in pp collisions at $\sqrt{s} = 7$ TeV using the ATLAS detector at the LHC". In: *Eur. Phys. J.* C73.8 (2013), p. 2518. DOI: 10.1140/epjc/s10052-013-2518-3. arXiv: 1302.4393 [hep-ex].

[70] J. Pequenao. "Computer generated image of the whole ATLAS detector". 2008. URL: https://cds.cern.ch/record/1095924.

[71] K. Potamianos. "The upgraded Pixel detector and the commissioning of the Inner Detector tracking of the ATLAS experiment for Run-2 at the Large Hadron Collider". In: *PoS* EPS-HEP2015 (2015), p. 261. arXiv: 1608.07850 [physics.ins-det].

[72] G Aad et al. "ATLAS pixel detector electronics and sensors". In: *Journal of Instrumentation* 3.07 (2008), P07007. URL: http://stacks.iop.org/1748-0221/3/i=07/a=P07007.

[73] The ATLAS IBL Collaboration. "Production and integration of the ATLAS Insertable B-Layer". In: *Journal of Instrumentation* 13.05 (2018), T05008. URL: http://stacks.iop.org/1748-0221/13/i=05/a=T05008.

[74] ATLAS Collaboration. "Operation and performance of the ATLAS semiconductor tracker". In: *Journal of Instrumentation* 9.08 (2014), P08009. URL: http://stacks.iop.org/1748-0221/9/i=08/a=P08009.

[75] The ATLAS TRT Collaboration. "The ATLAS Transition Radiation Tracker (TRT) proportional drift tube: design and performance".
In: *Journal of Instrumentation* 3.02 (2008), P02013.
URL: http://stacks.iop.org/1748-0221/3/i=02/a=P02013.

[76] J. Pequenao. "Computer Generated image of the ATLAS calorimeter". 2008.
URL: https://cds.cern.ch/record/1095927.

[77] ATLAS Collaboration. *ATLAS liquid-argon calorimeter: Technical Design Report.*
Technical Design Report ATLAS. Geneva: CERN, 1996.
URL: https://cds.cern.ch/record/331061.

[78] ATLAS Collaboration. *ATLAS tile calorimeter: Technical Design Report.*
Technical Design Report ATLAS. Geneva: CERN, 1996.
URL: https://cds.cern.ch/record/331062.

[79] *ATLAS muon spectrometer: Technical Design Report.*
Technical Design Report ATLAS. Geneva: CERN, 1997.
URL: https://cds.cern.ch/record/331068.

[80] J. Pequenao. "Computer generated image of the ATLAS Muons subsystem". 2008.
URL: https://cds.cern.ch/record/1095929.

[81] ATLAS Collaboration. "Performance of the ATLAS trigger system in 2015".
In: *The European Physical Journal C* 77.5 (2017), p. 317. ISSN: 1434-6052.
DOI: 10.1140/epjc/s10052-017-4852-3.
URL: https://doi.org/10.1140/epjc/s10052-017-4852-3.

[82] ATLAS Collaboration. *2015 start-up trigger menu and initial performance assessment of the ATLAS trigger using Run-2 data.* Geneva, 2016.
URL: https://cds.cern.ch/record/2136007.

[83] ATLAS Collaboration. *Trigger Menu in 2016.* Tech. rep. ATL-DAQ-PUB-2017-001.
Geneva: CERN, 2017. URL: https://cds.cern.ch/record/2242069.

[84] W. Stirling. http://www.hep.ph.ic.ac.uk/~wstirlin/plots/plots.html.

[85] T. Gleisberg et al. "Event generation with SHERPA 1.1".
In: *Journal of High Energy Physics* 2009.02 (2009), p. 007.
URL: http://stacks.iop.org/1126-6708/2009/i=02/a=007.

[86] G. Altarelli and G. Parisi. "Asymptotic freedom in parton language".
In: *Nuclear Physics B* 126.2 (1977), pp. 298 –318. ISSN: 0550-3213.
DOI: https://doi.org/10.1016/0550-3213(77)90384-4. URL:
http://www.sciencedirect.com/science/article/pii/0550321377903844.

[87] ATLAS Collaboration. "The ATLAS Simulation Infrastructure".
In: *The European Physical Journal C* 70.3 (2010), pp. 823–874. ISSN: 1434-6052.
DOI: 10.1140/epjc/s10052-010-1429-9.
URL: https://doi.org/10.1140/epjc/s10052-010-1429-9.

[88] GEANT4 Collaboration, S. Agostinelli, et al. "GEANT4: A Simulation toolkit". In: *Nucl. Instrum. Meth. A* 506 (2003), p. 250. DOI: 10.1016/S0168-9002(03)01368-8.

[89] J Boudreau and V Tsulaia. "The GeoModel Toolkit for Detector Description". In: (2005). URL: https://cds.cern.ch/record/865601.

[90] E. Barberio et al. "The Geant4-Based ATLAS Fast Electromagnetic Shower Simulation". In: *Astroparticle, particle and space physics, detectors and medical physics applications. Proceedings, 10th Conference, ICATPP 2007, Como, Italy, October 8-12, 2007.* 2008, pp. 802–806. DOI: 10.1142/9789812819093_0133. URL: http://cdsweb.cern.ch/record/1064665/files/soft-conf-2007-002.pdf.

[91] D Cavalli et al. *Performance of the ATLAS fast simulation ATLFAST.* Tech. rep. ATL-PHYS-INT-2007-005. ATL-COM-PHYS-2007-012. Geneva: CERN, 2007. URL: https://cds.cern.ch/record/1019872.

[92] W. Lukas. "Fast Simulation for ATLAS: Atlfast-II and ISF". In: *Journal of Physics: Conference Series* 396.2 (2012), p. 022031. DOI: 10.1088/1742-6596/396/2/022031. URL: https://doi.org/10.1088%2F1742-6596%2F396%2F2%2F022031.

[93] M Dührssen. *The fast calorimeter simulation FastCaloSim.* Tech. rep. ATL-PHYS-INT-2008-043. ATL-COM-PHYS-2008-093. Geneva: CERN, 2008. URL: https://cds.cern.ch/record/1113510.

[94] K Edmonds et al. *The Fast ATLAS Track Simulation (FATRAS).* Tech. rep. ATL-SOFT-PUB-2008-001. ATL-COM-SOFT-2008-002. Geneva: CERN, 2008. URL: https://cds.cern.ch/record/1091969.

[95] P. Golonka and Z. Was. "PHOTOS Monte Carlo: A Precision tool for QED corrections in Z and W decays". In: *Eur. Phys. J. C* 45 (2006), p. 97. DOI: 10.1140/epjc/s2005-02396-4. arXiv: hep-ph/0506026 [hep-ph].

[96] S. Jadach, J. H. Kuhn, and Z. Was. "TAUOLA: A Library of Monte Carlo programs to simulate decays of polarized τ leptons". In: *Comput. Phys. Commun.* 64 (1991), p. 275. DOI: 10.1016/0010-4655(91)90038-M.

[97] D. J. Lange. "The EvtGen particle decay simulation package". In: *Nucl. Instrum. Meth.* A462 (2001), pp. 152–155. DOI: 10.1016/S0168-9002(01)00089-4.

[98] S. Frixione, P. Nason, and G. Ridolfi. "A Positive-weight next-to-leading-order Monte Carlo for heavy flavour hadroproduction". In: *JHEP* 0709 (2007), p. 126. DOI: 10.1088/1126-6708/2007/09/126. arXiv: 0707.3088 [hep-ph].

[99] P. Nason.
"A New method for combining NLO QCD with shower Monte Carlo algorithms".
In: *JHEP* 0411 (2004), p. 040. DOI: 10.1088/1126-6708/2004/11/040.
arXiv: hep-ph/0409146 [hep-ph].

[100] S. e. a. Frixione.
"Matching NLO QCD computations with Parton Shower simulations:
the POWHEG method". In: *JHEP* 11 (2007), p. 070. arXiv: 0709.2092 [hep-ph].

[101] S. Alioli et al. "A general framework for implementing NLO calculations in shower Monte Carlo programs: the POWHEG BOX". In: *JHEP* 1006 (2010), p. 043.
DOI: 10.1007/JHEP06(2010)043. arXiv: 1002.2581 [hep-ph].

[102] H.-L. Lai et al. "New parton distributions for collider physics".
In: *Phys. Rev. D* 82 (2010), p. 074024. DOI: 10.1103/PhysRevD.82.074024.
arXiv: 1007.2241 [hep-ph].

[103] K. A. Olive et al. "Review of Particle Physics".
In: *Chin. Phys. C* 38 (2014), p. 090001. DOI: 10.1088/1674-1137/38/9/090001.

[104] ATLAS Collaboration. *Comparison of Monte Carlo generator predictions to ATLAS measurements of top pair production at 7 TeV*. ATL-PHYS-PUB-2015-002. 2015.
URL: http://cds.cern.ch/record/1981319.

[105] T. Sjostrand, S. Mrenna, and P. Z. Skands. "PYTHIA 6.4 Physics and Manual".
In: *JHEP* 05 (2006), p. 026. arXiv: hep-ph/0603175 [hep-ph].

[106] J. Pumplin et al. In: *JHEP* 0207 (2002), p. 012. arXiv: hep-ph/0201195.

[107] P. Skands. "Tuning Monte Carlo Generators: The Perugia Tunes".
In: *Phys. Rev.* D82 (2010), p. 074018. DOI: 10.1103/PhysRevD.82.074018.
arXiv: 1005.3457 [hep-ph].

[108] M. Bahr et al. "Herwig++ Physics and Manual".
In: *Eur. Phys. J. C* 58 (2008), pp. 639–707.
DOI: 10.1140/epjc/s10052-008-0798-9. arXiv: 0803.0883 [hep-ph].

[109] J. Alwall et al. "The automated computation of tree-level and next-to-leading order differential cross sections, and their matching to parton shower simulations".
In: *JHEP* 07 (2014), p. 079. arXiv: 1405.0301 [hep-ph].

[110] ATLAS Collaboration. *Comparison of Monte Carlo generator predictions from Powheg and Sherpa to ATLAS measurements of top pair production at 7 TeV*.
ATL-PHYS-PUB-2015-011. 2015. URL: https://cds.cern.ch/record/2020602.

[111] M. Czakon and A. Mitov. "Top++: A Program for the Calculation of the Top-Pair Cross-Section at Hadron Colliders". In: *Comput.Phys.Commun.* 185 (2014), p. 2930.
DOI: 10.1016/j.cpc.2014.06.021. arXiv: 1112.5675 [hep-ph].

[112] M. Cacciari et al. "Top-pair production at hadron colliders with next-to-next-to-leading logarithmic soft-gluon resummation". In: *Phys. Lett.* B710 (2012), pp. 612–622. DOI: 10.1016/j.physletb.2012.03.013. arXiv: 1111.5869 [hep-ph].

[113] M. Beneke et al. "Hadronic top-quark pair production with NNLL threshold resummation". In: *Nucl. Phys.* B855 (2012), pp. 695–741. DOI: 10.1016/j.nuclphysb.2011.10.021. arXiv: 1109.1536 [hep-ph].

[114] P. Baernreuther, M. Czakon, and A. Mitov. "Percent Level Precision Physics at the Tevatron: First Genuine NNLO QCD Corrections to $q\bar{q} \to t\bar{t} + X$". In: *Phys. Rev. Lett.* 109 (2012), p. 132001. DOI: 10.1103/PhysRevLett.109.132001. arXiv: 1204.5201 [hep-ph].

[115] M. Czakon and A. Mitov. "NNLO corrections to top-pair production at hadron colliders: the all-fermionic scattering channels". In: *JHEP* 12 (2012), p. 054. DOI: 10.1007/JHEP12(2012)054. arXiv: 1207.0236 [hep-ph].

[116] M. Czakon and A. Mitov. "NNLO corrections to top pair production at hadron colliders: the quark-gluon reaction". In: *JHEP* 01 (2013), p. 080. DOI: 10.1007/JHEP01(2013)080. arXiv: 1210.6832 [hep-ph].

[117] M. H. Seymour and A. Siodmok. "Constraining MPI models using σ_{eff} and recent Tevatron and LHC Underlying Event data". In: *JHEP* 1310 (2013), p. 113. DOI: 10.1007/JHEP10(2013)113. arXiv: 1307.5015 [hep-ph].

[118] S. Frixione et al. "Single-Top Production in MC@NLO". In: *JHEP* 03 (2006), p. 092. DOI: 10.1088/1126-6708/2006/03/092. arXiv: hep-ph/0512250 [hep-ph].

[119] R. Frederix, E. Re, and P. Torrielli. "Single-top t-channel hadroproduction in the four-flavour scheme with POWHEG and aMC@NLO". In: *JHEP* 1209 (2012), p. 130. DOI: 10.1007/JHEP09(2012)130. arXiv: 1207.5391 [hep-ph].

[120] N. Kidonakis. "Next-to-next-to-leading-order collinear and soft gluon corrections for t-channel single top quark production". In: *Phys. Rev. D* 83 (2011), p. 091503. DOI: 10.1103/PhysRevD.83.091503. arXiv: 1103.2792 [hep-ph].

[121] N. Kidonakis. "Two-loop soft anomalous dimensions for single top quark associated production with a W- or H-". In: *Phys. Rev. D* 82 (2010), p. 054018. DOI: 10.1103/PhysRevD.82.054018. arXiv: 1005.4451 [hep-ph].

[122] N. Kidonakis. "NNLL resummation for s-channel single top quark production". In: *Phys. Rev. D* 81 (2010), p. 054028. DOI: 10.1103/PhysRevD.81.054028. arXiv: 1001.5034 [hep-ph].

[123] S. Frixione et al. "Single-top hadroproduction in association with a W boson". In: *Journal of High Energy Physics* 2008.07 (2008), p. 029. URL: http://stacks.iop.org/1126-6708/2008/i=07/a=029.

[124] E. Re. "Single-top Wt-channel production matched with parton showers using the POWHEG method". In: *The European Physical Journal C* 71.2 (2011), p. 1547. ISSN: 1434-6052. DOI: 10.1140/epjc/s10052-011-1547-z. URL: https://doi.org/10.1140/epjc/s10052-011-1547-z.

[125] ATLAS Collaboration. *Studies on top-quark Monte Carlo modelling for Top2016.* Tech. rep. ATL-PHYS-PUB-2016-020. Geneva: CERN, 2016. URL: https://cds.cern.ch/record/2216168.

[126] T. Gleisberg et al. "Event generation with SHERPA 1.1". In: *JHEP* 0902 (2009), p. 007. DOI: 10.1088/1126-6708/2009/02/007. arXiv: 0811.4622 [hep-ph].

[127] T. Gleisberg and S. Höche. "Comix, a new matrix element generator". In: *JHEP* 0812 (2008), p. 039. DOI: 10.1088/1126-6708/2008/12/039. arXiv: 0808.3674 [hep-ph].

[128] F. Cascioli, P. Maierhofer, and S. Pozzorini. "Scattering Amplitudes with Open Loops". In: *Phys. Rev. Lett.* 108 (2012), p. 111601. DOI: 10.1103/PhysRevLett.108.111601. arXiv: 1111.5206 [hep-ph].

[129] S. Schumann and F. Krauss. "A Parton shower algorithm based on Catani-Seymour dipole factorisation". In: *JHEP* 0803 (2008), p. 038. DOI: 10.1088/1126-6708/2008/03/038. arXiv: 0709.1027 [hep-ph].

[130] S. Höche et al. "QCD matrix elements + parton showers: The NLO case". In: *JHEP* 04 (2013), p. 027. DOI: 10.1007/JHEP04(2013)027. arXiv: 1207.5030 [hep-ph].

[131] T. D. Gottschalk. "A Realistic Model for e+ e- Annihilation Including Parton Bremsstrahlung Effects". In: *Nucl. Phys.* B214 (1983), pp. 201–222. DOI: 10.1016/0550-3213(83)90658-2.

[132] T. D. Gottschalk. "An improved description of hadronization in the QCD cluster model for e^+e^- annihilation". In: *Nuclear Physics B* 239 (July 1984), pp. 349–381. DOI: 10.1016/0550-3213(84)90253-0.

[133] B. R. Webber. "A QCD Model for Jet Fragmentation Including Soft Gluon Interference". In: *Nucl. Phys.* B238 (1984), pp. 492–528. DOI: 10.1016/0550-3213(84)90333-X.

[134] T. D. Gottschalk and D. A. Morris. "A new model for hadronization and e^+e^- annihilation". In: *Nuclear Physics B* 288 (1987), pp. 729 –781. ISSN: 0550-3213. DOI: https://doi.org/10.1016/0550-3213(87)90236-7. URL: http://www.sciencedirect.com/science/article/pii/0550321387902367.

[135] C. Anastasiou et al.
"High precision QCD at hadron colliders: Electroweak gauge boson rapidity distributions at NNLO". In: *Phys. Rev.* D69 (2004), p. 094008.
arXiv: hep-ph/0312266 [hep-ph].

[136] J. Alwall et al. "MadGraph 5 : Going Beyond". In: *JHEP* 06 (2011), p. 128.
arXiv: 1106.0522 [hep-ph].

[137] M. Botje et al. "The PDF4LHC Working Group Interim Recommendations".
In: (2011). arXiv: 1101.0538 [hep-ph].

[138] F. Derue. *Estimation of fake lepton background for top analyses using the Matrix Method with the 2015 dataset at $\sqrt{s}$=13 TeV with AnalysisTop-2.3.41.*
Tech. rep. ATL-COM-PHYS-2016-198. Geneva: CERN, 2016.
URL: https://cds.cern.ch/record/2135116.

[139] ATLAS Collaboration.
"Estimation of non-prompt and fake lepton backgrounds in final states with top quarks produced in proton-proton collisions at $\sqrt{8}$ TeV with the ATLAS detector".
In: *ATLAS-CONF-2014-058* (2014).

[140] ATLAS Collaboration. In: ().

[141] E. L. Berger et al.
"NNLO QCD corrections to t-channel single top quark production and decay".
In: *Phys. Rev. D* 94 (7 2016), p. 071501. DOI: 10.1103/PhysRevD.94.071501.
URL: https://link.aps.org/doi/10.1103/PhysRevD.94.071501.

[142] T Cornelissen et al. "The new ATLAS track reconstruction (NEWT)".
In: *Journal of Physics: Conference Series* 119.3 (2008), p. 032014.
URL: http://stacks.iop.org/1742-6596/119/i=3/a=032014.

[143] ATLAS Collaboration. "Performance of the ATLAS track reconstruction algorithms in dense environments in LHC Run 2".
In: *The European Physical Journal C* 77.10 (2017), p. 673. ISSN: 1434-6052.
DOI: 10.1140/epjc/s10052-017-5225-7.
URL: https://doi.org/10.1140/epjc/s10052-017-5225-7.

[144] R. Frühwirth. "Application of Kalman filtering to track and vertex fitting".
In: *Nuclear Instruments and Methods in Physics Research Section A: Accelerators, Spectrometers, Detectors and Associated Equipment* 262.2 (1987), pp. 444 –450.
ISSN: 0168-9002. DOI: https://doi.org/10.1016/0168-9002(87)90887-4. URL:
http://www.sciencedirect.com/science/article/pii/0168900287908874.

[145] ATLAS Collaboration. "Reconstruction of primary vertices at the ATLAS experiment in Run 1 proton–proton collisions at the LHC".
In: *The European Physical Journal C* 77.5 (2017), p. 332. ISSN: 1434-6052.
DOI: 10.1140/epjc/s10052-017-4887-5.
URL: https://doi.org/10.1140/epjc/s10052-017-4887-5.

[146] ATLAS Collaboration.
Vertex Reconstruction Performance of the ATLAS Detector at $\sqrt{s} = 13$ TeV.
Tech. rep. ATL-PHYS-PUB-2015-026. Geneva: CERN, 2015.
URL: http://cds.cern.ch/record/2037717.

[147] ATLAS Collaboration.
"Electron reconstruction and identification efficiency measurements with the ATLAS detector using the 2011 LHC proton-proton collision data".
In: *Eur. Phys. J.* C74 (2014), p. 2941. arXiv: 1404.2240 [hep-ex].

[148] ATLAS Collaboration.
"Electron and photon energy calibration with the ATLAS detector using LHC Run 1 data". In: *Eur. Phys. J.* C74 (2014), p. 3071. arXiv: 1407.5063 [hep-ex].

[149] ATLAS Collaboration. *Electron efficiency measurements with the ATLAS detector using the 2015 LHC proton-proton collision data.* Geneva, 2016.
URL: https://cds.cern.ch/record/2157687.

[150] ATLAS Inner Tracking Combined Performance Group. *TrackVertexAssociationTool.*
URL: https://twiki.cern.ch/twiki/bin/view/AtlasProtected/TrackVertexAssociationTool.

[151] ATLAS Collaboration. "Muon reconstruction performance of the ATLAS detector in proton–proton collision data at $\sqrt{s} = 13$ TeV".
In: *The European Physical Journal C* 76.5 (2016), p. 292. ISSN: 1434-6052.
DOI: 10.1140/epjc/s10052-016-4120-y.
URL: https://doi.org/10.1140/epjc/s10052-016-4120-y.

[152] ATLAS Collaboration. "Topological cell clustering in the ATLAS calorimeters and its performance in LHC Run 1".
In: *The European Physical Journal C* 77.7 (2017), p. 490. ISSN: 1434-6052.
DOI: 10.1140/epjc/s10052-017-5004-5.
URL: https://doi.org/10.1140/epjc/s10052-017-5004-5.

[153] M. Cacciari, G. P. Salam, and G. Soyez. "The Anti-k(t) jet clustering algorithm".
In: *JHEP* 04 (2008), p. 063. arXiv: 0802.1189 [hep-ph].

[154] M. Cacciari, G. P. Salam, and G. Soyez. "FastJet user manual".
In: *The European Physical Journal C* 72.3 (2012), p. 1896. ISSN: 1434-6052.
DOI: 10.1140/epjc/s10052-012-1896-2.
URL: https://doi.org/10.1140/epjc/s10052-012-1896-2.

[155] ATLAS Collaboration.
"Jet energy scale measurements and their systematic uncertainties in proton-proton collisions at $\sqrt{s} = 13$ TeV with the ATLAS detector".
In: *Phys. Rev. D* 96 (7 2017), p. 072002. DOI: 10.1103/PhysRevD.96.072002.
URL: https://link.aps.org/doi/10.1103/PhysRevD.96.072002.

[156] ATLAS Collaboration. "Performance of pile-up mitigation techniques for jets in pp collisions at $\sqrt{s} = 8$ TeV using the ATLAS detector". In: (2015). arXiv: 1510.03823 [hep-ex].

[157] ATLAS Collaboration. *b-tagging in dense environments.* Tech. rep. ATL-PHYS-PUB-2014-014. Geneva: CERN, 2014. URL: http://cds.cern.ch/record/1750682.

[158] ATLAS Collaboration. "Performance of b-jet identification in the ATLAS experiment". In: *Journal of Instrumentation* 11.04 (2016), P04008. URL: http://stacks.iop.org/1748-0221/11/i=04/a=P04008.

[159] ATLAS Collaboration. *Expected performance of the ATLAS b-tagging algorithms in Run-2.* Tech. rep. ATL-PHYS-PUB-2015-022. Geneva: CERN, 2015. URL: https://cds.cern.ch/record/2037697.

[160] ATLAS Collaboration. *Optimisation of the ATLAS b-tagging performance for the 2016 LHC Run.* Tech. rep. ATL-PHYS-PUB-2016-012. Geneva: CERN, 2016. URL: https://cds.cern.ch/record/2160731.

[161] ATLAS Flavour Tagging Working Group. *Flavour tagging recommendations in release 20.7.* URL: https://twiki.cern.ch/twiki/bin/view/AtlasProtected/BTagCalib2015.

[162] *Selection of jets produced in 13TeV proton-proton collisions with the ATLAS detector.* Tech. rep. ATLAS-CONF-2015-029. Geneva: CERN, 2015. URL: https://cds.cern.ch/record/2037702.

[163] ATLAS Jet and Etmiss Combined Performance Group. *HowToCleanJets2016 : Jet-Based Event Cleaning.* 2016. URL: https://twiki.cern.ch/twiki/bin/view/AtlasProtected/HowToCleanJets2016.

[164] B. Nachman et al. "Jets from jets: re-clustering as a tool for large radius jet reconstruction and grooming at the LHC". In: *Journal of High Energy Physics* 2015.2 (2015), p. 75. ISSN: 1029-8479. DOI: 10.1007/JHEP02(2015)075. URL: https://doi.org/10.1007/JHEP02(2015)075.

[165] D Adams et al. *Recommendations of the Physics Objects and Analysis Harmonisation Study Groups 2014.* Tech. rep. ATL-PHYS-INT-2014-018. Geneva: CERN, 2014. URL: https://cds.cern.ch/record/1743654.

[166] ATLAS Collaboration. *Performance of missing transverse momentum reconstruction with the ATLAS detector in the first proton–proton collisions at* $\sqrt{s} = 13$ *TeV.* ATL-PHYS-PUB-2015-027. 2015. URL: http://cdsweb.cern.ch/record/2037904.

[167] ATLAS Collaboration. "Search for single production of vector-like quarks decaying into Wb in pp collisions at $\sqrt{s} = 8$ TeV with the ATLAS detector". In: (2016). arXiv: 1602.05606 [hep-ex].

[168] ATLAS Collaboration. "Improved luminosity determination in pp collisions at sqrt(s) = 7 TeV using the ATLAS detector at the LHC". In: *Eur. Phys. J.* C73 (2013), p. 2518. arXiv: 1302.4393 [hep-ex].

[169] ATLAS LUCID Collaboration. *Measurement of the luminosity with the new LUCID-2 detector in 2015.* Tech. rep. ATL-COM-FWD-2016-008. Geneva: CERN, 2016. URL: https://cds.cern.ch/record/2154368.

[170] ATLAS Collaboration. *Tagging and suppression of pileup jets with the ATLAS detector.* Tech. rep. ATLAS-CONF-2014-018. Geneva: CERN, 2014. URL: http://cds.cern.ch/record/1700870.

[171] ATLAS Jet and Etmiss Combined Performance Group. *JVT Calibration.* URL: https://twiki.cern.ch/twiki/bin/view/AtlasProtected/JVTCalibration.

[172] ATLAS Collaboration. "Performance of the ATLAS Trigger System in 2010". In: *Eur. Phys. J. C* 72 (2012), p. 1849. DOI: 10.1140/epjc/s10052-011-1849-1. arXiv: 1110.1530 [hep-ex].

[173] ATLAS Collaboration. "Electron and photon energy calibration with the ATLAS detector using LHC Run 1 data". In: *The European Physical Journal C* 74.10 (2014), p. 3071. ISSN: 1434-6052. DOI: 10.1140/epjc/s10052-014-3071-4. URL: https://doi.org/10.1140/epjc/s10052-014-3071-4.

[174] ATLAS Collaboration. *Expected performance of missing transverse momentum reconstruction for the ATLAS detector at $\sqrt{s} = 13$ TeV.* ATL-PHYS-PUB-2015-023. 2015. URL: https://cds.cern.ch/record/2037700.

[175] ATLAS Jet and Etmiss Combined Performance Group. *JetEtMiss Recommendations for MC15 (Release 20.7).* URL: https://twiki.cern.ch/twiki/bin/view/AtlasProtected/JetEtmissRecommendations2016.

[176] ATLAS Collaboration. *Jet Calibration and Systematic Uncertainties for Jets Reconstructed in the ATLAS Detector at $\sqrt{s} = 13$ TeV.* ATL-PHYS-PUB-2015-015. 2015. URL: https://cds.cern.ch/record/2037613.

[177] ATLAS Jet and Etmiss Combined Performance Group. *Uncertainty release for analyses using 2015 and 2016 data in 20.7 (MC15c) releases.* URL: https://twiki.cern.ch/twiki/bin/view/AtlasProtected/JetUncertainties20152016Data20p7.

[178] ATLAS Collaboration. "Jet energy measurement and its systematic uncertainty in proton-proton collisions at $\sqrt{s} = 7$ TeV with the ATLAS detector". In: *Eur. Phys. J.* C75.1 (2015), p. 17. arXiv: 1406.0076 [hep-ex].

[179] J. Butterworth et al. "PDF4LHC recommendations for LHC Run II". In: *J. Phys.* G43 (2016), p. 023001. DOI: 10.1088/0954-3899/43/2/023001. arXiv: 1510.03865 [hep-ph].

[180] ATLAS Monte Carlo Tuning Group. *Recommendation for using PDFs.* URL: https://twiki.cern.ch/twiki/bin/view/AtlasProtected/PdfRecommendations.

[181] K. Melnikov and F. Petriello. "Electroweak gauge boson production at hadron colliders through $O(\alpha_S^2)$". In: *Phys. Rev. D* 74 (2006), p. 114017. DOI: 10.1103/PhysRevD.74.114017. arXiv: hep-ph/0609070 [hep-ph].

[182] W. Wagner et al. *Measurement of the inclusive cross-sections of single top-quark and top-antiquark t-channel production in pp collisions at $\sqrt{s}$ = 13 TeV.* Tech. rep. ATL-COM-PHYS-2016-102. Geneva: CERN, 2016. URL: https://cds.cern.ch/record/2129154.

[183] A. Bandyopadhyay et al. *Search for single production of vector-like quarks decaying into Wb in pp collisions at $\sqrt{s}$ = 13 TeV with the ATLAS detector.* Tech. rep. ATL-COM-PHYS-2016-027. Internal note for a Y/T->Wb VLQ search done in the HQT exotic group. Geneva: CERN, 2016. URL: https://cds.cern.ch/record/2120756.

[184] G. Cowan et al. "Asymptotic formulae for likelihood-based tests of new physics". In: *The European Physical Journal C* 71.2 (2011), p. 1554. ISSN: 1434-6052. DOI: 10.1140/epjc/s10052-011-1554-0. URL: https://doi.org/10.1140/epjc/s10052-011-1554-0.

[185] ATLAS Collaboration. *TtHFitter/TRexFitter framework.* URL: https://twiki.cern.ch/twiki/bin/view/AtlasProtected/TtHFitter.

[186] K. Cranmer et al. "HistFactory: A tool for creating statistical models for use with RooFit and RooStats". In: CERN-OPEN-2012-016 (2012).

[187] W. Verkerke and D. P. Kirkby. *The RooFit toolkit for data modeling.* 2003. arXiv: physics/0306116 [physics.data-an].

[188] W. Verkerke and D. Kirkby. *RooFit Users Manual.* URL: http://roofit.sourceforge.net/.

[189] G. Cowan et al. "Asymptotic formulae for likelihood-based tests of new physics". In: *Eur. Phys. J. C* 71 (2011), p. 1554. DOI: 10.1140/epjc/s10052-011-1554-0. arXiv: 1007.1727 [physics.data-an].

[190] G. Cowan et al.
"Erratum to: Asymptotic formulae for likelihood-based tests of new physics".
In: *Eur. Phys. J. C* 73.7 (2013), pp. 1–1. DOI: 10.1140/epjc/s10052-013-2501-z.
arXiv: 1007.1727 [physics.data-an].

[191] T. Junk.
"Confidence level computation for combining searches with small statistics".
In: *Nucl. Instrum. Meth. A* 434 (1999), p. 435.
DOI: 10.1016/S0168-9002(99)00498-2. arXiv: hep-ex/9902006 [hep-ex].

[192] A. L. Read. "Presentation of search results: The CL(s) technique".
In: *J. Phys. G* 28 (2002), p. 2693. DOI: 10.1088/0954-3899/28/10/313.

[193] J. Conway.
"Incorporating nuisance parameters in likelihoods for multisource spectra".
In: *arXiv preprint arXiv:1103.0354* (2011).